

NORTHWESTERN UNIVERSITY

Phase-Sensitive Second-Order Nonlinear Spectroscopy of Metal  
Oxide:Aqueous Interfaces

A DISSERTATION

SUBMITTED TO THE GRADUATE SCHOOL  
IN PARTIAL FULFILLMENT OF THE REQUIREMENTS

for the degree

DOCTOR OF PHILOSOPHY

Field of Chemistry

By

Emilie Lozier

EVANSTON, ILLINOIS

September 2023

© Copyright by Emilie Lozier 2023

All Rights Reserved

## Abstract

Phase-Sensitive Second-Order Nonlinear Spectroscopy of Metal Oxide:Aqueous Interfaces

Emilie Lozier

Many processes in nature and human-made settings rely on the unique properties of charged metal oxide:aqueous interfaces. Despite their ubiquity, these buried interfaces are challenging to study, since any analytical technique aiming to overcome the relatively small number density of interfacial *versus* bulk species must be highly sensitive and surface-selective. Nonlinear optical spectroscopies such as second harmonic generation (SHG) leverage the inherent anisotropy of metal oxide:aqueous interfaces to provide a direct optical probe of the E-field emanating from the charged solid, granting insight on properties such as interfacial charge density and surface coverage of adsorbed species. Moreover, recent advances in heterodyne detection (HD) have further empowered this technique to disentangle second- and third-order contributions to the measured SHG signal and facilitate the calculation of quantities such as interfacial potential and number of net aligned Stern layer water molecules without the use of traditional models describing charged surfaces. Although HD-SHG has developed extensively in its application to understanding dynamics at fused silica:aqueous interfaces, its application to strongly absorbing metal oxides remains nascent. In this thesis we demonstrate the application of HD-SHG analysis to the  $\alpha$ -hematite:aqueous interface as a model absorbing metal oxide and one of the most ecologically and economically important ores of iron. More specifically, we highlight best practices in sample deposition, cleaning, and storage; the advantages and disadvantages of different sample geometries; the benefits of using an oscillator-only laser system for HD-SHG analysis; and the first steps toward developing an optical model to

interpret phase-sensitive measurements performed at or near resonance. Major challenges remain for this system—including experimental design that fully accounts for the significant hysteresis of  $\alpha$ -hematite—however, this thesis aims to serve as a record of the long and iterative journey toward expanding the scope of HD-SHG to a broader range of metal oxide:aqueous interfaces of environmental and technological relevance.

## Acknowledgements

A thesis is not the work of one person. I would like to thank my advisor Professor Franz Geiger for seeing me as whole individual and understanding when research problems proved to be thornier than expected. Thank you to my committee, Professors Dayne Swearer and Chad Mirkin, as well as former committee member Professor Danna Freedman and former chair Professor Peter Stair. Each of these individuals took time to engage with my research and challenge me to improve it. I extend particular thanks to Professor Swearer for your willingness and enthusiasm in joining my committee within just a few months of my defense.

None of the work presented in this thesis was possible without the resources and experience of Northwestern's core facilities and the consummate professionals who run them. Thank you to Dr. Anil Dhote at the Materials Processing and Microfabrication facility (MPMF), Dr. Serkan Butun at the Micro/Nano Fabrication (NUFAB) facility, Jerry Carsello at the Jerome B.Cohen X-Ray Diffraction facility, Dr. Gajendra Shekhawat at the Scanned Probe Imaging and Development (SPID) facility, and Dr. Xinqi Chen at the Keck Interdisciplinary Surface Science (Keck-II) center.

To Dr. Alex Martinson and Dr. Aaron Taggart at Argonne National Laboratory, I send a hearty thank you for making hematite films with much more skill and consistency than I could ever manage as a deposition dilettante myself. I asked you for an awful lot of hematite over the last 5 years, and still you were always cheerful collaborators and communicators. Thank you both.

I offer a special thank you to Salomon Rodriquez and the staff of the Student Research Machine Shop. The hours spent in the shop creating custom flow cells, holders, faceplates,

and adapters not only served to enable my research, but also created an island of tranquility for me amid the stress of graduate school. As a graduate student, it is unusual to get to step away from the computer monitor and work with one's hands, and I count myself as incredibly fortunate to have had the opportunity to fabricate my own tools and parts. I know these skills will stay with me for years, especially thanks to Salomon's high standards for safety, professionalism, and craftsmanship. Thank you.

Much like on-campus core facilities, I found a great deal of support from off-campus institutions as well, namely Tomate Fresh Kitchen and Sketchbook Brewing Company. It is no secret that these are legendary locations in the mythos of the Northwestern graduate population, and I am not the only one to credit these burritos and brews for fueling my science. Thank you to the folks who work to make these places a home to those who visit, and being an escape from the grind.

To my former senior labmates Dr. Mavis Boamah, Dr. Paul Ohno, Dr. Ariana Gray-Bé, Dr. Johnny Varelas, Dr. Naomi Dalchand, and Dr. Yangdongling (Dawning) Liu—thank you for taking so many collective hours to make sure I knew what I needed to know to make it through 5 years of graduate school. I cannot understate how important it was to go through this experience knowing that my coworkers had my back, and so much of what I know now about leadership and mentorship, I learned from you all. Although this lab has existed long enough for there to be members I never met, I do also feel a sense of gratitude to the original graduate students who set the tone for what the Geiger group's values and expectations are. Thank you to all who came before.

To the workers who joined or passed through the lab after me, I also offer thanks. Catherine Walker—you were a great partner on a tricky project, and I wish you all

the best as you continue now on your own PhD journey. To Shichuan (Rico) Xi and Cat Ly—the way you both stick to your principles will always impress me, even in the midst of trying circumstances. To Alyssa Olson—one of my few fellow Wisconsinites at Northwestern—thank you for being so unwaveringly compassionate and supportive. To our rising 2<sup>nd</sup> years—Amani Alghamdi, Ezra Marker, and Raiden Speelman—you are the future of this lab, and I am eager to see how you helm this vessel now that all of us 5<sup>th</sup>-year “rats” have fled.

To my cohort-mates—there is truly no reality where I could have made it through this program without you. It is an honor to be able to refer to you all here as DOCTORS Jana Butman, HanByul Chang, Emily Ma, and Aleia Bellcross—and having gotten that honorific out of the way I will now dispense with formalities. Jana, thank you for always bringing a smile to my face and a bit of levity to the darkness with your axolotl antics or some niche joke from our overlapping video-game nerdoms. HanByul, goodness knows I have broken down crying in front of you too many times to count and you always manage to affirm my feelings while providing much needed insight to keep things in perspective. Emily, the road has not always been easy, but you bring a level of thoughtfulness and earnestness to all that you do that has left me the better for knowing you. Aleia, you get me, and whether we are taking on the monster that is graduate school, a rival rugby team, or some made-up Dungeons & Dragons boss, you are the kind of friend who makes any trial into an adventure.

Beyond my work at the laser table, one of the most meaningful projects I could hope to be involved with at Northwestern was the successful unionization of graduate workers. The road to our 94% favorable win in January of 2023 with over 1,700 eligible votes cast

begins back as far as 2016, to a time when unionization felt like a pipe dream at best. To Dr. Emily McClure, Dr. Chris Eckdahl, Dr. Emily Ma, and Dr. Alexandra Berl—it is scary to start organizing when it feels like you are alone. Thank you for being right there with me when the idea of unionization was so new to our program. Looking ahead, I am lucky to be leaving knowing that organizing in Chemistry will continue. To Stella Fors, Haley McCallister, Hannah Eckvahl, Emma-Rose Newmeyer, Elisabeth Latawicz, Alexis Martell, Ben Oxley, Clover Moisanu, and many more who I have doubtless overlooked—thank you all for being receptive to the call to fight for something better, on top of everything else you all are doing. Once upon a time we were few, and now we are many.

To take part in this fight within my own department was a gift unto itself, but I also could never have anticipated how rewarding it was to engage with my colleagues across Northwestern as an elected officer of Northwestern University Graduate Workers (NUGW-UE Local 1122). To Dr. Julie Ming Liang and Rose Werth—thank you for convincing me to take the plunge and run for co-chair, and for leading by your incredible example. To this day I can only dream of talking “union” as skillfully as you both do. To my successors, Kavi Chintam and Esther Kamm—I hope that a year from now when you are standing where I am, you can look back and enjoy the journey. You are both such skilled leaders and compassionate organizers, and I have no fear stepping away knowing the folks who take up the mantle.

To my fellow officers—Andy Holter, Jack Bandy, John Branch, Dr. Qining Wang, Jacob McLaughlin, and Emily Masincup—it was not a simple task, what we took on, but despite the long hours and suspenseful moments, we have left Northwestern a better place than we found it. To my co-chair—Sara Bowden—thank you for fielding those moments

of panic, being a sympathetic ear, trusting me with your own dreams and frustrations, and inspiring me to always make that extra push. For all of us, I am so proud of how we have built a tool for ourselves and future generations of graduate students to take an active role in determining our workplace conditions.

To my Dungeons & Dragons group—Aleia, Sebastian Bacon, Nic Vigilante, and Israel Da Silva—thank you for the many hours of wacky hijinks and gothic horror. Everyone needs a little escapism, especially when you are slogging through your graduate degree. Thank you for being the party to my DM, even if we never quite made it out of Vallaki.

To my other friends at Northwestern and beyond—Shobhana Panuganti, Shelby Cuthriell, Laura Nevill, Anika Burg, Elena Hartley, Grace Baldwin, Danielle Berkowsky, Monica Dix, and Eliza Cuevas—thank you for providing much needed respite from the storm, and for being brilliant and compassionate individuals in your own rights. To my dear friend Anjana Murali (who will soon be a doctor—yes, THAT kind of doctor)—although our paths have taken us to different parts of the country and different professional fields, I know that every time I pick up the phone and call you we will pick up right where we left off. From Girl Scouts in high school to graduate and medical school, my life has been better for having you in it. Thank you.

Of course, I would not be here without the steadfast support of my family. To my parents, Vashti and Luke Lozier, thank you for raising me to be the person, scientist, and organizer that I am today. I credit you both—and the Science Museum of Minnesota—with piquing my interest in how the world works, and I will carry that with me for the rest of my life. I am so fortunate to never doubt that you both love me unconditionally, and that truly means the world to me. To my sisters, Annalise and Bella Lozier—thank you

for being my closest friends and inexhaustible confidantes. There are not many people out there that I have known as long as you two, and the fact that you both still entertain my nonsense is a blessing. I even forgive you both for being massively talented and brilliant in ways I could never rival, even though it is frankly rude to be so amazing all the time.

To the McCollums—being with your family has always felt like a home away from home. Thank you, Tara, for fostering my love of good food and cooking with loved ones. Thank you, Angus, for introducing me to science fiction (and  $\LaTeX$ , of course). Thank you, Ian, for being a buddy in organizing from afar, and understanding the tribulations of GOTV and phonebanking. Thank you, Malia, for keeping me in stitches with your wry humor and always being a great companion in enjoying fiction and graphic novels. To my grandparents, Pappy and Betty Grace, thank you for making the long trip from Arkansas to be present at my defense—I am so proud to share this moment with you. To my cousin, Chloe McCollum—it has been such a joy to go through graduate school at the same time as you, knowing that I can always call you up to vent and you will immediately get what I am talking about. Thank you, and congratulations, Dr. McCollum.

To Andrew—thank you for being my partner in life, crime, and science, and the cat dad to our beautiful boys. You have my back in a way that makes me feel like everything will work out in the end. I look forward to the day when I get to cheerlead you through your own thesis-writing ordeal, returning the favor for all of the unconditional support, love, and patience you have shown me these last few months.

And to the real heroes in my life—Percy, Grover, Bo, and Daisy (with a shout-out to “Uncle” Arthur and Zulu)—you weirdos keep me on my toes.

## LIST OF ABBREVIATIONS

|  |  |
|--|--|
| <b>AdC:</b> Adventitious carbon                    | <b>MCET:</b> Metal-coupled electron transfer |
| <b>AFM:</b> Atomic force microscopy                | <b>MeOH:</b> Methanol                        |
| <b>ALD:</b> Atomic layer deposition                | <b>M:MO<sub>x</sub>:</b> Metal:metal oxide   |
| <b>APT:</b> Atom probe tomography                  | <b>NIR:</b> Near infrared                    |
| <b>au:</b> Arbitrary units                         | <b>OH:</b> Hydroxyl group                    |
| <b>BIF:</b> Banded iron formation                  | <b>PSU:</b> Phase shifting unit              |
| <b>cp100ms:</b> Counts per 100 milliseconds        | <b>PEC:</b> Photoelectrochemical             |
| <b>cps:</b> Counts per second                      | <b>PFAS:</b> Perfluoroalkyl substances       |
| <b>C/R:</b> Calibration and referencing            | <b>PFOA:</b> Perfluorooctanoic acid          |
| <b>DC:</b> Static                                  | <b>PFOS:</b> Perfluorooctane sulfonic acid   |
| <b>EBL:</b> Electron blocking layer                | <b>PTFE:</b> Polytetrafluoroethylene         |
| <b>EDL:</b> Electrical double layer                | <b>PVD:</b> Physical vapor deposition        |
| <b>GIXRD:</b> Grazing incidence X-ray diffraction  | <b>QAC:</b> Quaternary ammonium compound     |
| <b>GIXRR:</b> Grazing incidence X-ray reflectivity | <b>QCM:</b> Quartz crystal microbalance      |
| <b>HD:</b> Heterodyne-detected                     | <b>RO:</b> Reference oscillator              |
| <b>IL:</b> Ionic liquid                            | <b>SFG:</b> Sum frequency generation         |
| <b>LO:</b> Local oscillator                        | <b>SHG:</b> Second harmonic generation       |
| <b>LMCT:</b> Ligand metal charge transfer          | <b>TENG:</b> Triboelectric nanogenerator     |
|  | <b>UV:</b> Ultraviolet                       |
|  | <b>XPS:</b> X-ray photoelectron spectroscopy |

*Dedicated to the memory of my grandmother Elizabeth (Betty) McCollum.  
You departed this Earth to join the stars, but the night sky will forever be a blessing to  
those who continue to love you.*



*February 3, 1941—April 21, 2020*

## Table of Contents

|   |    |
|---|----|
| Abstract  | 3  |
| Acknowledgements  | 5  |
| List of Abbreviations   | 11 |
| List of Figures   | 17 |
| List of Tables  | 26 |
| Chapter 1. Metal Oxide:Aqueous Interfaces in Natural and Artificial Environments          | 28 |
| 1.1. Defining Interfaces and their Importance   | 28 |
| 1.2. Relevance of Metal Oxide:Aqueous Interfaces  | 30 |
| 1.3. Technical Challenges to Studying Buried Metal Oxide:Aqueous Interfaces               | 32 |
| 1.4. Scope and Organization of Thesis   | 34 |
| Chapter 2. Second Harmonic Generation (SHG) Spectroscopy and Phase-Sensitive Measurements | 37 |
| 2.1. Introduction to Second Harmonic Generation (SHG) Spectroscopy                        | 38 |
| 2.2. Phase Sensitive Measurements and Heterodyne Detection (HD)                           | 41 |
| 2.3. Heterodyne-Detected (HD) Second Harmonic Generation (SHG) Set-Ups                    | 46 |
| 2.4. Experimental   | 54 |

|   |     |
|---|-----|
|   | 14  |
| Chapter 3. Metal: Metal Oxide Nanofilms for Energy Transduction                       | 57  |
| 3.1. Background   | 58  |
| 3.2. Experimental   | 61  |
| 3.3. Results  | 67  |
| 3.4. Summary and Future Directions  | 73  |
| Chapter 4. Adapting Heterodyne Detected Second Harmonic Generation (HD-SHG)           |     |
| Spectroscopy to Metals and Metal Oxides   | 76  |
| 4.1. Background   | 76  |
| 4.2. Optimization   | 78  |
| 4.3. Calculations   | 93  |
| 4.4. Summary  | 98  |
| Chapter 5. Understanding the Electrostatics of $\alpha$ -Hematite: Aqueous Interfaces | 101 |
| 5.1. Background   | 101 |
| 5.2. Experimental   | 107 |
| 5.3. Results  | 110 |
| 5.4. Summary and Future Directions  | 133 |
| REFERENCES  | 139 |
| References for Chapter 1  | 139 |
| References for Chapter 2  | 143 |
| References for Chapter 3  | 146 |
| References for Chapter 4  | 153 |
| References for Chapter 5  | 158 |

|   |     |
|---|-----|
|   | 15  |
| Appendix A. Proof of Concept: HD-SHG on <i>c</i> -Cut Sapphire Optical Windows  | 166 |
| A.1. Background   | 166 |
| A.2. Experimental   | 168 |
| A.3. Results  | 169 |
| A.4. Summary and Future Directions  | 173 |
| Appendix B. Interaction of Perfluorooctanoic Acid (PFOA) and Perfluorooctane<br>Sulfonic Acid (PFOS) with Fused Silica:Aqueous Interfaces | 174 |
| B.1. Background   | 175 |
| B.2. Experimental   | 177 |
| B.3. Results  | 178 |
| B.4. Summary and Future Directions  | 185 |
| Appendix C. Original Research Proposal: Nonlinear Spectroscopy of Ionic Liquids<br>Interacting with Model Mineral Surfaces                | 187 |
| C.1. Abstract   | 187 |
| C.2. Background and Previous Work   | 188 |
| C.3. Hypotheses   | 190 |
| C.4. Scientific Objectives  | 192 |
| C.5. Proposed Research  | 192 |
| C.6. Summary  | 198 |
| References for Appendix A   | 201 |
| References for Appendix B   | 205 |
| References for Appendix C   | 211 |

Curriculum Vitae

## List of Figures

- 2.1 Graphical depictions of (a) the quantum mechanical description of the generalized SHG process, including energy levels, and (b) the triple layer model (*a.k.a.* the Gouy-Chapman-Stern model.<sup>4-6</sup>) 40
- 2.2 Graphical depictions of the contributions of  $\chi^{(2)}$ ,  $\chi^{(3)}$ ,  $\Phi(0)$ , and  $\varphi_{DC}$  to the observables of a typical HD-SHG experiment ( $E_{sig}$  and  $\varphi_{sig}$ ) under (a) low and (b) high ionic strength conditions. 43
- 2.3 Graphical depiction of the refraction angles of the fundamental ( $\omega$ ) and SHG ( $2\omega$ ) beams passing through a fused silica window of thickness  $d$  rotated at some angle  $\alpha$  relative to the beam path. Adapted from a figure by Kim and coworkers.<sup>18</sup> 45
- 2.4 The interference pattern in  $I_{SHG}$  (open circles) obtained using a rotational PSU (*i.e.* System 2). The sample under study was a 1-mm-thick fused silica window ALD-coated with 10 nm of  $\alpha$ -hematite in contact with an aqueous solution of 1 M NaCl pH-balanced to pH 6. The solid line shows the result of fitting the raw data with Eq. 2.2.4. 46
- 2.5 Schematic of the “System 1” HD-SHG set-up used to conduct the majority of experiments reported in Chapter 3. Set-up drawn using

|     |  |    |
|-----|--|----|
|     |  | 18 |
|     | and/or adapting some components from ComponentLibrary by Alexander Franzen.  | 47 |
| 2.6 | Schematic of the “System 2” HD-SHG set-up used to conduct the majority of experiments reported in Chapter 4. Set-up drawn using and/or adapting some components from ComponentLibrary by Alexander Franzen.  | 52 |
| 2.7 | Schematic of the house-machined flow set-up used for all experiments conducted with System 2, with components labeled. A different flow cell and holder set-up was used for experiments conducted with System 1, and is described elsewhere. <sup>11,20,21</sup>   | 55 |
| 3.1 | XPS spectra taken of the surface oxide layer (MO <sub>x</sub> ) and reduced metal layer (M) for a selection of M:MO <sub>x</sub> nanofilms. Binding energy ranges surveyed are those corresponding to the constituent metal of each nanofilm. Solid vertical lines indicate peaks associated with the reduced form of a metal and dashed vertical lines indicate those associated with oxidized species, as specified in the figure. | 63 |
| 3.2 | Current obtained from alternating pulses of salt- and freshwater over the surface of a 10-nm Fe:FeO <sub>x</sub> nanofilm mounted in a flow cell (left). Graphical representation of our house-machined custom flow cell (right). Graphic by elabarts.com.   | 66 |
| 3.3 | Graphical representation of static conditions of an Fe:FeO <sub>x</sub> nanofilm surface under static conditions (low and high ionic strength) and   |    |

“gate” conditions triggered by the presence of a salinity gradient.

Graphic by elabarts.com. 68

- 3.4 Measured current for different M:MOx nanofilms and gate conditions, including (a) alternating flow of salt- and freshwater over a nanofilm in a flow cell, (b) rolling alternating droplets of salt- and freshwater down a slanted nanofilm, (c) simulated ocean waves washing over a nanofilm in a wave tank, and (d) dipping a nanofilm into a beaker of phase-separated fomblin (a perfluoropolyether lubricant) and water. 69
- 3.5 Averaged peak current output for a 5-nm Fe:FeOx nanofilm as a function of  $[\text{NaCl}]_{\text{high}}/[\text{NaCl}]_{\text{low}}$ . 70
- 3.6 Current density measurements for 10-nm nanofilms of Al:AlOx, Cr:CrOx, Fe:FeOx, Ni:NiOx, and V:VOx exposed to alternating solutions of pure water and 0.6 M NaCl. 71
- 3.7 Current density measurements for Case A (30-nm Fe:FeOx nanofilm), Case B (30-nm Fe:FeOx nanofilm fully oxidized to form a purely FeOx film), and Case C (30-nm Fe:FeOx nanofilm capped with a 5-nm Cr:CrOx nanofilm) during exposure to an identical salinity-gradient gate in our flow cell set-up. Graphic by elabarts.com. 73
- 4.1 Plots including (a) the normalized absorbance spectra of zero-valent iron (ZVI) films of thicknesses between 5 and 50 nm and an uncoated borosilicate glass microscope slide (1 mm thick) as a point of

- comparison and (b) the absorbances measured at 500 nm and 1000 nm as a function of film thickness. 81
- 4.2 Comparison of the relative stability of three fitting parameters for HD scans taken using System 1 on fused silica:water samples tracked over multi-hour experiments with “sandwich” and flat geometry. 86
- 4.3 Results from an overnight stability study on an uncoated fused silica optical flat taken on System 2 (*i.e.* with the oscillator-only Flint system). Phase drift was calculated to be  $-0.03(4)^\circ/\text{h}$  over 12 h, or essentially flat. 88
- 4.4 Depiction of the reflection of the fundamental beam and the generation of an SHG beam from both the air:fused silica and fused silica:water interfaces. Using a beam block allows complete exclusion of the external beam from detection, since a 1-mm-thick fused silica substrate produces a separation of 0.75 mm between the external and internal beams’ centers. 90
- 4.5 Normalized change in  $I_{SHG}$  due to the transition of the aqueous phase of the fused silica:aqueous interface from pure water to 100 mM NaCl for a hemispherical fused silica sample, a 1-mm-thick flat fused silica sample in contact with a hemispherical fused silica optical coupler, and a 1-mm thick flat fused silica sample with the external reflection both unblocked and blocked. 91

- 4.6 The results of control experiments performed on the System 1 HD-SHG set-up on a silica:quartz interface with the external combined fundamental/SHG beam blocked and unblocked. These include (a) normalized homodyne intensity measurements and (b) power studies showing good quadratic dependence of raw  $I_{SHG}$  counts on input power. 93
- 4.7 Depiction of the refraction of the fundamental 1030-nm beam as it passes from air to the fused silica optical flat and from the fused silica optical flat to water. 95
- 5.1 Narrow-scan XPS spectra of ALD  $\text{Fe}_2\text{O}_3$  films before use (orange traces) and after several exposures to  $\text{CO}_2$ -equilibrated aqueous solutions of NaCl, NaOH, and/or HCl (grayscale traces). Spectra taken of the ALD- $\text{Fe}_2\text{O}_3$ -coated side (solid traces) are shown alongside spectra of the nominally uncoated backsides (dashed traces) of the fused silica substrates for comparison. 111
- 5.2 AFM images taken of a representative ALD  $\alpha$ -hematite film before and after exposure to typical experimental conditions. The color scale denotes profile height in nm. 113
- 5.3 Measured transmission in the UV-visible range for two different ALD  $\alpha$ -hematite films before and after exposure to flowing aqueous solutions of NaCl for day-long timescales. 114

- 5.4 Results from (a) a bandwidth study on a 10-nm ALD  $\alpha$ -hematite film in contact with 1 M NaCl, pH 2 solution and (b) a power study on the same system. 116
- 5.5 Results from a control experiment in which all conditions were held the same with the exception of  $yz$  stage position, allowing interference fringes to be collected from five fully distinct spots on the  $\alpha$ -hematite:aqueous interface. 117
- 5.6 Summary of results of several NaCl screening experiments on two different hematite films at a range of fixed pH values. Minimal change in intensity across the concentration range at pH 6.75 indicates this as the best approximation of the point of zero charge (PZC) for this particular set of ALD hematite films. 122
- 5.7 Homodyne SHG intensity plotted against time for alkalimetric pH jumps at the  $\alpha$ -hematite:aqueous interface starting from the PZC (pH 6.75) and going to (a) pH 9, (b) pH 10, and (c) pH 11. Each cycle (*i.e.* PZC to pH X to PZC) is normalized to its initial  $I_{SHG,PZC}$  value, and offset on the time axis for ease of comparison between consecutive runs. 126
- 5.8 Homodyne SHG intensity plotted against time for acidometric pH jumps at the  $\alpha$ -hematite:aqueous interface starting from the PZC (pH 6.75) and going to (a) pH 5 and (b) pH 3. Each cycle (*i.e.* PZC to pH X to PZC) is normalized to its initial  $I_{SHG,PZC}$  value, and offset on the time axis for ease of comparison between consecutive runs. 127

- 5.9 Summary of averaged  $I_{SHG}$  from six pH titration experiments starting at or near the PZC of  $\alpha$ -hematite and going to and from different target pH values at constant ionic strength (1 M, NaCl as electrolyte), excluding the first cycle of each experiment. Maximum intensities invariably occur at or near the PZC. 128
- 5.10 Corrected values of  $\varphi_{sig}$  (top plot) and normalized values of  $E_{sig}$  (bottom plot) obtained from fitting triplicate scans collected with HD detection. Data points from different days are shown in different colors. 129
- 5.11  $\Phi(0)$  calculated for the  $\alpha$ -hematite:aqueous interface as a function of pH for a range of possible  $\varphi_R$  values. The dataset for  $\varphi_R = 30^\circ$  is displayed alongside its least squares polynomial fit (solid trace), with the 95% confidence interval denoted (dashed traces). 130
- 5.12  $\chi_{NR}^{(2)}$  calculated for the  $\alpha$ -hematite:aqueous interface as a function of pH for a range of possible  $\varphi_R$  values. The dataset for  $\varphi_R = 30^\circ$  is displayed alongside its least squares polynomial fit (solid trace), with the 95% confidence interval denoted (dashed traces). 131
- 5.13 The number of net aligned water molecules in the Stern layer calculated for the  $\alpha$ -hematite:aqueous interface as a function of pH relative to the PZC (pH 6.75) when  $\varphi_R = 30^\circ$  (top plot) and the interfacial energy density associated with the net alignment of Stern layer water molecules (bottom plot). 132

- A.1 A combined homodyne and HD-SHG study in which a *c*-cut sapphire 1-mm-thick optical window, was exposed in sequence to ultrapure water, and then 1 M NaCl solutions at pH 2, 6, and 13. The results include (a) raw  $I_{SHG}$  as a function of lab time and (b) replicate interference patterns collected at each solution condition and fit to Eq. 2.2.1. 170
- A.2 The results of fitting the interference patterns shown in Figure A.1 (a) averaged values of  $\varphi_{sig}$  and  $E_{sig}$  referenced, or normalized, respectively, to the pH 6, 1 M NaCl condition and (b) calculated values of  $\chi_{eff}^{(2)}$  and  $\Phi(0)$ . 172
- B.1 Homodyne results for on/off reversibility experiments between pure water and 10 ppm PFOA (top two plots) and 10 ppm PFOS (bottom two plots). The leftmost plots show the transition from water to the respective PFAS, and the rightmost plots show the transition from the PFAS back to water. The vertical dashed lines denotes when the solution being introduced entered the flow cell. 179
- B.2 Selection of representative raw scans from each portion of the on/off experiments between pure water and (a) 10 ppm PFOA and (b) 10 ppm PFOS. 181
- B.3 Values of  $\varphi_{sig}$  and  $E_{SHG}$  obtained from the fit of the interference fringes for on/off reversibility experiments between pure water and (a) 10 ppm PFOA or (b) 10 ppm PFOS. 182

- B.4 Calculated values of  $\chi_{eff}^{(2)}$  and  $\Phi(0)$  for on/off reversibility experiments between pure water and (a) 10 ppm PFOA or (b) 10 ppm PFOS. 184

## List of Tables

|     |   |     |
|-----|---|-----|
| 2.1 | Group indices for all beams in fused silica.  | 49  |
| 3.1 | Summary of oxidation states identified <i>via</i> XPS within a selection of M:MOx films.  | 64  |
| 3.2 | Scalability of current density for selection of 10-nm M:MOx nanofilms.  | 72  |
| 4.1 | Refractive indices of a selection of optical materials, reduced metals, and metal oxides.   | 79  |
| 4.2 | Summary of sample geometries for HD-SHG investigation of metals and metal oxides evaluated in the course of this work.  | 82  |
| 4.3 | Comparison of the specifications and relevant operating conditions and performance of the Pharos and the Flint systems, used with System 1 (see Section 2.3.1) and 2 (see Section 2.3.2), respectively. | 87  |
| 4.4 | Refractive indices for all beams in all media.  | 94  |
| 4.5 | Incident angles relative to surface normal for all beams in all media.  | 95  |
| 5.1 | Roughness parameters calculated for unused and used $\alpha$ -hematite films.   | 113 |
| 5.2 | Experimental values of $E_{sig}$ and $\varphi_{obs}$ and calculated values of $\Phi(0)$ and $\chi_{NR}^{(2)}$ for $\varphi_R = 30^\circ$ for Run 1, Run 2, and Run 3 pH titrations.                     |     |

- Results are shown for normalization to the first  $E_{sig}$  of each PZC to pH X to PZC cycle (“Normalization 1”), as well as for normalization to only the first  $E_{sig}$  of the entire run (“Normalization 2”). 136
- 5.3 Experimental values of  $E_{sig}$  and  $\varphi_{obs}$  and calculated values of  $\Phi(0)$  and  $\chi_{NR}^{(2)}$  for  $\varphi_R = 30^\circ$  for Run 4 and Run 5 pH titrations. Results are shown for normalization to the first  $E_{sig}$  of each PZC to pH X to PZC cycle (“Normalization 1”), as well as for normalization to only the first  $E_{sig}$  of the entire run (“Normalization 2”). 137
- 5.4 Experimental values of  $E_{sig}$  and  $\varphi_{obs}$  and calculated values of  $\Phi(0)$  and  $\chi_{NR}^{(2)}$  for  $\varphi_R = 30^\circ$  for Run 6 pH titrations. Results are shown for normalization to the first  $E_{sig}$  of each PZC to pH X to PZC cycle (“Normalization 1”), as well as for normalization to only the first  $E_{sig}$  of the entire run (“Normalization 2”). 138
- C.1 Selection of representative 1,3-R,R'-imidazolium chloride ionic liquids to be used in the proposed work. 194

## CHAPTER 1

# **Metal Oxide:Aqueous Interfaces in Natural and Artificial Environments**

Interfaces are ubiquitous in both natural and human-made settings, playing a critical role in governing the chemical and physical phenomena that define our universe. Despite their ubiquity, interfaces present a unique set of challenges to those wishing to study them, with attempts to answer even basic questions about common interfacial systems progressing incrementally over decades as old analytical techniques advance and new ones arrive on the scene. In this introductory chapter, we will discuss the nature and properties of interfaces, why they are so important in our understanding of the world, and the challenges of studying interfaces while excluding bulk media from consideration. In particular, we will focus in on metal oxide:aqueous interfaces as a special subset of solid:liquid interfaces, and as the basis for the majority of experimental work presented within this thesis.

### **1.1. Defining Interfaces and their Importance**

Matter can exist in a variety of different forms, with distinctions between types of matter following from differences in composition and/or phase. Whenever two disparate forms of matter come into contact, we can define the finite region of inhomogeneity that exists between them as the “interface.” It is useful for us to study an interface as its own entity, since its properties can be distinct from the properties of either of the “bulk”

materials that bound it. This phenomenon enables chemical and physical processes that would not otherwise be possible in the absence of the interface, but it also introduces structural complexity to these systems.

Just as there is vast diversity in the forms and phases that matter can take, there is a compounding effect in the variety of interfaces that are present in both natural and artificial environments. We can define a specific interface by the two materials that compose it, and in the broadest sense, we can do this by naming the phases of these materials: solid, liquid, or gas. Under this convention we can define solid:gas, liquid:gas, and solid:liquid interfaces. In the case of solids and liquids, it is also possible to have interfaces between materials of like phase, provided those two phases are immiscible (*i.e.* solid:solid and liquid:liquid interfaces).

In nature, a variety of interfaces exist. Liquid:gas interfaces are especially prevalent on our planet, since over 70% of the Earth's surface consists of exposed water. Major phenomena of global importance such as aerosol production and ocean acidification are mediated through dynamics at the air:water interface, as chemical compounds evaporate, condense, dissolve, and generally undergo chemical and physical transformations as they partition between phases. Solid:liquid interfaces are present in groundwater aquifers, soils, bodies of water, and living organisms—where solid materials such as minerals, metals, and biological membranes come into contact with liquid water and the dissolved materials it carries.

Beyond the natural world, interfaces are also of critical importance in the daily lives and industrial activities of humans. Inside our homes and places of work, solid:air and liquid:air interfaces mediate the production of particulate and gaseous compounds that

can have positive or negative impacts on health and safety.<sup>1</sup> We rely on technologies enabled by interfacial interactions—such as batteries, electrodes, and fuel cells—to make it through our day-to-day lives.<sup>2-4</sup> Having outlined the ubiquity of interfaces and their relevance to natural and human processes, we now focus in our discussion on solid:liquid interfaces, with a particular emphasis on metal oxide:aqueous interfaces.

## 1.2. Relevance of Metal Oxide:Aqueous Interfaces

In nature, it is rare for metals to exist in their fully reduced, native form. In the presence of water, oxygen, and other harsh conditions, metals tend to oxidize, at which point they may be present in aqueous form as dissolved species in groundwater or surface water reservoirs, or in solid form as components of the solid minerals that compose Earth's rocks, soils, and sediments. On the biological side, living organisms incorporate metals in trace amounts, where they find application as active sites in enzymes or in mediating other biological processes. In larger amounts, however, metals can cause havoc in living things, and therefore an understanding of the fine balance between the cycling of metals in biogeochemical systems is critically important.

In the case of non-biological metals, the transformation between mobile (*i.e.* aqueous) and immobile (*i.e.* insoluble) species is mediated through processes occurring at metal oxide:aqueous interfaces, including mineral weathering, corrosion, and crystal nucleation and growth.<sup>5</sup> Many of these same processes occur in human-made settings and—in the case of unwelcome transformations such as corrosion or scaling—an understanding of the mechanisms by which they take place is important to preserving the longevity of our metal-based technologies and infrastructure.

At the same time, metal oxide:aqueous interfaces hold great promise in the ability to preferentially immobilize or scavenge harmful substances unleashed on our environment. A recent review of  $\text{TiO}_2$ ,  $\text{ZnO}$ ,  $\text{WO}_3$ ,  $\text{CuO}$ , and  $\text{Cu}_2\text{O}$  highlights the potential application of these metal oxides to the photodegradation of organic contaminants.<sup>6</sup> Nanoparticulate forms of iron oxides have long been known to display high sorption capacities for heavy-metal and anionic contaminants.<sup>7</sup> To assist in reducing the amount of contaminants we release into our air and water in the first place, metal oxides such as  $\alpha$ -hematite ( $\alpha\text{-Fe}_2\text{O}_3$ ) are gaining traction as Earth-abundant and relatively non-toxic photoanode materials for photoelectrochemical (PEC) water splitting, enabling the next generation of green fuels.<sup>4,8-13</sup>

Finally, having noted the variety of processes occurring at metal oxide:aqueous interfaces, we further emphasize that the dynamics of such processes often follow from the tendency of these interfaces to carry a charge. The charging of metal oxide:aqueous interfaces can be due to a variety of material-specific phenomena, including but not limited to the (de)protonation or hydroxylation of terminal groups on the solid, as well as the existence of permanent residual charges left over from cleaving of the bulk material. The net charge of a metal oxide:aqueous interface sets up an electrical field, which emanates some distance into both the solid and the liquid, polarizing and reorienting mobile molecules in the liquid phase to form what is known as an electrical double layer (EDL). The EDL has been known for decades in the literature, and many workers have sought to develop, refine, or correct models describing its behavior.<sup>14-18</sup>

As we will elaborate in Chapters 2 and 5, a great challenge for interface-selective analytical techniques is to separate and assign contributions from different portions of the

interfacial region. Under certain conditions—such as when a highly-charged metal oxide surface is in contact with an aqueous phase with minimal capacity to screen the E-field—the interfacial region may be better approximated as a three-dimensional space rather than a perfect two-dimensional boundary, complicating the generation of signal. Before digging into this area of ongoing work, we devote the remainder of this introduction to highlighting other methods for surface-specific analysis, why they fall short in the study of buried interfaces on their own, and what we require of an analytical technique in order to interrogate metal oxide:aqueous interfaces.

### **1.3. Technical Challenges to Studying Buried Metal Oxide:Aqueous Interfaces**

Earlier in this chapter, we defined interfaces as the plane of contact between two disparate materials. We can further distinguish “surfaces” as interfaces where one phase is gaseous, such as the case of liquid:gas or solid:gas interfaces (i.e. the surface of the ocean, the surface of a window). Generally, it is easier to study the properties of surfaces than it is those of interfaces, with classical techniques for this purpose including tensiometry to quantify surface tension; quartz crystal microbalance (QCM) to monitor mass uptake; and BET (Brunauer, Emmett, and Teller) surface area analysis to determine porosity. More recently, this suite of techniques has expanded to include direct perturbation methods such as atomic force microscopy (AFM)<sup>19</sup> or scanning tunneling microscopy (STM),<sup>20</sup> and non-contact techniques such as optical profilometry.

Many of the techniques we describe above probe an interface using an external perturbation or a beam of electrons. Such avenues are more difficult for “buried” interfaces

where both phases are solid or liquid and therefore interact strongly with these probing methods. For example, atomic force microscopy works best with solid:gas interfaces, but is notably weak with solid:liquid interfaces, and even soft materials may require significant accommodation.<sup>19</sup>

Other techniques—secondary ion mass spectrometry (SIMS),<sup>21</sup> X-ray photoelectron spectroscopy (XPS),<sup>22</sup> most electron microscopies,<sup>23</sup> low energy electron diffraction (LEED), and Auger electron spectroscopy,<sup>24</sup> to name a few—employ ultrahigh vacuum (UHV), which requires samples to be thin films or powders robust to vacuum conditions. Probing solid:liquid interfaces with such techniques is either impossible with existing technology, or requires the use of specialized environmental cells or flash freezing, which introduces unavoidable alterations to the interface under study.<sup>25,26</sup> When used to study a solid surface *ex situ*, such techniques benefit from the complementary use of approaches enabling *in situ* analysis of the same surface under hydrated conditions.<sup>27</sup>

Another challenge in the study of interfaces is the relatively negligible population of species present at an interface compared to those present in the bulk. An instructive thought experiment is to consider an ice cube with a volume of 1 cm<sup>3</sup>. For a cube of this volume, we would expect there to be  $\sim 10^{22}$  total water molecules. Of these molecules, only  $\sim 10^{14}$  are present exactly at one of the cube's sides. Put another way, this means that there are on the order of 100-million-fold more bulk water molecules than there are interfacial water molecules in this ice cube alone. For a surface analysis tool to be useful, therefore, it must have an adequate degree of *sensitivity* and *selectivity* in order to detect the signal of a vanishingly small number density of interfacial moieties against the overwhelming backdrop of bulk matter. We aim to demonstrate in the remainder of this

work how second harmonic generation (SHG) spectroscopy meets this demand and—in tandem with complementary surface analysis techniques—can provide detailed molecular information about the dynamics of buried metal oxide:aqueous interfaces.

#### 1.4. Scope and Organization of Thesis

The desire to understand the fundamental properties of charged metal oxide and mineral surfaces in contact with water and aqueous species underpins the work presented in this thesis. Chapter 1 gave the reader a taste of the ubiquity of these interfaces in our world and makes the case for why they are worth studying. Within this chapter, we also gave a brief overview of what the technical challenges are to studying buried solid:liquid interfaces under environmentally-relevant conditions, and the state of the field in overcoming those obstacles through surface-sensitive techniques.

Given that the bulk of work presented in this thesis relies on second harmonic generation (SHG) spectroscopy, Chapter 2 gives an introduction to the relevant theory needed to understand this technique. Further, we expand on the introduction to include a discussion of heterodyne-detected (HD) phase-sensitive SHG analysis, a method that allows for the direct measurement of the SHG field rather than simply measuring intensity, as is the case with “homodyne” SHG spectroscopy. The chapter concludes with a description of the two HD-SHG optical set-ups employed throughout this work, as well as the flow set-up used in parallel to experimentally control the liquid phase of our metal oxide:aqueous interfaces.

To provide an example of an application of metal:metal oxide:aqueous interfaces, Chapter 3 details early work carried out on metal:metal oxide (M:MOx) nanofilms as

a candidate material for triboelectric nanogenerators (TENGs). These low-dimensional, often layered, organic and/or inorganic structures leverage the combination of electrical properties of their constituent materials to convert low-frequency mechanical energy into useable electricity. Seeing as these materials can be deployed in device form to exploit mechanical energy resulting from sources as diverse as hydrokinetic motion to the movement of organisms, TENGs provide an instructive example of how interfacial properties directly tie into real-world problems and our attempts to solve them. The work presented in this chapter includes descriptions of film synthesis and characterization, flow experiments, and preliminary SHG analysis on the nickel:nickel oxide:aqueous interface.

Next, Chapter 4 details efforts to adapt the HD-SHG spectrometers presented in Chapter 2 to accommodate solid:liquid interfaces in which the solid phase is a metal oxide. Although past work by the group has involved interrogating solids of this nature *via* homodyne SHG or SFG, HD-SHG analysis has thus far been limited to fused silica or  $\alpha$ -quartz as the solid phase. The chapter provides an overview of the optimized sample format and geometry for HD-SHG studies of metal oxide:aqueous interfaces, as well as the benefits afforded by using the output of an oscillator rather than a combined oscillator and amplifier system. It concludes by describing the calculation of certain quantities required to interpret the raw HD-SHG data for our particular sample geometry, including the wavevector mismatch, Fresnel coefficients, and calibration and referencing ratio. Some initial results on sapphire ( $\text{Al}_2\text{O}_3$ ) are provided in Appendix A as a proof-of-concept for the use of optical windows fully composed of the desired sample material, rather than only relying on thin-film deposition techniques.

Finally, Chapter 5 presents experimental results obtained for the  $\alpha$ -hematite:aqueous interface using the best practices outlined in the preceding chapter. Leading off is a discussion of the relevance of  $\alpha$ -hematite to both natural and industrial processes, followed by a description of how we obtained tens-of-nm-thin  $\alpha$ -hematite films suitable for HD-SHG analysis. From here, the chapter outlines the characterization of these films before and after exposure to the optical and flow set-ups, including analysis by AFM, XPS, and UV-visible absorbance/transmission spectroscopy. We proceed with a discussion of the optical physics of hematite and the impact on the interpretation of our datasets. From here, we present experimental results, including the independent determination of the point of zero charge (PZC) of our  $\alpha$ -hematite and pH-dependent reversability studies. To conclude, the chapter digs into the relative insensitivity of  $\alpha$ -hematite's HD-SHG response, and proposes future research directions in wavelength-dependent HD-SHG studies to constrain on- and off-resonance contributions to second-order nonlinear susceptibility.

## CHAPTER 2

**Second Harmonic Generation (SHG) Spectroscopy and  
Phase-Sensitive Measurements**

**Portions of this chapter are reproduced in part with permission from the  
American Chemical Society:**

Ma, E.; Ohno, P. E.; Kim, J.; Liu, Y.; Lozier, E. H.; Miller, T. F. I.; Wang, H.-F.;  
Geiger, F. M. A New Imaginary Term in the Second-Order Nonlinear Susceptibility  
from Charged Interfaces. *J. Phys. Chem. Lett.* **2021**, *12*, 5649–5659.

Chang, H.; Ohno, P. E.; Liu, Y.; Lozier, E. H.; Dalchand, N.; Geiger, F. M. Direct  
Measurement of Charge Reversal on Lipid Bilayers Using Heterodyne-Detected Second  
Harmonic Generation Spectroscopy. *J. Phys. Chem. B* **2020**, *124*, 641–649.

## 2.1. Introduction to Second Harmonic Generation (SHG) Spectroscopy

Second harmonic generation (SHG) is a coherent, nonlinear optical (NLO) process in which two photons of a degenerate frequency ( $\omega$ ) interact simultaneously with an anisotropic medium or interface, leading to the emission of one photon at twice the initial frequency (*i.e.*  $\omega + \omega = 2\omega$ ), as shown in Figure 2.1a. The NLO phenomenon of SHG only occurs if light of sufficiently high intensity (such as that produced with lasers) interacts with matter; at lower intensities, only a linear response is observed. Under both regimes, the electrical field of the incident light source serves to perturb the electron density of the material under study, resulting in an induced polarization. When perturbed by a relatively weak field, the restoring force of electrons can be described harmonically, whereas with a relatively strong field, this response is anharmonic. Under this model, an observed SHG response is due to the nonlinearity of the restoring force of the polarized electron clouds under sufficiently high field strength.<sup>1</sup>

The SHG process is a special case of the more generalized NLO process known as sum frequency generation (SFG), in which the input frequencies need not be degenerate, and instead a fixed visible input beam is mixed with a tunable beam (IR in the case of vibrational SFG and visible or short-wave IR in the case of electronic SFG) to produce a spectrum. While SFG spectroscopy is a powerful tool to obtain information regarding the molecular orientation of bonds in interfacial regions, the remainder of this chapter will focus on the theory and principles of SHG spectroscopy as the workhorse technique for this thesis.

Due to symmetry considerations and the electric dipole approximation, the SHG process is forbidden in centrosymmetric media. Some examples of SHG-silent bulk materials

include most liquids and gases, which are disordered at the molecular scale. For solid phases, we draw a further distinction between long-range-disordered and -ordered materials. The former case includes amorphous solids, exemplified by glasses, plastics, and some metal-oxide thin films, which may have short-range ordering over small length scales but ultimately display identical properties in all directions. In the case of long-range-ordered—or crystalline—solids, most materials exhibit some degree of anisotropy, and therefore are SHG-active. A classic example is  $\alpha$ -quartz, a tectosilicate mineral belonging to the hexagonal (trigonal) crystal system ( $D_3$  point group) and lacking a center of inversion.<sup>2,3</sup> In contrast, isotropic minerals such as garnet or spinel each have a crystal structure that features a center of inversion, making them SHG-silent.

Moving beyond individual phases, another key location where centrosymmetry breaks down is the interface between two different phases. For example, the air:water interface comprises two individual phases that, on their own, are SHG-silent. However, in proximity to the interfacial plane, we can define a direction that is *toward* the interface and a direction that is *away* from the interface. The existence of such directionality indicates that the interface by nature breaks centrosymmetry, a principle that has cemented SHG and SFG as inherently surface-sensitive techniques.

When a noncentrosymmetric material or interface generates SHG, we can relate the electrical field of the output photon ( $E_{2\omega}$ ) to the electrical fields of its constituent input photons ( $E_\omega$ ) by the following expression:

$$(2.1.1) \quad E_{2\omega} = \chi^{(2)} E_\omega E_\omega + \chi^{(3)} E_\omega E_\omega \Phi(0)$$

where  $\chi^{(2)}$  and  $\chi^{(3)}$  are the second and third order nonlinear susceptibilities, respectively, and  $\Phi(0)$  is the interfacial potential at the zero plane of the interface (Figure 2.1b). The second order component,  $\chi^{(2)}$ , derives from the net orientation of molecules at the interface in response to an applied electrical field and is related to molecular hyperpolarizability.<sup>1,7</sup> Conversely, the  $\chi^{(3)}$  susceptibility has been shown to be a bulk property, encompassing the reorientation and polarization of water molecules within the diffuse layer of the electrical double layer (EDL; see Figure 2.1b) in the presence of a static (DC) field set up by a charged solid:liquid interface.<sup>1,8</sup> Tian and coworkers<sup>9</sup> and Roke and coworkers<sup>10</sup>

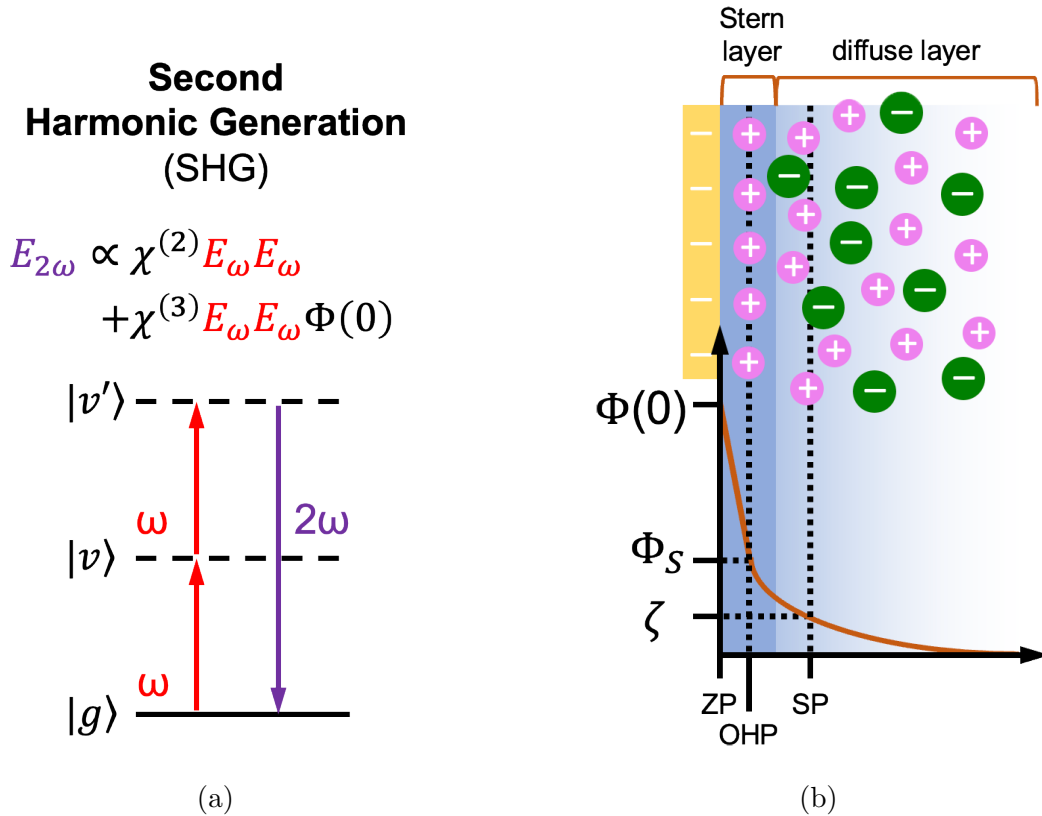


Figure 2.1. Graphical depictions of (a) the quantum mechanical description of the generalized SHG process, including energy levels, and (b) the triple layer model (*a.k.a.* the Gouy-Chapman-Stern model.<sup>4-6</sup>)

demonstrated that at sufficiently low ionic strengths, Equation 2.1.1 becomes invalid, requiring a correction to the third-order term to account for interference between SHG signal generated at different distances into the bulk solution relative to the zero-plane of the interface. This correction term is described below in terms of  $\kappa$  (equal to the inverse Debye length,  $\lambda_D^{-1}$ ) and  $\Delta k_z$  (or the wavevector mismatch of the optical process, calculated for the sample geometry used in this work in Section 4.3.1):

$$(2.1.2) \quad E_{SHG} \propto \chi^{(2)} + \chi_{water}^{(3)} \Phi(0) \frac{\kappa}{\kappa - i\Delta k_z}$$

Following the derivation of Geiger and coworkers<sup>11</sup> this expression can be rewritten in terms of the phase angle resulting from the DC-field-induced  $\chi_{water}^{(3)}$  contributions generated at a range of depths from the interface:

$$(2.1.3) \quad E_{SHG} \propto \chi^{(2)} + \chi_{water}^{(3)} \Phi(0) \cos(\varphi_{DC, EDL}) e^{i\varphi_{DC, EDL}}$$

where  $\varphi_{DC, EDL} = \arctan(\Delta k_z \lambda_D^{-1})$ . As long as the Debye screening length for the solution is known, we are able to leverage this formulation of  $E_{SHG}$  to disentangle the  $\chi^{(2)}$  and  $\chi_{water}^{(3)}$  terms, as will be described in the following section.

## 2.2. Phase Sensitive Measurements and Heterodyne Detection (HD)

Typical SHG experiments have only the intensity of the SHG signal as an observable, extrapolating the value of  $E_{SHG}$  by taking the square root of that measured intensity value. Using heterodyne detection (HD), conversely, it is possible to extract phase information by systematically interfering the SHG signal from the interface under study with the SHG signal generated by a reference NLO material, known as a local oscillator (LO).<sup>7,11-14</sup>

To obtain the experimental results reported in this thesis, we employed two distinct methods in order to vary the phase between our sample-generated and LO-generated SHG. The first method, described further in Section 2.3.1 and hereafter referred to as “System 1,” involves translating the LO in space parallel to the beam path downstream of the sample, leveraging the optical dispersion of the beam in air.<sup>11</sup> Using System 1, we can obtain an interference pattern in  $I_{SHG}$  (the measured SHG intensity of the combined sample and LO contributions) that we can fit to a cosine function of the form:

$$(2.2.1) \quad I_{SHG} = I_0 + A \cos(fx + \varphi_{fit})$$

where  $I_0$  is the intensity at the “zero” position of the LO,  $A$  is the amplitude of the interference pattern,  $f$  is its angular frequency, and  $\varphi_{fit}$  is its phase shift. While  $I_{SHG}$  is a direct observable, the remaining variables are fitting parameters open to optimization. Considering the following formulation of the contributions of the sample-generated and LO-generated SHG to the total measured intensity:

$$(2.2.2) \quad I_{SHG} \propto |E_{sig} + E_{LO}|^2 = |E_{sig}|^2 + |E_{LO}|^2 + 2E_{sig}E_{LO}\alpha \cos(\varphi_{sig} - \varphi_{LO} + \varphi_{PSU})$$

we can see that  $A \propto E_{sig}$ . In this system, while there is no mechanism to determine the absolute value of  $\varphi_{sig}$ , we can assume  $\Delta\varphi_{fit} = \Delta\varphi_{sig}$ , since  $\varphi_{LO}$  remains constant and the modulation of  $\varphi_{PSU}$  is consistent between disparate scans. Therefore, any phase measurements we obtained through System 1 are reported as  $\Delta\varphi_{sig}$ .

As shown in Figure 2.2, the  $E_{sig}$  observable from an HD-SHG experiment is complex-valued (unless  $\varphi_{sig} = 0$ ) and can be separated into its real and imaginary components. As demonstrated by Geiger and coworkers,<sup>11,15</sup> using trigonometric relationships allows

us to define  $\chi^{(2)}$  and  $\Phi(0)$  in the following terms:

$$(2.2.3a) \quad \Phi(0) = -\frac{C}{R} \frac{\sin(\varphi_{sig}) E_{sig}}{\chi_{water}^{(3)} \cos(\varphi_{DC, EDL}) \sin(\varphi_{DC, EDL}) + \chi_X^{(3)}}$$

$$(2.2.3b) \quad \chi^{(2)} = \frac{C}{R} \cos(\varphi_{sig}) E_{sig, sample} - \cos^2(\varphi_{DC, EDL}) \chi_{water}^{(3)} \Phi(0)$$

where  $E_{sig}$  and  $\varphi_{sig}$  are measured quantities in the HD-SHG experiment,  $\chi_{water}^{(3)}$  is taken to be  $9.6 \times 10^{-22} \text{ m}^2 \text{ V}^{-1}$ ,<sup>16,17</sup>  $\chi_X^{(3)}$  is an additional third-order term of bulk origin set to  $1.5 \times \chi_{water}^{(3)}$ .<sup>15</sup>

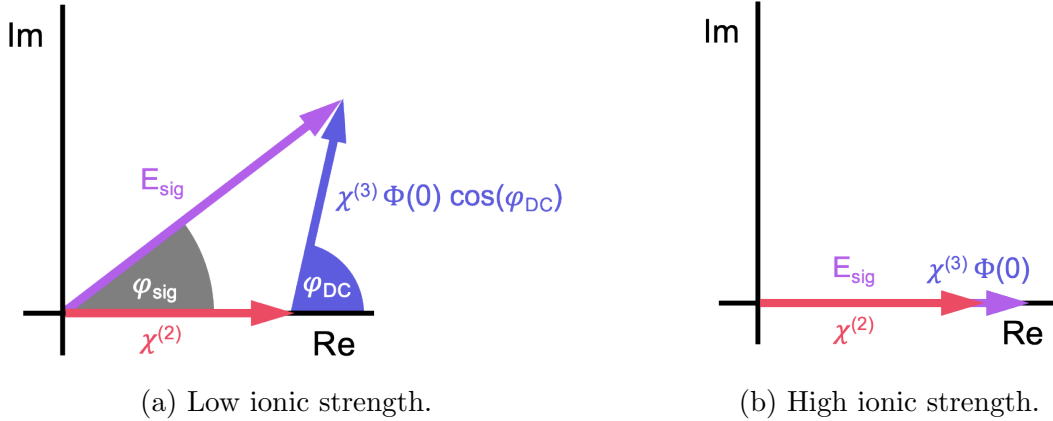


Figure 2.2. Graphical depictions of the contributions of  $\chi^{(2)}$ ,  $\chi^{(3)}$ ,  $\Phi(0)$ , and  $\varphi_{DC}$  to the observables of a typical HD-SHG experiment ( $E_{sig}$  and  $\varphi_{sig}$ ) under (a) low and (b) high ionic strength conditions.

Under this model we expect that at sufficiently high ionic strength the Debye screening length will approach zero, causing  $\varphi_{DC, EDL}$  to do the same. At this point we can assume  $\varphi_{sig}$  to be near  $0^\circ$  (as shown in Figure 2.2b) and therefore the high ionic strength conditions can serve as an external reference condition. To illustrate, say we take a measurement of  $\varphi_{sig}$  for the silica: pure water interface, and then another for the fused silica: 1 M NaCl

interface. By setting  $\varphi_{sig, 1 M NaCl} = 0^\circ$ , we can reference the value of  $\Delta\varphi_{sig}$  between 1 M NaCl and pure water, allowing us to obtain the “absolute” value of  $\varphi_{sig, water}$  by indirect means.

In contrast to the translational method described above, the second method for HD-SHG used in this work—or “System 2”—takes advantage of the wavelength-dependence of fused silica’s refractive index to modulate the phase difference between the sample-generated and LO-generated SHG signals. As shown in Figure 2.3, when two beams of different wavelengths pass through a fused silica window of some thickness  $d$ , their angles of refraction passing into the solid from air differ according to Snell’s Law. The difference in refraction angles contributes to two distinct path lengths for the fundamental beam and the SHG beam. By systematically varying the angle  $\alpha$  of the fused silica window relative to the beam path, we can modulate the path length difference and by consequence the phase difference between the sample-generated SHG (upstream of the PSU) and the LO-generated SHG (downstream of the PSU) to produce an interference pattern.<sup>12,18,19</sup> Following the method laid out by Stolle and coworkers<sup>12</sup> this pattern can be fit according to the following function:

(2.2.4)

$$f(\gamma) = K_0 + K_2 \cdot (\gamma - \delta\gamma)^2 + E_{sig} \cos \left\{ 4\pi \frac{d}{1.03 \times 10^{-6}} \left[ n_{air} \cdot n_{1, SiO_2} \cdot \cos \left( \sin^{-1} \left\{ \sin \left[ \frac{(\gamma - \delta\gamma) \cdot \frac{\pi}{180}}{n_{air} \cdot n_{1, SiO_2}} \right] \right\} \right) - \cos \left( \sin^{-1} \left\{ \sin \left[ \frac{(\gamma - \delta\gamma) \cdot \frac{\pi}{180}}{n_{0, SiO_2}} \right] \right\} \right) \cdot n_{0, SiO_2} \right] + \frac{\varphi_{sig} \cdot \pi}{180} \right\}$$

where the parameters to be fit are  $K_0$ , or the intensity of the combined signal from the sample and LO when  $\gamma = 0^\circ$ ;  $K_2$ , which accounts for the decrease in interference maxima at increasing values of  $\gamma$ ;  $\delta\gamma$ , which is a correction term to account for any deviation of the “zero” position of the PSU from true beam normal;  $E_{sig}$ , or the amplitude; and  $\varphi_{sig}$ , or the phase shift. The PSU thickness, or  $d$ , was determined using a precision caliper at nine separate positions on the PSU plate, yielding a value of 1.0757(14) mm. Using a 4-parameter Cauchy fit to the refractive index data for the IR-grade fused silica substrate, we obtain  $n_{1, SiO_2} = 1.4619$  and  $n_{0, SiO_2} = 1.4501$  and we take the value of  $n_{air}$  to be 1.0003. In Figure 2.4 we show an example of this fitting procedure applied to a representative interference pattern obtained using System 2.

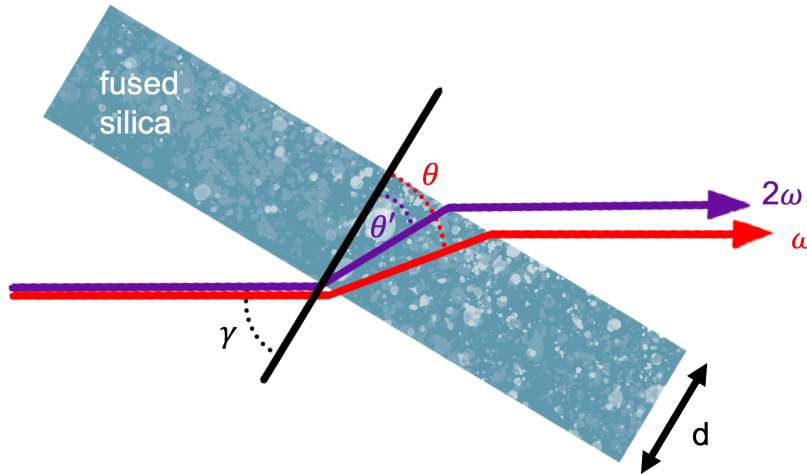


Figure 2.3. Graphical depiction of the refraction angles of the fundamental ( $\omega$ ) and SHG ( $2\omega$ ) beams passing through a fused silica window of thickness  $d$  rotated at some angle  $\alpha$  relative to the beam path. Adapted from a figure by Kim and coworkers.<sup>18</sup>

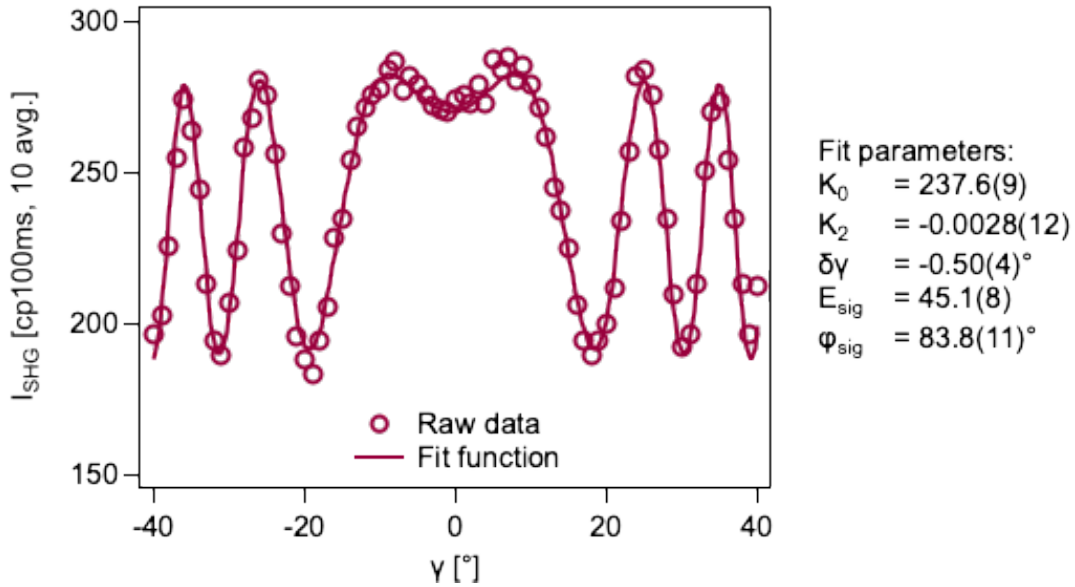


Figure 2.4. The interference pattern in  $I_{SHG}$  (open circles) obtained using a rotational PSU (*i.e.* System 2). The sample under study was a 1-mm-thick fused silica window ALD-coated with 10 nm of  $\alpha$ -hematite in contact with an aqueous solution of 1 M NaCl pH-balanced to pH 6. The solid line shows the result of fitting the raw data with Eq. 2.2.4.

### 2.3. Heterodyne-Detected (HD) Second Harmonic Generation (SHG)

#### Set-Ups

All HD-SHG studies reported within this work resulted from experiments carried out on either of two different optical set-ups: System 1 and System 2. System 1 is described extensively elsewhere<sup>11,20-22</sup> and will be discussed only briefly within the context of this thesis, with more focus being dedicated to System 2.

#### 2.3.1. System 1: Translational Phase Shifting Unit (PSU)

The first system for HD-SHG studies was developed by former members of the Geiger group and relies on the translational movement of a phase-shifting unit (PSU) to produce

interference between the sample SHG and LO SHG. We depict System 1 schematically in Figure 2.5.

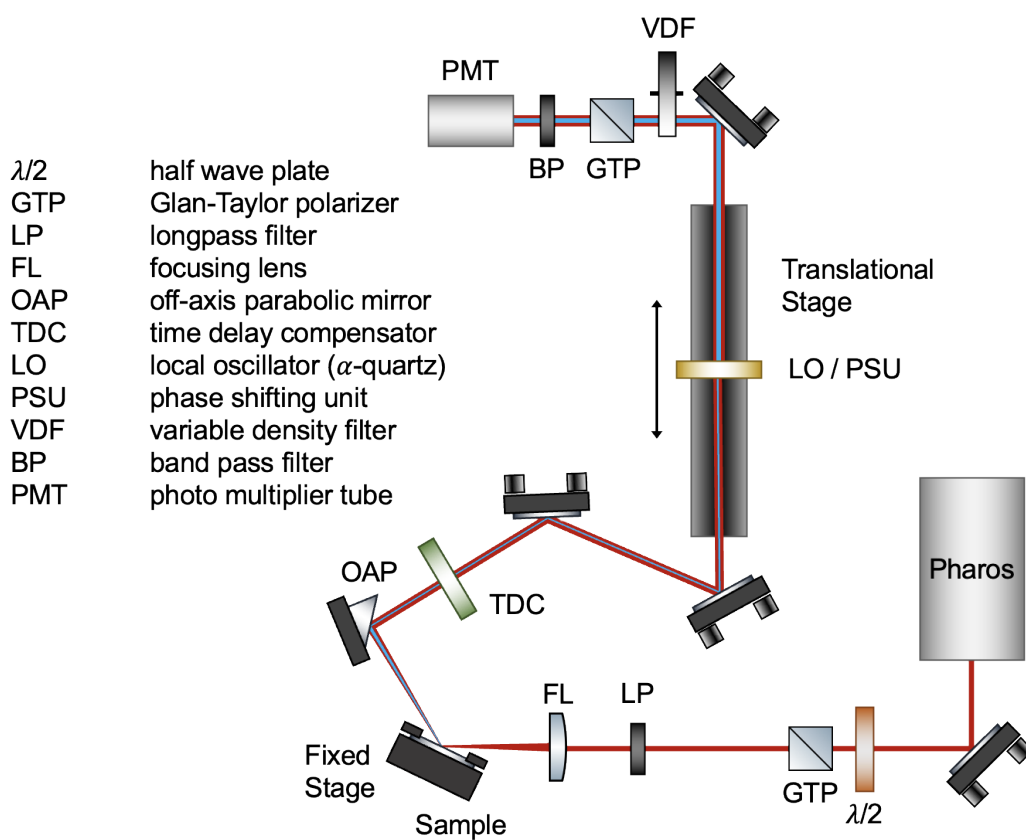


Figure 2.5. Schematic of the “System 1” HD-SHG set-up used to conduct the majority of experiments reported in Chapter 3. Set-up drawn using and/or adapting some components from ComponentLibrary by Alexander Franzen.

In brief, we directed 200-fs pulses centered around 1030 nm with a repetition rate of 200 kHz (Light Conversion, Pharos) through a longpass filter to exclude residual SHG and a variable attenuator consisting of a half-waveplate (Thorlabs, AHWP05M-980) and Glan-Taylor polarizer (Thorlabs, GT-10) in series. The operational principle of the variable

attenuator is Malus' law, which states:

$$(2.3.1) \quad I = I_0 \cos^2(\theta)$$

where  $I$  is the intensity,  $I_0$  is the input intensity, and  $\theta$  is the angle between the initial polarization of the input light and the polarizer's axis. By placing a half-waveplate in a rotational mount in front of the polarizer, we can continuously rotate the polarization direction of the input beam by adjusting the angle of the half-waveplate, as described by the following relationship:

$$(2.3.2) \quad I = I_0 \cos^2(2\phi)$$

where  $\phi$  is the azimuthal angle of the half-waveplate. Thus, rotating the half-waveplate by  $\phi$  degrees produces  $2\phi$  degrees of rotation in the polarization direction of the fundamental beam.

Following attenuation, we focused the beam onto the sample (mounted on a fixed stage) *via* a focusing lens (Thorlabs, LA1608,  $f = 7.5$  cm). The reflected fundamental and SHG beam originating from the sample interface were then recollimated with an off-axis parabolic (OAP) mirror (Thorlabs, MPD149-P01). Due to the wavelength dependence of fused silica's refractive and group indices (summarized in Table), the fundamental beam will lead the SHG beam after passing through and exiting the 1-mm fused silica window. Starting from the formula for the group velocity of a pulse, we obtain an expression for

the time difference per unit of common path length:

$$(2.3.3) \quad v_g = \frac{c}{n_g}$$

$$\Delta\left(\frac{1}{v_g}\right) = \frac{1}{c}(n_{g,2\omega} - n_{g,\omega})$$

In the case of a common path length of 1.25 mm for the two beams (based on the geometry of a 1-mm-thick fused silica window), and using the group indices for fused silica listed in Table 2.1, we obtain an expected time delay of 104 fs. With a pulse duration of 80 fs, this delay is nontrivial and requires correction in order to achieve efficient heterodyning. To do this, we passed the co-propagating beams through a time delay compensator (TDC) consisting of a calcite plate (Newlight Photonics, CAL12030-A) with a thickness of 0.3 mm and a corresponding time delay of  $\sim 150$  fs.\*

| $\lambda$ [nm] | $n_g$  |
|----------------|--------|
| 515 nm         | 1.4877 |
| 1030 nm        | 1.4627 |

Table 2.1. Group indices for all beams in fused silica.

To enable HD-SHG phase-sensitive measurements, we then passed the overlapping beams through a 50- $\mu$ m-thick window of  $z$ -cut  $\alpha$ -quartz (Precision Micro-Optics, PWQB-368252) mounted on a translational stage (Standa, 8MT193-100) with a track length of 100 mm. Finally, the beams passed through a final Glan-Taylor polarizer, a shortpass filter (Edmund Optics, 45-646), and a bandpass filter (Thorlabs, FBH520-40) prior to

---

\*Although not a perfect match, HD-SHG experiments performed with this TDC plate generated well-resolved interference patterns with good phase stability, indicating sufficient temporal and spatial overlap of the fundamental and SHG beams.

detection with a photomultiplier tube (PMT, Hamamatsu, R585 and H8259-01) and a photon counter (Stanford Research Systems, SR400 and SR445A).

### 2.3.2. System 2: Rotational Phase Shifting Unit (PSU)

The second system—described for the first time elsewhere<sup>23</sup> and depicted schematically in Figure 2.6—served as the basis for the majority of experiments reported in Chapters 4 and 5. We directed 80-fs pulses centered around 1034 nm with a repetition rate of 75.5 MHz (Light Conversion, Flint) through a NIR longpass filter to remove any residual visible light, and then through a half-waveplate (Thorlabs, AHWP05M-980) to allow for polarization selection. Turning the half-waveplate enabled the linearly-polarized output beam to be rotated to either *s*- or *p*-polarization. All results reported within this work were obtained with the oscillator output *s*-polarized, with no further polarization selection downstream of the sample, unless otherwise noted.

Following the half-waveplate, the beam passed through a variable density filter to enable power attenuation. As needed, we attenuated the output power from a maximum of >2.5 W to a working power between 200 mW and 2 W, corresponding to an incident pulse energy of roughly 2.6-26 nJ.<sup>†</sup> From here, we steered and focused the beam with an  $f = 10$  cm lens onto the sample surface at an incident angle of  $60^\circ$ .<sup>‡</sup> We mounted the sample holder (described in more detail in Section 2.4) on a 3-axis manual stage

---

<sup>†</sup>Most experiments involving ALD oxides employed a power of 200 mW, while those involving bare fused silica employed 2 W.

<sup>‡</sup>For experiments involving ALD oxides, we intentionally defocused ( $-1$  cm) the beam to avoid burning the sample surface (spot size *ca.* 100  $\mu\text{m}$  diameter). This was not a concern for experiments involving fused silica samples, therefore we tightly focused the beam in those cases to maximize signal.

(Thorlabs) to allow for the interrogation of multiple analysis spots within a single sample without the need to remount.

When probing a sample with flat geometry, we placed a small beam block made of anodized aluminum within a few cm of the sample's external surface to block the external reflection of the beam, while allowing the beam resulting from internal reflection to pass. By mounting the beam block on a micrometer-adjusted stage we could precisely position it in the mm-scale separation between the two beams. As discussed later in Section 4.2.5, blocking the external beam was necessary to avoid overwhelming the SHG signal originating from the internal solid:liquid interface with that of the external air:solid interface.

Immediately downstream of the sample, an OAP mirror (Thorlabs, MPD149-P01) recollimated the reflected fundamental beam (1034 nm) and sample-generated SHG (517 nm) and a calcite TDC (Newlight Photonics, CAL12030-A) with a thickness of 0.3 mm and a corresponding time delay of about 150 fs re-overlapped the beams in time. We direct the reader to refer to Section 2.3.1 for the full calculation of the temporal delay stemming from the two beams' common path through the 1-mm fused silica window serving as the sample substrate.

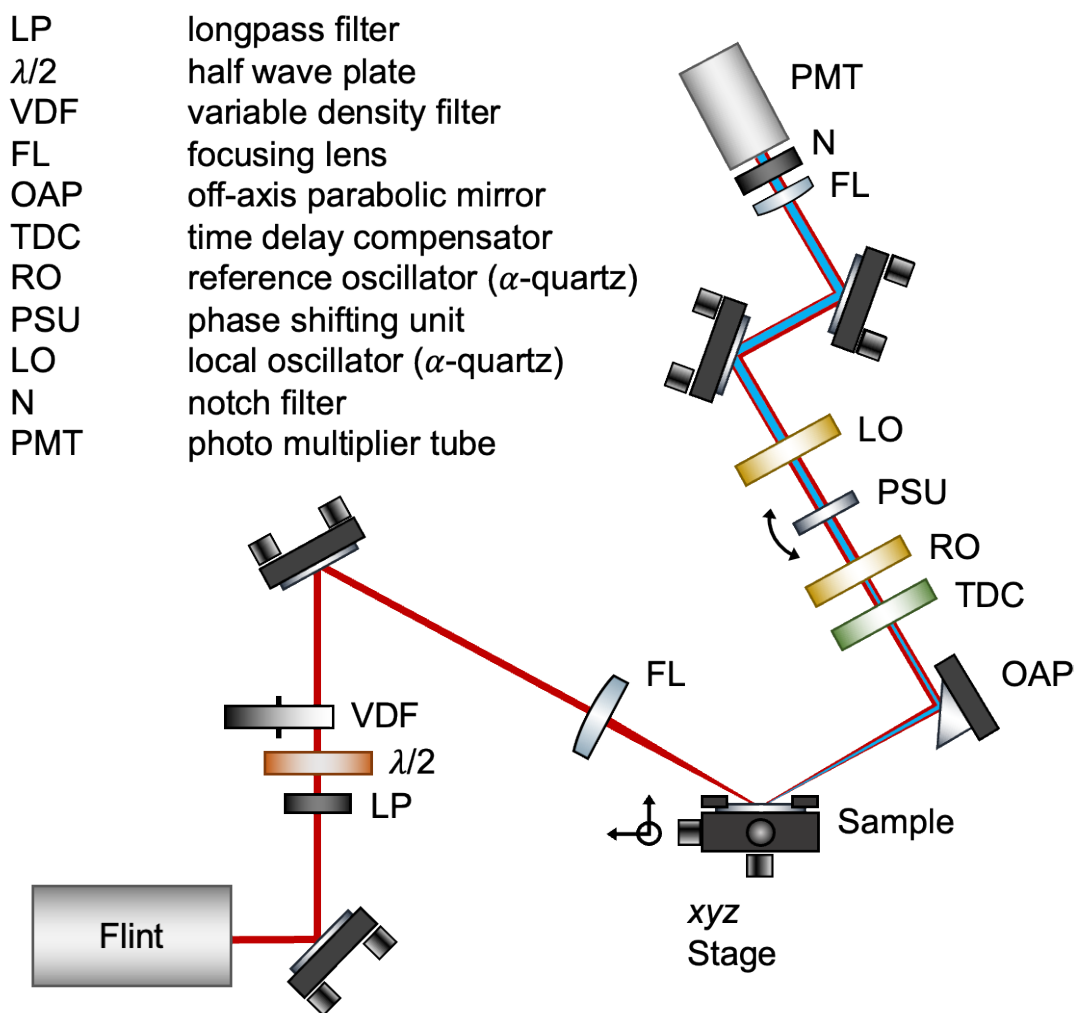


Figure 2.6. Schematic of the “System 2” HD-SHG set-up used to conduct the majority of experiments reported in Chapter 4. Set-up drawn using and/or adapting some components from ComponentLibrary by Alexander Franzen.

We then allowed the now-overlapping pulses to pass through a 50- $\mu\text{m}$ -thick window of z-cut  $\alpha$ -quartz (Precision Micro-Optics, PWQB-368252) to generate a reference oscillator (RO) signal, a 1-mm-thick fused silica window serving as the phase-shifting unit (PSU), and finally a second  $\alpha$ -quartz window of identical specifications to the first to generate

the local oscillator (LO) signal. We hereafter refer to the SHG signal produced by the combined contributions of the sample interface, the RO, and the LO as the “SHG pulse triplet” ( $\varphi_{signal+ROLO}$ , or  $\varphi_{obs}$ ). Finally, the SHG pulse triplet passed through a notch filter centered at the SHG wavelength and was focused directly into a photomultiplier tube (PMT, Hamamatsu, R585 and H8259-01) connected to a gated photon counter (Stanford Research Systems, SR400) and preamplifier.

To modulate the relative phase between the SHG electric fields of the sample and the LO, we varied the PSU angle  $\alpha$  between  $-40^\circ$  and  $40^\circ$  using  $1^\circ$  steps, by means of a motorized rotational stage (Standa, 8MR174-11). We recorded the SHG signal with a 100-ms acquisition time and 10-fold averaging. This acquisition scheme resulted in a fringe acquisition period of about 80 sec, not counting the time to reset the rotational stage to  $\gamma = 0$ . By keeping the RO and LO on flip mounts, it was possible within a single experiment to obtain both HD-SHG and homodyne measurements. By introducing a longpass filter to the beam path immediately upstream of the RO, we were able to measure the fixed phase relationship between the RO and the LO with the sample SHG excluded—referred to hereafter as the “ROLO-only SHG doublet” ( $\varphi_{ROLO}$ ). This measurement provided the basis for this set-up to measure absolute phase ( $\varphi_{sig}$ ) by subtracting  $\varphi_{ROLO}$  from  $\varphi_{signal+ROLO}$  rather than being required to reference the observed phase to a standard condition, as is the case with System 1. In general, we collected and fit three replicate interference fringes per aqueous phase condition, monitoring  $I_{SHG}$  in homodyne to ensure equilibrium conditions before beginning the measurements.

## 2.4. Experimental

### 2.4.1. Sample and Flow Cell Preparation

Uncoated 1-mm-thick IR-grade fused silica optical windows (ISP Optics, QI-W-25-1) and 25.4-mm-diameter IR-grade fused silica hemispheres (Hyperion Optics, Corning #7979) were prepared for use in experiments by first soaking for 1 h in ALNOCHROMIX™ (Alconox) and concentrated sulfuric acid (Sigma-Aldrich, 339741, 99.999%). Then, the substrates were rinsed with copious amounts of ultrapure water (18.2 M $\Omega$ -cm, Millipore-Sigma), sonicated in MeOH for 10 min, rinsed again, sonicated in ultrapure water for 10 min, and rinsed once more. Finally, the substrates were dried with N<sub>2</sub> and air plasma-cleaned for 30 sec on the highest setting. We performed all rinses with ultrapure water and stored cleaned substrates under ultrapure water until use. We describe the cleaning protocol for ALD  $\alpha$ -hematite-coated substrates in detail in Section 5.2.2.

A house-machined polytetrafluoroethylene (PTFE) custom flow cell was prepared for use the night before an experiment by sonicating for 10 min in MeOH, rinsing with ultrapure water, sonicating for 10 min in ultrapure water, rinsing once more, and storing under ultrapure water overnight. The morning of an experiment, the cell was dried under N<sub>2</sub> and air plasma cleaned for 30 sec on the highest setting. Viton or fluoroelastomer O-rings were cleaned in a similar manner, omitting the first sonicating step in MeOH.

As depicted in Figure 2.7, internal reflection flow experiments were carried out by clamping the desired substrate to the flow cell. In the case of both hemispheres and flat optical windows, a Viton or fluoroelastomer O-ring was placed between the cell and the substrate to form a seal and ensure the wetted interior of the cell is composed only of

PTFE, Viton/fluoroelastomer, and the material of the sample. The cell was then inserted in an aluminum sleeve for additional stability. Finally, in the case of flat optical windows, a house-machined aluminum faceplate was sealed to the exterior of the sample with an additional fluoroelastomer O-ring and tightened to fix the window in place and completely seal the wetted interior of the flow cell.

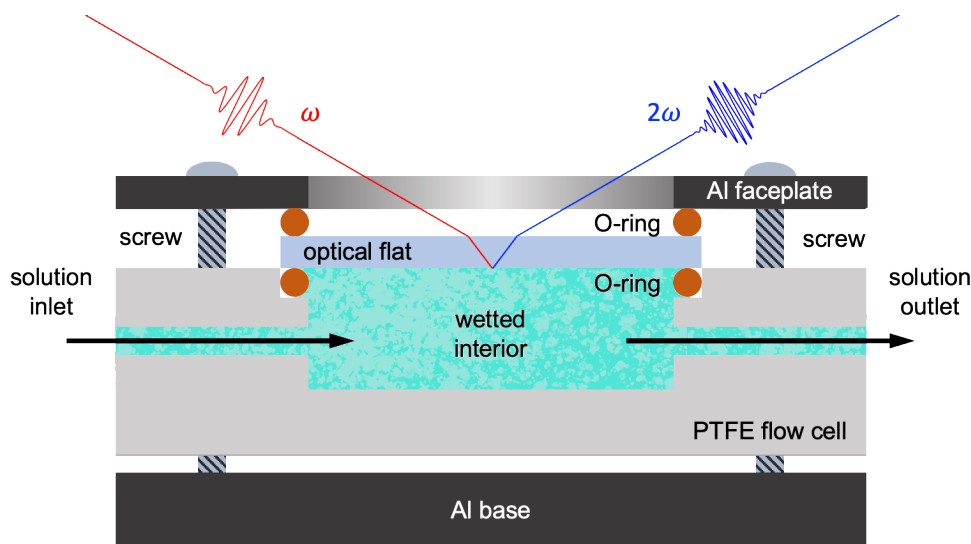


Figure 2.7. Schematic of the house-machined flow set-up used for all experiments conducted with System 2, with components labeled. A different flow cell and holder set-up was used for experiments conducted with System 1, and is described elsewhere.<sup>11,20,21</sup>

#### 2.4.2. Solution Preparation

NaCl and NaOH were procured from Sigma Aldrich (746398, >99% and 306576, 99.99%; respectively) and HCl was obtained from Fisher Scientific (A144, 36.5 to 38.0% w/w). Solutions of NaCl were prepared in ultrapure water (18.2 M $\Omega$ -cm; MilliporeSigma) at least 12 h before being used in flow experiments. Unless otherwise specified, solutions

were left partially covered with perforated Parafilm in order to come to equilibrium with atmospheric CO<sub>2</sub>. For pH-dependent studies, solutions were initially formulated using stock solutions of HCl and NaOH. Conductivity and pH measurements were made the morning of experiments using a portable meter (Thermo Scientific, STARA3250) equipped with a combination pH/ATC combination electrode (Thermo Scientific, 8107UWMMD) and a 4-cell conductivity probe (Thermo Scientific, 013010MD). Solution pH was adjusted using small amounts of dilute (<0.01 M) or concentrated (~1 M) HCl and/or NaOH solutions. For experiments conducted with solutions near neutral pH conditions, solution pH was remeasured every 30 min and readjusted as necessary. For 1 M NaCl solutions balanced in this manner to near  $\alpha$ -hematite's point of zero charge (PZC), the measured pH on six different days from at least four timepoints per day was pH 6.75(3).

Solutions were drawn from reservoirs and flown across the exposed sample surface by means of a single-channel peristaltic pump (New Era, NE-9000B) and lengths of ID: 1/8 in, OD: 3/16 in Tygon tubing (Saint Gobain, E-3603) attached to the PTFE sample cell using Kynar fittings (Cole Parmer, EW-40621-45). Flow rates around 2 mL/min were used to maintain laminar flow and avoid shearing during the acquisition of interference patterns at steady-state conditions. When switching between solutions, a flow rate of 12 mL/min was used to enable complete and efficient cycling of the flow cell's internal volume. For the length of tubing used in our experiments, the amount of time needed for a new solution to reach the sample surface was determined to be 2.5 min. Before moving the intake tubing to a new solution reservoir, it was thoroughly rinsed with ultrapure water to avoid cross-contamination between solutions of different salinities and/or pH values.

## CHAPTER 3

**Metal: Metal Oxide Nanofilms for Energy Transduction**

**Portions of this chapter are reproduced in part with permission from the  
National Academy of Sciences:**

Boamah, M. D.; Lozier, E. H.; Kim, J.; Ohno, P. E.; Walker, C. E.; Miller, T. F.;  
Geiger, F. M. Energy Conversion via Metal Nanolayers. *Proc. Natl. Acad. Sci. U.S.A.*  
**2019**, *116*, 16210–16215.

### 3.1. Background

Adverse climate impacts are likely unavoidable or irreversible in light of cumulative anthropogenic greenhouse gas (GHG) emissions leading up to the present.<sup>1-3</sup> However, immediate and sustained action in reducing future emissions can reduce the severity of climate impacts, and extend the efficacy and feasibility of existing climate adaptations. Limiting anthropogenic climate change therefore remains an imperative for the global community, and necessitates a goal of net-zero CO<sub>2</sub> emissions across as many sectors of human activity as possible.<sup>3,4</sup>

The energy sector in particular poses a challenge for any decarbonization scenario, as the need to provide electricity and heating equitably must be balanced with the imperative to reduce CO<sub>2</sub> emissions. In 2021 the biggest individual increase in CO<sub>2</sub> emissions—accounting for 46% of the annual global increase—was within the energy sector.<sup>5</sup> Although renewable energy was the only sub-sector to experience growth during the initial onset of COVID-19, the long-term outlook for alternative energy remains unclear.<sup>6</sup> Nevertheless, we must adopt a multi-pronged approach to decarbonization, leveraging both extant and emerging technologies that can meet the energy needs of our growing global population while simultaneously achieving net-zero, or better, -negative CO<sub>2</sub> emissions.

While solar and wind energy have reached a high level of commercialization, the intermittence of their sources and subsequent variability in their energy output means that they will be most effective when deployed in tandem with high-capacity energy storage methods, as well as technologies that provide uninterrupted baseline power.<sup>7</sup> Hydrokinetic energy stands out as a promising candidate to fill this gap, with the potential to produce

comparatively continuous power by harnessing the mechanical energy of hydrologic processes such as waves, currents, and tides.<sup>8-11</sup>

To this end, triboelectric nanogenerators (TENGs) for hydrokinetic energy conversion have garnered interest in the last two decades, consisting of low-dimensional organic or inorganic materials that produce electricity due to the motion of liquids across their exposed surface. Many nanogenerators are carbon-derived, including monolayer graphene on silicon,<sup>12-14</sup> glass,<sup>15</sup> polymer,<sup>16,17</sup> and piezoelectric supports;<sup>18,19</sup> carbon nanotube arrays;<sup>20-23</sup> and reduced graphene oxide and graphene oxide films.<sup>24-27</sup> More recently, polymer-ionic liquid (PIL) membranes have been advanced as a candidate nanogenerator material with IL-enabled tunability and durability.<sup>28</sup>

As understanding of these materials and their modes of operation has improved, there have been further reports of devices leveraging the energy harvest capabilities of TENGs to generate electricity from river currents<sup>29</sup> and underwater ocean currents.<sup>30</sup> On a smaller scale, applications for TENGs have been explored in the realm of self-powered biomedical devices,<sup>31</sup> biomonitors and sensors,<sup>32,33</sup> and wearable electronics.<sup>33-35</sup> With applications running the gamut from low- to zero-carbon hydrokinetic energy generation to self-powered devices enabling technologies as wide-ranging as the “internet of things” (IoT) and remote sensing, there is considerable interest in improving the biocompatibility, cost, ease of manufacture, and power density of TENG materials.

Generally, researchers studying TENG architectures attribute their mode of operation to some combination of contact electrification and electrostatic induction, with minor distinctions between TENGs resulting from differences in the physical, electrical, and optical properties of the constituent material or materials.<sup>16-20,25,36,37</sup> Wang advanced

a systematic theory from first principles to describe the electromagnetic dynamics of TENGs, from which device output could be calculated and an accompanying framework to guide the optimization of TENG materials.<sup>38</sup> In particular, this theory proposes that the origin for TENG operation lies in Maxwell’s displacement current, which is related to a particular material’s surface morphology, relative permittivity, and surface charge density. Accordingly, there is impetus to investigate a range of organic and inorganic materials and mixed-material architectures for TENGs in order to access a ratio of energy output to cost to enable their transition from the benchtop to commercial application.

As noted in a recent review of inorganic nanomaterials for TENGs,<sup>39</sup> some key directives for researchers in this field are to expand the contact area of triboelectric surfaces, to reduce the barrier to charge transport between electrode and triboelectric materials, to tune the dielectric properties of composite triboelectric materials, and to enable flexible or stretchable materials that retain their electrical properties. A notable set of TENG materials that enable inquiry in these directions include inorganic nanogenerators of semi-conducting thin films<sup>40,41</sup> and insulator/semiconductor layered architectures.<sup>42</sup>

Our group added to this suite of inorganic layered TENGs when we investigated the performance and mechanism of operation of two-dimensional metal:metal oxide (M:MOx) nanofilms deposited by physical vapor deposition (PVD). Initial reports by our group demonstrated that M:MOx nanofilms produce several tens of mV and tens of  $\mu\text{A}/\text{cm}^2$  under modest flow conditions (*i.e.* 0.2-1  $\text{cm s}^{-1}$ ), due to the creation of a dynamic electrical double layer (EDL) gradient, or a “gate.”<sup>43</sup> Although the competitiveness of M:MOx nanofilms in current output already distinguishes them as an emergent class of TENG materials worth pursuing, they are also promising due to their scalability and tunability.

As a line-of-sight technique, PVD enables the production of M:MOx nanofilms in a single synthetic step over areas in excess of dozens of in<sup>2</sup>, with arbitrarily large areas enabled by industrial-scale electron beam apparatuses. Depending on the source metal used, the majority of metallic elements are synthetically accessible, allowing for fundamental studies into the impact of properties such as relative permittivity, reduction potential, redox activity, and electronic configuration, among others. Further, by leveraging the inherent tendency of most PVD films of zero-valent metals to spontaneously form a mixed- or single-oxide overlayer upon exposure to air, the resulting M:MOx nanofilms naturally take on an architecture of an insulating dielectric underlaid with a conductive metal to serve as an electrode material, with no need for a separate synthetic step. The thickness and identity of the dielectric and metallic layers can be further tuned through the use of multi-layer depositions, or the subsequent application of PVD and atomic layer deposition (ALD) processes.

This chapter provides an experimental overview of the synthesis and characterization of M:MOx nanofilms followed by a discussion of insights on the mechanism of current generation from flow experiment results, as well as a brief proof-of-concept for how the interfacial electrostatic properties of the M:MOx nanofilm:electrolyte interface may be investigated using the tool of SHG spectroscopy.

## 3.2. Experimental

### 3.2.1. Synthesis and Characterization of M:MOx Nanofilms

Single-element M:MOx nanofilms were prepared *via* physical vapor deposition (PVD) in e-beam mode on an ATS500 coating system (HHV) from 3N5 (99.95%) purity metal

sources (Al, Co, Cr, Cu, Fe, Ni, Ti, and V; Lesker) on standard  $3\times 1$  in<sup>2</sup> and  $9\times 2$  in<sup>2</sup> borosilicate glass microscope slides (VWR). Following the method of Faurie-Wisniewski and coworkers to ensure high purity, we used deposition rates between 0.15 nm/s and 1.00 nm/s in order to obtain a suite of films at thicknesses of 5, 10, 20, 50 and 100 nm.<sup>44</sup>

In advance of performing a deposition, the borosilicate glass substrates underwent a cleaning procedure consisting of a 1-h soak in ALNOCHROMIX™ (Alconox) and concentrated sulfuric acid (Sigma-Aldrich, 339741, 99.999%) followed by copious rinsing with ultrapure water (18.2 M $\Omega$ -cm; MilliporeSigma). Then, the substrate was sonicated in methanol (MeOH) for 10 min, rinsed with ultrapure water, sonicated in ultrapure water for 10 min, and rinsed once more with ultrapure water. Finally, the substrate was dried with N<sub>2</sub>, air plasma-cleaned for 10 min on the highest setting, and stored in a clean 50-mL conical centrifuge tube until use.

During the PVD process, the sample substrate and source material are kept within a chamber kept at ultra high vacuum (UHV,  $<6\times 10^{-6}$  mbar). Following deposition and prior to chamber venting, the nanofilm consists of the zero-valent form of the source metal (*i.e.* M(0)). Upon removal from the PVD chamber and exposure to ambient air, the fully reduced M(0) film spontaneously passivates, forming a native oxide layer whose growth self-terminates at a depth of  $\sim 3$ -5 nm.<sup>43,45</sup> Previous work by Boamah and coworkers using atom probe tomography (APT) found evidence that for Fe:FeOx nanofilms, the subsurface morphology of the oxide passivation layer features  $\sim 5\times 10$  nm dendritic structures, rather than being an atomically smooth contact.<sup>45</sup> Although APT studies have not been conducted with film compositions beyond Fe:FeOx, X-ray photoelectron spectroscopy (XPS) surface and depth profiling analysis—performed on a Thermo Scientific

ESCALAB 250Xi—confirmed the layered morphology for all studied film compositions (see Figure 3.1).

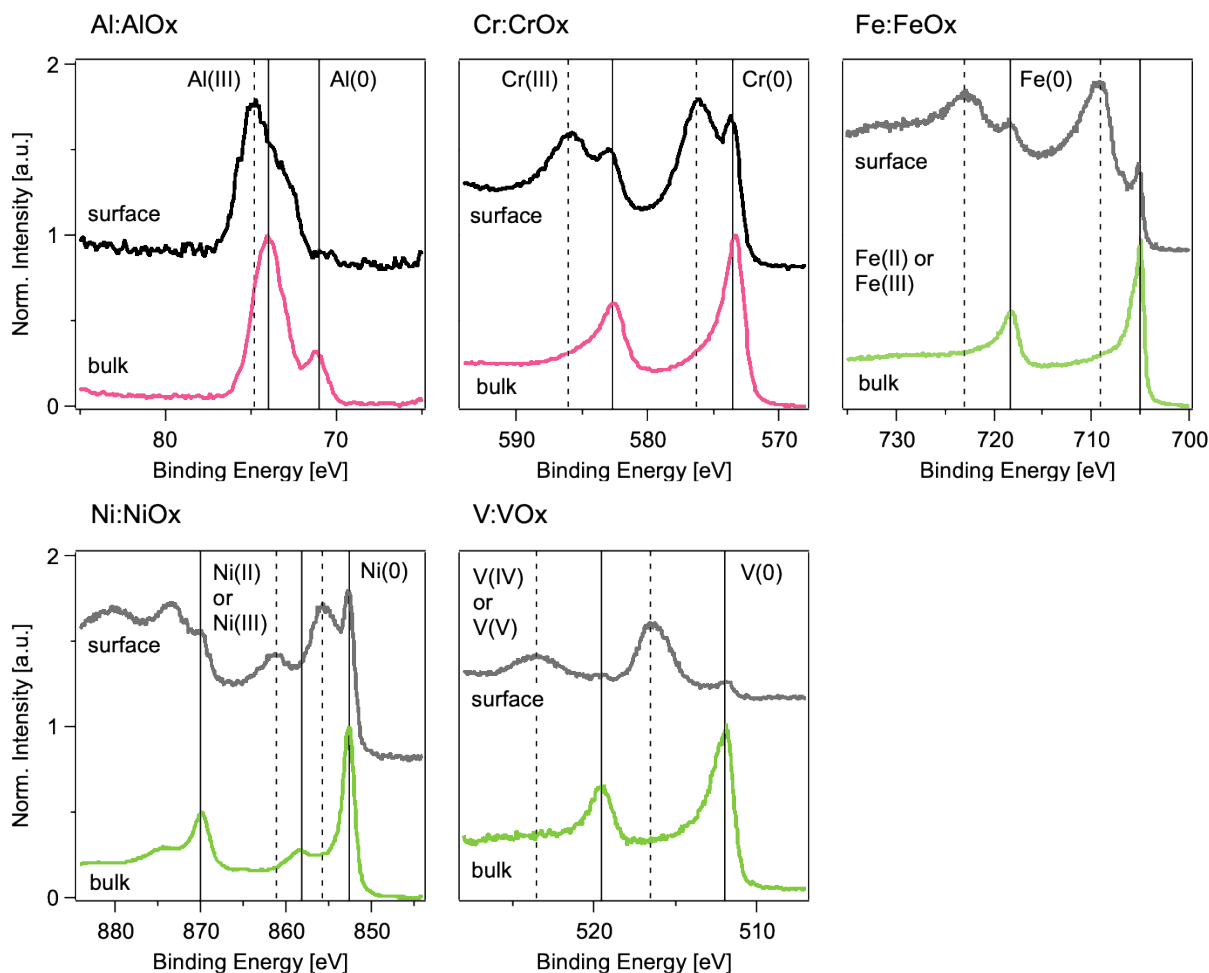


Figure 3.1. XPS spectra taken of the surface oxide layer ( $\text{MO}_x$ ) and reduced metal layer ( $\text{M}$ ) for a selection of  $\text{M}:\text{MO}_x$  nanofilms. Binding energy ranges surveyed are those corresponding to the constituent metal of each nanofilm. Solid vertical lines indicate peaks associated with the reduced form of a metal and dashed vertical lines indicate those associated with oxidized species, as specified in the figure.

Further XPS analysis conducted at binding energy ranges corresponding with common contaminants (*e.g.* Cl, Na, Zn) confirmed their absence both at the  $\text{M}:\text{MO}_x$  film

surface and within the bulk. Adventitious carbon (AdC) contamination of the M:MOx films consistently produced a peak around  $\sim 284.8$  eV corresponding with the C-C component of the C1s spectrum, which was used as a charge reference to correct all spectra obtained within a single session on the instrument.\* Carbonaceous surface contamination of this nature is well-documented by XPS for metallic samples that have undergone air exposure.<sup>49,50</sup> Therefore, we ascribe its presence on the surface of M:MOx films as a post-deposition occurrence, as opposed to an impurity introduced from the source material or PVD process. Following ablation of the sample surface under vacuum with an ion beam, the 284.8 eV peak completely disappeared, further supporting this conclusion.

For each M:MOx film investigated, we identified multiple XPS peaks within the range of expected binding energies for the respective source metal, as shown in Figure 3.1. Tentative peak assignments indicated that while some M:MOx films bear oxide layers displaying two oxidation states, others have only one oxidation state represented (results summarized in Table 3.1). The implications of this observation are discussed further in Section 3.3.

| Metal | Oxidation State(s) |    |    |
|-------|--------------------|----|----|
| Al    | +3                 |    |    |
| Cr    | +3                 |    |    |
| Fe    | +2                 | +3 |    |
| Ni    | +2                 | +3 |    |
| V     |                    | +4 | +5 |

Table 3.1. Summary of oxidation states identified *via* XPS within a selection of M:MOx films.

\*Some recent publications have expressed concern over the use of the AdC peak to correct XPS spectra.<sup>46,47</sup> However, given a report from a multi-user facility that this method of charge referencing gave satisfactory results in 95% of 522 cases surveyed, we have determined to proceed with this correction method for this work.<sup>48</sup>

### 3.2.2. Flow Experiments

To more precisely investigate the gate-controlled current induction in M:MOx nanofilms we employed a flow cell consisting of a  $6 \times 7.5 \times 35$ -mm channel machined in a polytetrafluoroethylene (PTFE) block, with threaded inlet and outlet holes. Using a Viton O-ring between the PTFE and the coated side of a M:MOx nanofilm, a faceplate could be screwed in to hold the nanofilm firmly in place and prevent solution leaks. The inlet was fitted with a Y-junction barbed fitting connected with Tygon tubing to two separate solution reservoirs. Two programmable peristaltic pumps (New Era, NE-9000B) enabled the driving of these solutions either simultaneously or alternately through the Y-junction and into the cell channel. With a nanofilm mounted in the cell, this set-up allowed us to rapidly alter the electrostatic conditions of the M:MOx:aqueous interface, creating gate conditions and eliciting electrical conversion. Further, by purposefully machining the flow cell to be shorter than the length of a standard borosilicate microscope slide, we ensured that our M:MOx nanofilms would overshoot the cell on either side, providing contacts for monitoring current and voltage across a film's long axis while actively exposing it to gate conditions. As shown in Figure 3.2, this flow cell enabled us to collect electrical measurements in the time domain while modulating experimental conditions such as solution flow velocity and solution switch frequency, as well as properties of the solutions themselves, including ionic strength, pH, and specific ion identity.

Measurements of current and voltage were performed *in operando* with leads attaching the M:MOx nanofilm under study to a multimeter (Keithley 2100) and a picoammeter (Keithley 6485). Current density was calculated by taking raw current measurements and dividing by the estimated area of the gate's footprint in  $\text{cm}^2$ . In the case of the flow

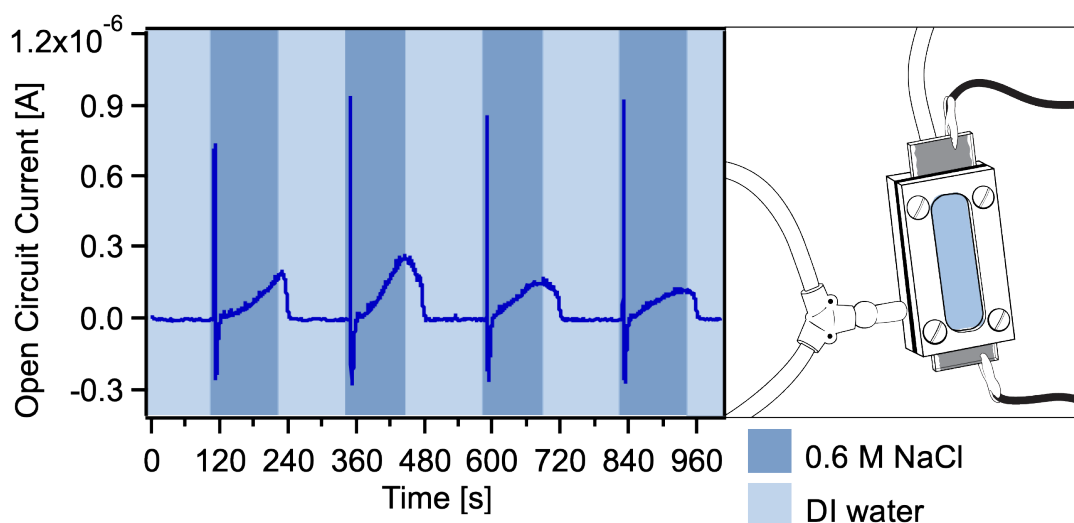


Figure 3.2. Current obtained from alternating pulses of salt- and freshwater over the surface of a 10-nm Fe:FeOx nanofilm mounted in a flow cell (left). Graphical representation of our house-machined custom flow cell (right). Graphic by elabarts.com.

cell described above, the gate's footprint was taken to be the width of the flow channel multiplied by the width of the nominal gradient between solution A and solution B.<sup>†</sup> To test our hypothesis that output current would scale with the area of the gate's footprint, we constructed a second flow cell of larger dimensions that could accommodate M:MOx nanofilms coated on 9×2-in<sup>2</sup>. The gate footprint areas of the standard and large flow cells were found to be 0.15 cm<sup>2</sup> and 1.0 cm<sup>2</sup>, respectively.

<sup>†</sup>The approximate width of the solution gradient was determined by mounting an uncoated glass slide in the flow cell and alternating flow between pure water and water containing food dye. A window machined in the faceplate of the flow cell allowed for the width of the gradient to be estimated by visual inspection.

### 3.3. Results

#### 3.3.1. Mechanism Part 1: Pseudocapacitance

The first part of our hypothesized two-part mechanism relies on the presence of rapidly changing interfacial electrostatic conditions at the M:MOx nanofilm:aqueous interface. Consider a M:MOx nanofilm in contact with pure water; depending on the pH of the water and the  $pK_a$  of the metal oxides in question, the film surface will carry a net negative charge. The interfacial potential originating from this charge will decay into the aqueous phase over a distance of several  $\mu\text{m}$  as it is screened by water dipoles. According to the local dielectric properties of the oxide, we hypothesize that at low ionic strength this potential extends past the oxide layer to polarize underlying atoms in the reduced metal layer, creating a rectifier (see Figure 3.3, leftmost box). At high ionic strength, counter-ions in the aqueous phase screen the interfacial potential much more efficiently, resulting in a Debye length of mere nanometers (see Figure 3.3, middle box).

While neither of the static cases described above constitutes a gate condition on its own, the rapid change from high to low ionic strength and *vice versa* does generate measurable current and voltage (see Figure 3.3, rightmost box). Consider the rapid replacement of the low-ionic-strength phase with a high-ionic-strength phase. We hypothesize that the leading edge of the high-ionic-strength phase draws electrons toward the film surface and holds them in place to form a pseudocapacitor with positive ions in the aqueous phase. Then, the leading edge of the impinging low-ionic-strength phase releases the electrons back into the bulk of the M:MOx nanofilm. This behavior can be approximated

by the charging and discharging of a capacitor and forms the basis for part one of our hypothesized mechanism, which is shared with carbon-based TENGs.

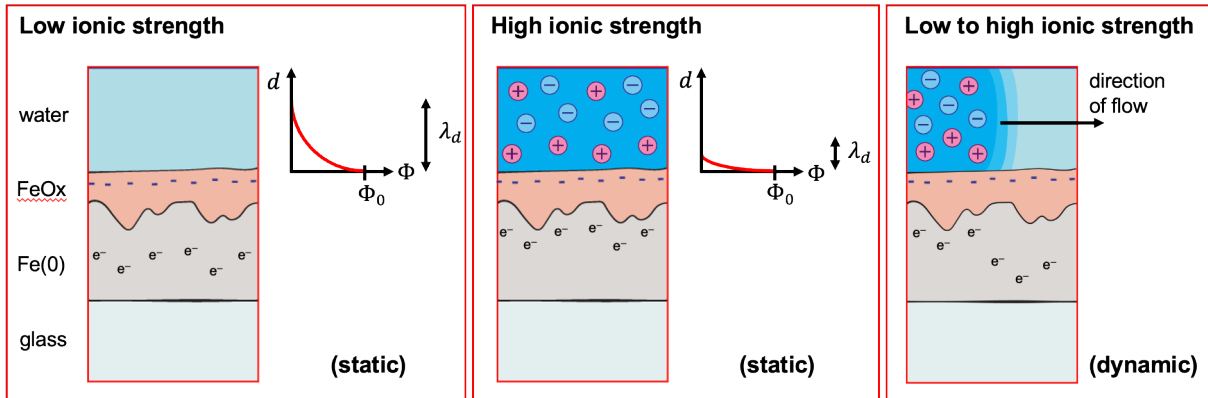


Figure 3.3. Graphical representation of static conditions of an Fe:FeOx nanofilm surface under static conditions (low and high ionic strength) and “gate” conditions triggered by the presence of a salinity gradient. Graphic by elabarts.com.

While M:MOx nanofilms generate pulses of electricity upon exposure to spatially and temporally varying salinity gradients—*i.e.*  $d[\text{NaCl}]/d(x, t)$ —this is not the only condition under which energy conversion occurs. In addition to salinity gradients, M:MOx nanofilms generate electricity when exposed to rolling saltwater droplets, rising and falling saltwater waves, and the oscillating boundary between immiscible liquids. Representative current generation profiles measured for each of these conditions are summarized in Figure 3.4. Although the pulse profile varies based on the geometry of the experimental set-up and the direction of flow, we see that each of these gate conditions has a common ability to produce pulses of current flow, provided there is a gradient in EDL conditions present. We further confirmed the necessity of the gate condition to energy conversion by modulating the size of the gate’s footprint. Using a larger flow cell and  $9 \times 2 \text{ in}^2$  metal nanofilms,

we were able to demonstrate that current scales directly with the estimated area of the salinity gradient footprint.

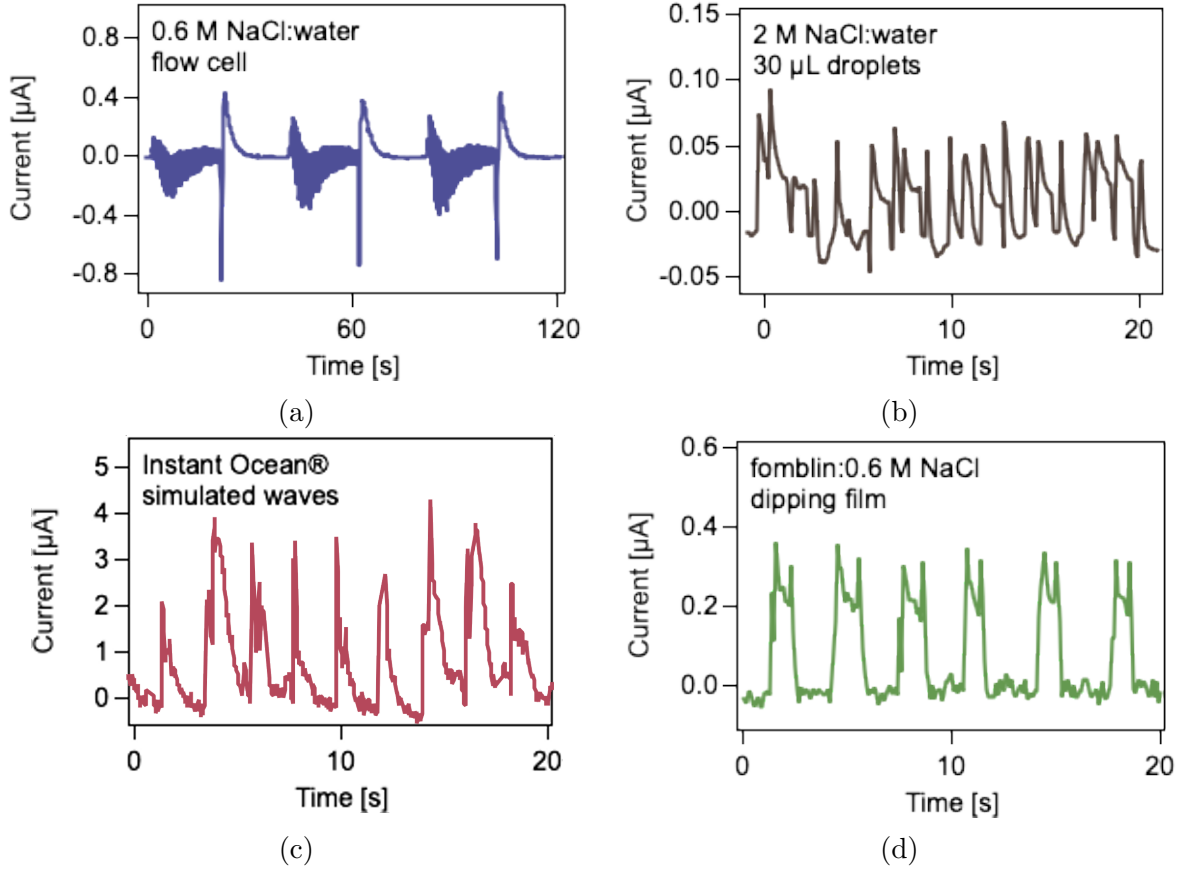


Figure 3.4. Measured current for different M:MOx nanofilms and gate conditions, including (a) alternating flow of salt- and freshwater over a nanofilm in a flow cell, (b) rolling alternating droplets of salt- and freshwater down a slanted nanofilm, (c) simulated ocean waves washing over a nanofilm in a wave tank, and (d) dipping a nanofilm into a beaker of phase-separated fomblin (a perfluoropolyether lubricant) and water.

Returning to the case of a M:MOx nanofilm actuated with a salinity gradient gate, we hypothesized that the extent of surface charging of the MOx layer would impact the capacity for energy conversion. To test this hypothesis, we conducted subsequent flow experiments with a 5-nm Fe:FeOx nanofilm in which we varied the value of  $[\text{NaCl}]_{\text{low}}$  and

$[\text{NaCl}]_{\text{high}}$  systematically, producing different ratios of low-to-high concentration. To start, we tracked induced current while alternating flow between  $[\text{NaCl}]_{\text{low}} = 0.1 \text{ mM}$  and ran alternating flow experiments for  $[\text{NaCl}]_{\text{high}}$  between 1 mM to 1 M. A similar process was then repeated for sets of  $[\text{NaCl}]$  with  $[\text{NaCl}]_{\text{low}}$  starting at 1, 10, and 100 mM. The results of these flow experiments—depicted in Figure 3.5—show that as the  $[\text{NaCl}]_{\text{high}}/[\text{NaCl}]_{\text{low}}$  ratio increases, so does the average peak current produced by the Fe:FeOx nanofilm.

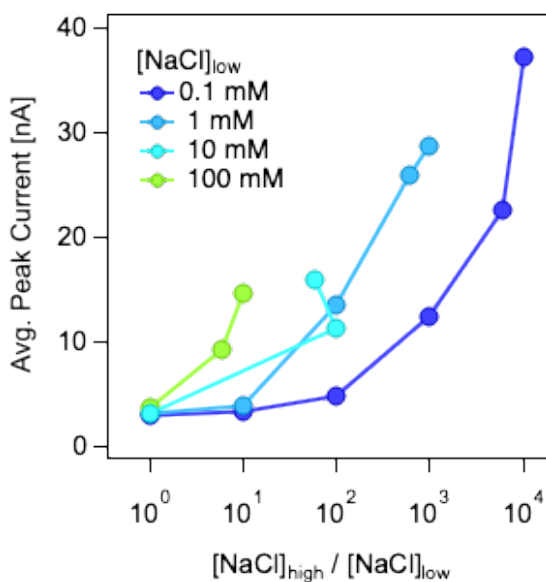


Figure 3.5. Averaged peak current output for a 5-nm Fe:FeOx nanofilm as a function of  $[\text{NaCl}]_{\text{high}}/[\text{NaCl}]_{\text{low}}$ .

### 3.3.2. Mechanism Part 2: Metal-Coupled Electron Transfer (MCET)

Figure 3.6 shows the results of replicate flow experiments conducted on the full suite of M:MOx nanofilms, with alternating flow of pure water and 0.6 M NaCl serving to create a salinity-gradient gate. We determined that peak current density and induced voltage scaled linearly with flow velocity, with the exception of single-element M:MOx nanofilms

of Al and Cr, which were insensitive to flow velocity. M:MOx nanofilms composed of Fe, Ni, or V, on the other hand, exhibited scalability of current density with flow velocity. The current density scalabilities as a function of flow velocity for every nanofilm composition investigated are summarized in Table 3.2. As noted in Section 3.2.1, XPS analysis of the native oxide overlayers of Al:AlOx and Cr:CrOx nanofilms demonstrated them to be composed of only a single oxidation state of their constituent metals, whereas Fe:FeOx, Ni:NiOx, and V:VOx nanofilms accessed at least two distinct oxidation states.

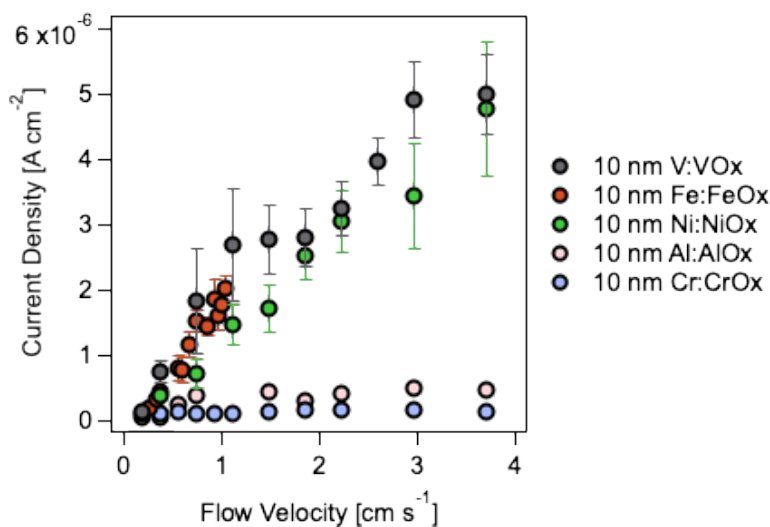


Figure 3.6. Current density measurements for 10-nm nanofilms of Al:AlOx, Cr:CrOx, Fe:FeOx, Ni:NiOx, and V:VOx exposed to alternating solutions of pure water and 0.6 M NaCl.

Since only M:MOx nanofilms with redox-active oxide overlayers display significant current density scalability, these results led us to hypothesize that EDL-enabled pseudocapacitance in M:MOx nanofilms is enhanced by the redox activity of the oxide overlayer, likely by some combination of intra-oxide electron transfer between  $M^{n+}$  and  $M^{m+}$  and electron transfer between the oxide and  $M(0)$ . Linked reactivity of the sort proposed here

has been reported in the past—notably by Rosso and Yanina, who found that charge accumulation on the surface of hematite can facilitate electron transfer and current flow in the bulk crystal.<sup>51</sup> Taken in sum, this proposed two-part mechanism accounts for the different behavior of M:MOx nanofilms of different compositions. For nanofilms whose oxide overlayers are composed of a single oxidation state of the metal (Al, Cr), only part 1 of the mechanism holds, with energy conversion occurring primarily through contact electrification. For nanofilms with multiple oxidation states present in their oxide overlayers (Fe, Ni, V), both part 1 and part 2 of the mechanism are operable, and not only does energy conversion occur, but it is also enhanced as a result of metal-coupled electron transfer (MCET).

| M:MOx | Current Density Scalability [ $\mu\text{A s cm}^{-3}$ ] |
|-------|---|
| Al    | 0.04(4)   |
| Cr    | 0.003(3)  |
| Fe    | 2.8(2)  |
| Ni    | 1.25(15)  |
| V     | 2.1(3)  |

Table 3.2. Scalability of current density for selection of 10-nm M:MOx nanofilms.

From here, we evaluated whether the underlying zero-valent metal was indeed necessary to current induction. In brief, we exposed a 10-nm Fe:FeOx nanofilm to high-temperature quantitative ozone oxidation, resulting in a film composed exclusively of mixed iron oxides (FeOx) with no Fe(0) present. Subjecting this FeOx nanofilm to the same salinity-gradient gate conditions, we observed negligible current density, as expected (Figure 3.7). Predicting that capping an “active” M:MOx nanofilm with a less active nanofilm would similarly suppress current generation, we exposed a 30-nm Fe:FeOx

nanofilm topped with a 5-nm Cr:CrOx nanofilm to our salinity-gradient gate and indeed, the output current density was more comparable to a nanofilm composed entirely of FeOx than it was to a 30-nm Fe:FeOx nanofilm with no capping layer (see Figure 3.7).

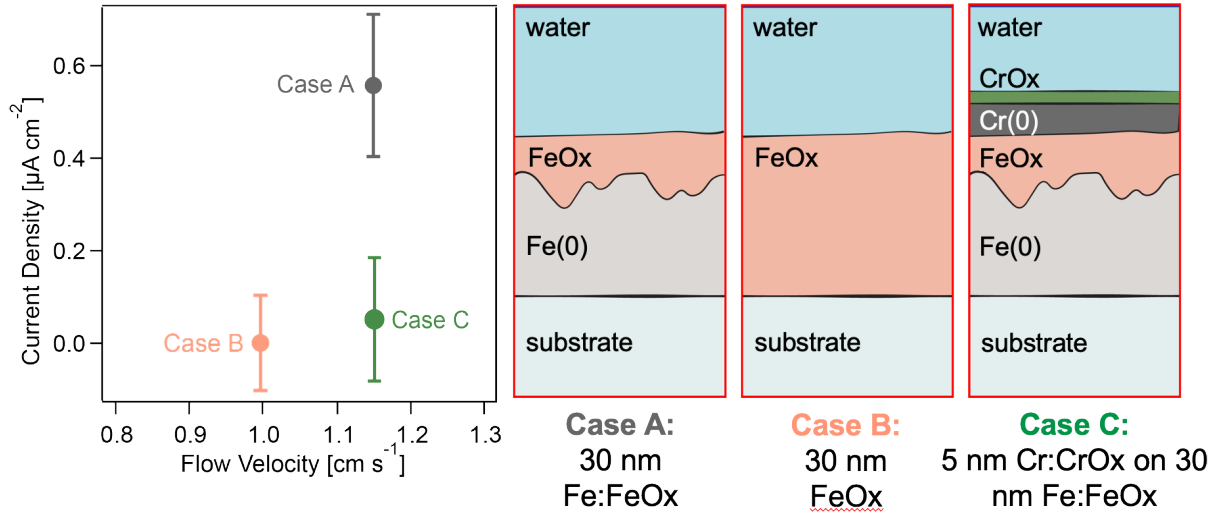


Figure 3.7. Current density measurements for Case A (30-nm Fe:FeOx nanofilm), Case B (30-nm Fe:FeOx nanofilm fully oxidized to form a purely FeOx film), and Case C (30-nm Fe:FeOx nanofilm capped with a 5-nm Cr:CrOx nanofilm) during exposure to an identical salinity-gradient gate in our flow cell set-up. Graphic by elabarts.com.

### 3.4. Summary and Future Directions

In this chapter we demonstrate the capacity of M:MOx nanofilms composed of several Earth-abundant elements (Al, Cr, Fe, Ni, and V) to generate measurable current and voltage on the order of several tens of mV and tens of  $\mu\text{A}/\text{cm}^2$  in the presence of an EDL gradient—or “gate”—conditions. We show that any set of conditions that produces a modulation in the EDL at the M:MOx nanofilm surface that varies in time and space can enable energy conversion, including falling droplets, rolling saltwater waves, or the oscillation of the phase boundary between two immiscible liquids. Based on a series

of experiments testing the roles of the underlying M(0) and the overlying MOx layers and the impact of the metal composing the nanofilm, we propose a two-part mechanism to explain energy conversion in M:MOx nanofilms. In part 1, we hypothesize that the EDL forms a pseudocapacitor with electrons in the M:MOx nanofilm, resulting in contact electrification. In part 2, we further hypothesize that this initial contact electrification can be further enhanced by the capacity of M:MOx nanofilms with redox-active MOx overlayers to undergo MCET.

Aspects of our hypothesized mechanism of current generation in M:MOx nanofilms remain to be verified. One outstanding question is the extent to which charge flow is divided between the M(0) layer and the MOx layer. This question could be investigated by using a system of masks to deposit M:MOx nanofilms in geometries that allow for the monitoring of charge flow predominantly in either one layer or the other. The use of sputtered gold nanolayers as electrical contacts followed by a M:MOx nanofilm may allow us to isolate the contribution from the reduced metal layer. Conversely, by sputtering the gold contacts on top of an already deposited M:MOx nanofilm we may isolate the contribution from the oxide layer. This approach would enable assessment of the relative contributions to current generation from the M(0) and MOx layers.

A related question is whether a MOx overlayer is required for the energy harvest mechanism to occur, or if MCET is indeed responsible for significant electrical output enhancements. As mentioned earlier, current flow is observed for a typical M:MOx nanofilm in which both the reduced metal and the oxide are present. Conversely, for a film composed entirely of the oxide—in our case, mixed FeOx—current flow is completely cut off. Extending this line of inquiry, a future direction would be to make a film with little to

no oxide layer and see to what extent it facilitates current flow. A good candidate for this experiment would be to deposit a film from iridium—the most corrosion-resistant element—and measure its performance under comparable conditions to our more studied films. Additionally, future work may seek to improve M:MOx performance by varying the nature and thickness of the M(0) and MOx layers by employing mixed-layer architectures, or by using alloys and nano-patterning of exposed oxide surfaces.

Finally, a recent report by Choi and coworkers<sup>52</sup> suggests that TENG performance can be enhanced through the introduction of a high-permittivity “electron blocking layer” (EBL) in order to drive electrons away from the interface and polarize the triboelectric material. In their study the EBL consisted of TiO<sub>x</sub> layer sandwiched between an aluminum (Al) electrode and a polydimethylsiloxane (PDMS) film. Future work may seek to investigate whether the performance of our M:MOx nanofilm-based TENGs reported in this work may see improvement through the introduction of various high-permittivity EBL materials.

## CHAPTER 4

## Adapting Heterodyne Detected Second Harmonic Generation (HD-SHG) Spectroscopy to Metals and Metal Oxides

### 4.1. Background

In the field of surface-specific analysis of buried solid:liquid interfaces, an enduring challenge is how to study complex or heterogeneous systems under conditions that reflect real-world environments, rather than the idealized laboratory setting.<sup>1</sup> In order to accommodate a particular analytical approach's mode of excitation (*e.g.* electron beam, ion beam, or photons) or means of detection, or to avoid adventitious surface contamination, there is often a requirement for certain sample preparations or operating conditions that diverge from those inherent to the natural systems we wish to study.

For example, ultra-high-vacuum (UHV) is a common requirement for many surface-specific techniques, including X-ray photoelectron spectroscopy (XPS),<sup>2</sup> scanning electron microscopy (SEM),<sup>3</sup> secondary ion mass spectrometry (SIMS),<sup>4</sup> and Auger electron spectroscopy (AES).<sup>5</sup> Although these techniques are powerful, the UHV requirement constrains sample selection to materials that are vacuum-compatible, complicating the study of wet or off-gassing materials. To address this, advances have been made in the use of closed cells for environmental scanning electron microscopy (ESEM),<sup>6</sup> as well as the parallel development of techniques that do not require UHV, such as some forms of atomic

force microscopy (AFM), scanning tunneling microscopy (STM), grazing incidence X-ray diffraction (GIXRD), and Fourier transform infrared (FTIR) spectroscopy.<sup>7,8</sup>

Beyond vacuum requirements, certain techniques such as SEM, SIMS, and STM require conductive sample substrates, which can serve to constrain sample material selection or require the use of sputtered or evaporated conductive coatings that may alter or interfere with the very surface species that were originally the analytical target. This is an important consideration in the selection of an analytical technique, along with the nature of certain methods to be destructive to the target surface.

In this regard, SHG offers a set of distinct advantages in the arena of surface analysis, as it is inherently surface-selective and non-destructive, and can probe both soft and buried interfaces at atmospheric pressures and under environmentally relevant conditions. Additionally, SHG works with both conducting and insulating solids, though certain considerations must be made with respect to field effects introduced by metallic materials.<sup>9</sup>

While these are indeed significant benefits, it is also true that the selection of strongly absorbing materials (*i.e.* metals and most metal oxides) can complicate sample preparation and data interpretation for SHG. This is even more so the case for HD-SHG, which has stringent requirements for sample stability and the understanding of a particular material's impact on measured phase. While it can be simpler to employ common optical materials such as fused silica or CaF<sub>2</sub> as the solid phase of the solid:liquid interface under study, this ultimately does not advance the technique toward broader applicability in the realm of environmental interfacial analysis.

Recognizing the challenges inherent to SHG analysis of strongly absorbing materials, but simultaneously acknowledging its power in tandem with heterodyne detection to act as a direct probe of interfacial potential and second- and third-order nonlinear susceptibilities, the aim of this chapter is to detail efforts to adapt our HD-SHG systems to the study of samples such as PVD metal thin films and ALD metal oxide thin films. To that end, we will first discuss attempts to optimize the sample preparation and geometry, as well as the relative stability afforded by using an oscillator-only rather than an integrated-oscillator-and-amplifier laser system. We follow this discussion with a description of best practices for aligning on flat optical windows, as well as the recalculation of several quantities critical for the interpretation of our HD-SHG results.

## 4.2. Optimization

### 4.2.1. Overcoming the Strong Absorber Problem

When performing SHG measurements using internal reflection geometry, the fundamental and SHG beams interact with the optical material composing the sample substrate. If this material is strongly absorbing at either of the two relevant wavelengths ( $\omega$  and  $2\omega$ ) then substantially less signal passes from the substrate to the detector. Therefore, the selection of sample substrates for SHG spectroscopy typically prioritizes transmissivity in the visible and IR range, in order to optimize signal. For SHG studies with a NIR fundamental beam, this is often an IR-grade fused silica or fused quartz window or lens.

While the fused silica:water interface has provided fertile ground for decades of fundamental studies of charged solid surfaces in aqueous environments, it is nonetheless a highly

idealized system.<sup>10</sup> Confining the solid component of the solid:liquid interface to fused silica, therefore, limits the generalizability of SHG as an analytical technique. Given the power of SHG to directly probe interface-specific electrostatic properties of buried aqueous interfaces that are otherwise analytically inaccessible, a major focus of this thesis is to demonstrate how the methods of SHG—and HD-SHG in particular—may be adjusted to accommodate a broader range of sample compositions and geometries for the solid phase of solid:liquid interfaces.

The two main classes of solid materials we aim to evaluate using HD-SHG are fully reduced, zero-valent metals and metal oxides. As shown in Table 4.1, the refractive indices of these materials are complex-valued due to their absorbing nature, in contrast to common optical materials like fused silica and sapphire.

| Material                                   | $\lambda$ [nm] | $n$    | $k$    |
|--|----------------|--------|--------|
| fused silica (SiO <sub>2</sub> )           | 515            | 1.4500 | —      |
|  | 1030           | 1.4615 | —      |
| sapphire (Al <sub>2</sub> O <sub>3</sub> ) | 515            | 1.7730 | —      |
|  | 1030           | 1.7551 | —      |
| hematite (Fe <sub>2</sub> O <sub>3</sub> ) | 515            | 3.2670 | 0.6045 |
|  | 1030           | 2.7650 | 0.0130 |
| aluminum (Al)                              | 515            | 0.8675 | 6.2231 |
|  | 1030           | 1.4033 | 9.8532 |
| iron (Fe)                                  | 515            | 2.8312 | 2.9028 |
|  | 1030           | 2.9421 | 3.9094 |

Table 4.1. Refractive indices of a selection of optical materials, reduced metals, and metal oxides.

Adjusting the Lambert-Beer law to include the imaginary portion of the refractive index ( $k$ ), we obtain for a plane wave traveling through a material in the  $x$ -direction:

$$(4.2.1) \quad I(x) = I_0 e^{-4\pi kx/\lambda_0}$$

where  $I$  is intensity,  $x$  is the distance traveled in the material, and  $\lambda_0$  is the vacuum wavelength. From this expression we see that absorption depends not just on  $k$ , but also on the depth of penetration in the optical medium. For this reason, we can circumvent the fact that  $k > 1$  for metals and many metal oxides by minimizing the thickness of our samples.

To access the sub-100-nm thicknesses needed to adequately compensate for the strongly-absorbing nature of metals and many metal oxides, we employed a range of thin film deposition techniques, as described more fully in Sections 3.2 and 5.2. Figure 4.1 demonstrates the measured absorbance of thin films of zero-valent iron (ZVI) at a range of film thicknesses at two wavelengths within 35 nm of the fundamental and SHG wavelengths used in this thesis' reported studies. Above 50 nm in thickness, ZVI films rapidly approach complete opacity. For our work, we found that a thickness of 10 nm was sufficient to access measured absorbances around 0.2—corresponding to about 80% transmission of incident light. As presented in more detail in Chapter 5,  $\alpha$ -hematite films deposited by ALD on fused silica substrates with a target thickness of 10 nm exhibited between 50 and 60% transmission at 515 nm, and over 90% transmission at 1030 nm, indicating that 10 nm was a workable sample thickness for this material as well.

#### 4.2.2. Selection of a Sample Geometry for SHG Studies

As described in Section 4.2.1, thin films of metals and metal oxides were necessary in order to circumvent their opacity at thicknesses in excess of a few tens of nms. These

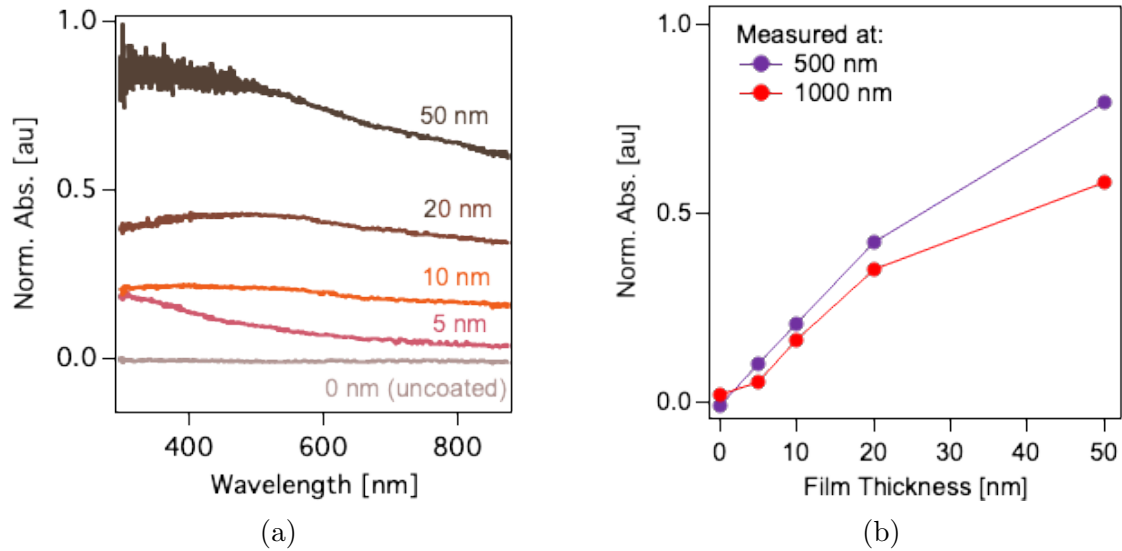


Figure 4.1. Plots including (a) the normalized absorbance spectra of zero-valent iron (ZVI) films of thicknesses between 5 and 50 nm and an uncoated borosilicate glass microscope slide (1 mm thick) as a point of comparison and (b) the absorbances measured at 500 nm and 1000 nm as a function of film thickness.

films require a substrate or support, and for our purposes we chose to proceed with IR-grade fused silica as the support material, given its durability, relatively low cost, SHG-silence, and good transmissivity at our working wavelengths. XPS characterization of films deposited *via* ALD or PVD confirmed that there was no detectable silicon contamination resulting from the choice of substrate. Having decided on the substrate composition, our next aim was to determine an appropriate sample geometry. We summarize the advantages and drawbacks of each combination of sample geometry and deposition method in Table 4.2, and expand on the process in the remainder of this section.

Most SHG studies on the solid:liquid interface are conducted in “internal” geometry—meaning that the fundamental beam must pass through the sample substrate before and after impinging on the interface under study before collection and do not pass through the

|     | Description  | Advantages                                   | Disadvantages  |
|-----|--|--|--|
| (1) |  Uncoated hemisphere.   | Low photon loss.                             | Access only limited set of materials.                          |
| (2) |  ALD-coated fused SiO <sub>2</sub> hemisphere.  | Low photon loss.<br>Access any ALD material. | Not ideal for ALD (disrupts air flow, conducts heat poorly).   |
| (3) |  ALD-coated fused SiO <sub>2</sub> window with fused SiO <sub>2</sub> hemisphere (optical coupler). | Ideal for ALD.<br>Low photon loss.           | Requires use of index-matching fluid.<br>Poor phase stability. |
| (4) |  ALD-coated fused SiO <sub>2</sub> window.  | Ideal for ALD.<br>Good phase stability.      | High photon loss.  |

Table 4.2. Summary of sample geometries for HD-SHG investigation of metals and metal oxides evaluated in the course of this work.

bulk water. Additionally, the spectroscopist often selects a sample substrate geometry to minimize photon loss, and ensure that laser beams of different colors encounter the same Fresnel losses at any incident angle and/or polarization.<sup>11</sup> Examples of such geometries include hemispherical half-ball lenses,<sup>11–15</sup> hemicylindrical lenses,<sup>16</sup> cylindrical cuvettes,<sup>17</sup> hollow domes,<sup>18</sup> and trapezoidal prisms.<sup>19</sup> The solid substrate either serves itself as the solid phase of the solid:liquid interface of interest, or else it serves as an optical coupler to a thin film or substrate of the desired sample material. Often, the latter case is preferred when materials of the desired geometry are not available commercially or are prohibitively expensive to obtain.

For most thin film deposition techniques, it is simpler to deposit on flat rather than irregular or oversized substrates. This presented challenges to our initial attempt to

deposit thin films directly on the fused silica hemispheres typically used in our SHG and HD-SHG spectrometers, which are 25.4 mm diameter. During ALD deposition, for instance, the height of the deposition chamber's door prevented the hemisphere from being loaded into the instrument. Even for an ALD system with dimensions large enough to accommodate our standard hemispheres, further challenges arose. Firstly, the bulkiness of the substrate disrupted air flow currents in the chamber, impeding gas-phase precursors from fully diffusing during the deposition process. Secondly, poor contact between the curved portion of the hemisphere and the sample chuck resulted in insufficient heating of the sample and large temperature gradients. The combination of these effects resulted in films with a high degree of heterogeneity in thickness, which made them unsuitable for our purposes. When attempting the same ALD process with a flat window of fused silica with a thickness of 1 mm, these issues were entirely avoided.

Although we were more readily able to deposit thin metal films *via* PVD on 25.4-mm-diameter fused silica hemispheres—since it is a line-of-sight deposition method with no need for substrate heating—the bulkiness and irregular shape of the substrate were still incompatible with most complementary surface characterization techniques, including AFM, XPS, and UV-vis/NIR absorption/transmission spectroscopy. Given the importance of these complementary techniques to judging whether chemical and physical alteration of films had taken place after exposure to experimental conditions, we abandoned direct deposition of thin films on fused silica hemispheres and proceeded with using 1-mm-thick, 25.4-mm-diameter fused silica windows as substrates.

### 4.2.3. Relative Stability of Flat *versus* “Sandwich” Geometry

Initial studies on metal and metal-oxide thin films employed a “sandwich”-like set-up in which we placed a coated window film-side-down on top of a fluoroelastomer or Viton O-ring, sealing a custom-machined polytetrafluoroethylene (PTFE) flow cell (see Section 2.4.1). We subsequently placed an uncoated, 25.4-mm-diameter fused silica hemisphere on top of the window’s uncoated side to serve as an optical coupler. To minimize photon loss between the coated window and the uncoated hemisphere, we placed a drop of index-matching optical fluid (Cargille, Series AA  $n = 1.4580 \pm 0.0002$  at 589.3 nm and 25°C) on the uncoated side of the window before clamping the uncoated hemisphere in place.

Previously published work in the Geiger group demonstrates the effectiveness of using a fused silica hemisphere as an optical coupler to a flat substrate—either composed of fused silica itself and coated with a metal oxide layer, or composed entirely of a material of interest.<sup>20,21</sup> However, all previous uses of this geometry were in the context of homodyne-detected SHG studies. In the case of HD-SHG measurements, a relatively higher degree of stability is required, as small changes in the positioning between the beam and the sample over the course of an experiment can alter the relative path lengths of the SHG and reflected fundamental beams, introducing drift in the measured phase. Due to the use of the index-matching optical fluid between the optical coupler and the flat sample, the “sandwich” geometry introduces a highly slippery contact plane to the sample assemblage. For subsequent HD-SHG phase measurements taken on this assemblage, we found a systematic phase drift of  $\pm 5^\circ/\text{h}$  (Figure 4.2a), compared to a previously published phase drift of  $< \pm 2^\circ/\text{h}$  for an uncoated fused silica hemisphere.<sup>14</sup>

With the aim of achieving comparable phase stability to the uncoated hemisphere sample geometry, we attempted to conduct HD-SHG measurements on coated and uncoated fused silica windows without the use of a fused silica hemisphere as an optical coupler. This geometry allowed us to forego the use of index-matching optical fluid entirely and eventually yielded phase drift of  $< \pm 3^\circ/\text{h}$  due to the enhanced stability of the sample-holding assemblage (Figure 4.2b).

With a phase drift comparable to the original reported sample geometry for our spectrometer, we proceeded with a coated fused silica window for all subsequent experiments. As will be discussed in Section 4.3, the omission of the optical coupler required certain quantities of the system to be recalculated in order to account for the refraction of the beams when passing from air to silica, including the wavevector mismatch and the Fresnel coefficients. Additionally, as will be discussed in Section 4.2.5, the flat geometry generated multiple reflections from both the internal and external faces of the sample substrate, requiring special considerations during the alignment process. Finally, the use of a flat geometry with no optical coupler unavoidably leads to some photon loss as the beam refracts upon entering and exiting the sample, particularly on the signal side. For an uncoated fused silica window, this results in a two-order-of-magnitude reduction in  $I_{SHG}$  compared to an uncoated fused silica hemisphere. Fortunately, the presence of an ALD  $\alpha$ -hematite film on a fused silica window serves to resonantly enhance the detected SHG signal, compensating for the relative reduction in signal intensity due to sample geometry, as we will show below.

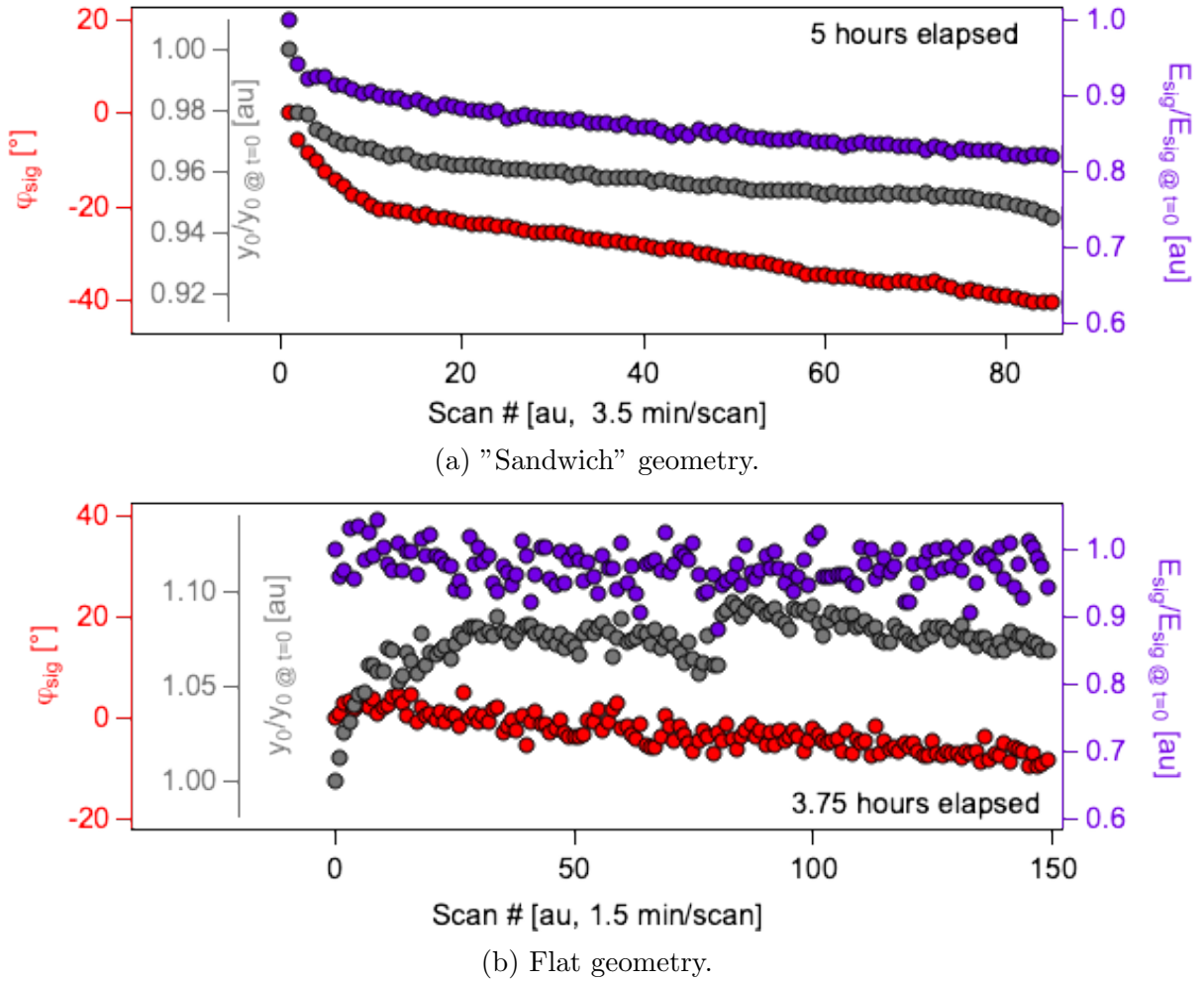


Figure 4.2. Comparison of the relative stability of three fitting parameters for HD scans taken using System 1 on fused silica:water samples tracked over multi-hour experiments with "sandwich" and flat geometry.

#### 4.2.4. Relative Stability of Oscillator + Amplifier *vs.* Oscillator-Only System

Phase drift was further improved by switching from System 1 to System 2 (see Sections 2.3.1 and 2.3.2, respectively), due to the improved stability of the ytterbium-based Flint femtosecond laser oscillator (Light Conversion). The relevant distinctions in specifications

and performance between the Flint and the Pharos femtosecond laser are enumerated in Table 4.3.

|   | <b>Pharos</b> | <b>Flint</b>        |
|---|---------------|---------------------|
| Description                               | Amplifier     | Oscillator          |
| Repetition Rate                           | 200 kHz       | 75.5 MHz            |
| Incident Power                            | <80 mW        | 200 mW–2 W          |
| Pulse Duration                            | 230 fs        | 80 fs               |
| Energy per Pulse                          | <0.4 $\mu$ J  | 2.6–26 nJ           |
| $I_{SHG}$ from fused silica:water @ 80 mW | 370 cps       | 20 cp100ms, 10 avg. |

Table 4.3. Comparison of the specifications and relevant operating conditions and performance of the Pharos and the Flint systems, used with System 1 (see Section 2.3.1) and 2 (see Section 2.3.2), respectively.

Although the Pharos can produce output power in excess of 1 W, our experiments typically require about 100-fold less incident power in order to not burn the sample surface, necessitating dramatic attenuation of the output beam. When the beam is attenuated by this much, the laser is running far from the maximum of its performance curve, an operating condition to which we attribute the long-term drift in measured phase observed in previous reports using the Pharos system.<sup>12,14,22</sup> On the other hand, due to the Flint’s higher repetition rate, the system produces pulses with energies that are two orders of magnitude smaller than those that the Pharos produces for comparable incident power. In other words, the Flint’s high repetition rate enables the use of higher incident power without increasing the pulse energy to the point of initiating optical breakdown of the sample substrate. Furthermore, in our experience, a 2-h warm-up period is required in order to achieve phase stability of  $< \pm 2^\circ$  while performing HD-SHG measurements on System 1 with the Pharos integrated oscillator and amplifier. Conversely, the Flint does

not show such an extended warm-up time, allowing experiments to commence immediately following sample mounting and spectrometer alignment.

We hypothesized that the use of the oscillator-only Flint system would reduce the observed phase drift over the course of a multi-hour experiment. To test this premise, we collected high-quality interference fringes (500-ms acquisitions, 10-point averaging, roughly 9-min scans) for a period of 12 h on an uncoated fused silica optical flat (Figure 4.3). Indeed, even without the 2-h warm-up period, phase measurements acquired on the Flint system displayed much better long-term stability ( $-0.03(4)^\circ/\text{h}$ ). Comparing these results to those shown in Figure 4.2 (which were obtained using the Pharos with System 1) makes clear that an improvement in phase stability was achieved beyond what we expected simply for using flat geometry.

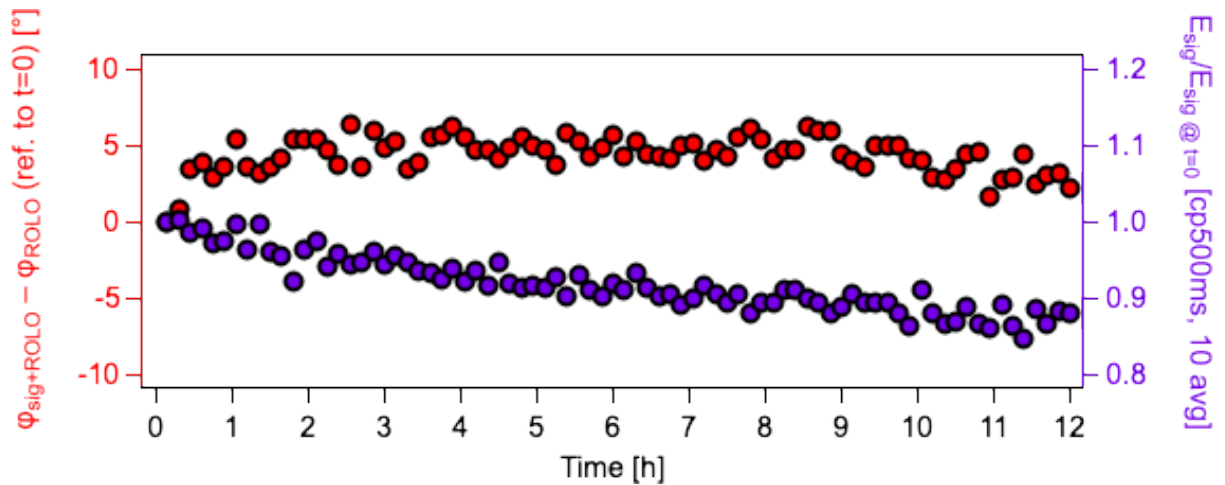


Figure 4.3. Results from an overnight stability study on an uncoated fused silica optical flat taken on System 2 (*i.e.* with the oscillator-only Flint system). Phase drift was calculated to be  $-0.03(4)^\circ/\text{h}$  over 12 h, or essentially flat.

Additionally, the original System 1 sample stage explicitly lacked micrometer adjustments. Both this choice to sacrifice  $xyz$ -control of the stage—as well as the use of a

custom-machined aluminum holder to house the PTFE flow cell and sample assembly—were taken in order to minimize the introduction of phase drift due to small changes in beam pointing or sample position. Conversely, the System 2 spectrometer—which is fed by the Flint oscillator—reintroduces micrometer adjustments to the sample stage. Despite this change, the enhanced stability of the oscillator output still resulted in a net stabilizing effect on long-term phase measurements.

#### 4.2.5. Internal Interface Beam Selection

As depicted graphically in Figure 4.4, the use of flat sample geometry and an input beam angle of  $60^\circ$  reflects a portion of the fundamental beam and generates SHG signal from both the desired internal fused silica:water interface as well as the external air:fused silica interface. In the case of our solid:liquid interface experiments (regardless whether the fused silica window is coated or uncoated), solution conditions (*e.g.* pH, ionic strength) are only changed in the liquid phase, meaning that any SHG signal generated from the air:fused silica interface should be invariant and therefore extraneous to our measurements. However, initial experiments with homodyne detection of SHG intensity suggested that co-detection of the external SHG beam obscures changes to the intensity of the internal SHG beam.

Figure 4.5 illustrates this phenomenon for the case of transitioning the aqueous phase of a fused silica:aqueous interface from pure water to 100 mM NaCl (both around pH 5.7 after overnight  $\text{CO}_2$ -equilibration). This transition from an almost entirely electrolyte-free aqueous environment to one with plenty of mobile ions is a useful proof-of-concept for a new SHG spectrometer or sample set-up, as we expect to see a readily apparent decrease

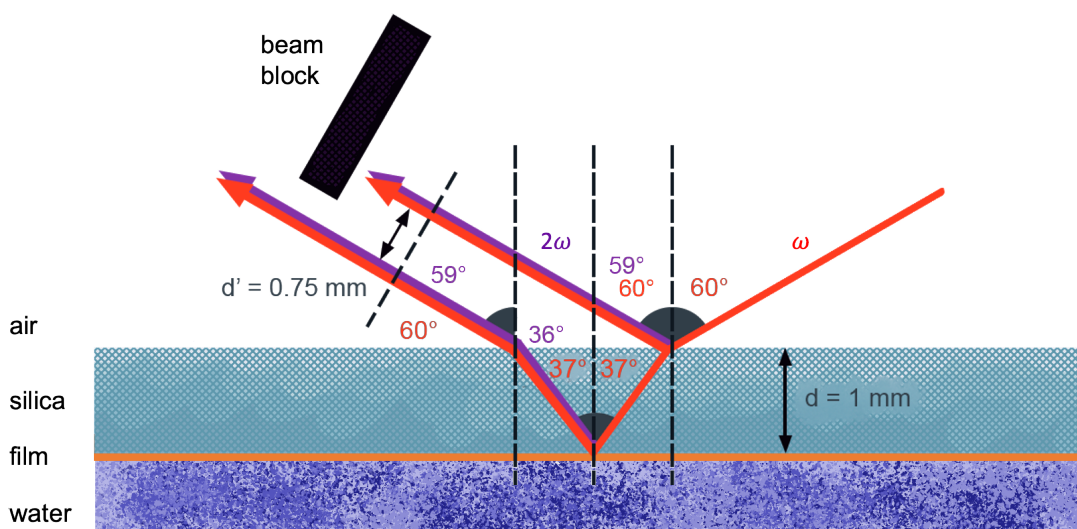


Figure 4.4. Depiction of the reflection of the fundamental beam and the generation of an SHG beam from both the air:fused silica and fused silica:water interfaces. Using a beam block allows complete exclusion of the external beam from detection, since a 1-mm-thick fused silica substrate produces a separation of 0.75 mm between the external and internal beams' centers.

in  $I_{SHG}$  due to the large relative increase in screening of the interfacial potential from fused silica's net negative surface charge. The dark blue trace in Figure 4.5 depicts an example of such a change in  $I_{SHG}$  for a fused silica hemisphere as the sample substrate. As the most-used substrate in the Geiger group's recent publications,<sup>12,14,22,23</sup> this is a useful point of comparison for determining the viability of alternative sample substrates. Indeed, the normalized response of a sample with "sandwich" geometry (*i.e.* a fused silica window in contact with a hemispherical fused silica optical coupler) shown in light blue overlaps the fused silica hemisphere's response almost perfectly. Conversely, the first attempt to use a fused silica optical flat in lieu of a fused silica hemisphere produced no change in intensity when transitioning from water to 100 mM NaCl (green trace). Only

once we blocked the external beam (as the pink trace in Figure 4.4 shows) did we observe any change in  $I_{SHG}$  in response to introducing ions to the interface.

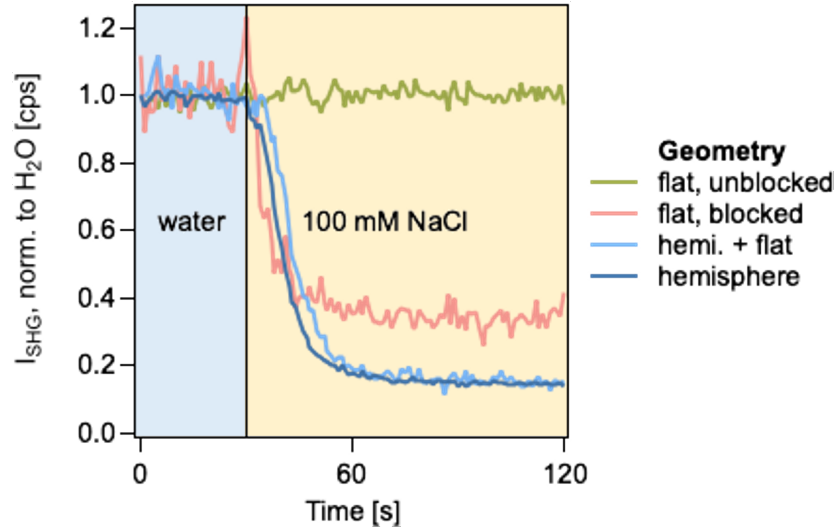


Figure 4.5. Normalized change in  $I_{SHG}$  due to the transition of the aqueous phase of the fused silica:aqueous interface from pure water to 100 mM NaCl for a hemispherical fused silica sample, a 1-mm-thick flat fused silica sample in contact with a hemispherical fused silica optical coupler, and a 1-mm thick flat fused silica sample with the external reflection both unblocked and blocked.

Using Snell's Law (Eq. 4.3.2) once again, we can determine the relative separation of the internal and external beams' centers. For a 1-mm-thick fused silica optical window, this separation is approximately 0.75 mm and can be confirmed visually through the use of a NIR laser detection card. To block the contribution from the external air:fused silica interface, we used a small piece of anodized aluminum sheeting mounted on a manual precision linear stage. By visual inspection, this micrometer-adjusted beam block could exclude the external beam while allowing the internal beam to pass unimpeded.

We note that both the internal and external beams include reflected fundamental as well as generated SHG, therefore blocking the external beam does not entirely inhibit the generation of SHG from the LO downstream, although it does result in diminished LO intensity. This principle is illustrated in Figure 4.6a, which shows the results of homodyne-detected  $I_{SHG}$  measurements on a fused silica:quartz interface constructed by fixing a rectangular piece of  $z$ -cut  $\alpha$ -quartz (10 mm  $\times$  5 mm  $\times$  3 mm, Knight Optical) to a 1-mm-thick fused silica window with index-matching optical adhesive (Norland, 146H). In this configuration, blocking the external beam diminishes the SHG signal from the sample interface by roughly 21.5(9)% relative to when the external beam is unblocked. This effect is even more pronounced for the homodyne intensity measured only from the LO, which was obtained by placing a longpass filter downstream of the sample and upstream of the LO to cut  $I_{SHG,sample}$  and pass  $I_{SHG,LO}$ . For the LO alone, blocking the external beam cut the measured homodyne intensity by 82.4(8)%. To further confirm the viability of this method, we performed power studies on the interface between an uncoated fused silica window in contact with a piece of  $z$ -cut  $\alpha$ -quartz with the external beam unblocked and blocked. As shown in Figure 4.6b, both cases showed good quadratic dependence of  $I_{SHG}$  on the input power.

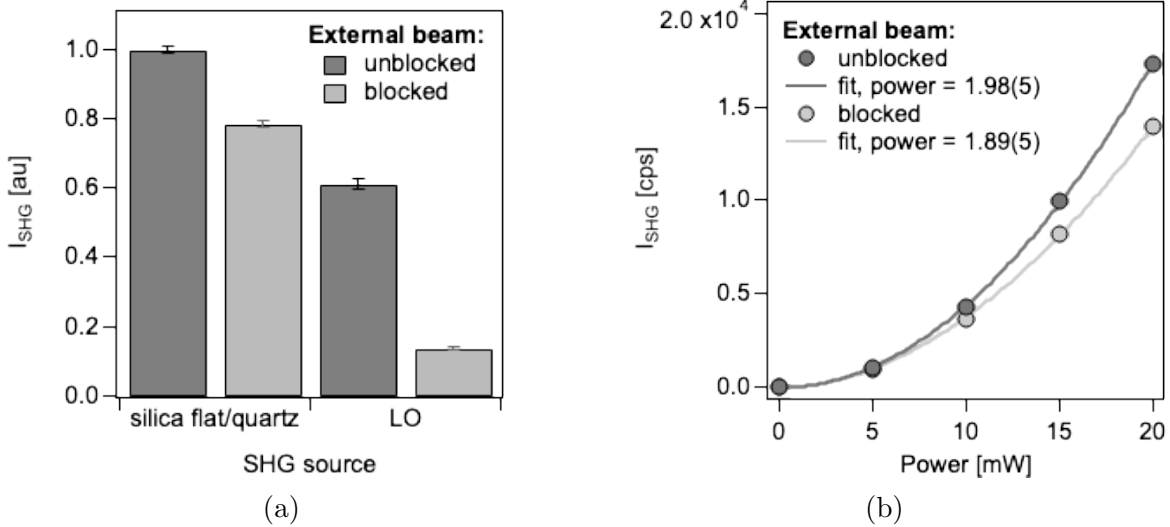


Figure 4.6. The results of control experiments performed on the System 1 HD-SHG set-up on a silica:quartz interface with the external combined fundamental/SHG beam blocked and unblocked. These include (a) normalized homodyne intensity measurements and (b) power studies showing good quadratic dependence of raw  $I_{SHG}$  counts on input power.

### 4.3. Calculations

#### 4.3.1. Calculating Wavevector Mismatch ( $\Delta k_z$ ) for Optical Flats

The quantity  $\Delta k_z$  describes the wavevector or phase mismatch of the beam reflected following the SHG optical process. The value of  $\Delta k_z$  depends on the optical properties of the media composing the interface—namely the indices of refraction—as well as the incident angles of the impinging fundamental beam and the exiting SHG output beam. These latter parameters themselves rely on the specific geometry of the sample under interrogation. Previous studies have determined a  $\Delta k_z$  value of  $1.1 \times 10^7 \text{ m}^{-1}$  for hemispherical fused silica lenses in contact with an aqueous phase.<sup>14</sup> For this work, however, the use of optical flats required the calculation of the value of  $\Delta k_z$  taking the new geometry into account.

In the following calculations, the subscripts *air*, *SiO<sub>2</sub>*, and *H<sub>2</sub>O* will refer to the three phases under consideration in this system: air, fused silica, and water, respectively. The subscript *0* will refer to the SHG output beam at 515 nm and the subscripts *1* and *2* will both refer to the input fundamental beam at 1030 nm. For an SHG process occurring in water, the following equations define  $\Delta k_z$ :<sup>24–27</sup>

$$(4.3.1) \quad \begin{aligned} \Delta k_z &= |k_{1z,\text{H}_2\text{O}} + k_{2z,\text{H}_2\text{O}} - k_{0z,\text{H}_2\text{O}}| \\ &= \frac{1}{c} (\omega_1 n_{1,\text{H}_2\text{O}} \cos \theta_{1,\text{H}_2\text{O}} + \omega_2 n_{2,\text{H}_2\text{O}} \cos \theta_{2,\text{H}_2\text{O}} + \omega_0 n_{0,\text{H}_2\text{O}} \cos \theta_{0,\text{H}_2\text{O}}) \end{aligned}$$

where  $\omega_{i,x}$  is the angular frequency,  $n_{i,x}$  is the refractive index, and  $\theta_{i,x}$  is the beam angle relative to surface normal—all three of which are specified for a particular beam wavelength in a particular medium. Table 4.4 enumerates the values of  $n_{i,x}$  for all beam wavelengths and media.

| $n_{i,x}$      | air    | SiO <sub>2</sub> | H <sub>2</sub> O |
|----------------|--------|------------------|------------------|
| 0 (515 nm)     | 1.0003 | 1.4615           | 1.3357           |
| 1, 2 (1030 nm) | 1.0003 | 1.4500           | 1.3247           |

Table 4.4. Refractive indices for all beams in all media.

Using a value of  $\theta_{1,\text{air}}$  for the incident fundamental 1030-nm beam along with the refractive indices from Table 4.4, the remaining values of  $\theta$  follow from the application of Snell’s Law for a beam passing from medium *x* to medium *y*:

$$(4.3.2) \quad n_{i,x} \sin \theta_{i,x} = n_{i,y} \sin \theta_{i,y}$$

and Table 4.5 enumerates the resulting calculated values of  $\theta$  relative to surface normal for a 1030-nm beam impinging from air on a flat optical window of fused silica in contact

with water. These angles of refraction are themselves depicted graphically in Figure 4.7 for the 1030-nm fundamental beam.

| $\theta_{i,x}$ | air   | SiO <sub>2</sub> | H <sub>2</sub> O |
|----------------|-------|------------------|------------------|
| 0 (515 nm)     | 59.2  | 36.4             | 40.4°            |
| 1, 2 (1030 nm) | 60.0° | 36.7°            | 40.8°            |

Table 4.5. Incident angles relative to surface normal for all beams in all media.

Finally, the angular velocity  $\omega_{i,x}$  was obtained for each beam using the relationship  $\omega_{i,x} = 2\pi c/\lambda_{i,x}$ , yielding values of  $1.829 \times 10^{15}$  Hz and  $3.658 \times 10^{15}$  Hz for the 1030-nm and 515-nm beams, respectively. These values—along with the literature-reported values of  $n_{i,x}$  and the calculated values of  $\theta_{i,x}$  from Tables 4.4 and 4.5—were used in conjunction with Equation 4.3.1 to obtain a  $\Delta k_z$  value of  $2.5 \times 10^7$  m<sup>-1</sup>.

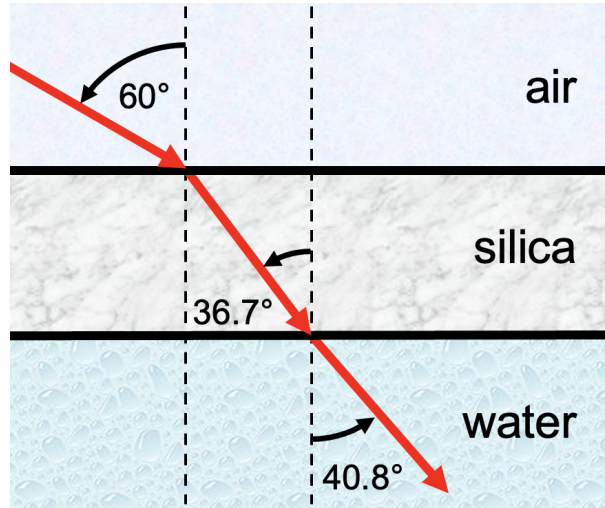


Figure 4.7. Depiction of the refraction of the fundamental 1030-nm beam as it passes from air to the fused silica optical flat and from the fused silica optical flat to water.

### 4.3.2. Fresnel Coefficients for Optical Flats

The macroscopic Fresnel coefficients of our system using s-in/all-out polarization are given by the following expressions:

$$(4.3.3a) \quad F_{sample} = \sin \theta_{1,SiO_2} L_{0,ZZ} L_{1,YY} L_{2,YY}$$

$$(4.3.3b) \quad F_{quartz} = \cos \theta_{1,SiO_2} L_{0,XX} L_{1,YY} L_{2,YY}$$

where  $L_{i,II}$  represents the Fresnel factors of both the excitation and emission fields, which we describe as follows for wavelength  $i$ , following the work of Shen and coworkers and Tyrode and coworkers:<sup>11,28</sup>

$$(4.3.4a) \quad L_{i,XX} = \frac{2n_{i,SiO_2} \cos \theta_{i,H_2O}}{n_{i,SiO_2} \cos \theta_{i,H_2O} + n_{i,H_2O} \cos \theta_{i,SiO_2}}$$

$$(4.3.4b) \quad L_{i,YY} = \frac{2n_{i,SiO_2} \cos \theta_{i,SiO_2}}{n_{i,SiO_2} \cos \theta_{i,SiO_2} + n_{i,H_2O} \cos \theta_{i,H_2O}}$$

$$(4.3.4c) \quad L_{i,ZZ} = \frac{2n_{i,H_2O} \cos \theta_{i,SiO_2}}{n_{i,SiO_2} \cos \theta_{i,H_2O} + n_{i,H_2O} \cos \theta_{i,SiO_2}} \left[ \frac{n_{i,SiO_2}}{n'_i} \right]^2$$

approximating the interfacial refractive index  $n'_i$  at wavelength  $i$  as:

$$(4.3.5) \quad n'_i = \sqrt{\frac{n_{i,H_2O}^2 (n_{i,H_2O}^2 + 5)}{4n_{i,H_2O}^2 + 2}}$$

Using the refractive indices and angles resulting for the experimental geometry presented in Tables 4.4 and 4.5, we obtain  $F_{sample} = 0.68$  and  $F_{quartz} = 0.80$ . Previously, our group reported  $F_{sample} = 2.58$  and  $F_{quartz} = 0.50$  for fused silica hemispheres.

### 4.3.3. Calibration and Referencing (C/R) Ratio for Optical Flats

Using the Fresnel factors calculated in the preceding section, we determined the calibration and referencing ratio for the optical flat geometry in our spectrometer following the method laid out by Ma and coworkers:<sup>22</sup>

$$(4.3.6) \quad \frac{C}{R} = \frac{E_{sig, sample} F_{quartz}}{E_{sig, quartz} F_{sample}} \left| \chi_{eff, quartz}^{(2)} \right|$$

where  $E_{sig, quartz}$  is measured and  $|\chi_{eff, quartz}^{(2)}|$  is calculated as follows:

$$(4.3.7) \quad \left| \chi_{eff, quartz}^{(2)} \right| = \left| \frac{\chi_{bulk, quartz}^{(2)}}{-i\Delta k_z} \right|$$

where  $\chi_{bulk, quartz}^{(2)}$  is known to be  $8 \times 10^{-13} \text{ m V}^{-1}$ ,<sup>28,29</sup> and  $\Delta k_z$  is calculated to yield  $2.8 \times 10^7 \text{ m}^{-1}$  for the fused silica:quartz interface formed by a 1-mm-thick fused silica optical window in contact with a piece of  $z$ -cut  $\alpha$ -quartz. This yielded  $|\chi_{eff, quartz}^{(2)}| = 2.9 \times 10^{-20} \text{ m}^2 \text{ V}^{-1}$ .

The value of  $E_{sig, sample}/E_{sig, quartz}$  for our system was determined by first recording the average SHG intensity from separately assembled samples of 1-mm-thick fused silica optical windows coated with 10 nm of ALD  $\alpha$ -hematite in contact with 1 M NaCl solution at pH 6.78(3) on six different days with a consistent input power of 200 mW and a  $-1 \text{ cm}$  defocused lens (as described in Section 2.3.2).<sup>\*</sup> The resulting SHG intensity for these

---

<sup>\*</sup>Coated samples were used in order to emulate experiments reported in Chapter 5, however we found the use of coated *versus* uncoated samples to be immaterial for the calculation of the  $C/R$  ratio.

assemblies was determined to be  $250 \pm 50$  cp100ms with 10-point averaging. Using a similar approach, the SHG intensity for a rectangular piece of  $z$ -cut  $\alpha$ -quartz affixed to a fused silica optical window with a drop of index-matching fluid was found to be 400,000 cp100ms with 10-point averaging using an input power of 100 mW (attenuated from 200 mW so as not to saturate the detector).<sup>30</sup> Multiplying  $I_{SHG, quartz}$  by a factor of 4 to account for the different input powers and then taking the square root of both values yielded  $E_{sig, sample} = 15.8$  and  $E_{sig, quartz} = 1.6 \times 10^6$ , and a  $E_{sig, sample}/E_{sig, quartz}$  ratio of  $\sim 1/100,000$ . Thus, we find that the  $C/R$  ratio in our spectrometer is  $4.2 \times 10^{-22} \text{ m}^2 \text{ V}^{-1}$ .

#### 4.4. Summary

To start, we overcame the strong absorber problem posed by metals and most metal oxides by depositing them as thin films rather than using bulk materials. For all materials of interest, a film thickness of 10 nm was deemed sufficient to attain optical transmission  $>50\%$  in the ranges of our fundamental and SHG beams (1030/1034 and 515/517 nm, respectively).

Next, we ruled out two different sample preparation methods: (1) direct coating of a 25.4-mm-diameter fused silica hemisphere and (2) direct coating of a 1-mm-thick, 25.4-mm-diameter fused silica window mounted in contact with index-matching optical fluid to a 25.4-mm-diameter fused silica hemisphere serving as an optical coupler, referred to as “sandwich” geometry. The first method was ruled out since the fused silica hemisphere at this scale is too bulky and irregularly shaped for ALD film synthesis. Additionally, the substrate’s curved face made it prohibitively difficult to perform complementary characterization on the synthesized film. The second method avoided the drawbacks of the first

by directly coating a film on a flat fused silica window, ideal for ALD, PVD, and complementary characterization. However, the second method was ultimately ruled out because the “slippery” contact between the substrate, index-matching optical fluid, and optical coupler introduced enough instability to the sample-holding assemblage to produce phase drifts in excess of  $\pm 5^\circ/\text{h}$ . We determined that the direct coating of a thin film on a fused silica window without the use of an optical coupler or index-matching optical fluid was therefore the preferred method for our purposes, as it enabled phase stability comparable to that obtained with an uncoated fused silica hemisphere—the standard substrate for past work on our HD-SHG systems.<sup>12,14,22,23</sup>

Having chosen a sample geometry, we needed to make further adjustments to accommodate flat samples in an optical set-up designed specifically to be used with hemispherical samples. This included calculating new values of the wavevector mismatch  $\Delta k_z$  ( $2.5 \times 10^7 \text{ m}^{-1}$ ), the macroscopic Fresnel factors  $F_{\text{sample}}$  and  $F_{\text{quartz}}$  (0.68 and 0.80 for the sample and quartz, respectively), and the  $C/R$  ratio ( $4.2 \times 10^{-22} \text{ m}^2 \text{ V}^{-1}$ ). Additionally, we developed a standard operating procedure for aligning on a flat optical substrate in order to exclude the combined reflected fundamental and generated SHG resulting from the external air:fused silica interface. The steps to this procedure are briefly enumerated:

- (1) Mount the sample in its holder and clamp it to the stage.
- (2) Optimize counts using the focus (in the case of uncoated silica as the sample) or set the focus to a consistent “de-focused” position (in the case of metal- or metal-oxide-coated fused silica—in order to avoid burning the sample).
- (3) Optimize the counts by aligning the beam path into the PMT using the final steering mirrors.

- (4) Use the micrometer-mounted beam block to block the external beam.
- (5) Repeat step 3 to optimize counts from only the internal beam.
- (6) Introduce the LO (and RO in the case of HD-SHG System 2) to the beam path and confirm good heterodyning.

All further experimental data and results reported in Chapter 5 were obtained employing the best practices described above, unless otherwise noted. As illustrated in Appendix A, the approaches described here are applicable not just to fused silica optical windows that are uncoated or coated with ALD or PVD thin films of metals or metal oxides, but also to optical windows composed entirely of amorphous or crystalline solids of interest, such as sapphire (*i.e.*  $\text{Al}_2\text{O}_3$ ).

## CHAPTER 5

## Understanding the Electrostatics of $\alpha$ -Hematite:Aqueous Interfaces

The basis of this chapter is to apply the methods introduced in Chapter 2 and refined for use with thin films of metal oxides or fully-reduced metals in Chapter 4. In particular, we focus on the study of the  $\alpha$ -hematite:aqueous interface and its accompanying electrostatic environment.

### 5.1. Background

#### 5.1.1. Relevance and Applications of $\alpha$ -Hematite

Hematite ( $\alpha$ -Fe<sub>2</sub>O<sub>3</sub>) stands out as one of the most important mineral sources of iron on Earth, with a higher compositional concentration of iron ( $\sim 70\%$ ) relative to other iron-bearing minerals. Iron itself is the 4<sup>th</sup> most abundant element in Earth's crust—and likely the most abundant element in the Earth as a whole. Thus iron and its cycling through environmental systems are perennial topics in geochemistry.<sup>1-3</sup> Most often,  $\alpha$ -hematite occurs as a constituent in precipitated sedimentary rock formations, particularly Precambrian banded iron formations (BIFs), which are targets for mining in dozens of countries around the world.<sup>2,4</sup> Beyond its importance as a feedstock for commercial iron and steel production,  $\alpha$ -hematite also has cultural and historical significance as a pigment, polishing abrasive, and medicinal ingredient.<sup>5</sup> Further, as a weathering or alteration product of

other iron-bearing minerals,  $\alpha$ -hematite is a major soil component around the world, with reddish or orange-ish sediments often owing their color to this mineral.<sup>5-7</sup>  $\alpha$ -Hematite itself may be altered to form iron hydroxides, but it is relatively stable to weathering environments, with reducing conditions chiefly responsible for its dissolution.<sup>2,5</sup>

Within the last few decades,  $\alpha$ -hematite has gained traction as an Earth-abundant and relatively low-cost candidate material for photoanodes for the purpose of photoelectrochemical (PEC) water splitting.<sup>8-17</sup> Part of its allure stems from its narrow band gap energy (2.1 eV) and theoretical capacity to capture  $\sim 40\%$  of incident solar energy,<sup>13,17,18</sup> as well as its non-toxicity and high stability.<sup>19</sup>  $\alpha$ -Hematite-derived photoanode materials often are “two-dimensional” in nature, constituting optically transmissive thin films, and featuring an accompanying suite of physical, electrochemical, and optical properties not observed in the bulk mineral. In microparticle form, researchers in the field of soft matter have used  $\alpha$ -hematite as a model colloidal system.<sup>20</sup> At the nanoscale, there are reports of  $\alpha$ -hematite nanoparticles as promising agents for removing inorganic and organic contaminants from environmental systems.<sup>21</sup>

Of the applications and occurrences described above, a common denominator is the interplay of  $\alpha$ -hematite’s bulk properties with its surface-specific properties, and more precisely the interface of  $\alpha$ -hematite and aqueous solutions. BIFs, for example, form due to chemical precipitation of aqueous iron cations, a process that occurs at or near solid:liquid interfaces. The weathering of other iron-bearing minerals to form  $\alpha$ -hematite is itself a surface-mediated process. Similarly, the use of  $\alpha$ -hematite in PEC water-splitting photoanodes requires a detailed understanding of the surface states and intermediates of this mineral while in contact with water.<sup>14,16</sup>

Within the realm of mining and ore refinement, the carbo-thermal reduction of hematite and other iron ores to obtain metallic iron is a complex, surface-mediated reaction.<sup>22</sup> Additionally the “beneficiation”—or improvement—of low-grade or mixed ores requires an understanding of  $\alpha$ -hematite’s interfacial properties while in contact with water or other solvents. A key technique in this field is flotation, during which a metallurgist separates and concentrates an ore’s constituents by selectively altering certain surface properties, such as hydrophobicity or hydrophilicity.<sup>23–27</sup> Flotation is a common technique in the separations of  $\alpha$ -hematite from chlorite,<sup>28</sup> from siderite and quartz,<sup>29</sup> and from silica and alumina,<sup>30</sup> each of which requires knowledge of the comparative surface properties of these minerals.

In sum,  $\alpha$ -hematite is a critically important mineral in our world, and many of the processes by which it is extracted and refined, or by which it interacts with other natural or artificial constituents in environmental systems, take place specifically at its interface with water. Therefore, any understanding of  $\alpha$ -hematite and its role in the world is incomplete without a dedicated consideration of its interfacial properties in contact with aqueous phases.

### 5.1.2. Chemistry of $\alpha$ -Hematite:Aqueous Interfaces

The  $\alpha$ -hematite films employed in this thesis are polycrystalline in nature, rather single crystals. While most work on  $\alpha$ -hematite in the literature concerns its (0001) face, these studies are still instructive in developing expectations for the behavior of our samples under hydrated conditions. Surface terminations of most  $\alpha$ -hematite:aqueous interfaces likely include—but are not limited to—Fe surface terminations coexisting with ferryl

( $\equiv\text{Fe(IV)=O}$ ) groups.<sup>31</sup> Due to near-surface Fe vacancies and the thermodynamic stability of hydroxylated surface groups in the presence of water, the  $\alpha$ -hematite surface can further diverge from stoichiometry upon hydration.<sup>32,33</sup> (Hydr)oxo functional groups exposed at the  $\alpha$ -hematite:aqueous interface around neutral pH may therefore include  $\equiv\text{Fe-OH}_2$ ,  $\equiv\text{Fe}_2\text{-OH}$ , and  $\equiv\text{Fe}_3\text{-O}$ .<sup>32</sup>

It is likely that post-deposition surface treatment of  $\alpha$ -hematite can introduce additional variation to surface groups. As early as 1988,  $\text{Ar}^+$  ion bombardment was found to produce  $\alpha$ -hematite surface phases divergent from those predicted by bulk phase diagrams for  $\text{Fe-O}$ .<sup>34</sup> Similarly, annealing (0001)  $\alpha$ -hematite films in air is known to result in hydroxylation of the stoichiometric surface terminations of the mineral.<sup>35</sup> Some workers have proposed that  $\alpha$ -hematite may develop a full surface coating of altered mineral phases, possibly comprising goethite ( $\text{FeO(OH)}$ ) under high-temperature conditions,<sup>36</sup> or magnetite ( $\text{Fe}_3\text{O}_4$ ) under reducing conditions.<sup>22</sup>

Some reports do exist in the literature on explicitly polycrystalline  $\alpha$ -hematite films. In one study, workers synthesized thin films of polycrystalline  $\alpha$ -hematite by filtered arc deposition and found them to exhibit a preferred orientation of the (006), (018), and (1010) faces, all corresponding to perpendicular alignment of the  $c$ -axis to the substrate surface.<sup>37</sup> Another study found that the crystallite size in these films plays a significant role in determining surface chemistry, with the removal of near-surface  $\text{Fe(III)}$  ions and subsequent addition of protons at the  $\alpha$ -hematite:water interface altering the surface composition to be more similar to  $\text{Fe(OH)}_3$ .<sup>33,38</sup> More fine-grained crystallites therefore would result in a relatively more hydrous  $\alpha$ -hematite surface. Another proposed impact

of the depletion of octahedral Fe(III) ions is the creation of more potential active sites for surface complexation that would not have otherwise existed under idealized conditions.<sup>38</sup>

Decades of study of the  $\alpha$ -hematite surface have indicated the existence of significant hysteresis under aqueous conditions. For example, Preocanin and coworkers conducted “slow” and “fast” pH titrations of a single-crystal  $\alpha$ -hematite electrode, observing significant hysteresis of the mineral’s surface near neutral pH, with more rapid equilibration kinetics at highly acidic or basic conditions.<sup>39</sup> Hysteresis disappeared with the extension of equilibration times up to 120 min, or with the application of ultrasound. Later, the same group conducted pH titrations of polycrystalline  $\alpha$ -hematite films and similarly noted significant hysteresis of the hematite:aqueous interface, further identifying a point of zero charge (PZC) for their sample at pH 7.<sup>40</sup> As will be discussed later in this chapter, we observe significant hysteresis for our own polycrystalline  $\alpha$ -hematite films, and indeed enhanced hysteresis at circumneutral pH.

### 5.1.3. $\alpha$ -Hematite Photoanodes

Although this thesis does not explore the interfacial properties of  $\alpha$ -hematite under illuminated or applied-potential conditions, we hope that the approaches we outline for using nonlinear spectroscopy as a direct probe of interfacial potential can serve in future studies to assist in identifying the mechanisms responsible for PEC performance of  $\alpha$ -hematite, which remains an open line of inquiry. Indeed, the authors of a recent review of  $\alpha$ -hematite photoanodes noted that there is still a great need for “accurate observation of surface states/surface intermediates of hematite photoanodes with spatial, temporal and energy resolution. . . ”<sup>14</sup>

As introduced in Section 5.1.1,  $\alpha$ -hematite is an attractive candidate for PEC water splitting due to its narrow band gap, Earth abundance, low cost, and durability. Although its band structure is still not precisely defined,  $\alpha$ -hematite's absorption features are generally understood to feature dominant contributions by two ligand metal charge transfer (LMCT) bands at 358 and 233 nm, with lesser contributions from d-d transitions posited and magnetically coupled Fe sites.<sup>16,41</sup> Many modifications intended to optimize the performance of  $\alpha$ -hematite PEC electrodes rely on altering charge carrier dynamics, electronic absorption, or kinetics through alterations to the mineral's surface. Accordingly, we require a firm understanding of the identity and chemistry of terminal surface groups at the  $\alpha$ -hematite:aqueous interface.

Although there is ample evidence of the presence of ferryl groups at the electrode surface, more work remains to be done to characterize other surface species before, during, and after electrode operation with more confidence.<sup>42,43</sup> Similar to how the surface groups of  $\alpha$ -hematite undergo significant alteration upon hydration, the same goes for illumination. For example, PEC water splitting has been shown to reduce some Fe groups at the  $\alpha$ -hematite:aqueous interface, which may have an impact on available active sites, concentration of dissolved Fe(II) species, and sorption.<sup>38</sup>

Taken in sum, it is evident that a better molecular-level understanding not only the surface sites of  $\alpha$ -hematite but also its interfacial water structure is critical for our ability to develop precise mechanistic models of PEC water splitting. As discussed in more detail in Chapter 2, phase-sensitive, heterodyne-detected second harmonic generation (HD-SHG) spectroscopy is a powerful tool for probing the electrostatics of buried metal oxide:aqueous interfaces to the exclusion of bulk phases, and we devote the remainder of

the current chapter to a detailed presentation of how this technique may be applied to  $\alpha$ -hematite in contact with aqueous electrolyte solutions.

## 5.2. Experimental

### 5.2.1. Atomic Layer Deposition (ALD) of $\alpha$ -Hematite Films

25.4 mm  $\times$  1 mm IR-grade fused silica windows (ISP Optics, QI-W-25-1) were prepared for atomic layer deposition (ALD) by soaking for 1 h in ALNOCHROMIX™ (Alconox) and concentrated sulfuric acid (Sigma-Aldrich, 339741, 99.999%), rinsing with ultrapure water (18.2 M $\Omega$ -cm, MilliporeSigma), sonicating in MeOH for 10 min, rinsing again with ultrapure water, sonicating in ultrapure water for 10 min, rinsing once more with ultrapure water, drying with N<sub>2</sub>, and air plasma-cleaning for 30 sec on the highest setting. Clean substrates were wrapped in fresh lens paper (Thorlabs) and shipped to Argonne National Laboratory where our collaborators—Drs. Alex Martinson and Aaron Taggart—performed ALD using a Savannah 200 ALD reactor (Cambridge Nanotech).

To synthesize polycrystalline ALD  $\alpha$ -hematite films, we followed the method developed by Martinson and coworkers to grow robust, self-limiting, and stoichiometric thin films.<sup>44</sup> Ferrocene (Fe(Cp)<sub>2</sub>, 98%, Aldrich) precursor was used without further purification and ozone was generated using a DelOzone generator. ALD reaction timing followed a  $t_1 - t_2 - t_3 - t_4$  sequence, with  $t_1$  and  $t_3$  corresponding to exposure and purge times for ferrocene, and  $t_2$  and  $t_4$  corresponding to exposure and purge times for ozone. For our recipe  $t_1 = 60$  sec (split into two 30-sec static exposures separated by a 5-sec purge),  $t_2 = 35$  sec,  $t_3 = 90$  sec (split into two 45-sec pulses separated by a 5-sec purge), and

$t_4 = 20$  sec. Witness silicon wafers (p-type) were included in the sample chamber alongside the fused silica substrates so that film thickness could be estimated *via* ellipsometric measurements performed on an M2000 variable angle spectroscopic ellipsometer (VASE, J.A. Woolam). After deposition the films were annealed at 500°C for 30 min in ultrahigh purity O<sub>2</sub> using a ramp rate of 10°C/min.

Past work in our group characterizing ALD  $\alpha$ -hematite films deposited in this manner *via* grazing incidence X-ray diffraction (GIXRD), Raman, and X-ray photoelectron spectroscopy (XPS) suggest the presence of  $\alpha$ -hematite in the film, along with the absence of  $\gamma$ -hematite ( $\gamma$ -Fe<sub>2</sub>O<sub>3</sub>) and magnetite (Fe<sub>3</sub>O<sub>4</sub>). Although the films were determined to be polycrystalline post-annealing step, GIXRD results further indicated some preferred orientation to the crystallites, as has been found for other polycrystalline  $\alpha$ -hematite thin films.<sup>37,45</sup>

### 5.2.2. Cleaning Protocol for $\alpha$ -Hematite Films

Prior to using ALD  $\alpha$ -hematite films in HD-SHG experiments, we sonicated the films for 10 min in ultrapure water, rinsed them with ultrapure water, dried them under N<sub>2</sub>, and air plasma cleaned them for 30 sec on the highest RF setting. For samples intended to be probed while in contact with air, we wrapped the cleaned films in new lens paper and stored them in a paper envelope until use. For samples intended to be probed while in contact with aqueous solutions, we left the cleaned films to soak overnight in an aliquot of the first solution to be used during the following day's experiment. Films did not remain soaking for longer than 18 h before use in a flow HD-SHG experiment.

### 5.2.3. X-ray Photoelectron Spectroscopy (XPS)

We performed X-ray photoelectron spectroscopy (XPS) analysis of ALD  $\alpha$ -hematite films using an ESCALAB 250Xi (Thermo Scientific) equipped with an electron flood gun, a scanning ion gun, and an XR6 monochromated X-ray source (500  $\mu\text{M}$ ) with an aluminum anode. We executed narrow scans in the binding energy ranges for each element of interest with a pass energy of 50 eV, a dwell time of 50 ms, and an energy step size of 0.1 eV. All reported spectra are the result of three to five averaged spectra.

### 5.2.4. Atomic Force Microscopy (AFM)

We performed atomic force microscopy (AFM) analysis of ALD  $\alpha$ -hematite films on a Dimension FastScan Atomic Force Microscope (Bruker) in tapping-in-air mode with a scan rate of 2 Hz and a scan area of  $5 \times 5 \mu\text{m}^2$ . We analyzed AFM images using ProfilMOnline and roughness was based on the arithmetic average ( $R_a$ ) and the root mean square average ( $R_q$ ) of profile height deviations from the mean height:

$$(5.2.1a) \quad R_a = \frac{1}{l_r} \int_0^{l_r} |z(x)| dx$$

$$(5.2.1b) \quad R_q = \sqrt{\frac{1}{l_r} \int_0^{l_r} z(x)^2 dx}$$

### 5.3. Results

#### 5.3.1. Robustness of $\alpha$ -Hematite Films to Experimental Conditions

In soil environments where water molecules, inorganic electrolytes, and organic media are present,  $\alpha$ -hematite commonly experiences a range of chemical transformations, provided that certain conditions are met.  $\alpha$ -Hematite can undergo dissolution by reduction to form inorganic  $\text{Fe}^{2+}$  ions, which can then precipitate and oxidize (with or without  $\text{CO}_2$  present) to form such minerals as siderite, maghemite, and lepidocrocite. Further dissolution and re-precipitation of these secondary iron-bearing minerals can result in the formation of goethite. The dissolution of  $\alpha$ -hematite by complexation can form inorganic  $\text{Fe}^{3+}$  ions or  $\text{Fe}^{3+}$  organic complexes, which by slow hydrolysis can also form goethite, or by fast hydrolysis can contribute to the formation of ferrihydrite.<sup>46</sup>

During the course of our flow HD-SHG experiments, we expose  $\alpha$ -hematite films to air, moisture, and electrolyte solutions at a range of pH values between 2 and 13. Although the goal of this study is not to avoid film alteration, it is imperative to the interpretation of our results that we understand any film alteration that may be occurring as a direct outcome of the experimental conditions, rather than assuming the films remain pristine. To this end, we performed UV-visible absorption and transmission spectroscopy, XPS, and AFM on synthesized ALD  $\alpha$ -hematite films both before and after use in our flow set-up and HD-SHG spectrometers.

Figure 5.1 shows the narrow-scan XPS spectra for iron and oxygen for three films prior to use (orange traces) and for two films from the same set after two to four multi-hour exposures to 0.5 M NaCl solutions adjusted with small amounts of dilute HCl and NaOH

to pH values between pH 2.75 and 8.00 (grayscale traces). For comparison, comparable spectra were obtained from the backsides of the substrates for the used  $\alpha$ -hematite films, which presumably should be largely uncoated fused silica. The XPS spectra for unused films for the Fe 2p region show peaks characteristic of published spectra for  $\alpha$ -hematite (724.5, 719.5, and 711.2 eV).<sup>47</sup> The same peaks are present in the XPS spectra taken in the same Fe 2p region for the two used films. Notably, the same peaks can also be seen on the XPS spectra taken of the “uncoated” sides of the used films, which is likely due to the tendency of ALD processes to “wrap” around the edges of a substrate during deposition. As expected, these peaks are relatively less intense, as the presence of any  $\alpha$ -hematite on the backsides of the substrate is only residual.

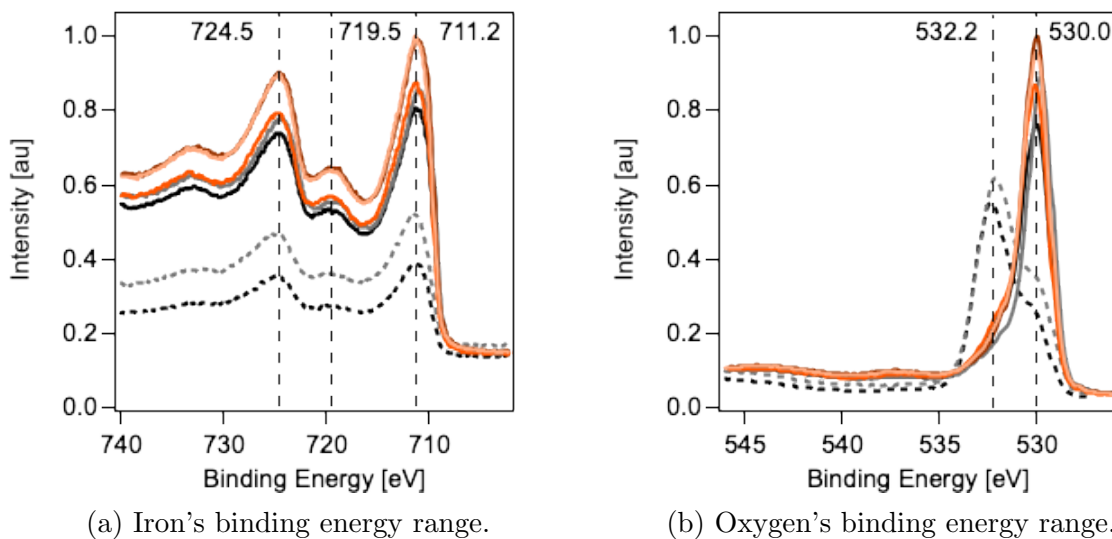


Figure 5.1. Narrow-scan XPS spectra of ALD  $\text{Fe}_2\text{O}_3$  films before use (orange traces) and after several exposures to  $\text{CO}_2$ -equilibrated aqueous solutions of NaCl, NaOH, and/or HCl (grayscale traces). Spectra taken of the ALD- $\text{Fe}_2\text{O}_3$ -coated side (solid traces) are shown alongside spectra of the nominally uncoated backsides (dashed traces) of the fused silica substrates for comparison.

XPS spectra from the O 1s region support this interpretation, because—for the coated sides of used and unused films—they show the characteristic O 1s peak corresponding to  $\alpha$ -hematite (530.0 eV).<sup>47</sup> Conversely, the XPS spectra in the O 1s region for the backsides of used films shows a greatly diminished peak at 530.0 eV, but also a new peak at  $\sim$ 532.2 eV that is barely perceptible as a shoulder in the XPS spectra for the films' coated sides. While we do not make an explicit assignment for this peak, it compares favorably to reported values for  $\alpha$ -quartz and adventitious surface hydroxyls.<sup>48,49</sup> In sum, we take the XPS results to not show significant evidence for chemical transformation of the ALD  $\alpha$ -hematite films following a typical degree of exposure to our experimental conditions.

To gain a sense of potential morphological alterations to the films in the course of our HD-SHG and flow experiments, we employed AFM imaging to measure surface roughness. Initial AFM analysis of at least two  $5 \times 5 \mu\text{m}^2$  spots on three different freshly deposited 10-nm ALD  $\alpha$ -hematite films before exposure to aqueous conditions yielded an average  $R_a$  value of 0.33(8) nm and an average  $R_q$  value of 0.44(11) nm.

Figure 5.2 shows the tapping mode AFM images taken for a single 5-nm ALD  $\alpha$ -hematite film before and after exposure to typical experimental conditions (*i.e.* four day-long exposures of flowing solutions of pure water and 0.5 M NaCl at pH 3, 5, and 7). Surface roughness parameters were calculated from two different  $5 \times 5 \mu\text{m}^2$  spots before and after exposure and displayed in Table 5.1. The calculated average values of  $R_a$  and  $R_q$  each increase by more than twofold after exposure. Since this increase is of larger magnitude than the natural variation seen between freshly deposited samples, we conclude this indicates an increase in surface roughness due to the conditions of our HD-SHG flow experiments. We note that while the  $R_a$  values from the AFM images of all

as-deposited films are somewhat lower than reported values for polycrystalline hematite thin films deposited by the same method,<sup>45</sup> they are in agreement with other reported values for  $\alpha$ -hematite films of comparable thickness.<sup>37</sup>

| Sample condition | $R_a$ [nm] | $R_q$ [nm] |
|------------------|------------|------------|
| unused           | 0.247(9)   | 0.314(10)  |
| used             | 0.59(6)    | 0.77(7)    |

Table 5.1. Roughness parameters calculated for unused and used  $\alpha$ -hematite films.

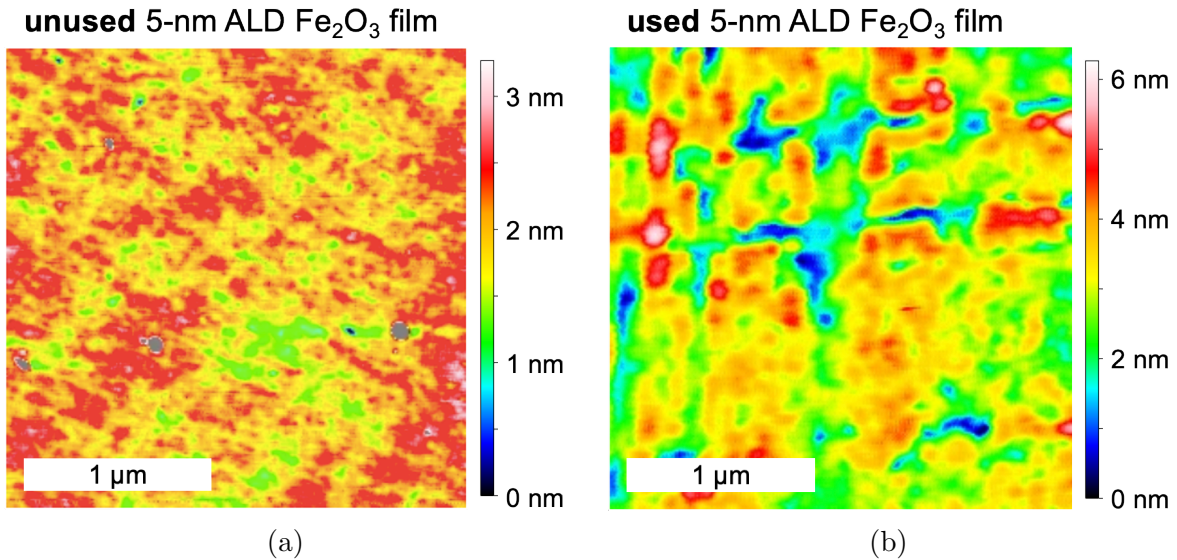


Figure 5.2. AFM images taken of a representative ALD  $\alpha$ -hematite film before and after exposure to typical experimental conditions. The color scale denotes profile height in nm.

As discussed in Section 4.2.1, measured film absorbance (or transmission) can serve as a proxy for thickness with a sensitivity of tens of nm in the case of highly absorbing films. We leveraged this relationship to evaluate whether film thinning was occurring over the course of HD-SHG flow experiments. Figure 5.3 shows a representative example

of four different  $\alpha$ -hematite films of a nominal starting thickness of 10 nm. The difference in average transmission measured at 517 nm was  $-10.4(5)\%$  for the set of films and across the full range of wavelengths probed (*i.e.* 224-876 nm) the average difference in % transmission was  $-10.0(4)\%$ . Although the transmission across the full UV-visible range varies by as much as 3.5% for the films shown in Figure 5.3, this value is smaller than that observed between the same film measured before and after exposure to experimental conditions. Further, given that the % transmission difference between used and unused films is consistent for all films at all wavelengths in the UV-visible range, we conclude that thinning is occurring in the same manner for all films, regardless of small differences in the nominal starting thickness immediately following deposition.

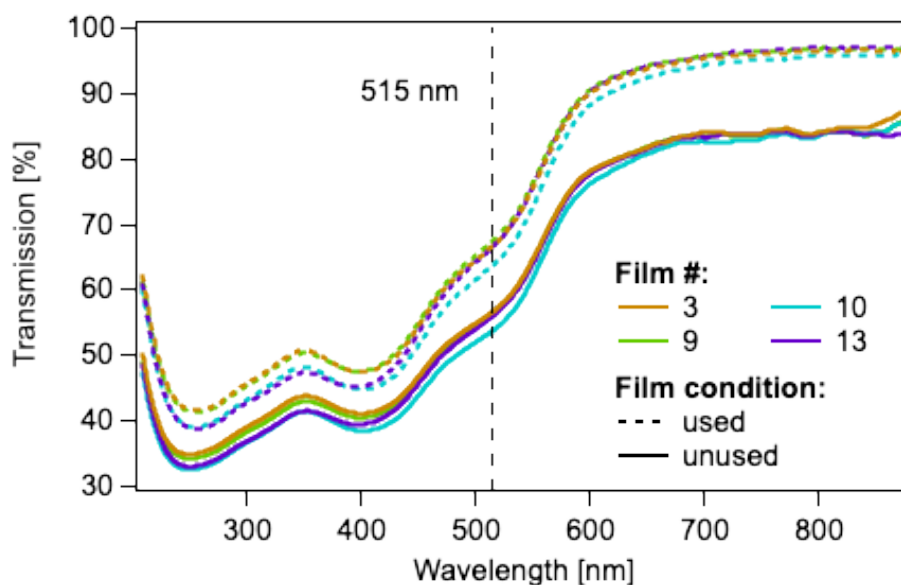


Figure 5.3. Measured transmission in the UV-visible range for two different ALD  $\alpha$ -hematite films before and after exposure to flowing aqueous solutions of NaCl for day-long timescales.

### 5.3.2. SHG Controls

The  $\alpha$ -hematite films deposited by ALD on fused silica substrates with a target thickness of 10 nm exhibited between 50 and 60% transmission at 515 nm, and over 90% transmission at 1034 nm (refer to Figure 5.3). Power studies conducted in internal and external reflection geometry on System 1 showed that the nonlinear optical response from 10-nm  $\alpha$ -hematite films with a tightly focused incident beam depends quadratically on input power below 10 mW, with optical breakdown occurring at powers in excess of 20 mW. Conversely, using our  $-1$  cm defocusing technique on System 2 (see Section 2.3.2), we observed  $I_{SHG}$  to depend quadratically on input power up to at least 1 W (see Figure 5.4a), though we found 200 mW to produce sufficient signal for our experiments. We performed this power study on a 10-nm ALD  $\alpha$ -hematite film in contact with 1 M NaCl, pH 2 solution. We conducted bandwidth studies on the same film and solution system by introducing a monochromator to the System 2 HD-SHG set-up prior to the PMT and detector and scanning a range of wavelengths centered around the expected  $2\omega$  wavelength (*i.e.* 517 nm). A single Voigt peak centered at 517.40(4) nm and with a full width half maximum (FWHM) of 8.3(4) nm best fits the results of this study (see Figure 5.4b).

### 5.3.3. Beam Position in $yz$ -Plane

When using hemispherical sample geometry, there is only one position on the flat face of the hemisphere upon which the fundamental beam can be focused in order to ensure that the  $60^\circ$ -input beam is impinging normal to the hemispherical face. Consequently, beam energy exposure is relegated to one finite region of the hemisphere's flat face, with limited ability to scan the beam position in the  $yz$ -plane (taking the  $x$ -direction to be normal to

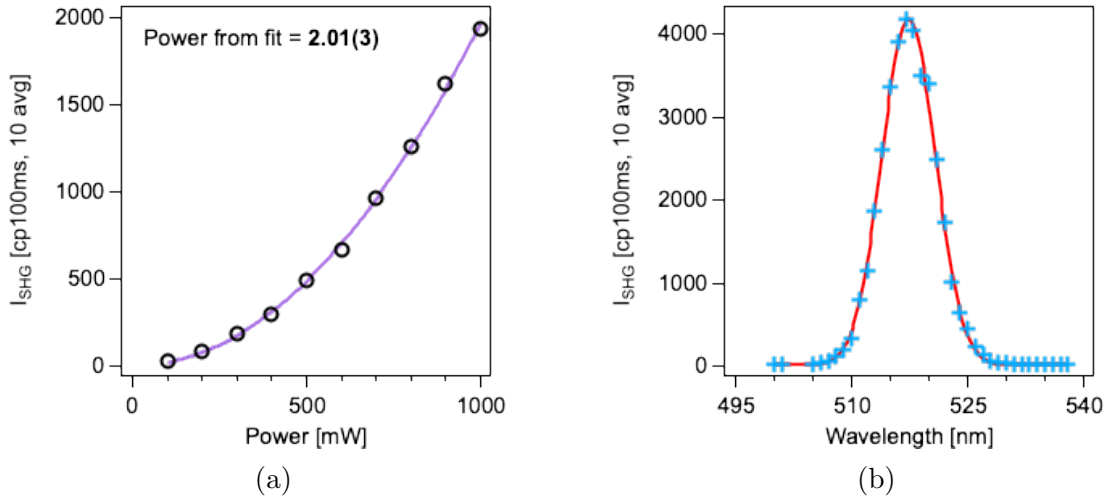


Figure 5.4. Results from (a) a bandwidth study on a 10-nm ALD  $\alpha$ -hematite film in contact with 1 M NaCl, pH 2 solution and (b) a power study on the same system.

the hemisphere's flat face). Conversely, in the case of flat sample geometry, scanning the beam in the  $yz$ -plane has no impact on the angle relative to surface normal at which the fundamental beam is striking the air:silica interface. Therefore, beam scanning is possible in this geometry at no detriment to the spectrometer's alignment. Taking advantage of this capability, we investigated film uniformity at the macroscopic scale. Keeping all other conditions the same, we collected three interference fringes at five different positions on a single  $\alpha$ -hematite film in contact with 1 M NaCl held at pH 6. Upon fitting, we obtained the average values of  $\varphi_{\text{obs}}$  and  $E_{\text{sig}}$  for all positions (Figure 5.5). All individual values of  $E_{\text{sig}}$  for the five positions were within one  $\sigma$  of the mean and all individual values of  $\varphi_{\text{obs}}$  for the five positions were within  $2\sigma$ , indicating that the  $\alpha$ -hematite films are macroscopically homogeneous.

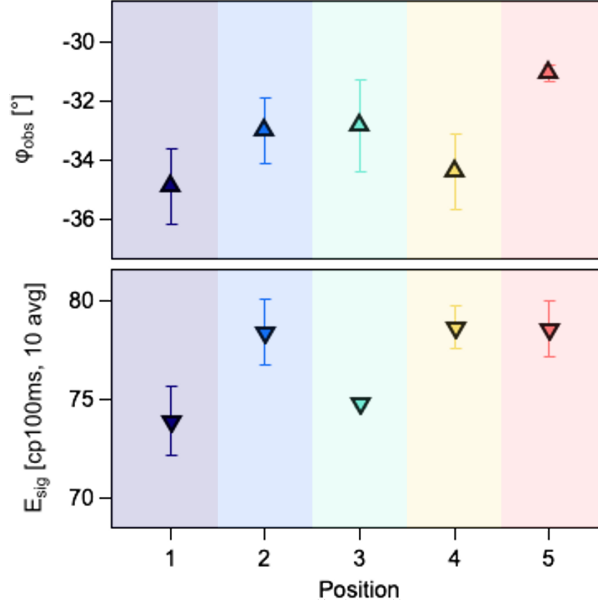


Figure 5.5. Results from a control experiment in which all conditions were held the same with the exception of  $yz$  stage position, allowing interference fringes to be collected from five fully distinct spots on the  $\alpha$ -hematite:aqueous interface.

### 5.3.4. Optical Physics of $\alpha$ -Hematite

For HD-SHG and homodyne SHG experiments on  $\alpha$ -hematite, we employ a model wherein the SHG E-field experiences resonant enhancement, and therefore consists of both a non-resonant contribution to SHG combined with a resonant contribution. These contributions relate to one another and the overall SHG E-field as follows, taking their phase relationship ( $\varphi_R$ ) into account:

$$(5.3.1) \quad \sqrt{I_{SHG}} = E_{SHG} \propto \sqrt{|\chi_{NR}^{(2)} + \chi_R^{(2)} e^{i\varphi_R}|^2}$$

In the case of  $\alpha$ -hematite,  $\chi_{NR}^{(2)}$ —or the non-resonant second-order nonlinear susceptibility—comprises the contribution of surface hydroxyl groups, Stern layer water molecules, and

adsorbed ions. whereas  $\chi_R^{(2)}$ —or the resonant second-order nonlinear susceptibility—includes only the contribution of the FeO bonds of terminal surface groups. Theoretically,  $\chi_R^{(2)}$  should remain insensitive to the protonation or deprotonation of surface sites, and therefore should not depend on pH. Further, due to our input wavelength of 1034 nm, we expect our SHG wavelength (517 nm) to be near resonance for at least two of hematite’s proposed single and pair ligand field (d-d) transitions, and on the shoulder of a proposed ligand metal charge transfer (LMCT) band centered at 385 nm.<sup>41</sup> Since we are not probing fully on-resonance, we do not expect a phase relationship of exactly 90° between  $\chi_{NR}^{(2)}$  and  $\chi_R^{(2)}$ , and rather anticipate  $\varphi_R = 10$  to 20°. <sup>50</sup>

We express the total SHG response from the  $\alpha$ -hematite samples in the form of  $\chi_{eff,sample}^{(2)}$  as follows:

$$\begin{aligned}
 (5.3.2) \quad \chi_{eff,sample}^{(2)} &= \frac{C}{R} E_{sig} e^{i\varphi_{sig}} \\
 &= \chi_{NR}^{(2)} + e^{i\varphi_R} \cdot \chi_R^{(2)} + \chi_{water}^{(3)} \Phi(0) (\cos(\varphi_{DC}) e^{i\varphi_{DC}} + i \cdot 1.5)
 \end{aligned}$$

We direct the reader to refer to Section 4.3.3 for a detailed discussion of how we determined the  $C/R$  ratio for our spectrometer and our particular sample (*i.e.* a 10-nm ALD  $\alpha$ -hematite thin film coated on an 1-mm fused silica optical window). The  $C/R$  ratio accounts for the Fresnel coefficients of the sample and a reference condition, described in Section 4.3.2.

All pH screening or dual-pH jumps described in this section were performed at 1 M total ionic strength (NaCl). Under this condition,  $\varphi_{DC} < 1^\circ$  and Equation 5.3.2 reduces

to:

$$(5.3.3) \quad \frac{C}{R} E_{sig} e^{i \cdot \varphi_{sig}} = \chi_{NR}^{(2)} + e^{i \varphi_R} \cdot \chi_R^{(2)} + \chi_{water}^{(3)} \Phi(0) (1 + 1.5 \cdot i)$$

which, applying Euler's formula, becomes:

$$(5.3.4) \quad \frac{C}{R} E_{sig} e^{i \cdot \varphi_{sig}} = \chi_{NR}^{(2)} + \cos(\varphi_R) \chi_R^{(2)} + i \sin(\varphi_R) \chi_R^{(2)} + \chi_{water}^{(3)} \Phi(0) (1 + 1.5 \cdot i)$$

From here, we collect the real and imaginary terms and rearrange, obtaining:

$$(5.3.5a) \quad \chi_{NR}^{(2)} = \frac{C}{R} E_{sig} \cos(\varphi_{sig}) - \cos(\varphi_R) \chi_R^{(2)} - \chi_{water}^{(3)} \Phi(0)$$

$$(5.3.5b) \quad \chi_R^{(2)} = \frac{C}{R} E_{sig} \sin(\varphi_{sig}) - 1.5 \Phi(0) \chi_{water}^{(3)}$$

By rearranging Equation 5.3.5b we obtain an expression for  $\Phi(0)$  only in terms of  $\varphi_R$  and the observables  $E_{sig}$  and  $\varphi_{sig}$ :

$$(5.3.6) \quad \Phi(0) = \frac{\frac{C}{R} E_{sig} \sin(\varphi_{sig}) - \sin(\varphi_R) \chi_R^{(2)}}{1.5 \cdot \chi_{water}^{(3)}}$$

Unlike fused silica, which has no resonant contribution to the SHG E-field at 1034 or 517 nm,  $\alpha$ -hematite's  $\chi_R^{(2)}$  contribution is non-zero, and we can approximate it using our calibration and referencing ( $C/R$ ) ratio, or  $4.0 \times 10^{-22} \text{ m}^2 \text{ V}^{-1}$ . We therefore substitute  $C/R$  for  $\chi_R^{(2)}$  in Equation 5.3.6 to obtain:

$$(5.3.7) \quad \Phi(0) = \frac{\frac{C}{R} [E_{sig} \sin(\varphi_{sig}) - \sin(\varphi_R)]}{1.5 \cdot \chi_{water}^{(3)}}$$

By applying a similar substitution to Equation 5.3.5a, we obtain an expression for  $\chi_{NR}^{(2)}$  in terms of  $E_{sig}$ ,  $\varphi_{sig}$ ,  $\varphi_R$ , and the calculated  $\Phi(0)$ :

$$(5.3.8) \quad \chi_{NR}^{(2)} = \frac{C}{R} [E_{sig} \cos(\varphi_{sig}) - \cos(\varphi_R)] - \chi_{water}^{(3)} \Phi(0)$$

We employ Equations 5.3.7 and 5.3.8 in the remainder of this chapter to obtain values of  $\Phi(0)$  and  $\chi_{NR}^{(2)}$  for our  $\alpha$ -hematite:aqueous interfacial system, noting that as of writing  $\varphi_R$  remains unknown for our system, given that we are unlikely to be fully on- or off-resonance. In order to interpret our data, we present proposed ranges of  $\Phi(0)$  and  $\chi_{NR}^{(2)}$  for  $-60^\circ < \varphi_R < 90^\circ$ .

### 5.3.5. Determining the Point of Zero Charge (PZC) of $\alpha$ -Hematite

In the study of aqueous geochemistry, a common property of interest for a given solid:liquid interface is its point of zero charge (PZC)—or the pH value at which it displays a net neutral charge. This quantity is distinct from the isoelectric point (IEP) of a given surface, which marks the pH value at which the measured zeta potential reverses and may differ by several pH units. SHG is a powerful tool to determine the PZC—which is related more to the true interfacial potential, as opposed to zeta potential—and past work by Jordan and coworkers used SHG spectroscopy to experimentally determine the PZC of ALD  $\alpha$ -hematite, which they constrained to pH 5.5.<sup>45</sup> This determination was consistent with PZC values reported for natural  $\alpha$ -hematite samples (pH 5-7), but lower than reported values for commercial or synthetic  $\alpha$ -hematite samples (pH 6-9 or 7-10, respectively)—a difference tentatively ascribed to the polycrystallinity of the material and/or the presence of adventitious carbon at the film's surface.

Although we employ the same synthetic method for the deposition of our films, we sought to independently confirm the PZC of our films using our HD-SHG System 2, allowing for the possibility that small changes in our film preparation and surface treatment may result in different surface properties, as literature reports on  $\alpha$ -hematite amply demonstrate elsewhere.<sup>32,34,35,51–53</sup> To do this, we conducted charge screenings of the  $\alpha$ -hematite:aqueous interface at constant pH by tracking  $I_{SHG}$  in homodyne detection while systematically increasing [NaCl]. We repeated these screenings at pH 5.75, 6.25, 6.50, 6.75, and 7.00—a range chosen based on the reported PZC values for synthetic and commercial  $\alpha$ -hematite, as well as the past reports by our group for this material.<sup>45</sup> Figure 5.6 displays the normalized results of these experiments, showing that  $I_{SHG}$  becomes invariant with increasing [NaCl] at pH 6.75, which we therefore identify as the experimentally-determined PZC of this particular batch of polycrystalline ALD  $\alpha$ -hematite films.

We provisionally ascribe this relatively higher PZC value to our cleaning protocol for the thin films, which includes sonicating in ultrapure water, drying under house  $N_2$ , and air plasma cleaning on the “high” RF setting for 30 sec. The last step in particular should serve to decrease the amount of adventitious carbon (AdC) contamination on the film surface, to which Jordan and coworkers attributed their low PZC value.

Typically, charge screenings carried out at pH values more alkaline than the PZC result in a relative decrease in  $I_{SHG}$  with increasing electrolyte concentration. Generally this is thought to be due to the decreasing depth of the electrical double layer (EDL) as ions screen the electrical field emanating from the interface, coupled with constructive interference between the  $\chi^{(2)}$  and  $\chi^{(3)}$  contributions to the signal intensity. Conversely, below the PZC,  $\chi^{(2)}$  and  $\chi^{(3)}$  interfere destructively, and therefore progressive shortening

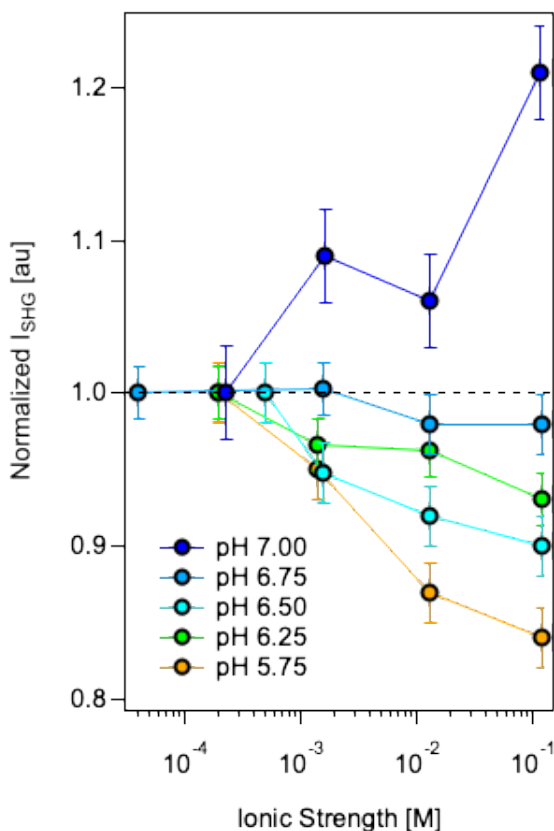


Figure 5.6. Summary of results of several NaCl screening experiments on two different hematite films at a range of fixed pH values. Minimal change in intensity across the concentration range at pH 6.75 indicates this as the best approximation of the point of zero charge (PZC) for this particular set of ALD hematite films.

of the EDL and the participation of fewer water molecules in the SHG process should result in a relative increase in  $I_{SHG}$ . As shown in Figure 5.6, this is not the case for our  $\alpha$ -hematite thin films, which show a relative decrease in  $I_{SHG}$  below rather than above the PZC, and a relative increase in  $I_{SHG}$  for the pH 7.00 condition. This behavior is somewhat distinct from what Jordan and coworkers observed for their ALD  $\alpha$ -hematite thin films, which displayed a decrease in  $I_{SHG}$  at all pH values studied. To explain this result, they posited that they were performing their experiments on-resonance for one

of  $\alpha$ -hematite's LMCT bands, since their SHG system employed a 600-nm fundamental beam and therefore collected SHG generated at 300 nm.<sup>45</sup>

### 5.3.6. pH Titration of $\alpha$ -Hematite at Constant Ionic Strength

We performed pH-dependent studies of the  $\alpha$ -hematite:aqueous interface using solutions of constant 1 M total ionic strength and differing pH values, made by dissolving the appropriate amount of NaCl and NaOH or HCl in ultrapure water (see Section 2.4.2 for more details). We left solutions open to atmosphere overnight before each experiment and measured pH and conductivity before use in our flow system. If additional pH adjustment was necessary, we used drop-wise additions of 1 M concentrated HCl or NaOH so as to maintain our target ionic strength. We note that some workers have conducted investigations of the  $\alpha$ -hematite:aqueous interface under idealized conditions, including working within a N<sub>2</sub>-atmosphere glove box and using fully degassed solutions.<sup>54</sup> Although such experimental set-ups do allow for the interrogation of nearly pristine  $\alpha$ -hematite faces with minimal adventitious carbon or oxygen, there is a limit to how applicable results obtained in this manner are to environmental systems, where contamination is a reality. Even human-built systems such as  $\alpha$ -hematite photoanodes for PEC water splitting exist in complex aqueous systems where it is better to understand the impact of surface contamination rather than attempt to obviate it.<sup>55,56</sup> Motivated to develop a spectroscopic approach capable of achieving meaningful data about real-world systems, we proceeded with aqueous solutions equilibrated to the atmosphere.

Having observed significant hysteresis of our sample  $\alpha$ -hematite:aqueous interface—consistent with literature reports of similar systems—we began each experiment with

1 M NaCl at pH 6.75 (near-PZC), having mounted the  $\alpha$ -hematite sample to be used in the flow cell filled with the solution the night before and allowing it to soak for at least 12 h. The rationale in beginning each experiment at pH 6.75 was to start with a minimally charged interface, and progressively charge it by titrating the pH in either the acidometric or alkalimetric direction. Each experiment therefore consisted of a consistent 1 M NaCl pH 6.75 starting point, and one to two 1 M NaCl solutions at higher or lower pH values.

After aligning (following the method outlined in Chapter 4) and collecting the initial homodyne SHG intensity and three replicate HD scans at pH 6.75, we introduced the first solution at pH X to the flow cell. A peristaltic pump system maintained a constant flow rate of 12 mL/min at all times during the experiment, so as to ensure a complete change-out of the cell's internal volume after  $\sim 2.5$  min. During the introduction of a new solution to the cell, we tracked SHG intensity with homodyne detection and waited at least 10 min for the measured intensity to stabilize as a proxy for the interface reaching steady state, at which point we switched to HD detection and collected three replicate scans.

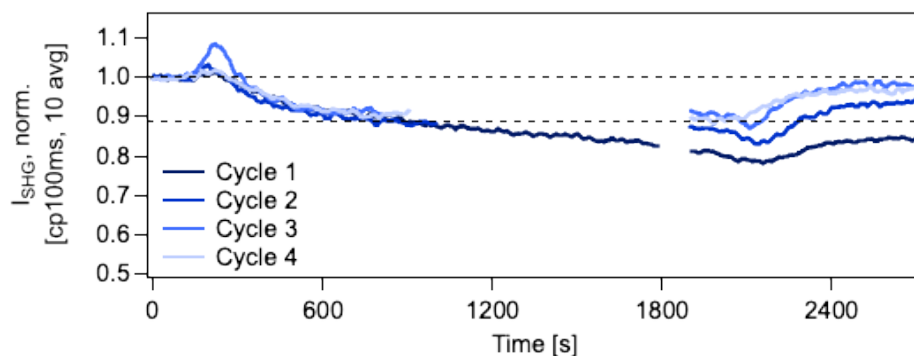
For most experiments, we noted a consistent initial decrease in  $I_{SHG}$  going from the PZC to pH X for the first time of the day, regardless of whether  $\text{pH X} > \text{PZC}$  or  $\text{pH X} < \text{PZC}$ . This decrease in intensity ranged from a 20-60% decrease depending on the value of pH X and was consistently irreversible, even upon returning to 1 M NaCl solution at the PZC. Figures 5.7 and 5.8 display this phenomenon, with  $I_{SHG}$  collected in homodyne as described in Section 2.3.2 and subsequently smoothed using 25-point boxcar

averaging. Subsequent cycles between the PZC and pH X eventually resulted in a locally reversible change in  $I_{SHG}$  for all pH values investigated.

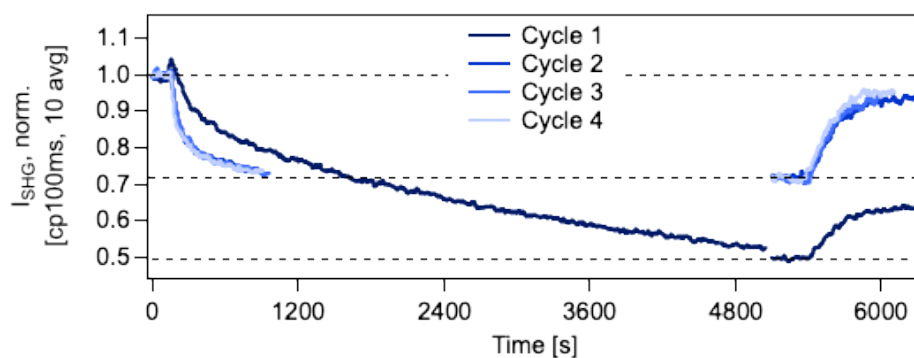
Following the procedure described above, we conducted six separate experiments with three distinct ALD  $\alpha$ -hematite films, surveying a total of nine different pH X values, always relative to the PZC at pH 6.75. To better compare between different experiments, we took the average values of  $I_{SHG}$  for each solution condition and normalized to the most recent preceding value of  $I_{SHG,PZC}$ . We show these results in Figure 5.9, omitting the first cycle (*i.e.* PZC to pH X to PZC) of each day to minimize skewing of the results due to hysteresis.

As mentioned above, we collected triplicate HD scans for each solution condition of the pH titrations alternately with homodyne intensities. We show the values of  $\varphi_{sig}$  and  $E_{sig}$  collected for the full set of experiments in Figure 5.10. Before calculating  $\Phi(0)$  and  $\chi_{NR}^{(2)}$ , we normalized each  $E_{sig}$  data point to the most recent prior value of  $E_{sig,PZC}$ , which served as our referencing condition. We corrected the raw measured phase of the SHG pulse triplet ( $\varphi_{obs}$ ) by subtracting the reference phase measurement (*i.e.*  $\varphi_{ROLO}$ ; see Section 2.3.2), which we collected at the start of each day before beginning experiments.

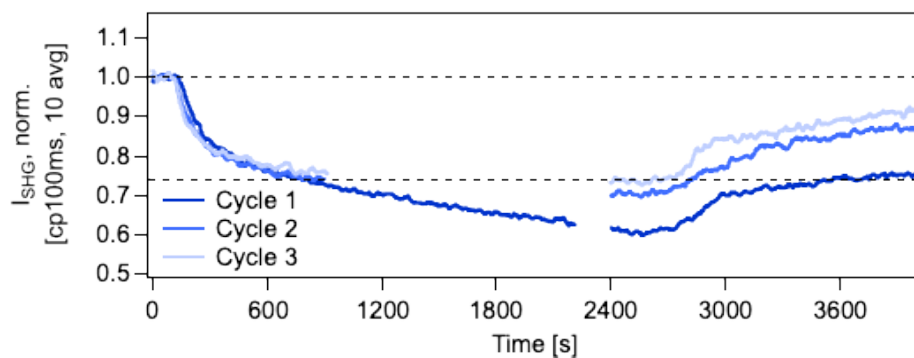
To obtain values of  $\Phi(0)$  and  $\chi_{NR}^{(2)}$ , we used the normalized values of  $E_{sig,pHX}$  and the corrected  $\varphi_{sig}$  phase measurements as inputs for Equations 5.3.7 and 5.3.8 (as described Section 5.3.4). Due to the SHG wavelength (517 nm) being on the shoulder of a likely LMCT band of  $\alpha$ -hematite, we do not expect  $\varphi_R$  to be exactly  $90^\circ$ , but at the time of writing  $\varphi_R$  remains unknown for our system. Therefore, we present several sets of calculated values of  $\Phi(0)$  and  $\chi_{NR}^{(2)}$  varying the value of  $\varphi_R$  between  $-60^\circ$  and  $90^\circ$ .



(a)



(b)



(c)

Figure 5.7. Homodyne SHG intensity plotted against time for alkalimetric pH jumps at the  $\alpha$ -hematite:aqueous interface starting from the PZC (pH 6.75) and going to (a) pH 9, (b) pH 10, and (c) pH 11. Each cycle (*i.e.* PZC to pH X to PZC) is normalized to its initial  $I_{SHG,PZC}$  value, and offset on the time axis for ease of comparison between consecutive runs.

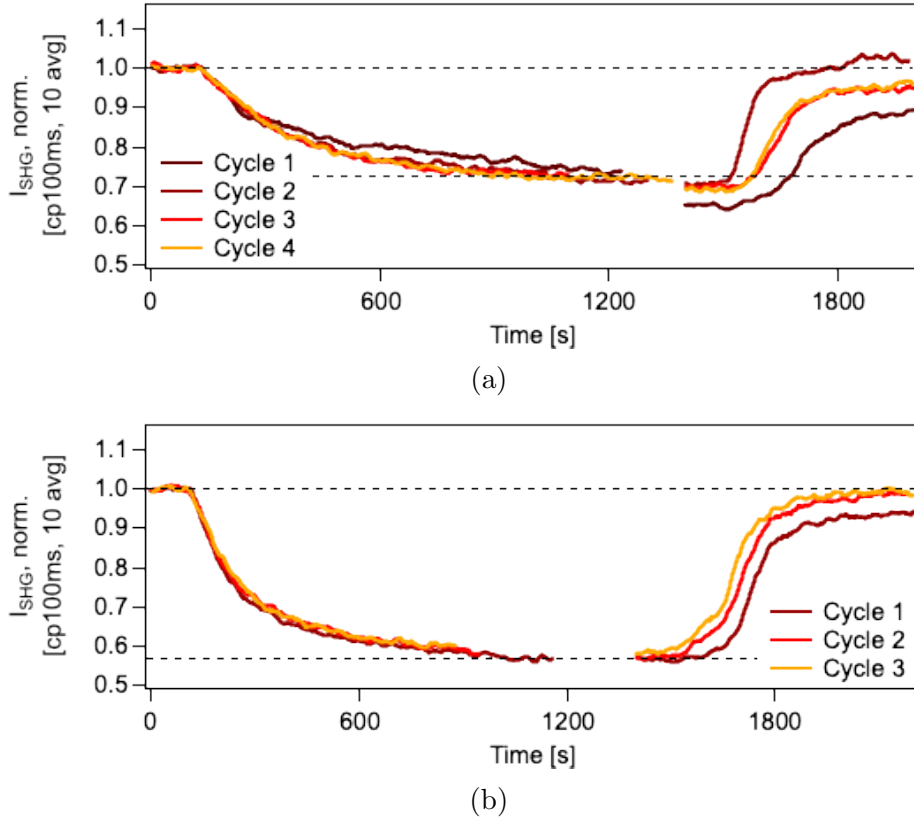


Figure 5.8. Homodyne SHG intensity plotted against time for acidometric pH jumps at the  $\alpha$ -hematite:aqueous interface starting from the PZC (pH 6.75) and going to (a) pH 5 and (b) pH 3. Each cycle (*i.e.* PZC to pH X to PZC) is normalized to its initial  $I_{SHG,PZC}$  value, and offset on the time axis for ease of comparison between consecutive runs.

As shown in Figure 5.11, for every value of  $\varphi_R$  surveyed, the total interfacial potential increases both above and below the PZC. Since we obtained these interfacial potentials from interference fringes taken after at least one cycle of exposures to 1 M NaCl solution at the PZC and 1 M NaCl solution at pH X, we believe this phenomenon is not an artifact of the initial large decrease in both  $I_{SHG}$  and  $E_{sig}$  observed for the first PZC to pH X transition of each experiment. However, the existence of a minimum in total interfacial potential at the PZC is an unexpected result. Rather, we would expect to see a sign flip

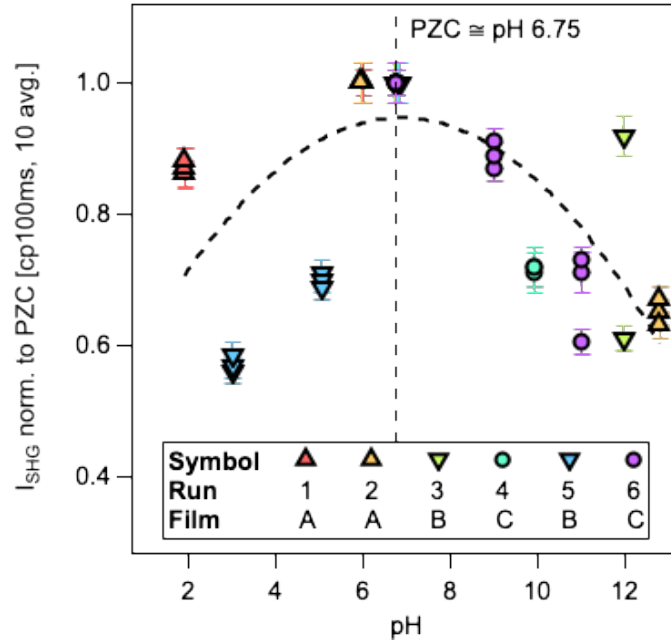


Figure 5.9. Summary of averaged  $I_{SHG}$  from six pH titration experiments starting at or near the PZC of  $\alpha$ -hematite and going to and from different target pH values at constant ionic strength (1 M, NaCl as electrolyte), excluding the first cycle of each experiment. Maximum intensities invariably occur at or near the PZC.

in  $\Phi(0)$  with close to zero potential observed at the PZC.<sup>39,40,57,58</sup> The only values of  $\varphi_R$  where we begin to observe positive potentials are  $< -30^\circ$ , and even at  $\varphi_R = -60^\circ$ , where the interfacial potential at the PZC is indeed near-zero, we still do not observe the expected sign flip. One possible explanation for these results is that the  $\alpha$ -hematite:aqueous interface did not overcome the hysteresis known to exist at circumneutral pH during the 10-min equilibration period allowed in our experiments.<sup>39,40</sup> Alternatively, it is possible that beginning the experiment near the PZC or at high background electrolyte concentration “jammed” the dynamics of acid-base reactions at the  $\alpha$ -hematite:aqueous interface, as past workers in our group have observed for the fused silica:aqueous interface.<sup>59</sup> To test

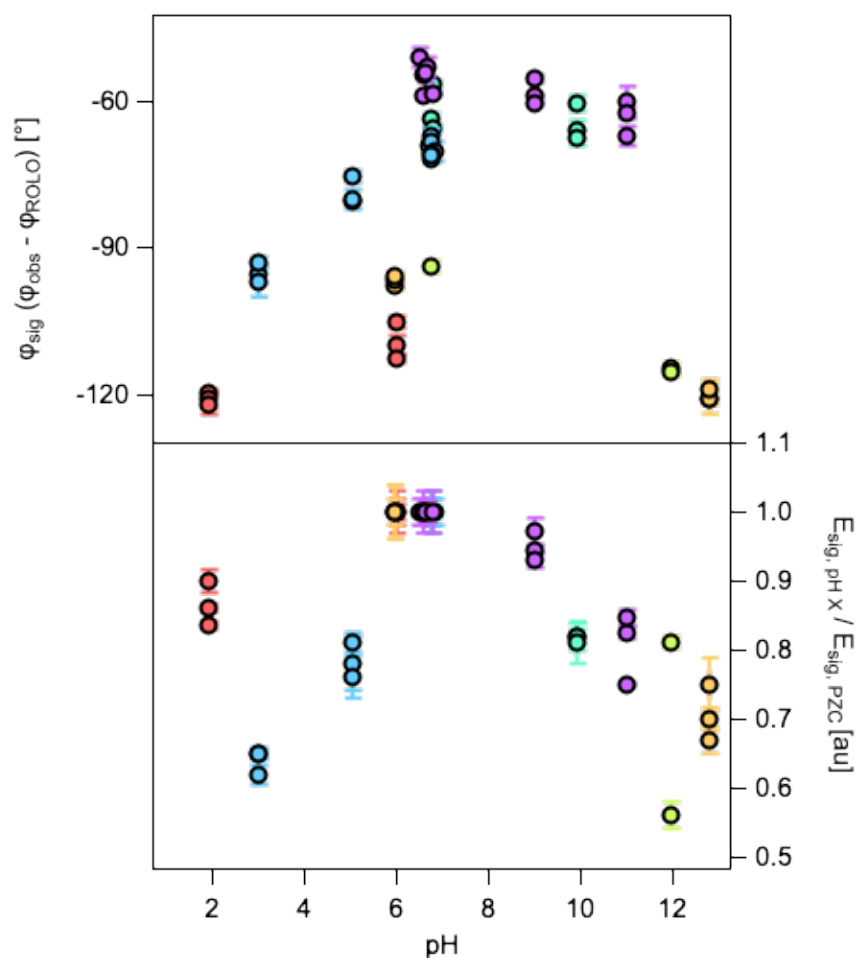


Figure 5.10. Corrected values of  $\varphi_{sig}$  (top plot) and normalized values of  $E_{sig}$  (bottom plot) obtained from fitting triplicate scans collected with HD detection. Data points from different days are shown in different colors.

these hypotheses, future work might involve performing analogous pH titrations beginning from either pH 2 or pH 13 and proceeding entirely in the alkalimetric or acidometric direction, rather than beginning every experiment at the PZC. Additionally, future experiments could include longer equilibration times—20, 30, or 60+ min—and compare results obtained in this manner to those in this work taken with shorter equilibration times.

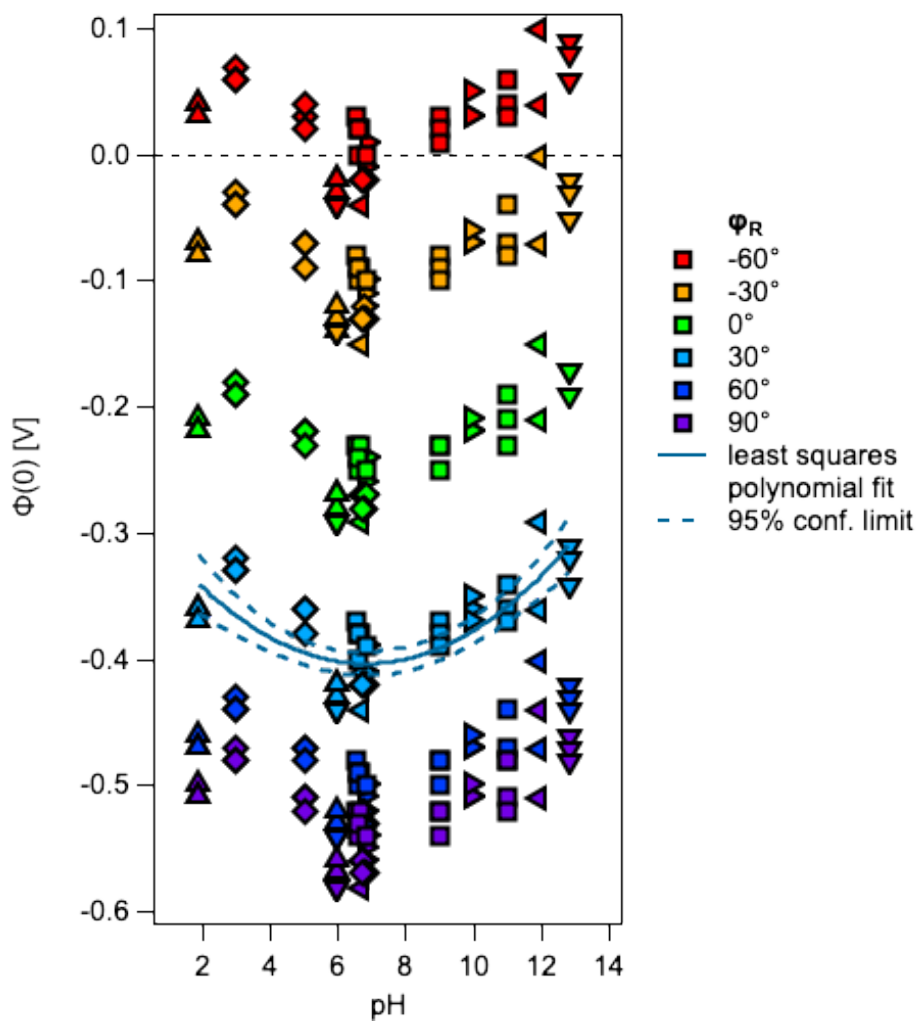


Figure 5.11.  $\Phi(0)$  calculated for the  $\alpha$ -hematite:aqueous interface as a function of pH for a range of possible  $\varphi_R$  values. The dataset for  $\varphi_R = 30^\circ$  is displayed alongside its least squares polynomial fit (solid trace), with the 95% confidence interval denoted (dashed traces).

Although the total interfacial potentials calculated for our experiments do not conform to our expectations for the  $\alpha$ -hematite:aqueous interface, the values of  $\chi_{NR}^{(2)}$  are more in line with expected values. We therefore used these values to calculate the number of net

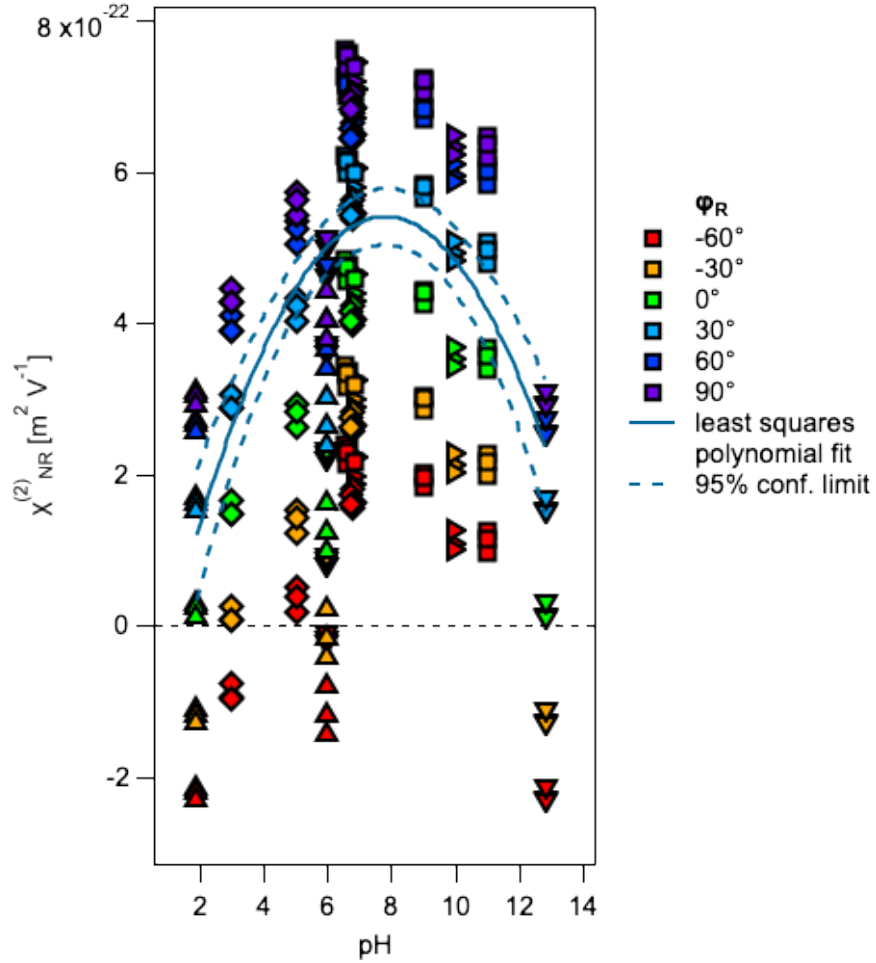


Figure 5.12.  $\chi_{NR}^{(2)}$  calculated for the  $\alpha$ -hematite:aqueous interface as a function of pH for a range of possible  $\varphi_R$  values. The dataset for  $\varphi_R = 30^\circ$  is displayed alongside its least squares polynomial fit (solid trace), with the 95% confidence interval denoted (dashed traces).

aligned water molecules within the Stern layer ( $\mathcal{N}_\dagger$ ) of our system, according to the expression:

$$(5.3.9) \quad \mathcal{N}_\dagger = \frac{\Delta\chi_{NR}^{(2)} \cdot \varepsilon \cdot \varepsilon_0}{\alpha^{(2)} \cdot (10^4 \text{ cm}^2 \text{ m}^{-2})}$$

where  $\Delta\chi_{NR}^{(2)}$  is the difference in the non-resonant second-order nonlinear susceptibilities at pH X *versus* the PZC,  $\varepsilon$  is the permittivity of Stern layer water ( $\varepsilon = 1.77$  to 2),  $\varepsilon_0$  is the

vacuum permittivity, and  $\alpha^{(2)}$  is an estimate of molecular hyperpolarizability for a liquid water model developed elsewhere.<sup>60</sup> Subsequently multiplying  $\Delta\chi_{NR}^{(2)}$  by the elementary charge and the value of  $\Phi(0)$  corresponding to the appropriate pH X condition yields the interfacial energy density ( $\Delta E_{water}$ ) in  $\text{J cm}^{-2}$ . As shown in Figure 5.13, the transition from the PZC to pH 2 corresponds with relatively more net aligned Stern layer water molecules—and therefore relatively more associated energy density—than the transition from the PZC to pH 13. The values of  $\mathcal{N}_\uparrow$  and  $\Delta E_{water}$  obtained for our system are within the same order of magnitude as those calculated recently for the fused silica:water interface.<sup>61</sup>

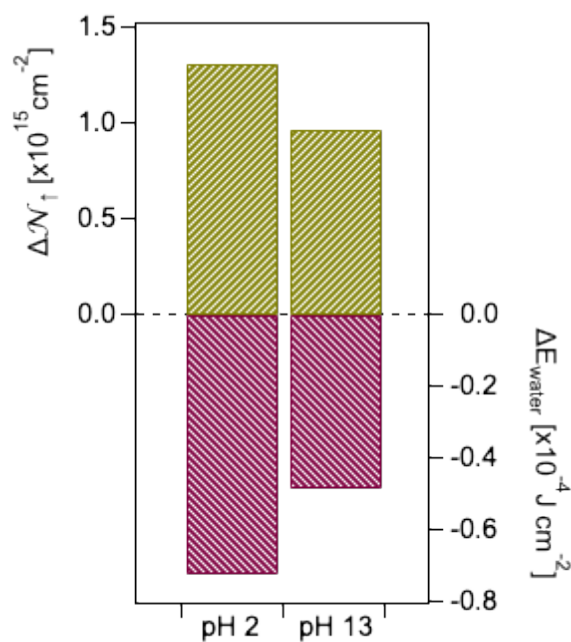


Figure 5.13. The number of net aligned water molecules in the Stern layer calculated for the  $\alpha$ -hematite:aqueous interface as a function of pH relative to the PZC (pH 6.75) when  $\varphi_R = 30^\circ$  (top plot) and the interfacial energy density associated with the net alignment of Stern layer water molecules (bottom plot).

In the interest of maintaining a thorough record of the pH titration data and to aid future work with this system should  $\varphi_R$  be determined, we enumerate the raw values of  $\varphi_{obs}$ , the corrected values of  $\varphi_{sig}$ , the raw and normalized values of  $E_{sig}$ , and the accompanying calculated values of  $\Phi(0)$  and  $\chi_{NR}^{(2)}$  for all runs in Tables 5.2, 5.3, and 5.4.

#### 5.4. Summary and Future Directions

In this chapter we have described the application of the principles and methods outlined in Chapters 2 and 4 to the  $\alpha$ -hematite:aqueous interface as a model metal oxide:aqueous system with important implications for natural environments such as soils and groundwater aquifers, as well as developing technologies such as photoanodes for PEC water splitting.

We start by describing the synthesis *via* ALD and the cleaning of  $\alpha$ -hematite films, as well as their subsequent characterization before and after exposure to aqueous electrolytes by AFM, XPS, and UV-visible absorption and transmission spectroscopy. We found that although  $\alpha$ -hematite films undergo some thinning—detected as an increase in % transmission—and roughening upon multi-hour exposures to high salinity electrolyte solutions at a range of acidic and basic pH values, there is no appreciable change in XPS features observed, indicating minimal chemical transformation of the films' surfaces due to our experimental conditions.

Control experiments of  $\alpha$ -hematite films studied with our System 2 optical set-up (see Section 2.3.2) indicated good quadratic dependence of  $I_{SHG}$  on input power as long as we employ a  $-1$  cm defocusing technique during alignment. We also found that there is no significant difference in measured phase or amplitude for interference patterns collected

under HD detection at different  $yz$  positions on the film surface, suggesting that the use of the flat geometry proposed in Chapter 4 can allow for the collection of multiple replicates by using macroscopically different locations of the laser spot on a single film's surface without the need for remounting the flow cell or realigning the spectrometer.

We proposed an optical model for obtaining  $\Phi(0)$  and  $\chi_{NR}^{(2)}$  for our system under varying aqueous conditions while accounting for anticipated resonant and non-resonant contributions to our SHG signal due to the proximity of our SHG wavelength to a proposed LMCT band for  $\alpha$ -hematite. This model allows us to calculate these values using only the absolute phase (see Section 2.3.2) and normalized amplitude of our HD-SHG measurements as inputs.

From here, using homodyne SHG charge-screening experiments, we determined the PZC for our particular batch of  $\alpha$ -hematite films to be located at pH 6.75. Using this PZC value as our starting (and referencing) point, we conducted acidometric and alkalimetric pH titrations of the  $\alpha$ -hematite:aqueous interface at constant ionic strength using HD-SHG, which allowed us to directly measure  $\Phi(0)$  and  $\chi_{NR}^{(2)}$  for the system at different pH conditions. We observed an unexpected minimum in  $\Phi(0)$  near the PZC, with more positive values at both acidic and basic pH conditions. Due to the resonant phase angle ( $\varphi_R$ ) being undetermined for our system at 517 nm at the time of writing, we report  $\Phi(0)$  and  $\chi_{NR}^{(2)}$  as a function of possible  $\varphi_R$  values. Finally, we determine the number of net aligned water molecules in the Stern layer of the  $\alpha$ -hematite:aqueous interface at pH 2 and pH 13 relative to the PZC, as well as the energy density associated with that net alignment. We found relatively more net aligned water molecules at pH 2 *versus* pH 13, relative to the PZC.

Future work on this system should seek to determine  $\varphi_R$  so as to obtain more constrained calculations of  $\Phi(0)$  and  $\chi_{NR}^{(2)}$ . By using System 2 in tandem with an optical parametric amplifier (OPA), it would be possible to conduct HD-SHG experiments at different selected fundamental and SHG wavelengths, thus allowing for either a fully resonantly-enhanced measurement, or a fully non-resonant measurement. Both experiments would broaden our understanding of the electrostatics and electronics of the  $\alpha$ -hematite:aqueous interface. To constrain the impact of hysteresis on our calculated  $\Phi(0)$  and  $\chi_{NR}^{(2)}$  values, future work could also be to conduct pH titrations beginning at maximally-charged conditions (*i.e.* pH 2 or pH 13) with longer equilibration times. Finally, we note that work is in progress to investigate the  $\alpha$ -hematite:aqueous interface using HD-SHG measurements in tandem with an electrochemical workstation, such that an external potential can be applied to the  $\alpha$ -hematite:aqueous interface as an electrode while optically monitoring interfacial potential.<sup>62</sup> Such studies will build on the work presented here, which concerns itself primarily with the behavior and electrostatics of the  $\alpha$ -hematite:aqueous interface under environmentally relevant conditions, and without the application of external potentials.

| Run  | pH    | $E_{sig}$ [cp100ms] |          | $\varphi_{obs}$ [°] |          | $\varphi_{sig}$ [°] | Normalization 1 |               | Normalization 2                                     |                |               |   |          |          |
|------|-------|---------------------|----------|---------------------|----------|---------------------|-----------------|---------------|---|----------------|---------------|---|----------|----------|
|      |       | $\mu$               | $\sigma$ | $\mu$               | $\sigma$ |                     | $E_{sig}$ [au]  | $\Phi(0)$ [V] | $\chi_{NR}^{(2)}$ [m <sup>2</sup> V <sup>-1</sup> ] | $E_{sig}$ [au] | $\Phi(0)$ [V] | $\chi_{NR}^{(2)}$ [m <sup>2</sup> V <sup>-1</sup> ] |          |          |
| 1    | 6.02  | 45.1                | 0.5      | 83.8                | 0.9      | -96.9               | 1.00            | 0.01          | -0.44   | 3.7e-22        | 1.00          | 0.01  | -0.44    | 3.7e-22  |
|      | 1.90  | 32.1                | 1.0      | 63.2                | 0.8      | -117.6              | 0.71            | 0.02          | -0.33   | 1.8e-22        | 0.71          | 0.02  | -0.33    | 1.8e-22  |
|      | 6.02  | 37.6                | 1.2      | 75.6                | 1.2      | -105.2              | 1.00            | 0.03          | -0.43   | 3.0e-22        | 0.83          | 0.03  | -0.38    | 2.7e-22  |
|      | 1.90  | 31.4                | 0.2      | 60.8                | 0.4      | -119.9              | 0.84            | 0.01          | -0.36   | 1.7e-22        | 0.696         | 0.004   | -0.32    | 1.6e-22  |
|      | 6.02  | 36.3                | 0.4      | 71.1                | 1.5      | -109.7              | 1.00            | 0.01          | -0.42   | 2.6e-22        | 0.80          | 0.01  | -0.37    | 2.4e-22  |
|      | 1.90  | 31.3                | 0.2      | 60.0                | 1.8      | -120.7              | 0.86            | 0.01          | -0.36   | 1.6e-22        | 0.694         | 0.004   | -0.32    | 1.6e-22  |
| 2    | 6.02  | 34.6                | 0.8      | 68.2                | 0.9      | -112.6              | 1.00            | 0.02          | -0.42   | 2.4e-22        | 0.77          | 0.02  | -0.35    | 2.1e-22  |
|      | 1.90  | 31.1                | 0.6      | 58.5                | 1.5      | -122.3              | 0.90            | 0.02          | -0.37   | 1.5e-22        | 0.69          | 0.01  | -0.32    | 1.5e-22  |
|      | 6.02  | 29.6                | 0.8      | 65.2                | 1.3      | -115.6              | 0.86            | 0.02          | -0.37   | 2.0e-22        | 0.66          | 0.02  | -0.32    | 1.9e-22  |
|      | 5.96  | 29.9                | 0.5      | 73.8                | 1.0      | -104.9              | 1.00            | 0.02          | -0.43   | 3.0e-22        | 1.00          | 0.02  | -0.43    | 3.0e-22  |
|      | 12.80 | 23.0                | 0.7      | 59.0                | 3.0      | -119.5              | 0.77            | 0.02          | -0.34   | 1.7e-22        | 0.77          | 0.02  | -0.34    | 1.7e-22  |
|      | 5.96  | 32.3                | 1.2      | 81.1                | 0.6      | -97.6               | 1.00            | 0.04          | -0.44   | 3.6e-22        | 1.08          | 0.04  | -0.46    | 3.8e-22  |
| 3    | 12.80 | 21.6                | 0.7      | 57.6                | 1.2      | -121.1              | 0.67            | 0.02          | -0.31   | 1.6e-22        | 0.72          | 0.02  | -0.33    | 1.6e-22  |
|      | 5.96  | 31.4                | 0.6      | 81.9                | 1.5      | -96.7               | 1.00            | 0.02          | -0.44   | 3.7e-22        | 1.05          | 0.02  | -0.45    | 3.8e-22  |
|      | 12.80 | 22.0                | 0.5      | 57.0                | 3.0      | -121.5              | 0.70            | 0.02          | -0.32   | 1.5e-22        | 0.74          | 0.02  | -0.33    | 1.5e-22  |
|      | 5.96  | 30.3                | 1.2      | 82.7                | 0.3      | -95.9               | 1.00            | 0.04          | -0.44   | 3.8e-22        | 1.01          | 0.04  | -0.44    | 3.8e-22  |
|      | 12.80 | 22.7                | 1.3      | 60.0                | 2.0      | -118.8              | 0.75            | 0.04          | -0.34   | 1.7e-22        | 0.76          | 0.04  | -0.34    | 1.7e-22  |
|      | 5.96  | 30.9                | 0.7      | 86.0                | 2.0      | -93.1               | 1.02            | 0.02          | -0.44   | 4.0e-22        | 1.03          | 0.02  | -0.45    | 4.1e-22  |
| 3    | 6.77  | 63.6                | 0.6      | 117.8               | 1.2      | -60.0               | 1.00            | 0.01          | -0.40   | 2.3e-22        | 1.00          | 0.01  | -0.40    | 2.3e-22  |
|      | 11.96 | 28.0                | 0.4      | 79.1                | 1.5      | -98.6               | 0.44            | 0.01          | -0.27   | -1.3e-22       | 0.44          | 0.01  | -0.27    | -1.3e-22 |
|      | 6.72  | 44.6                | 0.3      | 108.7               | 1.3      | -69.0               | 1.00            | 0.01          | -0.42   | 1.9e-22        | 0.701         | 0.005   | -0.34    | 6.5e-23  |
|      | 11.96 | 24.9                | 0.7      | 63.2                | 1.2      | -114.6              | 0.56            | 0.02          | -0.29   | -1.8e-22       | 0.39          | 0.01  | -0.25    | -1.9e-22 |
|      | 6.73  | 30.2                | 1.0      | 84.2                | 1.0      | -93.6               | 1.00            | 0.03          | -0.44   | 3.0e-23        | 0.47          | 0.01  | -0.28    | -1.0e-22 |
|      | 11.96 | 24.6                | 0.2      | 62.4                | 0.6      | -115.3              | 0.81            | 0.01          | -0.36   | -1.6e-22       | 0.387         | 0.003   | -0.25    | -2.0e-22 |
| 6.76 | 29.3  | 0.3                 | 79.2     | 1.4                 | -98.5    | 0.97                | 0.01            | -0.43         | -1.5e-23  | 0.461          | 0.005         | -0.28   | -1.2e-22 |          |

Table 5.2. Experimental values of  $E_{sig}$  and  $\varphi_{obs}$  and calculated values of  $\Phi(0)$  and  $\chi_{NR}^{(2)}$  for  $\varphi_R = 30^\circ$  for Run 1, Run 2, and Run 3 pH titrations. Results are shown for normalization to the first  $E_{sig}$  of each PZC to pH X to PZC cycle (“Normalization 1”), as well as for normalization to only the first  $E_{sig}$  of the entire run (“Normalization 2”).

| Run  | pH   | $E_{sig}$ [cp100ms] |          | $\varphi_{obs}$ [°] |          | $\varphi_{sig}$ [°] | Normalization 1 |               |   | Normalization 2 |               |   |       |         |
|------|------|---------------------|----------|---------------------|----------|---------------------|-----------------|---------------|---|-----------------|---------------|---|-------|---------|
|      |      | $\mu$               | $\sigma$ | $\mu$               | $\sigma$ |                     | $E_{sig}$ [au]  | $\Phi(0)$ [V] | $\chi_{NR}^{(2)}$ [m <sup>2</sup> V <sup>-1</sup> ] | $E_{sig}$ [au]  | $\Phi(0)$ [V] | $\chi_{NR}^{(2)}$ [m <sup>2</sup> V <sup>-1</sup> ] |       |         |
| 4    | 6.76 | 37.3                | 0.4      | 300.9               | 1.6      | -59.1               | 1.00            | 0.01          | -0.40   | 6.0e-22         | 1.00          | 0.01  | -0.40 | 6.0e-22 |
|      | 9.93 | 25.1                | 0.7      | 292.6               | 0.6      | -67.4               | 0.67            | 0.02          | -0.33   | 4.2e-22         | 0.67          | 0.02  | -0.33 | 4.2e-22 |
|      | 6.76 | 28.0                | 0.9      | 296.7               | 1.2      | -63.3               | 1.00            | 0.03          | -0.41   | 5.8e-22         | 0.75          | 0.02  | -0.34 | 4.7e-22 |
|      | 9.93 | 22.9                | 0.5      | 294.2               | 2.4      | -65.8               | 0.82            | 0.02          | -0.36   | 4.9e-22         | 0.61          | 0.01  | -0.31 | 4.0e-22 |
|      | 6.79 | 26.9                | 0.2      | 294.4               | 0.8      | -65.6               | 1.00            | 0.01          | -0.41   | 5.7e-22         | 0.72          | 0.01  | -0.34 | 4.5e-22 |
|      | 9.93 | 21.9                | 0.3      | 292.6               | 1.5      | -67.4               | 0.82            | 0.01          | -0.37   | 4.8e-22         | 0.59          | 0.01  | -0.30 | 3.9e-22 |
|      | 6.81 | 25.8                | 0.8      | 303.4               | 0.7      | -56.6               | 1.00            | 0.03          | -0.39   | 6.1e-22         | 0.69          | 0.02  | -0.31 | 4.6e-22 |
|      | 9.93 | 20.9                | 0.7      | 299.8               | 1.7      | -60.2               | 0.81            | 0.03          | -0.35   | 5.1e-22         | 0.56          | 0.02  | -0.29 | 3.9e-22 |
|      | 6.79 | 26.1                | 0.9      | 301.4               | 1.1      | -58.6               | 1.01            | 0.03          | -0.40   | 6.0e-22         | 0.70          | 0.02  | -0.32 | 4.6e-22 |
|      | 6.80 | 45.1                | 0.5      | 292.4               | 0.6      | -67.6               | 1.00            | 0.01          | -0.42   | 5.6e-22         | 1.00          | 0.01  | -0.42 | 5.6e-22 |
| 5    | 5.03 | 35.9                | 0.8      | 287.1               | 1.0      | -72.9               | 0.80            | 0.02          | -0.37   | 4.5e-22         | 0.80          | 0.02  | -0.37 | 4.5e-22 |
|      | 6.76 | 43.5                | 0.8      | 293.1               | 1.4      | -66.9               | 1.00            | 0.02          | -0.41   | 5.6e-22         | 0.96          | 0.02  | -0.40 | 5.5e-22 |
|      | 5.03 | 33.7                | 1.5      | 284.8               | 1.0      | -75.2               | 0.78            | 0.04          | -0.36   | 4.3e-22         | 0.75          | 0.03  | -0.36 | 4.2e-22 |
|      | 6.73 | 43.3                | 1.1      | 291.7               | 1.6      | -68.3               | 1.00            | 0.03          | -0.42   | 5.6e-22         | 0.96          | 0.02  | -0.41 | 5.4e-22 |
|      | 5.03 | 32.7                | 1.2      | 279.6               | 0.1      | -80.4               | 0.76            | 0.03          | -0.36   | 4.0e-22         | 0.73          | 0.03  | -0.35 | 3.9e-22 |
|      | 6.82 | 41.1                | 0.9      | 289.9               | 1.9      | -70.1               | 1.00            | 0.02          | -0.42   | 5.5e-22         | 0.91          | 0.02  | -0.40 | 5.1e-22 |
|      | 5.03 | 33.1                | 0.6      | 280.1               | 1.8      | -79.9               | 0.81            | 0.01          | -0.38   | 4.2e-22         | 0.73          | 0.01  | -0.36 | 4.0e-22 |
|      | 6.77 | 42.3                | 0.2      | 288.4               | 0.5      | -71.6               | 1.000           | 0.005         | -0.42   | 5.4e-22         | 0.937         | 0.004   | -0.41 | 5.1e-22 |
|      | 3.00 | 26.1                | 0.6      | 264.7               | 1.8      | -95.3               | 0.62            | 0.01          | -0.32   | 2.9e-22         | 0.58          | 0.01  | -0.31 | 2.8e-22 |
|      | 6.77 | 40.5                | 0.9      | 289.3               | 1.3      | -70.7               | 1.00            | 0.02          | -0.42   | 5.4e-22         | 0.90          | 0.02  | -0.39 | 5.0e-22 |
| 3.00 | 6.73 | 40.5                | 0.1      | 289.1               | 1.6      | -70.9               | 1.000           | 0.003         | -0.42   | 5.4e-22         | 0.898         | 0.002   | -0.39 | 5.0e-22 |
|      | 3.00 | 26.3                | 0.3      | 263.0               | 2.5      | -97.0               | 0.65            | 0.01          | -0.33   | 2.9e-22         | 0.58          | 0.01  | -0.31 | 2.7e-22 |
|      | 6.71 | 40.7                | 0.7      | 288.5               | 0.5      | -71.5               | 1.00            | 0.02          | -0.42   | 5.4e-22         | 0.90          | 0.02  | -0.40 | 5.0e-22 |

Table 5.3. Experimental values of  $E_{sig}$  and  $\varphi_{obs}$  and calculated values of  $\Phi(0)$  and  $\chi_{NR}^{(2)}$  for  $\varphi_R = 30^\circ$  for Run 4 and Run 5 pH titrations. Results are shown for normalization to the first  $E_{sig}$  of each PZC to pH X to PZC cycle (“Normalization 1”), as well as for normalization to only the first  $E_{sig}$  of the entire run (“Normalization 2”).

| Run  | pH    | $E_{sig}$ [cp100ms] |          | $\varphi_{obs}$ [°] |          | $\varphi_{sig}$ [°] | Normalization 1 |               |   | Normalization 2 |               |   |         |         |
|------|-------|---------------------|----------|---------------------|----------|---------------------|-----------------|---------------|---|-----------------|---------------|---|---------|---------|
|      |       | $\mu$               | $\sigma$ | $\mu$               | $\sigma$ |                     | $E_{sig}$ [au]  | $\Phi(0)$ [V] | $\chi_{NR}^{(2)}$ [m <sup>2</sup> V <sup>-1</sup> ] | $E_{sig}$ [au]  | $\Phi(0)$ [V] | $\chi_{NR}^{(2)}$ [m <sup>2</sup> V <sup>-1</sup> ] |         |         |
| 6    | 6.82  | 51.2                | 0.2      | 315.2               | 1.4      | -44.8               | 1.000           | 0.005         | -0.35   | 6.4e-22         | 1.00          | 0.00  | -0.35   | 6.4e-22 |
|      | 9.05  | 44.3                | 1.2      | 310.6               | 0.9      | -49.4               | 0.86            | 0.02          | -0.34   | 5.6e-22         | 0.87          | 0.02  | -0.34   | 5.6e-22 |
|      | 6.51  | 44.4                | 0.9      | 309.3               | 1.8      | -50.7               | 1.00            | 0.02          | -0.37   | 6.2e-22         | 0.87          | 0.02  | -0.34   | 5.6e-22 |
|      | 9.05  | 41.9                | 0.3      | 304.9               | 0.9      | -55.1               | 0.94            | 0.01          | -0.37   | 5.8e-22         | 0.82          | 0.01  | -0.34   | 5.2e-22 |
|      | 6.60  | 43.3                | 0.1      | 305.6               | 0.7      | -54.4               | 1.000           | 0.002         | -0.38   | 6.1e-22         | 0.846         | 0.002   | -0.35   | 5.4e-22 |
|      | 9.05  | 40.3                | 0.5      | 301.3               | 0.4      | -58.7               | 0.93            | 0.01          | -0.38   | 5.7e-22         | 0.79          | 0.01  | -0.34   | 5.0e-22 |
|      | 6.59  | 41.2                | 1.1      | 301.3               | 0.7      | -58.7               | 1.00            | 0.03          | -0.40   | 6.0e-22         | 0.80          | 0.02  | -0.35   | 5.1e-22 |
|      | 9.05  | 40.1                | 0.8      | 299.8               | 0.5      | -60.2               | 0.97            | 0.02          | -0.39   | 5.8e-22         | 0.78          | 0.02  | -0.34   | 4.9e-22 |
|      | 6.66  | 41.8                | 0.7      | 307.0               | 2.0      | -52.9               | 1.00            | 0.02          | -0.38   | 6.2e-22         | 0.82          | 0.01  | -0.34   | 5.3e-22 |
|      | 10.98 | 31.3                | 0.2      | 300.0               | 3.0      | -59.8               | 0.750           | 0.004         | -0.34   | 4.8e-22         | 0.611         | 0.004   | -0.30   | 4.2e-22 |
|      | 6.62  | 35.1                | 0.3      | 306.0               | 2.0      | -54.2               | 1.00            | 0.01          | -0.38   | 6.1e-22         | 0.69          | 0.01  | -0.31   | 4.6e-22 |
|      | 10.98 | 29.0                | 0.3      | 297.7               | 1.1      | -62.3               | 0.83            | 0.01          | -0.36   | 5.1e-22         | 0.57          | 0.01  | -0.29   | 3.9e-22 |
|      | 6.81  | 33.0                | 0.8      | 301.5               | 0.5      | -58.5               | 1.00            | 0.03          | -0.39   | 6.0e-22         | 0.64          | 0.02  | -0.31   | 4.4e-22 |
|      | 10.98 | 27.9                | 0.3      | 293.2               | 1.8      | -66.8               | 0.85            | 0.01          | -0.37   | 5.0e-22         | 0.54          | 0.01  | -0.29   | 3.7e-22 |
| 6.90 | 32.5  | 1.4                 | 299.6    | 0.2                 | -60.4    | 0.98                | 0.04            | -0.40         | 5.8e-22   | 0.63            | 0.03          | -0.31   | 4.3e-22 |         |

Table 5.4. Experimental values of  $E_{sig}$  and  $\varphi_{obs}$  and calculated values of  $\Phi(0)$  and  $\chi_{NR}^{(2)}$  for  $\varphi_R = 30^\circ$  for Run 6 pH titrations. Results are shown for normalization to the first  $E_{sig}$  of each PZC to pH X to PZC cycle (“Normalization 1”), as well as for normalization to only the first  $E_{sig}$  of the entire run (“Normalization 2”).

## REFERENCES

### References for Chapter 1

- (1) Yao, W.; Dal Porto, R.; Gallagher, D. L.; Dietrich, A. M. Human Exposure to Particles at the Air-Water Interface: Influence of Water Quality on Indoor Air Quality from Use of Ultrasonic Humidifiers. *Environment International* **2020**, *143*, 105902.
- (2) Euvrard, M.; Membrey, F.; Filiatre, C.; Foissy, A. Crystallization of Calcium Carbonate at a Solid/Liquid Interface Examined by Reflection of a Laser Beam. *Journal of Crystal Growth* **2004**, *265*, 322–330.
- (3) Chang, J.; Wang, G.; Chang, X.; Yang, Z.; Wang, H.; Li, B.; Zhang, W.; Kovarik, L.; Du, Y.; Orlovskaya, N.; Xu, B.; Wang, G.; Yang, Y. Interface Synergism and Engineering of Pd/Co@N-C for Direct Ethanol Fuel Cells. *Nat Commun* **2023**, *14*, 1346.
- (4) Najaf, Z.; Nguyen, D. L. T.; Chae, S. Y.; Joo, O.-S.; Shah, A. U. H. A.; Vo, D.-V. N.; Nguyen, V.-H.; Le, Q. V.; Rahman, G. Recent Trends in Development of Hematite (-Fe<sub>2</sub>O<sub>3</sub>) as an Efficient Photoanode for Enhancement of Photoelectrochemical Hydrogen Production by Solar Water Splitting. *International Journal of Hydrogen Energy* **2021**, *46*, 23334–23357.
- (5) O'Day, P. A. Molecular Environmental Geochemistry. *Reviews of Geophysics* **1999**, *37*, 249–274.

- (6) Danish, M. S. S.; Estrella, L. L.; Alemaida, I. M. A.; Lisin, A.; Moiseev, N.; Ahmadi, M.; Nazari, M.; Wali, M.; Zaheb, H.; Senjyu, T. Photocatalytic Applications of Metal Oxides for Sustainable Environmental Remediation. *Metals* **2021**, *11*, 80.
- (7) Waychunas, G. A.; Kim, C. S.; Banfield, J. F. Nanoparticulate Iron Oxide Minerals in Soils and Sediments: Unique Properties and Contaminant Scavenging Mechanisms. *J Nanopart Res* **2005**, *7*, 409–433.
- (8) Tamirat, A. G.; Rick, J.; Dubale, A. A.; Su, W.-N.; Hwang, B.-J. Using Hematite for Photoelectrochemical Water Splitting: A Review of Current Progress and Challenges. *Nanoscale Horiz.* **2016**, *1*, 243–267.
- (9) Zandi, O.; Hamann, T. W. The Potential versus Current State of Water Splitting with Hematite. *Phys. Chem. Chem. Phys.* **2015**, *17*, 22485–22503.
- (10) Zhou, D.; Fan, K. Recent Strategies to Enhance the Efficiency of Hematite Photoanodes in Photoelectrochemical Water Splitting. *Chinese Journal of Catalysis* **2021**, *42*, 904–919.
- (11) Phuan, Y. W.; Ong, W.-J.; Chong, M. N.; Ocon, J. D. Prospects of Electrochemically Synthesized Hematite Photoanodes for Photoelectrochemical Water Splitting: A Review. *Journal of Photochemistry and Photobiology C: Photochemistry Reviews* **2017**, *33*, 54–82.
- (12) Bora, D. K.; Braun, A.; Constable, E. C. “In Rust We Trust”. Hematite – the Prospective Inorganic Backbone for Artificial Photosynthesis. *Energy Environ. Sci.* **2013**, *6*, 407–425.
- (13) Tolod, K. R.; Hernández, S.; Quadrelli, E. A.; Russo, N. In *Studies in Surface Science and Catalysis*, Albonetti, S., Perathoner, S., Quadrelli, E. A., Eds.; Horizons

- in Sustainable Industrial Chemistry and Catalysis, Vol. 178; Elsevier: 2019, pp 65–84.
- (14) Ohno, P. E.; Chang, H.; Spencer, A. P.; Liu, Y.; Boamah, M. D.; Wang, H.-f.; Geiger, F. M. Beyond the Gouy–Chapman Model with Heterodyne-Detected Second Harmonic Generation. *J. Phys. Chem. Lett.* **2019**, *10*, 2328–2334.
- (15) Davis, J. A.; Leckie, J. O. Surface Ionization and Complexation at the Oxide/Water Interface. 3. Adsorption of Anions. *Journal of Colloid and Interface Science* **1980**, *74*, 32–43.
- (16) Davis, J. A.; James, R. O.; Leckie, J. O. Surface Ionization and Complexation at the Oxide/Water Interface: I. Computation of Electrical Double Layer Properties in Simple Electrolytes. *Journal of Colloid and Interface Science* **1978**, *63*, 480–499.
- (17) Davis, J. A.; Leckie, J. O. Surface Ionization and Complexation at the Oxide/Water Interface II. Surface Properties of Amorphous Iron Oxyhydroxide and Adsorption of Metal Ions. *Journal of Colloid and Interface Science* **1978**, *67*, 90–107.
- (18) Stumm, W.; Morgan, J., *Aquatic Chemistry: Chemical Equilibria and Rates in Natural Waters, 3rd Edition* — Wiley, 3rd ed.; Wiley: 1995.
- (19) Liu, Q.; Fu, Y.; Qin, Z.; Wang, Y.; Zhang, S.; Ran, M. Progress in the Applications of Atomic Force Microscope (AFM) for Mineralogical Research. *Micron* **2023**, *170*, 103460.
- (20) Itaya, K. In Situ Scanning Tunneling Microscopy in Electrolyte Solutions. *Progress in Surface Science* **1998**, *58*, 121–247.

- (21) MacDonald, R. J.; King, B. V. In *Surface Analysis Methods in Materials Science*, O'Connor, D. J., Sexton, B. A., Smart, R. S. C., Eds.; Springer Series in Surface Sciences; Springer: Berlin, Heidelberg, 2003, pp 127–154.
- (22) Kibel, M. H. In *Surface Analysis Methods in Materials Science*, O'Connor, D. J., Sexton, B. A., Smart, R. S. C., Eds.; Springer Series in Surface Sciences; Springer: Berlin, Heidelberg, 2003, pp 175–201.
- (23) Turner, P. S.; Nockolds, C. E.; Bulcock, S. In *Surface Analysis Methods in Materials Science*, O'Connor, D. J., Sexton, B. A., Smart, R. S. C., Eds.; Springer Series in Surface Sciences; Springer: Berlin, Heidelberg, 2003, pp 85–105.
- (24) Dastoor, P. C. In *Surface Analysis Methods in Materials Science*, O'Connor, D. J., Sexton, B. A., Smart, R. S. C., Eds.; Springer Series in Surface Sciences; Springer: Berlin, Heidelberg, 2003, pp 155–174.
- (25) Abrams, I. M.; McBain, J. W. A Closed Cell for Electron Microscopy. *Journal of Applied Physics* **1944**, *15*, 607–609.
- (26) Thompson, R. F.; Walker, M.; Siebert, C. A.; Muench, S. P.; Ranson, N. A. An Introduction to Sample Preparation and Imaging by Cryo-Electron Microscopy for Structural Biology. *Methods* **2016**, *100*, 3–15.
- (27) Henderson, M. A. Insights into the (1×1)-to-(2×1) Phase Transition of the -Fe<sub>2</sub>O<sub>3</sub>(012) Surface Using EELS, LEED and Water TPD. *Surface Science* **2002**, *515*, 253–262.

## References for Chapter 2

- (1) Subir, M.; Rao, Y., *Environmental Interfacial Spectroscopy*; American Chemical Society: 2022; 331 pp.
- (2) Deer, W. A.; Howie, R. A.; Zussman, J., *An Introduction to the Rock-Forming Minerals*; Mineralogical Society of Great Britain and Ireland: 2013.
- (3) Nesse, W. D., *Introduction to Mineralogy*; Oxford University Press: 2017; 495 pp.
- (4) Davis, J. A.; James, R. O.; Leckie, J. O. Surface Ionization and Complexation at the Oxide/Water Interface: I. Computation of Electrical Double Layer Properties in Simple Electrolytes. *Journal of Colloid and Interface Science* **1978**, *63*, 480–499.
- (5) Davis, J. A.; Leckie, J. O. Surface Ionization and Complexation at the Oxide/Water Interface II. Surface Properties of Amorphous Iron Oxyhydroxide and Adsorption of Metal Ions. *Journal of Colloid and Interface Science* **1978**, *67*, 90–107.
- (6) Davis, J. A.; Leckie, J. O. Surface Ionization and Complexation at the Oxide/Water Interface. 3. Adsorption of Anions. *Journal of Colloid and Interface Science* **1980**, *74*, 32–43.
- (7) Ohno, P. E.; Saslow, S. A.; Wang, H.-f.; Geiger, F. M.; Eienthal, K. B. Phase-Referenced Nonlinear Spectroscopy of the -Quartz/Water Interface. *Nat Commun* **2016**, *7*, 13587.
- (8) Joutsuka, T.; Hirano, T.; Sprik, M.; Morita, A. Effects of Third-Order Susceptibility in Sum Frequency Generation Spectra: A Molecular Dynamics Study in Liquid Water. *Phys. Chem. Chem. Phys.* **2018**, *20*, 3040–3053.

- (9) Wen, Y.-C.; Zha, S.; Liu, X.; Yang, S.; Guo, P.; Shi, G.; Fang, H.; Shen, Y. R.; Tian, C. Unveiling Microscopic Structures of Charged Water Interfaces by Surface-Specific Vibrational Spectroscopy. *Phys. Rev. Lett.* **2016**, *116*, 016101.
- (10) Gonella, G.; Lütgebaucks, C.; de Beer, A. G. F.; Roke, S. Second Harmonic and Sum-Frequency Generation from Aqueous Interfaces Is Modulated by Interference. *J. Phys. Chem. C* **2016**, *120*, 9165–9173.
- (11) Ohno, P. E.; Chang, H.; Spencer, A. P.; Liu, Y.; Boamah, M. D.; Wang, H.-f.; Geiger, F. M. Beyond the Gouy–Chapman Model with Heterodyne-Detected Second Harmonic Generation. *J. Phys. Chem. Lett.* **2019**, *10*, 2328–2334.
- (12) Stolle, R.; Marowsky, G.; Schwarzberg, E.; Berkovic, G. Phase Measurements in Nonlinear Optics. *Appl. Phys. B* **1996**, *63*, 491–498.
- (13) Chang, R. K.; Ducuing, J.; Bloembergen, N. Relative Phase Measurement Between Fundamental and Second-Harmonic Light. *Phys. Rev. Lett.* **1965**, *15*, 6–8.
- (14) Kemnitz, K.; Bhattacharyya, K.; Hicks, J. M.; Pinto, G. R.; Eisenthal, B.; Heinz, T. F. The Phase of Second-Harmonic Light Generated at an Interface and Its Relation to Absolute Molecular Orientation. *Chemical Physics Letters* **1986**, *131*, 285–290.
- (15) Ma, E.; Ohno, P. E.; Kim, J.; Liu, Y.; Lozier, E. H.; Miller, T. F. I.; Wang, H.-F.; Geiger, F. M. A New Imaginary Term in the Second-Order Nonlinear Susceptibility from Charged Interfaces. *J. Phys. Chem. Lett.* **2021**, *12*, 5649–5659.
- (16) Dalstein, L.; Chiang, K.-Y.; Wen, Y.-C. Direct Quantification of Water Surface Charge by Phase-Sensitive Second Harmonic Spectroscopy. *J. Phys. Chem. Lett.* **2019**, *10*, 5200–5205.

- (17) Lütgebaucks, C.; Gonella, G.; Roke, S. Optical Label-Free and Model-Free Probe of the Surface Potential of Nanoscale and Microscopic Objects in Aqueous Solution. *Phys. Rev. B* **2016**, *94*, 195410.
- (18) Jeon, Y.; Min, H.; Kim, D.; Oh-e, M. Determination of the Crystalline X-Axis of Quartz by Second-Harmonic Phase Measurement. *Journal of the Korean Physical Society* **2005**, *46*.
- (19) Yang, W.-C.; Hore, D. K. Determining the Orientation of Chemical Functional Groups on Metal Surfaces by a Combination of Homodyne and Heterodyne Non-linear Vibrational Spectroscopy. *J. Phys. Chem. C* **2017**, *121*, 28043–28050.
- (20) Boamah, M. D.; Isheim, D.; Geiger, F. M. Dendritic Oxide Growth in Zerovalent Iron Nanofilms Revealed by Atom Probe Tomography. *J. Phys. Chem. C* **2018**, *122*, 28225–28232.
- (21) Chang, H.; Ohno, P. E.; Liu, Y.; Lozier, E. H.; Dalchand, N.; Geiger, F. M. Direct Measurement of Charge Reversal on Lipid Bilayers Using Heterodyne-Detected Second Harmonic Generation Spectroscopy. *J. Phys. Chem. B* **2020**, *124*, 641–649.
- (22) Ma, E.; Geiger, F. M. Divalent Ion Specific Outcomes on Stern Layer Structure and Total Surface Potential at the Silica:Water Interface. *J. Phys. Chem. A* **2021**, *125*, 10079–10088.
- (23) Geiger, F.; Speelman, R. Interfacial Water Flipping and Electrostatic Fields at the Electrode:Electrolyte Interface from Operando Nonlinear Optical Spectroscopy preprint.

### References for Chapter 3

- (1) Eyring, V.; Gillett, N. P.; Achutarao, K. M.; Barimalala, R.; Barreiro Parrillo, M.; Bellouin, N.; Cassou, C.; Durack, P. J.; Kosaka, Y.; McGregor, S.; Min, S.-K.; Morgenstern, O.; Sun, Y. In *Climate Change 2021: The Physical Science Basis. Contribution of Working Group I to the Sixth Assessment Report of the Intergovernmental Panel on Climate Change*, Masson-Delmotte, V. et al., Eds.; Cambridge University Press: Cambridge, United Kingdom and New York, NY, USA, 2021, pp 423–552.
- (2) Lee, J.-Y.; Marotzke, J.; Bala, G.; Cao, L.; Corti, S.; Dunne, J. P.; Engelbrecht, F.; Fischer, E.; Fyfe, J. C.; Jones, C.; Maycock, A.; Mutemi, J.; Ndiaye, O.; Panickal, S.; Zhou, T. In *Climate Change 2021: The Physical Science Basis. Contribution of Working Group I to the Sixth Assessment Report of the Intergovernmental Panel on Climate Change*, Masson-Delmotte, V. et al., Eds.; Cambridge University Press: Cambridge, United Kingdom and New York, NY, USA, 2021, pp 553–672.
- (3) Canadell, J. G. et al. In *Climate Change 2021: The Physical Science Basis. Contribution of Working Group I to the Sixth Assessment Report of the Intergovernmental Panel on Climate Change*, Masson-Delmotte, V. et al., Eds.; Cambridge University Press: Cambridge, United Kingdom and New York, NY, USA, 2021, pp 673–816.
- (4) Gilmore, E. A.; Ghosh, M.; Johnston, P.; Siddiqui, M.-S.; Macaluso, N. Modeling the Energy Mix and Economic Costs of Deep Decarbonization Scenarios in a CGE Framework. *Energy and Climate Change* **2023**, *4*, 100106.
- (5) IEA *Global Energy Review: CO<sub>2</sub> Emissions in 2021*; Paris: IEA, 2022.

- (6) Alam, M. M.; Aktar, M. A.; Idris, N. D. M.; Al-Amin, A. Q. World Energy Economics and Geopolitics amid COVID-19 and Post-COVID-19 Policy Direction. *World Development Sustainability* **2023**, *2*, 100048.
- (7) Jacobson, M. Z.; Delucchi, M. A. Providing All Global Energy with Wind, Water, and Solar Power, Part I: Technologies, Energy Resources, Quantities and Areas of Infrastructure, and Materials. *Energy Policy* **2011**, *39*, 1154–1169.
- (8) Bane, J. M.; He, R.; Muglia, M.; Lowcher, C. F.; Gong, Y.; Haines, S. M. Marine Hydrokinetic Energy from Western Boundary Currents. *Annual Review of Marine Science* **2017**, *9*, 105–123.
- (9) Azrulhisham, E. A.; Jamaluddin, Z. Z.; Azri, M. A.; Yusoff, S. B. M. Potential Evaluation of Vertical Axis Hydrokinetic Turbine Implementation in Equatorial River. *J. Phys.: Conf. Ser.* **2018**, *1072*, 012002.
- (10) Septyaningrum, E.; Hantoro, R.; Utama, I. K. a. P.; Prananda, J.; Nugroho, G.; Mahmasani, A. W.; Satwika, N. A. Performance Analysis of Multi-Row Vertical Axis Hydrokinetic Turbine–Straight Blade Cascaded (VAHT-SBC) Turbines Array. *Journal of Mechanical Engineering and Sciences* **2019**, *13*, 5665–5688.
- (11) Tampier, G.; Troncoso, C.; Zilic, F. Numerical Analysis of a Diffuser-Augmented Hydrokinetic Turbine. *Ocean Engineering* **2017**, *145*, 138–147.
- (12) Dhiman, P.; Yavari, F.; Mi, X.; Gullapalli, H.; Shi, Y.; Ajayan, P. M.; Koratkar, N. Harvesting Energy from Water Flow over Graphene. *Nano Lett.* **2011**, *11*, 3123–3127.
- (13) Yin, J.; Zhang, Z.; Li, X.; Zhou, J.; Guo, W. Harvesting Energy from Water Flow over Graphene? *Nano Lett.* **2012**, *12*, 1736–1741.

- (14) Zhong, H.; Li, X.; Wu, Z.; Zhang, S.; Xu, Z.; Chen, H.; Lin, S. Two Dimensional Graphene Nanogenerator by Coulomb Dragging: Moving van Der Waals Heterostructure. *Applied Physics Letters* **2015**, *106*, 243903.
- (15) Ho Lee, S.; Jung, Y.; Kim, S.; Han, C.-S. Flow-Induced Voltage Generation in Non-Ionic Liquids over Monolayer Graphene. *Applied Physics Letters* **2013**, *102*, 063116.
- (16) Yin, J.; Zhang, Z.; Li, X.; Yu, J.; Zhou, J.; Chen, Y.; Guo, W. Waving Potential in Graphene. *Nat Commun* **2014**, *5*, 3582.
- (17) Yin, J.; Li, X.; Yu, J.; Zhang, Z.; Zhou, J.; Guo, W. Generating Electricity by Moving a Droplet of Ionic Liquid along Graphene. *Nature Nanotech* **2014**, *9*, 378–383.
- (18) Zhong, H.; Xia, J.; Wang, F.; Chen, H.; Wu, H.; Lin, S. Graphene-Piezoelectric Material Heterostructure for Harvesting Energy from Water Flow. *Advanced Functional Materials* **2017**, *27*, 1604226.
- (19) Kwak, S. S.; Lin, S.; Lee, J. H.; Ryu, H.; Kim, T. Y.; Zhong, H.; Chen, H.; Kim, S.-W. Triboelectrification-Induced Large Electric Power Generation from a Single Moving Droplet on Graphene/Polytetrafluoroethylene. *ACS Nano* **2016**, *10*, 7297–7302.
- (20) Ghosh, S.; Sood, A. K.; Kumar, N. Carbon Nanotube Flow Sensors. *Science* **2003**, *299*, 1042–1044.
- (21) Kim, S. H. et al. Harvesting Electrical Energy from Carbon Nanotube Yarn Twist. *Science* **2017**, *357*, 773–778.

- (22) Xu, Y.; Chen, P.; Zhang, J.; Xie, S.; Wan, F.; Deng, J.; Cheng, X.; Hu, Y.; Liao, M.; Wang, B.; Sun, X.; Peng, H. A One-Dimensional Fluidic Nanogenerator with a High Power Conversion Efficiency. *Angewandte Chemie International Edition* **2017**, *56*, 12940–12945.
- (23) Yuan, Q.; Zhao, Y.-P. Hydroelectric Voltage Generation Based on Water-Filled Single-Walled Carbon Nanotubes. *J. Am. Chem. Soc.* **2009**, *131*, 6374–6376.
- (24) Kumar Arun, R.; Singh, P.; Biswas, G.; Chanda, N.; Chakraborty, S. Energy Generation from Water Flow over a Reduced Graphene Oxide Surface in a Paper–Pencil Device. *Lab on a Chip* **2016**, *16*, 3589–3596.
- (25) Li, W.; Zhang, Y.; Liu, L.; Li, D.; Liao, L.; Pan, C. A High Energy Output Nanogenerator Based on Reduced Graphene Oxide. *Nanoscale* **2015**, *7*, 18147–18151.
- (26) Zhao, F.; Cheng, H.; Zhang, Z.; Jiang, L.; Qu, L. Direct Power Generation from a Graphene Oxide Film under Moisture. *Advanced Materials* **2015**, *27*, 4351–4357.
- (27) Zhao, F.; Liang, Y.; Cheng, H.; Jiang, L.; Qu, L. Highly Efficient Moisture-Enabled Electricity Generation from Graphene Oxide Frameworks. *Energy & Environmental Science* **2016**, *9*, 912–916.
- (28) Vu, D. L.; Vo, C. P.; Le, C. D.; Ahn, K. K. Enhancing the Output Performance of Fluid-Based Triboelectric Nanogenerator by Using Poly(Vinylidene Fluoride-Co-Hexafluoropropylene)/Ionic Liquid Nanoporous Membrane. *International Journal of Energy Research* **2021**, *45*, 8960–8970.
- (29) Jing, Z.; Zhang, J.; Wang, J.; Zhu, M.; Wang, X.; Cheng, T.; Zhu, J.; Wang, Z. L. 3D Fully-Enclosed Triboelectric Nanogenerator with Bionic Fish-like Structure for Harvesting Hydrokinetic Energy. *Nano Res.* **2022**, *15*, 5098–5104.

- (30) Ahmed, A. Self-Powered Wireless Sensing Platform for Monitoring Marine Life Based on Harvesting Hydrokinetic Energy of Water Currents. *J. Mater. Chem. A* **2022**, *10*, 1992–1998.
- (31) Su, Y.; Chen, G.; Chen, C.; Gong, Q.; Xie, G.; Yao, M.; Tai, H.; Jiang, Y.; Chen, J. Self-Powered Respiration Monitoring Enabled By a Triboelectric Nanogenerator. *Advanced Materials* **2021**, *33*, 2101262.
- (32) Zhang, S.; Bick, M.; Xiao, X.; Chen, G.; Nashalian, A.; Chen, J. Leveraging Triboelectric Nanogenerators for Bioengineering. *Matter* **2021**, *4*, 845–887.
- (33) Khandelwal, G.; Dahiya, R. Self-Powered Active Sensing Based on Triboelectric Generators. *Advanced Materials* **2022**, *34*, 2200724.
- (34) Guan, X.; Xu, B.; Wu, M.; Jing, T.; Yang, Y.; Gao, Y. Breathable, Washable and Wearable Woven-Structured Triboelectric Nanogenerators Utilizing Electrospun Nanofibers for Biomechanical Energy Harvesting and Self-Powered Sensing. *Nano Energy* **2021**, *80*, 105549.
- (35) Jin, L.; Xiao, X.; Deng, W.; Nashalian, A.; He, D.; Raveendran, V.; Yan, C.; Su, H.; Chu, X.; Yang, T.; Li, W.; Yang, W.; Chen, J. Manipulating Relative Permittivity for High-Performance Wearable Triboelectric Nanogenerators. *Nano Lett.* **2020**, *20*, 6404–6411.
- (36) Chen, J.; Wang, Z. L. Reviving Vibration Energy Harvesting and Self-Powered Sensing by a Triboelectric Nanogenerator. *Joule* **2017**, *1*, 480–521.
- (37) He, Y.; Lao, J.; Yang, T.; Li, X.; Zang, X.; Li, X.; Zhu, M.; Chen, Q.; Zhong, M.; Zhu, H. Galvanism of Continuous Ionic Liquid Flow over Graphene Grids. *Applied Physics Letters* **2015**, *107*, 081605.

- (38) Wang, Z. L. On the First Principle Theory of Nanogenerators from Maxwell's Equations. *Nano Energy* **2020**, *68*, 104272.
- (39) Zhang, R.; Olin, H. Advances in Inorganic Nanomaterials for Triboelectric Nanogenerators. *ACS Nanosci. Au* **2022**, *2*, 12–31.
- (40) Aji, A. S.; Nishi, R.; Ago, H.; Ohno, Y. High Output Voltage Generation of over 5 V from Liquid Motion on Single-Layer MoS<sub>2</sub>. *Nano Energy* **2020**, *68*, 104370.
- (41) Li, X.; Shen, C.; Wang, Q.; Luk, C. M.; Li, B.; Yin, J.; Lau, S. P.; Guo, W. Hydroelectric Generator from Transparent Flexible Zinc Oxide Nanofilms. *Nano Energy* **2017**, *32*, 125–129.
- (42) Park, J.; Song, S.; Yang, Y.; Kwon, S.-H.; Sim, E.; Kim, Y. S. Identification of Droplet-Flow-Induced Electric Energy on Electrolyte–Insulator–Semiconductor Structure. *J. Am. Chem. Soc.* **2017**, *139*, 10968–10971.
- (43) Boamah, M. D.; Lozier, E. H.; Kim, J.; Ohno, P. E.; Walker, C. E.; Miller, T. F.; Geiger, F. M. Energy Conversion via Metal Nanolayers. *Proceedings of the National Academy of Sciences* **2019**, *116*, 16210–16215.
- (44) Faurie-Wisniewski, D.; Geiger, F. M. Synthesis and Characterization of Chemically Pure Nanometer-Thin Zero-Valent Iron Films and Their Surfaces. *J. Phys. Chem. C* **2014**, *118*, 23256–23263.
- (45) Boamah, M. D.; Isheim, D.; Geiger, F. M. Dendritic Oxide Growth in Zerovalent Iron Nanofilms Revealed by Atom Probe Tomography. *J. Phys. Chem. C* **2018**, *122*, 28225–28232.

- (46) Greczynski, G.; Hultman, L. C 1s Peak of Adventitious Carbon Aligns to the Vacuum Level: Dire Consequences for Material's Bonding Assignment by Photoelectron Spectroscopy. *Chemphyschem* **2017**, *18*, 1507–1512.
- (47) Greczynski, G.; Hultman, L. The Same Chemical State of Carbon Gives Rise to Two Peaks in X-ray Photoelectron Spectroscopy. *Sci Rep* **2021**, *11*, 11195.
- (48) Biesinger, M. C. Accessing the Robustness of Adventitious Carbon for Charge Referencing (Correction) Purposes in XPS Analysis: Insights from a Multi-User Facility Data Review. *Applied Surface Science* **2022**, *597*, 153681.
- (49) Piao, H.; McIntyre, N. S. Adventitious Carbon Growth on Aluminium and Gold–Aluminium Alloy Surfaces. *Surface and Interface Analysis* **2002**, *33*, 591–594.
- (50) Miller, D. J.; Biesinger, M. C.; McIntyre, N. S. Interactions of CO<sub>2</sub> and CO at Fractional Atmosphere Pressures with Iron and Iron Oxide Surfaces: One Possible Mechanism for Surface Contamination? *Surface and Interface Analysis* **2002**, *33*, 299–305.
- (51) Yanina, S. V.; Rosso, K. M. Linked Reactivity at Mineral-Water Interfaces Through Bulk Crystal Conduction. *Science* **2008**, *320*, 218–222.
- (52) Park, H.-W.; Huynh, N. D.; Kim, W.; Lee, C.; Nam, Y.; Lee, S.; Chung, K.-B.; Choi, D. Electron Blocking Layer-Based Interfacial Design for Highly-Enhanced Triboelectric Nanogenerators. *Nano Energy* **2018**, *50*, 9–15.

### References for Chapter 4

- (1) Bañuelos, J. L. et al. Oxide– and Silicate–Water Interfaces and Their Roles in Technology and the Environment. *Chem. Rev.* **2023**, DOI: 10.1021/acs.chemrev.2c00130.
- (2) Kibel, M. H. In *Surface Analysis Methods in Materials Science*, O'Connor, D. J., Sexton, B. A., Smart, R. S. C., Eds.; Springer Series in Surface Sciences; Springer: Berlin, Heidelberg, 2003, pp 175–201.
- (3) Turner, P. S.; Nockolds, C. E.; Bulcock, S. In *Surface Analysis Methods in Materials Science*, O'Connor, D. J., Sexton, B. A., Smart, R. S. C., Eds.; Springer Series in Surface Sciences; Springer: Berlin, Heidelberg, 2003, pp 85–105.
- (4) MacDonald, R. J.; King, B. V. In *Surface Analysis Methods in Materials Science*, O'Connor, D. J., Sexton, B. A., Smart, R. S. C., Eds.; Springer Series in Surface Sciences; Springer: Berlin, Heidelberg, 2003, pp 127–154.
- (5) Dastoor, P. C. In *Surface Analysis Methods in Materials Science*, O'Connor, D. J., Sexton, B. A., Smart, R. S. C., Eds.; Springer Series in Surface Sciences; Springer: Berlin, Heidelberg, 2003, pp 155–174.
- (6) Abrams, I. M.; McBain, J. W. A Closed Cell for Electron Microscopy. *Journal of Applied Physics* **1944**, *15*, 607–609.
- (7) Klauber, C. In *Surface Analysis Methods in Materials Science*, O'Connor, D. J., Sexton, B. A., Smart, R. S. C., Eds.; Springer Series in Surface Sciences; Springer: Berlin, Heidelberg, 2003, pp 71–81.
- (8) Subir, M.; Rao, Y., *Environmental Interfacial Spectroscopy*; American Chemical Society: 2022; 331 pp.

- (9) Covert, P. A.; Hore, D. K. Assessing the Gold Standard: The Complex Vibrational Nonlinear Susceptibility of Metals. *J. Phys. Chem. C* **2015**, *119*, 271–276.
- (10) Ong, S.; Zhao, X.; Eienthal, K. B. Polarization of Water Molecules at a Charged Interface: Second Harmonic Studies of the Silica/Water Interface. *Chemical Physics Letters* **1992**, *191*, 327–335.
- (11) Liljeblad, J. F. D.; Tyrode, E. Vibrational Sum Frequency Spectroscopy Studies at Solid/Liquid Interfaces: Influence of the Experimental Geometry in the Spectral Shape and Enhancement. *J. Phys. Chem. C* **2012**, *116*, 22893–22903.
- (12) Chang, H.; Ohno, P. E.; Liu, Y.; Lozier, E. H.; Dalchand, N.; Geiger, F. M. Direct Measurement of Charge Reversal on Lipid Bilayers Using Heterodyne-Detected Second Harmonic Generation Spectroscopy. *J. Phys. Chem. B* **2020**, *124*, 641–649.
- (13) Rehl, B.; Rashwan, M.; DeWalt-Kerian, E. L.; Jarisz, T. A.; Darlington, A. M.; Hore, D. K.; Gibbs, J. M. New Insights into (3) Measurements: Comparing Non-resonant Second Harmonic Generation and Resonant Sum Frequency Generation at the Silica/Aqueous Electrolyte Interface. *J. Phys. Chem. C* **2019**, *123*, 10991–11000.
- (14) Ohno, P. E.; Chang, H.; Spencer, A. P.; Liu, Y.; Boamah, M. D.; Wang, H.-f.; Geiger, F. M. Beyond the Gouy–Chapman Model with Heterodyne-Detected Second Harmonic Generation. *J. Phys. Chem. Lett.* **2019**, *10*, 2328–2334.
- (15) Ma, E.; Geiger, F. M. Divalent Ion Specific Outcomes on Stern Layer Structure and Total Surface Potential at the Silica:Water Interface. *J. Phys. Chem. A* **2021**, *125*, 10079–10088.

- (16) Mattiucci, N.; D'Aguanno, G.; Bloemer, M. J. Second Harmonic Generation from Metallo-Dielectric Multilayered Structures in the Plasmonic Regime. *Opt. Express, OE* **2010**, *18*, 23698–23710.
- (17) Lütgebaucks, C.; Gonella, G.; Roke, S. Optical Label-Free and Model-Free Probe of the Surface Potential of Nanoscale and Microscopic Objects in Aqueous Solution. *Phys. Rev. B* **2016**, *94*, 195410.
- (18) Ohno, P. E.; Saslow, S. A.; Wang, H.-f.; Geiger, F. M.; Eisenthal, K. B. Phase-Referenced Nonlinear Spectroscopy of the -Quartz/Water Interface. *Nat Commun* **2016**, *7*, 13587.
- (19) Abdelmonem, A.; Lützenkirchen, J.; Leisner, T. Probing Ice-Nucleation Processes on the Molecular Level Using Second Harmonic Generation Spectroscopy. *Atmospheric Measurement Techniques* **2015**, *8*, 3519–3526.
- (20) Jordan, D. S.; Hull, C. J.; Troiano, J. M.; Riha, S. C.; Martinson, A. B. F.; Rosso, K. M.; Geiger, F. M. Second Harmonic Generation Studies of Fe(II) Interactions with Hematite (-Fe<sub>2</sub>O<sub>3</sub>). *J. Phys. Chem. C* **2013**, *117*, 4040–4047.
- (21) Saslow Gomez, S. A.; Jordan, D. S.; Troiano, J. M.; Geiger, F. M. Uranyl Adsorption at the Muscovite (Mica)/Water Interface Studied by Second Harmonic Generation. *Environ. Sci. Technol.* **2012**, *46*, 11154–11161.
- (22) Ma, E.; Ohno, P. E.; Kim, J.; Liu, Y.; Lozier, E. H.; Miller, T. F. I.; Wang, H.-F.; Geiger, F. M. A New Imaginary Term in the Second-Order Nonlinear Susceptibility from Charged Interfaces. *J. Phys. Chem. Lett.* **2021**, *12*, 5649–5659.

- (23) Boamah, M. D.; Isheim, D.; Geiger, F. M. Dendritic Oxide Growth in Zerovalent Iron Nanofilms Revealed by Atom Probe Tomography. *J. Phys. Chem. C* **2018**, *122*, 28225–28232.
- (24) Wen, Y.-C.; Zha, S.; Liu, X.; Yang, S.; Guo, P.; Shi, G.; Fang, H.; Shen, Y. R.; Tian, C. Unveiling Microscopic Structures of Charged Water Interfaces by Surface-Specific Vibrational Spectroscopy. *Phys. Rev. Lett.* **2016**, *116*, 016101.
- (25) Gonella, G.; Lütgebaucks, C.; de Beer, A. G. F.; Roke, S. Second Harmonic and Sum-Frequency Generation from Aqueous Interfaces Is Modulated by Interference. *J. Phys. Chem. C* **2016**, *120*, 9165–9173.
- (26) Wang, H.-F. Sum Frequency Generation Vibrational Spectroscopy (SFG-VS) for Complex Molecular Surfaces and Interfaces: Spectral Lineshape Measurement and Analysis plus Some Controversial Issues. *Progress in Surface Science* **2016**, *91*, 155–182.
- (27) Okuno, M. (; Ishibashi, T.-a. ( Bulk-or-Interface Assignment of Heterodyne-Detected Chiral Vibrational Sum Frequency Generation Signal by Its Polarization Dependence. *The Journal of Chemical Physics* **2018**, *149*, 244703.
- (28) Wei, X.; Hong, S.-C.; Lvovsky, A. I.; Held, H.; Shen, Y. R. Evaluation of Surface vs Bulk Contributions in Sum-Frequency Vibrational Spectroscopy Using Reflection and Transmission Geometries. *J. Phys. Chem. B* **2000**, *104*, 3349–3354.
- (29) Yamaguchi, S. (; Shiratori, K. (; Morita, A. (; Tahara, T. ( Electric Quadrupole Contribution to the Nonresonant Background of Sum Frequency Generation at Air/Liquid Interfaces. *The Journal of Chemical Physics* **2011**, *134*, 184705.

- (30) Geiger, F.; Speelman, R. Interfacial Water Flipping and Electrostatic Fields at the Electrode:Electrolyte Interface from Operando Nonlinear Optical Spectroscopy preprint.

### References for Chapter 5

- (1) Tolod, K. R.; Hernández, S.; Quadrelli, E. A.; Russo, N. In *Studies in Surface Science and Catalysis*, Albonetti, S., Perathoner, S., Quadrelli, E. A., Eds.; Horizons in Sustainable Industrial Chemistry and Catalysis, Vol. 178; Elsevier: 2019, pp 65–84.
- (2) Williamson, M. A. In *Geochemistry*; Encyclopedia of Earth Science; Springer Netherlands: Dordrecht, 1998, pp 348–353.
- (3) Hans Wedepohl, K. The Composition of the Continental Crust. *Geochimica et Cosmochimica Acta* **1995**, *59*, 1217–1232.
- (4) Klein, C. Presidential Address To The Mineralogical Society Of America, Boston, November 6, 2001: Some Precambrian Banded Iron-Formations (BiIFs) From Around The World: Their Age, Geologic Setting, Mineralogy, Metamorphism, Geochemistry, And Origin. *American Mineralogist* **2005**, *90*, 1473–1499.
- (5) Nesse, W. D., *Introduction to Mineralogy*; Oxford University Press: 2017; 495 pp.
- (6) Schwertmann, U. In *Soil Color*; John Wiley & Sons, Ltd: 1993, pp 51–69.
- (7) Yapp, C. Rusty Relics of Earth History: Iron(III) Oxides, Isotopes, and Surficial Environments. *Annu. Rev. Earth Planet. Sci.* **2001**, *29*, 165–199.
- (8) Lin, Y.; Yuan, G.; Sheehan, S.; Zhou, S.; Wang, D. Hematite-Based Solar Water Splitting: Challenges and Opportunities. *Energy Environ. Sci.* **2011**, *4*, 4862–4869.
- (9) Tamirat, A. G.; Rick, J.; Dubale, A. A.; Su, W.-N.; Hwang, B.-J. Using Hematite for Photoelectrochemical Water Splitting: A Review of Current Progress and Challenges. *Nanoscale Horiz.* **2016**, *1*, 243–267.

- (10) Zandi, O.; Hamann, T. W. The Potential versus Current State of Water Splitting with Hematite. *Phys. Chem. Chem. Phys.* **2015**, *17*, 22485–22503.
- (11) Bora, D. K.; Braun, A.; Constable, E. C. “In Rust We Trust”. Hematite – the Prospective Inorganic Backbone for Artificial Photosynthesis. *Energy Environ. Sci.* **2013**, *6*, 407–425.
- (12) Shen, S.; Lindley, S. A.; Chen, X.; Zhang, J. Z. Hematite Heterostructures for Photoelectrochemical Water Splitting: Rational Materials Design and Charge Carrier Dynamics. *Energy Environ. Sci.* **2016**, *9*, 2744–2775.
- (13) Phuan, Y. W.; Ong, W.-J.; Chong, M. N.; Ocon, J. D. Prospects of Electrochemically Synthesized Hematite Photoanodes for Photoelectrochemical Water Splitting: A Review. *Journal of Photochemistry and Photobiology C: Photochemistry Reviews* **2017**, *33*, 54–82.
- (14) Tang, P.; Arbiol, J. Engineering Surface States of Hematite Based Photoanodes for Boosting Photoelectrochemical Water Splitting. *Nanoscale Horiz.* **2019**, *4*, 1256–1276.
- (15) Zhang, J.; Eslava, S. Understanding Charge Transfer, Defects and Surface States at Hematite Photoanodes. *Sustainable Energy Fuels* **2019**, *3*, 1351–1364.
- (16) Li, J.; Chen, H.; Triana, C. A.; Patzke, G. R. Hematite Photoanodes for Water Oxidation: Electronic Transitions, Carrier Dynamics, and Surface Energetics. *Angewandte Chemie International Edition* **2021**, *60*, 18380–18396.
- (17) Najaf, Z.; Nguyen, D. L. T.; Chae, S. Y.; Joo, O.-S.; Shah, A. U. H. A.; Vo, D.-V. N.; Nguyen, V.-H.; Le, Q. V.; Rahman, G. Recent Trends in Development of Hematite

- (-Fe<sub>2</sub>O<sub>3</sub>) as an Efficient Photoanode for Enhancement of Photoelectrochemical Hydrogen Production by Solar Water Splitting. *International Journal of Hydrogen Energy* **2021**, *46*, 23334–23357.
- (18) Gilbert, B.; Frandsen, C.; Maxey, E. R.; Sherman, D. M. Band-Gap Measurements of Bulk and Nanoscale Hematite by Soft x-Ray Spectroscopy. *Phys. Rev. B* **2009**, *79*, 035108.
- (19) Zhou, D.; Fan, K. Recent Strategies to Enhance the Efficiency of Hematite Photoanodes in Photoelectrochemical Water Splitting. *Chinese Journal of Catalysis* **2021**, *42*, 904–919.
- (20) Meijer, J. M.; Rossi, L. Preparation, Properties, and Applications of Magnetic Hematite Microparticles. *Soft Matter* **2021**, *17*, 2354–2368.
- (21) Ashraf, M.; Khan, I.; Usman, M.; Khan, A.; Shah, S. S.; Khan, A. Z.; Saeed, K.; Yaseen, M.; Ehsan, M. F.; Tahir, M. N.; Ullah, N. Hematite and Magnetite Nanostructures for Green and Sustainable Energy Harnessing and Environmental Pollution Control: A Review. *Chem. Res. Toxicol.* **2020**, *33*, 1292–1311.
- (22) Parkinson, G. S. Iron Oxide Surfaces. *Surface Science Reports* **2016**, *71*, 272–365.
- (23) Quast, K. B. A Review of Hematite Flotation Using 12-Carbon Chain Collectors. *Minerals Engineering* **2000**, *13*, 1361–1376.
- (24) Quast, K. Direct Measurement of Oleate Adsorption on Hematite and Its Consequences for Flotation. *Minerals Engineering* **2018**, *118*, 122–132.
- (25) Quast, K. Use of Conditioning Time to Investigate the Mechanisms of Interactions of Selected Fatty Acids on Hematite. Part 1: Literature Survey. *Minerals Engineering* **2015**, *79*, 295–300.

- (26) Luo, X.-m.; Yin, W.-z.; Wang, Y.-f.; Sun, C.-y.; Ma, Y.-q.; Liu, J. Effect and Mechanism of Dolomite with Different Size Fractions on Hematite Flotation Using Sodium Oleate as Collector. *J. Cent. South Univ.* **2016**, *23*, 529–534.
- (27) Fu, Y.-f.; Yin, W.-z.; Yang, B.; Li, C.; Zhu, Z.-l.; Li, D. Effect of Sodium Alginate on Reverse Flotation of Hematite and Its Mechanism. *Int J Miner Metall Mater* **2018**, *25*, 1113–1122.
- (28) Jiang, W.; Zhou, Y.; Zhang, Y. The Effect of New Modified Fatty Acid (CY-23) Collector on Chlorite/Hematite Separation. *Journal of Chemistry* **2018**, *2018*, e5380480.
- (29) Hao, H.; Li, L.; Yuan, Z.; Liu, J. pH-controlled Dispersion of Micro-Fine Siderite from Hematite and Quartz. *Powder Technology* **2018**, *339*, 710–716.
- (30) Nunna, V.; Suthers, S. P.; Pownceby, M. I.; Sparrow, G. J. Beneficiation Strategies for Removal of Silica and Alumina from Low-Grade Hematite-Goethite Iron Ores. *Mineral Processing and Extractive Metallurgy Review* **2022**, *43*, 1049–1067.
- (31) Barbier, A.; Stierle, A.; Kasper, N.; Guittet, M.-J.; Jupille, J. Surface Termination of Hematite at Environmental Oxygen Pressures: Experimental Surface Phase Diagram. *Phys. Rev. B* **2007**, *75*, 233406.
- (32) Tanwar, K. S.; Lo, C. S.; Eng, P. J.; Catalano, J. G.; Walko, D. A.; Brown, G. E.; Waychunas, G. A.; Chaka, A. M.; Trainor, T. P. Surface Diffraction Study of the Hydrated Hematite Surface. *Surface Science* **2007**, *601*, 460–474.
- (33) Trainor, T. P.; Chaka, A. M.; Eng, P. J.; Newville, M.; Waychunas, G. A.; Catalano, J. G.; Brown, G. E. Structure and Reactivity of the Hydrated Hematite (0001) Surface. *Surface Science* **2004**, *573*, 204–224.

- (34) Lad, R. J.; Henrich, V. E. Structure of  $\alpha$ -Fe<sub>2</sub>O<sub>3</sub> Single Crystal Surfaces Following Ar<sup>+</sup> Ion Bombardment and Annealing in O<sub>2</sub>. *Surface Science* **1988**, *193*, 81–93.
- (35) Tanwar, K. S.; Catalano, J. G.; Petitto, S. C.; Ghose, S. K.; Eng, P. J.; Trainor, T. P. Hydrated  $\alpha$ -Fe<sub>2</sub>O<sub>3</sub>(11 $\bar{1}$ 0<sub>2</sub>) Surface Structure: Role of Surface Preparation. *Surface Science* **2007**, *601*, L59–L64.
- (36) Brendlé, E.; Dentzer, J.; Papirer, E. Variation of the Surface Properties of Hematite upon Heat Treatment Evidenced by Inverse Gas Chromatography and Temperature Programmed Desorption Techniques: Influence of Surface Impurities and Surface Reconstruction. *Journal of Colloid and Interface Science* **1998**, *199*, 63–76.
- (37) Glasscock, J.; Barnes, P.; Plumb, I.; Bendavid, A.; Martin, P. Structural, Optical and Electrical Properties of Undoped Polycrystalline Hematite Thin Films Produced Using Filtered Arc Deposition. *Thin Solid Films* **2008**, *516*, 1716–1724.
- (38) Waychunas, G. A.; Kim, C. S.; Banfield, J. F. Nanoparticulate Iron Oxide Minerals in Soils and Sediments: Unique Properties and Contaminant Scavenging Mechanisms. *J Nanopart Res* **2005**, *7*, 409–433.
- (39) Preočanin, T.; Čop, A.; Kallay, N. Surface Potential of Hematite in Aqueous Electrolyte Solution: Hysteresis and Equilibration at the Interface. *Journal of Colloid and Interface Science* **2006**, *299*, 772–776.
- (40) Preočanin, T.; Stipić, F.; Selmani, A.; Kallay, N. Surface Potential of Polycrystalline Hematite in Aqueous Medium. *International Journal of Electrochemistry* **2011**, *2011*, e412731.
- (41) Hayes, D.; Hadt, R. G.; Emery, J. D.; Cordones, A. A.; Martinson, A. B. F.; Shelby, M. L.; Fransted, K. A.; Dahlberg, P. D.; Hong, J.; Zhang, X.; Kong, Q.; Schoenlein,

- R. W.; Chen, L. X. Electronic and Nuclear Contributions to Time-Resolved Optical and X-ray Absorption Spectra of Hematite and Insights into Photoelectrochemical Performance. *Energy Environ. Sci.* **2016**, *9*, 3754–3769.
- (42) Sun, S.-W.; Wu, S.-H.; Meng, Z.-H.; Zhang, X.-C.; Wang, S.-J.; Wang, X.-M.; Liu, Y.; Ren, H.-T.; Jia, S.-Y.; Yao, K.-X.; Bai, H.; Han, X. Hydroperoxo [Fe(III)-OOH] and Ferryl-Oxo [Fe(IV)=O] Oxidative Species Involved in As(III) Oxidation Catalyzed by Pyrite under Alkaline Conditions. *Chemical Geology* **2020**, *538*, 119480.
- (43) Otte, K.; Schmahl, W. W.; Pentcheva, R. Density Functional Theory Study of Water Adsorption on FeOOH Surfaces. *Surface Science* **2012**, *606*, 1623–1632.
- (44) Martinson, A. B. F.; DeVries, M. J.; Libera, J. A.; Christensen, S. T.; Hupp, J. T.; Pellin, M. J.; Elam, J. W. Atomic Layer Deposition of Fe<sub>2</sub>O<sub>3</sub> Using Ferrocene and Ozone. *J. Phys. Chem. C* **2011**, *115*, 4333–4339.
- (45) Jordan, D. S.; Hull, C. J.; Troiano, J. M.; Riha, S. C.; Martinson, A. B. F.; Rosso, K. M.; Geiger, F. M. Second Harmonic Generation Studies of Fe(II) Interactions with Hematite (-Fe<sub>2</sub>O<sub>3</sub>). *J. Phys. Chem. C* **2013**, *117*, 4040–4047.
- (46) Schwertmann, U.; Taylor, R. In *Minerals in Soil Environments*; John Wiley & Sons, Ltd: 1989, pp 379–438.
- (47) Boily, J.-F.; Shchukarev, A. X-Ray Photoelectron Spectroscopy of Fast-Frozen Hematite Colloids in Aqueous Solutions. 2. Tracing the Relationship between Surface Charge and Electrolyte Adsorption. *J. Phys. Chem. C* **2010**, *114*, 2613–2616.
- (48) Kumagai, R.; Hatakeyama, A. Light-Induced Atom Desorption from Glass Surfaces Characterized by X-ray Photoelectron Spectroscopy. *Appl. Phys. B* **2016**, *122*, 186.

- (49) Idriss, H. On the Wrong Assignment of the XPS O1s Signal at 531–532 eV Attributed to Oxygen Vacancies in Photo- and Electro-Catalysts for Water Splitting and Other Materials Applications. *Surface Science* **2021**, *712*, 121894.
- (50) Covert, P. A.; Hore, D. K. Assessing the Gold Standard: The Complex Vibrational Nonlinear Susceptibility of Metals. *J. Phys. Chem. C* **2015**, *119*, 271–276.
- (51) Henderson, M. A.; Joyce, S. A.; Rustad, J. R. Interaction of Water with the (1×1) and (2×1) Surfaces of -Fe<sub>2</sub>O<sub>3</sub>(012). *Surface Science* **1998**, *417*, 66–81.
- (52) Gautier-Soyer, M.; Pollak, M.; Henriot, M.; Guittet, M. J. The (1 × 2) Reconstruction of the -Fe<sub>2</sub>O<sub>3</sub> (1012) Surface. *Surface Science* **1996**, *352–354*, 112–116.
- (53) Henderson, M. A. Insights into the (1×1)-to-(2×1) Phase Transition of the -Fe<sub>2</sub>O<sub>3</sub>(012) Surface Using EELS, LEED and Water TPD. *Surface Science* **2002**, *515*, 253–262.
- (54) Yanina, S. V.; Rosso, K. M. Linked Reactivity at Mineral-Water Interfaces Through Bulk Crystal Conduction. *Science* **2008**, *320*, 218–222.
- (55) Klahr, B.; Gimenez, S.; Fabregat-Santiago, F.; Hamann, T.; Bisquert, J. Water Oxidation at Hematite Photoelectrodes: The Role of Surface States. *J. Am. Chem. Soc.* **2012**, *134*, 4294–4302.
- (56) Klahr, B. M.; Martinson, A. B. F.; Hamann, T. W. Photoelectrochemical Investigation of Ultrathin Film Iron Oxide Solar Cells Prepared by Atomic Layer Deposition. *Langmuir* **2011**, *27*, 461–468.
- (57) Chatman, S.; Zarzycki, P.; M. Rosso, K. Surface Potentials of (001), (012), (113) Hematite (-Fe<sub>2</sub>O<sub>3</sub>) Crystal Faces in Aqueous Solution. *Physical Chemistry Chemical Physics* **2013**, *15*, 13911–13921.

- (58) Lützenkirchen, J.; Heberling, F.; Supljika, F.; Preocanin, T.; Kallay, N.; Johann, F.; Weisser, L.; Eng, P. J. Structure–Charge Relationship – the Case of Hematite (001). *Faraday Discuss.* **2015**, *180*, 55–79.
- (59) Gibbs-Davis, J. M.; Kruk, J. J.; Konek, C. T.; Scheidt, K. A.; Geiger, F. M. Jammed AcidBase Reactions at Interfaces. *J. Am. Chem. Soc.* **2008**, *130*, 15444–15447.
- (60) GUBSKAYA, A. V.; KUSALIK, P. G. The Multipole Polarizabilities and Hyperpolarizabilities of the Water Molecule in Liquid State: An Ab Initio Study. *Molecular Physics* **2001**, *99*, 1107–1120.
- (61) Chang, H.; Lozier, E. H.; Ma, E.; Geiger, F. M. Ion Specific Adsorption at Silica:Water Interfaces Probed with Heterodyne-Detected Second Harmonic Generation: From the Alkali Chlorides to CTAB, PFOA, and PFAS, Submitted. 2023.
- (62) Geiger, F.; Speelman, R. Interfacial Water Flipping and Electrostatic Fields at the Electrode:Electrolyte Interface from Operando Nonlinear Optical Spectroscopy preprint.

## APPENDIX A

**Proof of Concept: HD-SHG on *c*-Cut Sapphire Optical Windows**

The methods laid out in Chapter 4 primarily serve as a how-to guide for studying solids in the form of thin films coated on IR-grade fused silica optical flats. However, there is added flexibility in enabling the interrogation of sample substrates machined entirely from the solid of interest, particularly if the thin-film form of the material is unstable or not yet accessible by common deposition techniques. The case of sapphire, also known as corundum or by its chemical formula,  $\text{Al}_2\text{O}_3$ , is illustrative of this phenomenon. This appendix will expand on why the interfacial properties of sapphire are worth studying, why thin films of amorphous  $\text{Al}_2\text{O}_3$  are not ideal for studies under aqueous conditions, and finally a proof-of-concept of how the methods of Chapter 4 may be applied to optical flats composed of *c*-cut sapphire.

**A.1. Background**

Sapphire is a hexagonal (trigonal) mineral of exceptional hardness that is both naturally-occurring and commercially significant.<sup>1</sup> Often found in igneous rocks with very high purity, even trace amounts of dopants such as titanium (Ti), chromium (Cr), and iron ( $\text{Fe}^{2+}$  and  $\text{Fe}^{3+}$ ) can result in varieties of sapphire that are blue, red, and yellow-green, respectively.<sup>1,2</sup>

Due to sapphire's physical and optical properties, it perennially finds use in technologies as wide-ranging as abrasives,<sup>1</sup> LED substrates,<sup>3</sup> optical gratings,<sup>4</sup> transparent

capillary needles for laser-based therapies,<sup>5</sup> optical windows for aerospace applications,<sup>6</sup> and even the fs-pulsed Ti:sapphire lasers that sustain the field of nonlinear optical spectroscopy to which this thesis is contributing.<sup>7</sup> Many of these applications involve exposure of sapphire crystals to air, moisture, and even full submersion in water, making an understanding of the properties of the charged sapphire:aqueous interface critical. For example, the performance of certain photovoltaics has been shown to be reduced by progressive corrosion of the Al<sub>2</sub>O<sub>3</sub>-encapsulated Al-doped zinc oxide (AZO) window layers by atmospheric aerosols under humid conditions.<sup>2,8</sup>

From a more fundamental perspective, sapphire provides an important counterpoint to fused silica, particularly in the realm of pH-dependent studies of the solid:aqueous interface. Fused silica has a relatively low point of zero charge (PZC) around pH 2.3, constraining the range of acidities accessible for sub-PZC studies.<sup>9</sup> Sapphire, on the other hand, has a PZC around pH 5.7 on its *c*-plane (*i.e.* the (0001) surface), allowing access to a broader range of pH studies both above and below the PZC. For this reason, sapphire has been a substrate of choice in a number of SHG and SFG studies of the charged sapphire:aqueous interface.<sup>10–13</sup>

The use of thin-film deposition techniques such as atomic layer deposition (ALD) to obtain Al<sub>2</sub>O<sub>3</sub> samples has a few main drawbacks. To start, amorphous Al<sub>2</sub>O<sub>3</sub> films deposited by ALD have been demonstrated to dissolve<sup>14–18</sup> or hydrate<sup>15</sup> when exposed to aqueous conditions, complicating their use as a proxy for sapphire or other aluminum-containing minerals in environmental or industrial conditions. Although some reports indicate that post-deposition treatments such as plasma cleaning<sup>19</sup> or the use of thicker,

multilayer films<sup>20</sup> may improve long-term stability of ALD AlO<sub>3</sub> films to aqueous conditions, there is still considerable variability of response, in particular when dealing with systems containing electrolytes or other dissolved species. In addition, the thin films produced from the ALD process are amorphous, which removes any possibility of doing crystal-face-dependent studies—a significant drawback considering that certain interfacial properties such as the isoelectric point (IEP) have been shown to vary with the exposed crystal face as well as the degree of the initial miscut.<sup>21</sup>

Conversely, by using precision-machined optical windows of single-crystal sapphire, it is possible to access substrates with exposed faces corresponding to the *c*-, *m*-, *a*-, or *r*-planes of sapphire’s hexagonal (trigonal) unit cell. These substrates exhibit better stability to aqueous conditions than their thin-film counterparts. Past work in the group has employed hemispherical lenses machined from  $\alpha$ -Al<sub>2</sub>O<sub>3</sub> with the (1 $\bar{1}$ 02) plane aligned with the flat face in order to conduct homodyne SHG studies of hexavalent chromium’s surface interactions,<sup>22</sup> but such a sample geometry suffers the same drawbacks as fused silica hemispheres coated with ALD oxides, as outlined in Section 4.2.2. For these reasons, this appendix presents a proof-of-concept for the use of single-crystal *c*-cut Al<sub>2</sub>O<sub>3</sub> optical windows within the experimental framework put forth in Chapter 4.

## A.2. Experimental

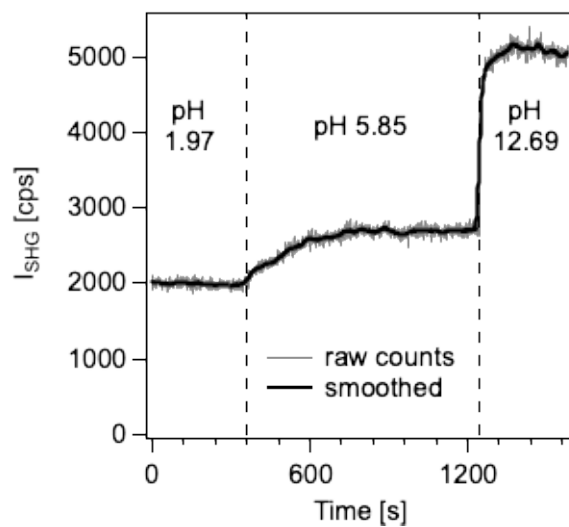
All results shown in this appendix were obtained using System 1, described in detail in Section 2.3.1. Flow experiments were conducted in a manner consistent with other results displayed throughout this thesis, as described in Section 2.4. Interference patterns were collected using a 10-mm step size and 5-point averaging—resulting in a single-scan

duration of roughly 2 min—and fit according to the framework described in Section 2.2. For the calculation of  $\chi_{eff}^{(2)}$  and  $\Phi(0)$ , we found that the value of  $\Delta k_z$  as determined for a fused silica optical window (*i.e.*  $2.5 \times 10^7 \text{ m}^{-1}$ ) also holds for a sapphire optical window, in spite of the higher refractive index of the latter material.

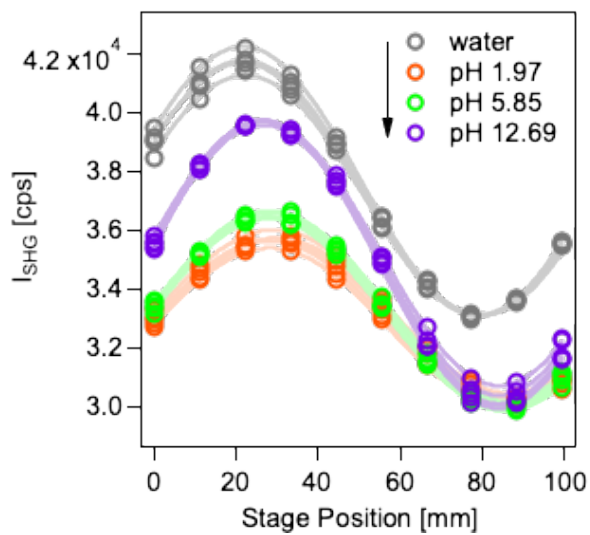
Sapphire substrate discs (Ted Pella, 16005-1040) with dimensions of  $25.4 \times 1.0 \text{ mm}$  were cleaned before use in our spectrometer following the cleaning protocol described in Section 2.4. Aqueous solutions of 1 M NaCl at pH values ranging between pH 2-13 were prepared following the method also described in Section 2.4. The sapphire substrates were determined to be *c*-cut ( $1^\circ$  miscut) by means of a high-resolution Laue X-ray camera (Photonic Science).

### A.3. Results

System 1 was used to perform combined homodyne and HD-SHG studies on a 1-mm-thick *c*-cut sapphire window (Figure A.1). The sapphire (0001) surface was first exposed to air-equilibrated ultrapure water (pH 5.74), and once steady state had been reached for  $I_{SHG}$  under low-flow (*i.e.*  $< 5 \text{ mL/min}$ ) conditions, a set of five replicate scans was performed. Next, homodyne  $I_{SHG}$  was recorded while introducing 1 M NaCl at pH 1.97. Again, once steady state had been reached, five replicate scans were collected. These steps were repeated for 1 M NaCl at pH 5.85, followed by 1 M NaCl at pH 12.69. Homodyne results indicate minimum counts at pH 1.97, followed by a 134% increase at pH 5.85, and a subsequent 255% increase (relative to  $I_{SHG}$  at pH 1.97). The progressive increase in  $I_{SHG}$  in the alkalimetric direction corresponds to an increasing SHG E-field and more ordering of molecules at the interface. This result is in agreement with literature reports



(a)



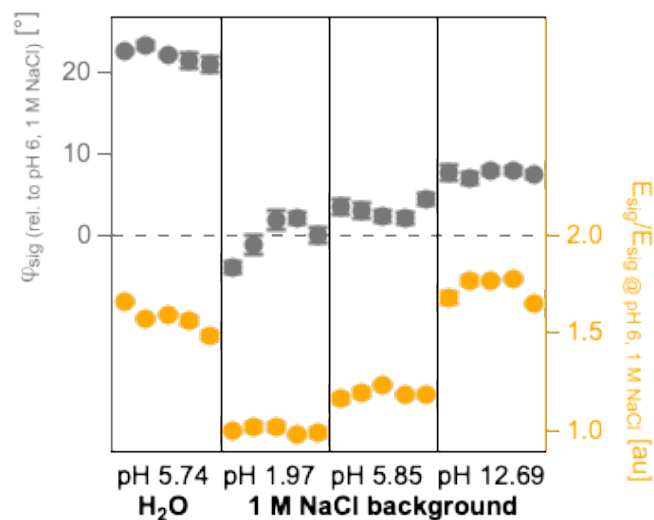
(b)

Figure A.1. A combined homodyne and HD-SHG study in which a *c*-cut sapphire 1-mm-thick optical window, was exposed in sequence to ultrapure water, and then 1 M NaCl solutions at pH 2, 6, and 13. The results include (a) raw  $I_{SHG}$  as a function of lab time and (b) replicate interference patterns collected at each solution condition and fit to Eq. 2.2.1.

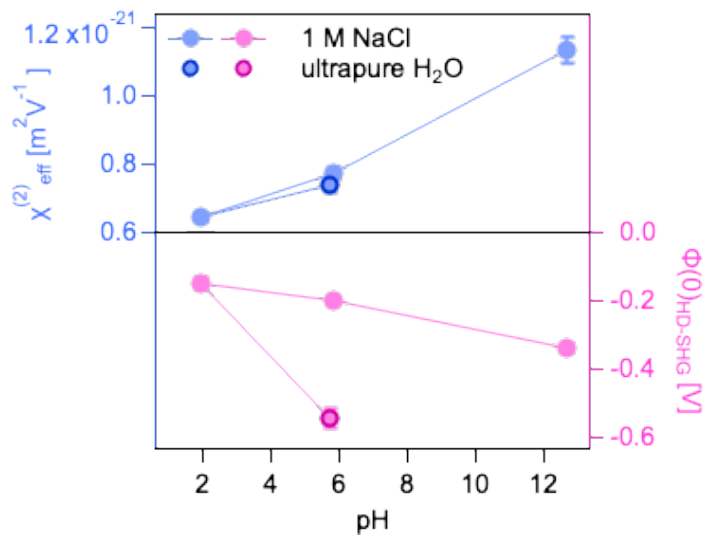
on the surface chemistry of sapphire's  $c$ -plane, and is further supported by the HD-SHG results from the same experiment.

Interference patterns taken at each solution condition show the most dramatic relative shift in  $\varphi_{sig}$  and  $Ei_{sig}$  (Figure A.2a) switching from ultrapure water to 1 M NaCl at pH 1.97. The  $-20^\circ$  phase shift and over 1.5-fold decrease in amplitude carry through to a change in  $\Phi(0)$  of roughly 400 mV (Figure A.2b). The change in  $\chi_{eff}^{(2)}$ , on the other hand, is minimal between the ultrapure water and 1 M NaCl at pH 1.97 conditions. This quantitative evidence of a transition of the  $c$ -cut sapphire:water interface from highly charged to minimally charged complements the homodyne results presented above, without the need for any model of interfacial potential.

During the pH titration portion of the experiment, changes in  $\Phi(0)$  are much smaller—on the order of 50-100 mV—whereas  $\chi_{eff}^{(2)}$  undergoes a 1.75-fold increase between pH 1.97 and pH 12.69. The value of  $\chi_{eff}^{(2)}$  for 1 M NaCl at pH 5.69 is comparable to the value obtained for ultrapure water, although there is a difference of nearly 350 mV between the corresponding  $\Phi(0)$  values.



(a)



(b)

Figure A.2. The results of fitting the interference patterns shown in Figure A.1 (a) averaged values of  $\varphi_{sig}$  and  $E_{sig}$  referenced, or normalized, respectively, to the pH 6, 1 M NaCl condition and (b) calculated values of  $\chi_{eff}^{(2)}$  and  $\Phi(0)$ .

#### A.4. Summary and Future Directions

The theoretical framework described in Chapter 2 and the practical considerations laid out in Chapter 4 were applied to the case of a sample consisting of an optical flat composed entirely of *c*-cut sapphire rather than a fused silica or CaF<sub>2</sub> optical flat coated with a thin film of ALD Al<sub>2</sub>O<sub>3</sub>. We demonstrated the capability of our System 1 HD-SHG set-up to obtain homodyne and HD-SHG results within the course of a single pH-titration experiment on the *c*-cut sapphire:water interface, providing insight on the extent of interfacial charging over a range of pH values.

Future directions based on this work may include exploring specific ion effects at the *c*-cut sapphire:water interface, interrogating the responses of  $\chi_{eff}^{(2)}$  and  $\Phi(0)$  for pH titrations of different crystal faces of sapphire (*e.g.* the *m*-, *a*-, or *r*-planes), determining the effect of degree of miscut on surface charge density and  $\Phi(0)$ , and further generalizing the method to apply to a broader suite of amorphous or crystalline solids. Additionally, the  $\chi_{eff}^{(2)}$  and  $\Phi(0)$  results presented in the preceding section will be improved by the independent determination of the macroscopic Fresnel coefficients for sapphire's *c*-plane in order to obtain a more accurate C/R ratio.

## APPENDIX B

**Interaction of Perfluorooctanoic Acid (PFOA) and  
Perfluorooctane Sulfonic Acid (PFOS) with Fused  
Silica:Aqueous Interfaces**

**Portions of this chapter are reproduced in part:**

Chang, H.; Lozier, E. H.; Ma, E.; Geiger, F. M. Ion-Specific Effects Involving  
Monovalent Cations Observed by Heterodyne-Detected Second Harmonic Generation  
Spectroscopy. *Submitted.*

## B.1. Background

Perfluoroalkyl substances (PFAS) are a class of synthetic organic chemicals defined as containing at least one perfluorinated methyl or methylene carbon. By various estimates, the number of extant PFAS may range from the tens of thousands to the millions.<sup>1</sup> PFAS exhibit certain properties that have made them desirable for many commercial and industrial applications since the mid-20<sup>th</sup> century, including hydrophobicity, oil- and stain-resistance, and thermal and chemical stability. However, these same properties have the accompanying impact of making PFAS persistent in environmental settings and prone to bioaccumulation and biomagnification.

The potential hazards of PFAS exposure to human health are well-summarized in a number of recent literature reviews. Of note are associations between PFAS and adverse health outcomes, including endocrine disruption and altered fertility,<sup>2</sup> lower kidney functioning,<sup>3,4</sup> oxidative stress and immunosuppression,<sup>5</sup> and disrupted thyroid function and metabolic syndrome.<sup>4</sup> Due to these concerns, the use of legacy PFAS in consumer products has greatly decreased in the 21<sup>st</sup> century, although the emerging use of novel PFAS purported to be more biodegradable or less harmful to human health than their predecessors has allowed for the continued use of these chemicals while research and regulatory bodies catch up.

In spite of this, human exposure to PFAS can still occur through a variety of pathways, including physical contact, inhalation, and consumption. Physical contact with PFAS is facilitated through their presence in food packaging, cosmetics and personal care products, clothing, non-stick cookware, and cleaning products. Secondary exposure to PFAS can also happen due to the release of these compounds into environmental systems, where they

can enter drinking water reservoirs, as well as the fresh- and saltwater bodies near which humans live and recreate. Other applications of PFAS that contribute to environmental release and contamination include the disposal of PFAS-containing consumer products, as well as the outdoor use of paints, sealants, varnishes, pesticides, and fire-fighting foams that include these compounds.<sup>6</sup>

Previous work in the group has demonstrated the capability of homodyne SHG studies to investigate topics as wide-ranging as the kinetics and mobility of aqueous chromium species with quartz and functionalized fused silica surfaces as proxies for soil systems,<sup>7–11</sup> the interactions of agricultural antibiotics with fused silica surfaces,<sup>12–14</sup> and the disruption of supported lipid bilayers (SLBs) by metallic nanoparticles<sup>15–17</sup> and nickel ions.<sup>18</sup> Advances in conducting phase-sensitive, heterodyne-detected (HD) SHG studies have enabled further studies of the specific interactions of monovalent and divalent ions with fused silica surfaces,<sup>19,20</sup> as well as detecting unexpected charge reversal phenomena on SLBs—previously undetectable *via* homodyne detection alone.<sup>21</sup>

The use of SHG analysis to understand phenomena related to surfactants and surfactant-like species is also well-established, including the adsorption of methacrylate polymeric surfactants to the surfaces of colloidal microparticles,<sup>22</sup> rate of malachite green-butyl-1 and -octyl-1 transfer between emulsion particles,<sup>23</sup> orientation of 4-(4-dimethylaminostyryl)-octadecylpyridinium bromide molecules at the surface of a pendant water droplet,<sup>24</sup> and interaction of cetyltrimethylammonium with fused silica surfaces.<sup>25</sup> Based on these precedents, we determined that HD-SHG could serve as powerful tool for directly probing interfacial properties of select PFAS at model mineral:aqueous interfaces.

Since perfluorooctane sulfonic acid (PFOS), perfluorooctanoic acid (PFOA), perfluorononanoic acid (PFNA), and perfluorohexane sulfonate (PFHxS) have been identified as the PFAS contributing most to human exposure,<sup>26</sup> we opted to select our model surfactants from this group. We ultimately chose to focus this work on PFOA and PFOS because they are two of the most widely used legacy PFAS in commercial and industrial settings, with health advisory levels set by the United States Environmental Protection Agency (EPA).<sup>27</sup>

## B.2. Experimental

All results reported in this appendix were obtained using System 1 (see Section 2.3.1) in tandem with the flow set-up and protocol for flow experiments described in Section 2.4. Interference patterns were collected using a roughly 3.5-mm step size and 5-point averaging—resulting in a single-scan duration of slightly over 4 min—and fit according to the procedure outlined in Section 2.2. For the calculation of  $\chi_{eff}^{(2)}$  and  $\Phi(0)$ , we used the process described previously by our group for aqueous solutions in contact with a 25.4-mm-diameter fused silica hemisphere with no further changes.<sup>20</sup>

IR-grade fused silica hemispheres with a 25.4-mm diameter (Hyperion) were cleaned following the protocol described in Section 2.4.1 and used as the sample substrate in all results presented in this appendix. PFOA and PFOS were procured from Sigma Aldrich (171468, 95% and 77282,  $\geq 98.0\%$ ). Aqueous solutions of PFOA and PFOS at 10 ppm were prepared using ultrapure water (18.2 M $\Omega$ -cm, MilliporeSigma) and allowed to come to equilibrium with atmospheric CO<sub>2</sub> overnight preceding each experiment the following day. 10 ppm solutions of PFOA and PFOS had conductivities of 10.20  $\mu\text{S}/\text{cm}$  and 3.628  $\mu\text{S}/\text{cm}$

and measured acidities of pH 4.58 and pH 5.88, respectively. We note that 10 ppm is well below the critical micelle concentration (CMC) for both PFOA and PFOS (15,696 and 4,573 mg/L, respectively).<sup>28,29</sup> Stocks of pure water used in the course of flow experiments were also dispensed the night before and allowed to come to equilibrium with atmospheric CO<sub>2</sub> overnight, with a measured conductivity and acidity of 1.160  $\mu\text{S}/\text{cm}$  and pH 5.60.

### B.3. Results

We conducted on/off experiments by tracking  $I_{SHG}$  with homodyne detection (with the TDC and LO removed from the beam path) while alternating the liquid phase of the fused silica:aqueous interface between pure water and 10 ppm solutions of either PFOA or PFOS. After allowing at least 5 min for the SHG signal to stabilize with pure water in the flow cell, we replaced the TDC and LO and took five replicate interference patterns as described in the previous section. At the conclusion of scan collection, we removed the TDC and LO and resumed homodyne detection while transitioning flow to the 10 ppm of PFOA or PFOS. After 5 min, we once again replaced the TDC and LO and took five replicate interference patterns. We performed this cycle three times consecutively on the same sample and with the same solutions to assess the reversibility of the PFAS' interactions with the fused silica:aqueous interface, since the fused silica:aqueous interface has been demonstrated to exhibit significant hysteresis, particularly in response to pH changes.<sup>20,30</sup>

We present homodyne results for  $I_{SHG}$  in Figure B.1. Initially we observe only a minor decrease in intensity between water and the 10 ppm PFOA solution (<3%). Returning to water in the cell does not result in a reversal of this decrease, rather an additional decrease

in intensity is observed, this time closer to 5% relative to the first value of  $I_{SHG, PFOA}$ . Subsequent cycles, however, recreate the relationship of a lower observed intensity for pure water and a roughly 5% higher observed intensity for 10 ppm PFOA.

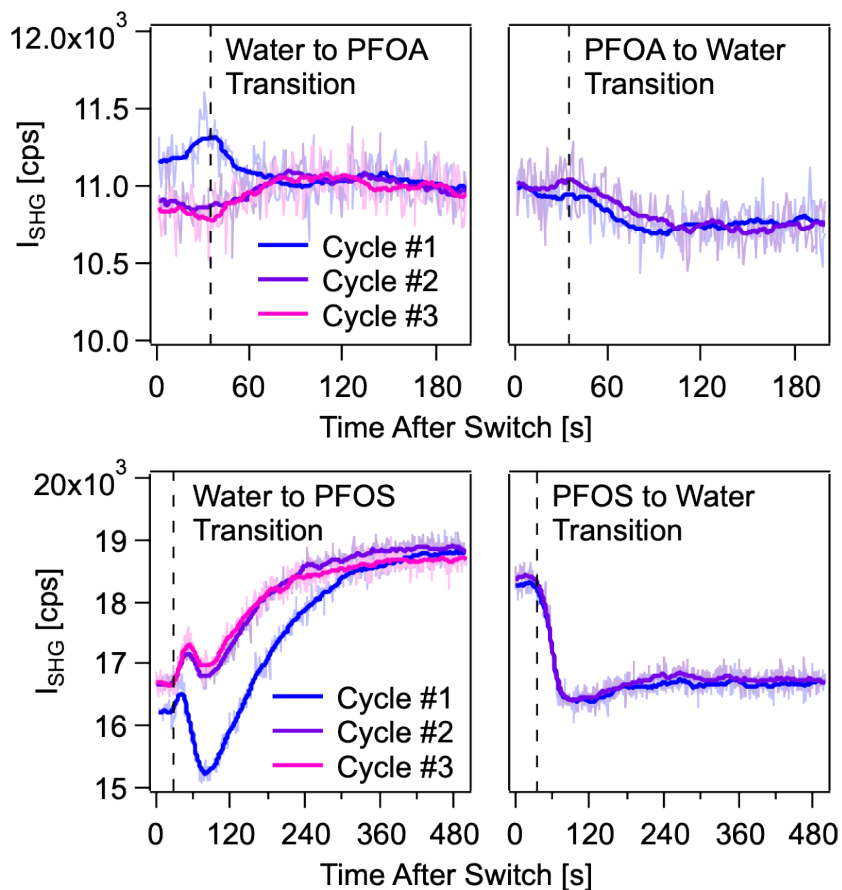


Figure B.1. Homodyne results for on/off reversibility experiments between pure water and 10 ppm PFOA (top two plots) and 10 ppm PFOS (bottom two plots). The leftmost plots show the transition from water to the respective PFAS, and the rightmost plots show the transition from the PFAS back to water. The vertical dashed lines denotes when the solution being introduced entered the flow cell.

Conversely, homodyne results for the same experiment with PFOS show more dramatic changes in relative intensity, with a  $>10\%$  observed increase in  $I_{SHG}$  between pure

water and 10 ppm PFOS. Similar to PFOA, the initial transition is not fully reversible, however we do not observe the same sign change in  $\Delta I_{SHG}$  between the first water-to-PFOS transition and subsequent ones, as we do with PFOA. Rather, the transition from water to PFOS always results in a relative increase in intensity, whereas the direction of this change for PFOA depends on whether it is the first or a subsequent transition. Further, we note that the changes in  $I_{SHG}$  cannot be explained simply by the pH changes occurring for the water-to-PFOA transition (pH 5.60 to 4.58) or the water-to-PFOS transition (pH 5.60 to 5.88). Indeed, if we take Eisenthal and coworkers' pH titration of the fused silica:aqueous interface by homodyne-detected SHG as our model,<sup>31</sup> we would expect to see exclusively a decrease in intensity for the water-to-PFOA transition and a relatively smaller increase in intensity for the water-to-PFOS transition. Additionally, while the transition from pure water to either 10 ppm PFOA or PFOS constitutes a 2- to 8-fold increase in solution conductivity, we do not see an overall decrease in  $I_{SHG}$  for either to water-to-PFOA or water-to-PFOS transitions, with the only exception being the very first water-to-PFOA transition.

Differences in the behavior of PFOA and PFOS near the fused silica:aqueous interface are also captured within the heterodyne results, for which we depict the raw scans in Figure B.2. For PFOA,  $\varphi_{sig}$  increases by  $3.5(6)^\circ$  for the first water-to-PFOA transition, and then increases an additional  $6.2(6)^\circ$  for the first PFOA-to-water transition (Figure B.3). The subsequent two cycles show a reversible  $\pm 7.6(6)^\circ$  phase shift between the two solution conditions. The amplitude is relatively more reversible, with an initial decrease of about 23% for the water-to-PFOA transition followed by a highly reversible  $\pm 19.1(7)\%$  relative change in  $E_{SHG}$  between the two solution conditions.

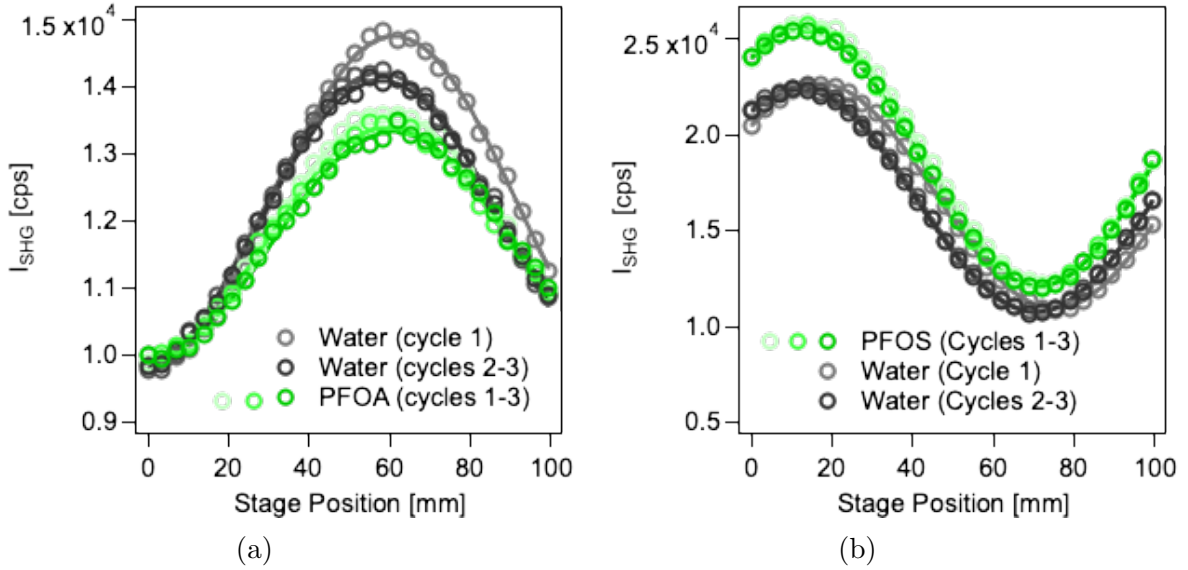
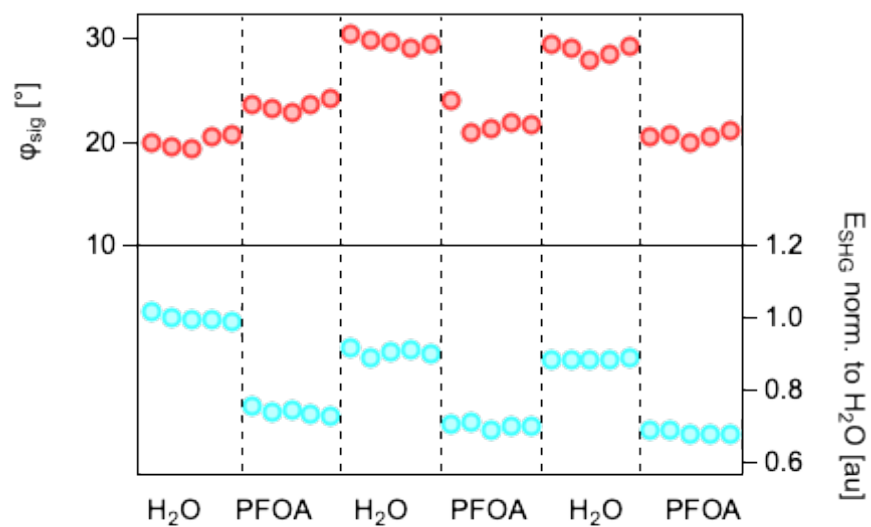


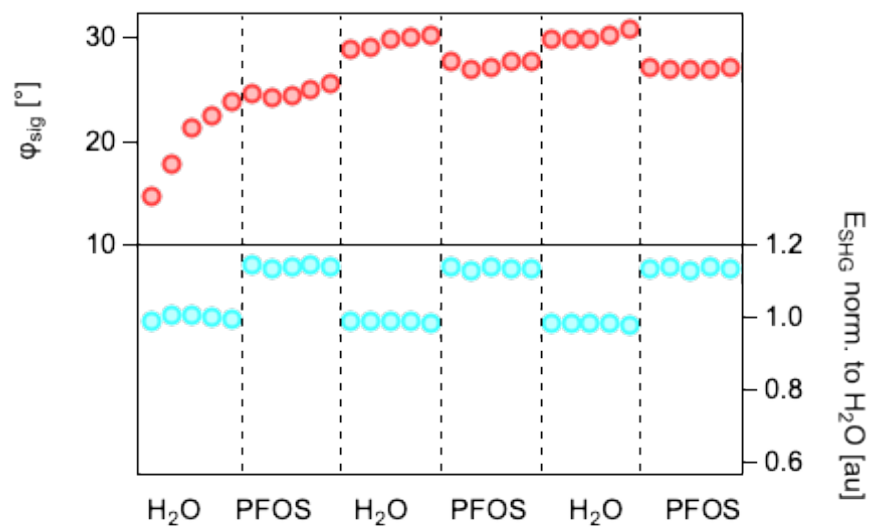
Figure B.2. Selection of representative raw scans from each portion of the on/off experiments between pure water and (a) 10 ppm PFOA and (b) 10 ppm PFOS.

The phase shifts observed for PFOS are appreciably smaller (Figure B.3), with a reversible  $\pm 2.7(4)^\circ$  shift between water and 10 ppm PFOS, excluding the first water-to-PFOS transition due to systematic phase drift in the measurement. The relative change in amplitude is highly reversible, with the initial 13.9(3)% increase for the first water-to-PFOS transition followed by a consistent  $\pm 15.0(2)\%$  change for subsequent cycles.

Calculating the accompanying values of  $\chi_{eff}^{(2)}$  and  $\Phi(0)$  from our phase and amplitude (referencing to a hypothetical high-ionic-strength condition of 100 mM NaCl through the known phase relationship between this condition and pure water), we find that the primary difference between the behavior of PFOA and PFOS at the fused silica:aqueous interface is that  $\chi_{eff}^{(2)}$  is smaller for 10 ppm PFOA relative to pure water, and greater for 10 ppm PFOS relative to pure water (Figure B.4).  $\Phi(0)$  is reproducibly around  $-0.204(19)$  V for 10 ppm PFOA and  $-0.407(13)$  V for pure water after an initial value of  $-0.319(7)$  V,



(a)



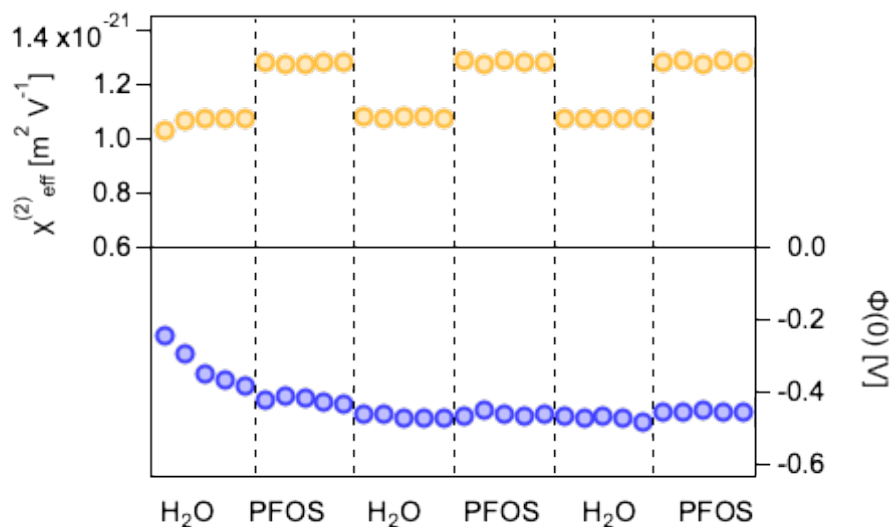
(b)

Figure B.3. Values of  $\varphi_{sig}$  and  $E_{SHG}$  obtained from the fit of the interference fringes for on/off reversibility experiments between pure water and (a) 10 ppm PFOA or (b) 10 ppm PFOS.

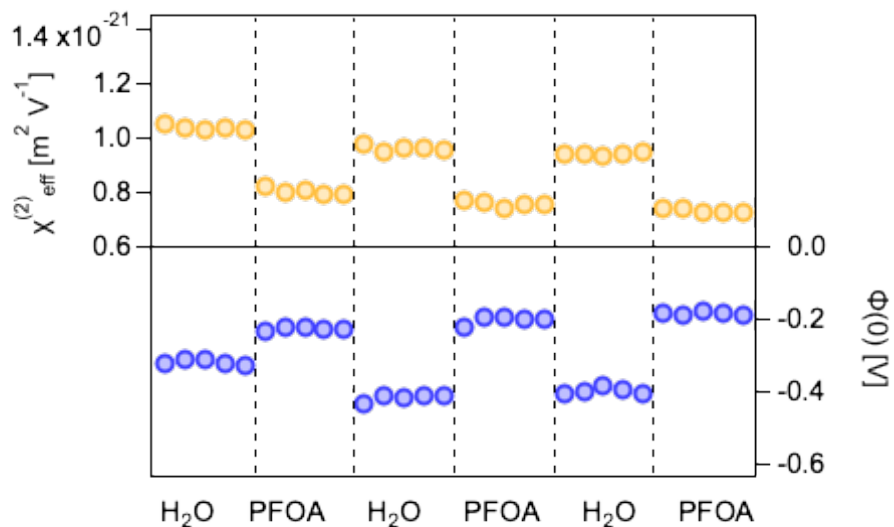
whereas for the transitions between pure water and 10 ppm PFOS,  $\Phi(0)$  hardly deviates from a value of  $-0.46(2)$  V. Notably, this apparent asymptote of the fused silica:aqueous interface's total potential after exposure to 10 ppm PFOS is approached from an initial value of  $-0.244$  V for the first interference pattern taken in water, which is near to the value of  $\Phi(0)$  observed reversibly for the same interface having been flushed with water after experiencing exposure to 10 ppm PFOA.

At pH 4.58, PFOA is considered to be entirely in its anionic form, since its  $pK_a$  is estimated to be around 2-3.<sup>32</sup> Similarly, at pH 5.88, PFOS is also likely completely deprotonated, with a  $pK_a$  estimated to be around -3.3.<sup>32</sup> At both of these pH values, the fused silica:aqueous interface is known to carry a net negative charge, which by Coulomb's law one would expect to repel the negatively charged head groups of PFOA and PFOS. However, although negatively charged overall, the fused silica:aqueous interface is also influenced by the presence of neutral SiOH groups, which account for  $\sim 85\%$  of all surface groups.<sup>33</sup> PFOA and PFOS may adsorb to these neutral groups *via* hydrogen bonding and hydrophobic interactions, with the driving force for adsorption owing to the favorable  $\sim 2.5$  kJ mol<sup>-1</sup> interaction energy for each methylene group within the perfluorinated alkyl tails of these compounds.

Another consideration is the likely minimization of organic matter in the form of carbonaceous surface contamination due to air plasma cleaning of the fused silica hemispheres before each experiment. Natural organic matter contaminating solid aluminum-based waste treatment residuals (WTS) has been shown to facilitate adsorption of PFAS by means of hydrophobic interactions between organic carbon and the perfluorinated tail



(a)



(b)

Figure B.4. Calculated values of  $\chi_{eff}^{(2)}$  and  $\Phi(0)$  for on/off reversibility experiments between pure water and (a) 10 ppm PFOA or (b) 10 ppm PFOS.

groups of PFOA and PFOS.<sup>29,34</sup> Therefore, for our plasma-cleaned substrates, the extent of ad- and desorption of PFOA and PFOS is more likely dominated by electrostatic interactions.

To account for the difference in behavior between PFOA and PFOS, we note that the sulfonic head group of PFOS is more electronegative than the carboxylic acid head group of PFOA<sup>35</sup> and that PFOS is more hydrophobic than PFOA.<sup>35</sup> Although the homodyne response in  $I_{SHG}$  for PFOS appears to be mostly reversible, the response in  $\Phi(0)$ , which asymptotically approaches  $-0.46(2)$  V, suggests a more complicated story. Further studies, as elaborated in the following section, would be needed to gain more detailed insight into ad- and desorption mechanisms for PFOA and PFOS at the fused silica:aqueous interface.

#### B.4. Summary and Future Directions

The results presented in this appendix indicate the viability of HD-SHG analysis to be applied to the study of surfactant interactions with fused silica:aqueous interfaces, and in particular to PFOA and PFOS as major PFAS whose mobility and fate in environmental systems remain as outstanding research questions. Our HD-SHG System 1 is found to be sensitive to concentrations of PFOA and PFOS at least as low as 10 ppm and perhaps as low as 100 ppb for PFOA. Initial results appear to be in accordance with reports of PFOA and PFOS ad- and desorption behavior at charged oxide:aqueous interfaces.

Future directions include testing the hypothesis that electrostatic interactions dominate the interaction of PFOA and PFOS with the fused silica:aqueous interface. To do this, similar HD-SHG experiments could be carried out against varying background electrolyte concentrations in order to facilitate the collection of adsorption isotherms at a number of different pH values (held constant for a single isotherm, along with the overall ionic strength of the aqueous phase). This would help to rule out the influence of the slightly different conductivities of 10 ppm solutions of PFOA and PFOS, facilitating comparison

between the two compounds. Additionally, this would allow for us to test whether adsorption capacities increase under more acidic conditions, as has been suggested elsewhere.<sup>34</sup> The concentration and identity of the background electrolyte could also be varied to study the impact of total ionic strength on these interactions.

Another avenue to explore includes the orientation of individual PFAS molecules in proximity to the fused silica:aqueous interface. Sum frequency generation (SFG)—as a more generalized form of SHG that can provide information about vibrational modes at interfaces—could be a useful tool to deploy to this end, either to attempt to predict through polarization-dependent studies the absolute orientation of PFOA's carbonyl, for instance, or to study whether different concentrations of the surfactants completely displace water molecules from the Stern layer of the fused silica:aqueous interface.

## APPENDIX C

**Original Research Proposal: Nonlinear Spectroscopy of Ionic Liquids Interacting with Model Mineral Surfaces****C.1. Abstract**

Ionic liquids (ILs) have garnered attention over the last three decades as “designer” or “green” solvents, due to their chemical tunability, low vapor pressure, and thermal stability. Despite evidence that ILs pose less risk of atmospheric pollution, a body of work points to their potential cyto- and ecotoxicity, though the large number of ILs and their physical and chemical variability leads to great uncertainty on the nature of the hazard for different species and environments. Further, there is a dearth of studies on the mobility, fate, and transport of ILs in terrestrial and aquatic settings, casting uncertainty on the routes by which ILs might undergo uncontrolled release. As ILs see increasing industrial use there is a need for a more fundamental understanding of how these solvents behave in aqueous environments and at dilute concentrations, and how these behaviors may map onto predictable structural properties of ILs’ constituent cations and anions. Although some studies exist investigating the adsorption of ILs to certain minerals or soil constituents, these approaches rely on measurements of zeta potential or isotherms derived from batch experiments, thus lacking molecular insight on interfacial-specific dynamics. To fill this gap, this original research proposal seeks to use heterodyne-detected second harmonic generation (HD-SHG) spectroscopy to determine the impact of

imidazolium-based ILs on Stern layer water molecules at a selection of mineral:aqueous interfaces. Selection of a variety of IL cations featuring different side chain lengths will enable the investigation of the impact of steric hindrance on IL surface interactions. The use of both positively and negatively charged mineral surfaces will allow specific evaluation of the role of electrostatic dynamics, with a particular focus on implications for the cationic portions of the selected ILs. Finally, tuning of bulk solution conditions such as pH and ionic strength (using a background electrolyte) will allow this study to more closely emulate real-world environmental settings, where uncontrolled releases of ILs may result in relatively small concentrations of the contaminant within a complex, heterogeneous interfacial region.

## C.2. Background and Previous Work

Ionic liquids (ILs) are a broad class of compounds including any non-molecular liquid at or below the boiling point of water (100°C) and composed entirely of ions. With the ability to access practically infinite combinations of cation and anion pairs, ILs have earned the moniker of “designer solvents.” Broadly, the properties that caused ILs to gain attention from academics and industry alike are their thermal stability and low vapor pressure at room temperature, while other properties including viscosity and solubility vary with the selection of constituent ions.

The first report of ILs emerged in 1914, however it was not until the 1990s that research output on ILs underwent a surge.<sup>1</sup> This was thanks to the first reports on imidazolium-based cations, which offered significant practical benefits relative to earlier ILs due to their diminished sensitivity to air and moisture. By the 2010s, this output peaked around

7,000 publications per year, with the number of annual patents climbing steadily since the turn of the century to reach 2,000 in 2019.<sup>2</sup>

Though the industrial sector has shown significant interest in implementing ILs, movement from the benchtop to production scale has been sluggish—likely due to the solvents' expense, which is 2-100 times more than organic counterparts, as well as the limited commercial production of ILs at any useable volume.<sup>2</sup> However, the range of potential applications for ILs is broad, encompassing catalytic materials,<sup>3-7</sup> stabilizers perovskite-based photovoltaics,<sup>8-11</sup> triboelectric nanogenerators (TENGs),<sup>12-14</sup> mobile and stationary phase for analytical methods,<sup>15-17</sup> media for gas and heavy metal capture and storage,<sup>18</sup> additives for lubricants and hydraulic fluids,<sup>19-22</sup> and wastewater remediation agents.<sup>23</sup> As of 2020, 57 commercial or pilot-scale projects where ILs play a principal role are underway.<sup>24</sup> Some reviewers predict a gradual increase in IL commercialization for applications as a specialty chemical rather than a bulk solvent, such as supercapacitors, lithium-ion batteries, and electrochemical sensors.<sup>2</sup>

Anticipating an increase in IL commercialization, another aspect worth considering are the potential effects of these chemicals upon environmental release, a risk that multiple high-profile train derailments in the United States within the last year highlight.<sup>25,26</sup> Indeed, within the last 5 years a study found detectable amounts of quaternary ammonium compounds (QACs)—which can be the cationic portions of ILs—in wastewater effluent and sediment cores.<sup>27</sup>

The cationic portions of ILs in particular raise biotoxicity concerns due to their high lipophilicity and electrostatic attraction to negatively charged biological membranes.<sup>28</sup> Certain studies on the human cytotoxicity of ILs have suggested amphiphilic IL cations

may insert themselves into lipid bilayers, causing swelling and disruption of the membrane.<sup>29,30</sup> Given the massive library of ILs that exist and may reach commercialization, some reviews call for a toxicological classification of ILs, while noting that the extant literature is insufficient to support such a classification.<sup>28</sup> Beyond human toxicity, initial looks into the ecotoxicity of ILs indicates some adverse effects for certain plants, animals, bacteria, and fungi—however, the vast diversity of living species, their modes of protection, and ILs leads to broad variability in how hazardous any individual IL may be for any individual organism.<sup>31</sup> Suffice to say, we need to quickly advance our understanding not just of ILs’ degree of toxicity, but also the routes by which humans and other organisms are exposed to them.

Previous work has sought to elucidate the fate, transport, and mobility of ILs in the environment,<sup>32</sup> or enumerate methods to remove ILs from the environment, where they are present in much more dilute conditions than in commercial settings.<sup>33</sup> Adsorption of long-chained QACs to  $\alpha$ -quartz surfaces has been shown to reverse zeta potential at a certain threshold concentration, a phenomenon linked to electrostatic interfacial interactions.<sup>34</sup> However, this conclusion follows from zeta potential measurements alone, which do not capture potential charge reversal that may be occurring at the true zero-plane of the mineral:aqueous interface.

### C.3. Hypotheses

We hypothesize that muscovite mica will stabilize longer-chained imidazolium-based ILs to a greater extent than either  $\alpha$ -quartz or the K-feldspars, due to its documented

stabilization of cationic species through inner-, outer-, and “extended” outer-sphere complexation interactions. Conversely, we hypothesize that  $\alpha$ -quartz and the K-feldspars will adsorb shorter-chained ILs more readily than muscovite mica, since they bear an overall negative charge for most naturally-occurring pH values. We further hypothesize that IL adsorption on  $\alpha$ -quartz will exhibit pH-dependence, reflecting the pH-dependence of  $\alpha$ -quartz’s interfacial potential.

It is important to test these hypotheses, as there is ample evidence that ILs cannot be treated as a monolith, with vastly different properties resulting from the very tunability that makes them attractive as solvents. Environmental regulation and remediation approaches will similarly need to be responsive to the composition of any uncontrolled IL spill, and constraining the behavior of ILs based on tail length will expand and refine our toolbox of responses, so that we do not have to resort to brute-force remediation approaches. Furthermore, it is understood that pollutant releases can behave differently on a macroscopic scale depending on the particular geological makeup of surrounding rocks, soils, and sediments. By testing the above hypotheses against a selection of common rock-building minerals, we will enable the understanding of IL behavior in environmental systems to be informed by local geology. As will be described further in Section C.5, we will test these hypotheses by monitoring interfacial properties (*via* heterodyne-detected second harmonic generation (HD-SHG) spectroscopy) while performing flow experiments in which we can systematically vary the IL cation chain length, the background ionic strength, the solution pH, and the mineral surface.

## C.4. Scientific Objectives

In the proposed work, we will guide our inquiry with the following three scientific objectives, aiming to:

- (1) Determine the effect of steric hindrance on imidazolium-based cations' interactions with model mineral surfaces and their disruptions to Stern layer water molecules while under dilute aqueous conditions.
- (2) Determine the relative capacity of three model mineral surfaces to adsorb and desorb dissolved imidazolium-based cations—and seek to assign this effect to some property of the interface (*e.g.* availability/density of surface sites, point of zero charge (PZC), interfacial potential).
- (3) Distinguish the extent and distribution of ILs' disruptions to the Stern layer of mineral:aqueous interfaces by detecting changes in the occupancy of surface sites, charge density, interfacial potential, and Debye length.

## C.5. Proposed Research

### C.5.1. Selection of ILs

We propose using 1,3-R,R'-imidazolium chlorides for this work, in which R is a methyl group and R' is an *n*-alkyl group with the chain length varied between one and ten carbons. We select imidazolium-based cations as the basis for this study as they are one of the few families of commercialized ionic liquids, they are stable to moisture and air, and they are readily obtained with a variety of R-groups and counterions. Some industrial entities have applied imidazolium-based ILs in gas capture,<sup>35</sup> as stationary phases in gas

capture,<sup>15</sup> and as catalysts in a number of pilot-scale processes, including dimerisation,<sup>4</sup> hydrosilylation,<sup>5</sup> and hydroformylation.<sup>3</sup>

For the counterion, we propose using chloride ( $\text{Cl}^-$ ) exclusively for early studies, with the focus being on the interaction of the imidazolium-based cation with the muscovite surface. By using KCl, KOH, and HCl we will be able to modulate solution conditions (*e.g.*, ionic strength, pH) while avoiding ion substitution between the structural  $\text{K}^+$  ions of muscovite or K-feldspar (as discussed further in Section C.5.2) and dissolved counterion species.

To target the effect of steric hindrance, we propose using a selection of imidazolium cations of systematically varying R' chain lengths, which are enumerated in Table C.1. The IL exhibiting least steric hindrance will be 1,3-dimethylimidazolium chloride and for the most steric hindrance we propose the use of 1-decyl-3-methylimidazolium chloride. Investigations into anion effects of ILs in interactions with mineral:aqueous interfaces are beyond the scope of this proposed work, but would be worthy of inclusion in subsequent studies, particularly given the existence of studies indicating that anion identity holds implications for IL aggregation behavior and toxicity.<sup>28,32</sup>

### C.5.2. Selection and Preparation of Mineral Surfaces

In the interest of evaluating a suite of silicate mineral surfaces representing the variety of crystallographic morphologies commonly represented in rock-building minerals, we have selected  $\alpha$ -quartz, cleaved muscovite mica ( $\text{KAl}_2(\text{SiAl})\text{O}_{10}(\text{OH})_2$ ), and potassium

| R1 C # | Cation                        | Anion    | CAS RN      |
|--------|-------------------------------|----------|-------------|
| 1      | 1,3-Dimethylimidazolium       | Chloride | 79917-88-7  |
| 2      | 1-Ethyl-3-methylimidazolium   | Chloride | 65039-09-0  |
| 3      | 1-Methyl-3-propylimidazolium  | Chloride | 79917-89-8  |
| 4      | 1-Butyl-3-methylimidazolium   | Chloride | 79917-90-1  |
| 5      | —                             | —        | —           |
| 6      | 1-Hexyl-3-methylimidazolium   | Chloride | 171058-17-6 |
| 7      | —                             | —        | —           |
| 8      | 1-Methyl-3-n-octylimidazolium | Chloride | 64697-40-1  |
| 9      | —                             | —        | —           |
| 10     | 1-Decyl-3-methylimidazolium   | Chloride | 171058-18-7 |

Table C.1. Selection of representative 1,3-R,R'-imidazolium chloride ionic liquids to be used in the proposed work.

(K) feldspar. Silicate minerals make up roughly 90% of the Earth's crust, and are therefore highly representative of the kinds of mineral surfaces likely exposed to water-borne contaminants in our soils and groundwater aquifers.<sup>36</sup>

Quartz is a tectosilicate (also called “framework” silicate) mineral accounting for approximately 12% of the Earth's crust.<sup>37</sup> In its purest form composed of just oxygen-coordinated silicon tetrahedra, quartz is a colorless, transparent mineral. Although each individual tetrahedron can be described with the formula  $\text{SiO}_4$ , the overall mineral takes the formula  $\text{SiO}_2$ , given that each oxygen is shared between two adjacent tetrahedra. In natural environments on Earth,  $\alpha$ -quartz is the most important polymorph of  $\text{SiO}_2$ .<sup>36</sup> Therefore, for the purpose of this work, we propose using anisotropic  $z$ -cut  $\alpha$ -quartz optical windows that can be obtained ready-made from a variety of vendors with relative ease. As demonstrated in the literature, the trigonal crystal structure of  $\alpha$ -quartz—and accompanying lack of centrosymmetry—makes it inherently SHG-active, and therefore a common selection for a local oscillator material.<sup>38–41</sup> Following the example of previous spectroscopic studies on  $\alpha$ -quartz, the samples will be sonicated subsequently in MeOH

and water, oven dried, and plasma cleaned in order to minimize carbon contamination of the exposed surface.<sup>38</sup>

Micas are a family of phyllosilicate (or sheet silicate) minerals accounting for roughly 4% of the Earth's crust.<sup>42</sup> Although less dominant than quartz within the realm of rock-building minerals, mica is a common weathering product of granites, thus making it an important soil constituent and worthy of consideration within the scope of contamination studies.<sup>43</sup> Muscovite mica ( $\text{KAl}_2(\text{SiAl})\text{O}_{10}(\text{OH})_2$ ) in particular is known for its near-perfect basal cleavage along the (001) plane, and its resultant atomically flat cleaved surfaces studded with exposed  $\text{K}^+$  ions make it ideal for many optical applications.<sup>44</sup> Muscovite mica displays a monoclinic ( $2/m$ ) crystal structure with a center of inversion, making it SHG-silent.

Discrete aluminosilicate layers of muscovite consist of two tetrahedral sheets (75%  $\text{SiO}_4$  and 25%  $\text{AlO}_4$ ) sandwiching an octahedral sheet ( $\text{Al}_2\text{O}_2(\text{OH})_2$ ), with interstitial  $\text{K}^+$  ions occupying ditrigonal rings between neighboring tetrahedral sheets and compensating for the  $-1$  charge introduced by Al ions. Surface-specific studies of cleaved muscovite have shown that in solution, ion exchange occurs readily between  $\text{K}^+$  and dissolved alkali metal cations.<sup>45</sup> Furthermore, AFM studies have indicated there is short-range ordering of  $\text{K}^+$  ions,<sup>46</sup> whose arrangement is expected to have some bearing on ion adsorption to the surface.

For the purpose of this work, we propose using V1 quality muscovite mica discs, which can be obtained from vendors of optical materials ready-made. Similar to the  $\alpha$ -quartz samples, muscovite samples will be prepared for analysis by sonicating subsequently in

MeOH and water, oven drying, and plasma cleaning. The samples will be further treated prior to experimentation by an overnight soak in ultrapure water.

Even before  $\alpha$ -quartz and mica, the feldspars are the most abundant group of minerals in the Earth's crust, making up nearly 60% of the planet's rock-forming minerals.<sup>36</sup> Similar to  $\alpha$ -quartz, feldspar minerals are a class of framework silicates, although their chemical structure incorporates allows for a much broader range of compositional variety. The three principal endmembers of the feldspar group include: (1) albite ( $\text{NaAlSi}_3\text{O}_8$ ), (2) anorthite ( $\text{CaAl}_2\text{Si}_2\text{O}_8$ ), and (3) K-feldspar ( $\text{KAlSi}_3\text{O}_8$ ).<sup>42</sup> We propose using K-feldspar as the initial mineral surface to represent the feldspar group within this work, as it is known to weather slowly and therefore is a likely constituent in sandstones, a common aquifer-building rock with high hydraulic conductivity.<sup>47</sup>

Since K-feldspars are known to exhibit polymorphism, we propose focusing on two polymorphs with distinctive crystallographic properties: sanidine and microcline.<sup>42</sup> Sanidine's crystal structure is monoclinic ( $2/m$ ) and notably features a center of inversion, making it SHG-silent (see Section 2.1 for a detailed discussion of the relationship between SHG and symmetry). Microcline, on the other hand, is triclinic ( $\bar{1}$ ), with no center of inversion, meaning that it is inherently SHG-active.

Unlike  $\alpha$ -quartz and muscovite, feldspars are not commercially manufactured as windows or lenses for optical purposes, and synthetic feldspars are reported only in the sub-mm size range.<sup>48</sup> Given these constraints, we propose using museum-grade natural samples of sanidine and microcline to prepare thin section samples for use in SHG spectroscopy. Thin samples are used extensively in mineralogical analysis by optical light microscopy, and are prepared by first cleaving mm-scale fragments from a source crystal,

then attaching the fragments to a glass slide using epoxy resin, and then using a polishing protocol to reduce the thickness of the glass-mounted mineral fragment to  $\sim 30 \mu\text{m}$ . At this thickness scale, feldspars will readily transmit light in the visible region of the electromagnetic spectrum, enabling interrogation by SHG spectroscopy. We will ensure that we select an epoxy that is transmissive at the relevant wavelengths to our HD-SHG experiments.

### C.5.3. SHG Spectroscopy of IL Interaction with Mineral Surfaces

The fundamental principles of second harmonic generation (SHG) as an optical process and the principles of SHG spectroscopy are discussed in more detail in Chapter 2. Past work in our group has used HD-SHG spectroscopy to identify unanticipated interfacial phenomena such as charge reversal on supported lipid bilayers (SLBs).<sup>40</sup> Already, a great number of studies exist using SHG—and sum-frequency generation (SFG)—to study the interfacial properties and dynamics of the  $\alpha$ -quartz:aqueous interface.<sup>38,49–51</sup> To a slightly lesser extent, SHG studies exist for muscovite surfaces in contact with aqueous solutions, providing insight on processes such as contaminant adsorption or heterogeneous ice nucleation.<sup>52–54</sup> K-feldspars are not yet widely studied using traditional SHG spectroscopy, however, some workers have used SHG activity as a complementary means to identify these minerals.<sup>55,56</sup>

Using the principles and best practices laid out in Chapter 4 of this thesis, we aim to prepare samples of muscovite and K-feldspar for HD-SHG analysis, which will allow us to directly probe interfacial potential and second-order nonlinear susceptibility. Muscovite discs should be straightforward to interrogate using the adjustments to alignment and

data processing that we outline in Sections 4.2 and 4.3. Due to reports of the successful analysis of  $\alpha$ -quartz using HD-SHG—including from our own group—we are confident that IL interactions with this mineral surface should be straightforward to study without the need for further adaptation of the sample or spectrometer. We expect the K-feldspars to be the most difficult samples to accommodate for HD-SHG analysis, since they are not yet accessible by synthetically by thin-film deposition or through commercial optics suppliers. We will attempt to circumvent this obstacle by preparing sub-30- $\mu\text{m}$  thin sections of museum-grade sanidine and microcline samples, for use in flat geometry on our HD-SHG spectrometer (described in Section 2.3.2). If this approach is unsuccessful, we still anticipate that studies on muscovite and  $\alpha$ -quartz will be sufficient to advance our understanding of IL mobility, transport, and fate in soil and groundwater systems.

## C.6. Summary

As discussed in Section C.5.2, the set of proposed mineral surfaces to be studied in the course of this work account for the major constituents of rocks and soils on Earth, while also presenting the opportunity investigate the impact of the identity, density, and availability of surface sites on the hydration structure and electrostatics of the respective mineral:water interface. We expect this natural variation between mineral surfaces to result in different proclivities of our selected imidazolium-based ionic liquids to adsorb and desorb under aqueous conditions.

For example, it is known that water plays an important role in determining cation occupancy in the interfacial region of hydrated mica. Cation adsorption at muscovite's (001) plane has been shown to result in three distinct species: inner-sphere complexes,

outer-sphere complexes, and “extended” outer-sphere complexes that stabilize some ions as much as 5-10 Å away from the muscovite:water interface.<sup>57</sup> Therefore, we hypothesize that the ability of the muscovite:water interface to stabilize extended outer sphere complexes will enable stabilization of more sterically hindered ionic liquids than  $\alpha$ -quartz or either K-feldspar polymorph.

Another point of distinction between these three proposed model mineral surfaces is the nature of their surface charging under hydrated conditions. Within muscovite’s crystal lattice, the substitution of  $\text{Si}^{4+}$  for  $\text{Al}^{3+}$  imparts a permanent negative surface charge that is insensitive to variations in solution pH.<sup>57</sup> The  $\alpha$ -quartz:water interface, on the other hand, features a variety of terminal groups—including isolated silanols, siloxane bridges, vicinal silanols, and geminal silanols—many of which feature hydroxyl groups that can deprotonate and protonate as a function of changing pH.<sup>49,58,59</sup> As a result,  $\alpha$ -quartz’s surface charge density and resultant interfacial potentials are highly dependent on pH, with a measured isoelectric point—meaning, the point at which the surface bears a net zero charge—around pH 2.2.<sup>60,61</sup> Chemometric studies of IL adsorption to soils indicate that cation exchange capacity is a key metric governing IL immobilization and fate, with negatively charged surfaces favoring IL interactions and positively charged surfaces favoring dispersion.<sup>62</sup> We therefore expect better adsorption of our selected ILs to  $\alpha$ -quartz and the K-feldspars than to muscovite.

On the topic of steric hindrance, we expect based on existing literature that the longer-chained imidazolium cations will adsorb more strongly than their shorter-chained counterparts.<sup>62,63</sup> We also expect that for the muscovite:aqueous interface we will see insensitivity of IL adsorption to bulk solution pH, given the structurally fixed surface

charge density of the material, whereas with  $\alpha$ -quartz and the K-feldspars we should expect to see more of an impact.<sup>62,64-67</sup>

In sum, the proposed work will provide important insight on the interactions of imidazolium-based ILs with some of the most common minerals present on the Earth's surface. Using HD-SHG, we will be able to more directly probe interfacial properties such as total potential at the zero-plane, charge density, occupancy of surface sites, and Debye screening length. Further, given the strength of HD-SHG to interrogate systems under environmentally relevant conditions, we will be able to systematically tune conditions of the bulk solution such as ionic strength, background electrolyte identity, and pH, which we expect to have significant impact on the ILs' affinities for the different surfaces, depending on each mineral's PZC and expected terminal surface groups. We expect this work to significantly enhance the currently limited body of studies describing the behavior of common ILs within complex and heterogeneous aquatic environments.

### References for Appendix A

- (1) Nesse, W. D., *Introduction to Mineralogy*; Oxford University Press: 2017; 495 pp.
- (2) Deer, W. A.; Howie, R. A.; Zussman, J., *An Introduction to the Rock-Forming Minerals*; Mineralogical Society of Great Britain and Ireland: 2013.
- (3) Cao, L.; Zhang, X.; Yuan, J.; Guo, L.; Hong, T.; Hang, W.; Ma, Y. Study on the Influence of Sapphire Crystal Orientation on Its Chemical Mechanical Polishing. *Applied Sciences* **2020**, *10*, 8065.
- (4) Guo, Q.; Jia, Z.; Pan, X.; Liu, S.; Tian, Z.; Zheng, Z.; Chen, C.; Qin, G.; Yu, Y. Sapphire-Derived Fiber Bragg Gratings for High Temperature Sensing. *Crystals* **2021**, *11*, 946.
- (5) Dolganova, I. N.; Shikunova, I. A.; Katyba, G. M.; Zotov, A. K.; Mukhina, E. E.; Shchedrina, M. A.; Tuchin, V. V.; Zaytsev, K. I.; Kurlov, V. N. Optimization of Sapphire Capillary Needles for Interstitial and Percutaneous Laser Medicine. *JBO* **2019**, *24*, 128001.
- (6) Seitz, M.; Peterson, G. In *Advanced Optics for Defense Applications: UV through LWIR III*, *Advanced Optics for Defense Applications: UV through LWIR III*, SPIE: 2018; Vol. 10627, pp 53–58.
- (7) Curley, P. F.; Ferguson, A. I.; White, J. G.; Amos, W. B. Application of a Femtosecond Self-Sustaining Mode-Locked Ti:Sapphire Laser to the Field of Laser Scanning Confocal Microscopy. *Opt Quant Electron* **1992**, *24*, 851–859.
- (8) Zhang, S.-T.; Maltseva, A.; Herting, G.; Guillemoles, J.-F.; Schneider, N.; Odnevall, I.; Volovitch, P. Importance of Atmospheric Aerosol Pollutants on the Degradation

- of Al<sub>2</sub>O<sub>3</sub> Encapsulated Al-doped Zinc Oxide Window Layers in Solar Cells. *Progress in Photovoltaics: Research and Applications* **2022**, *30*, 552–566.
- (9) Kosmulski, M. The pH Dependent Surface Charging and Points of Zero Charge. IX. Update. *Advances in Colloid and Interface Science* **2021**, *296*, 102519.
- (10) Boamah, M. D.; Isheim, D.; Geiger, F. M. Dendritic Oxide Growth in Zerovalent Iron Nanofilms Revealed by Atom Probe Tomography. *J. Phys. Chem. C* **2018**, *122*, 28225–28232.
- (11) Liljeblad, J. F. D.; Tyrode, E. Vibrational Sum Frequency Spectroscopy Studies at Solid/Liquid Interfaces: Influence of the Experimental Geometry in the Spectral Shape and Enhancement. *J. Phys. Chem. C* **2012**, *116*, 22893–22903.
- (12) Abdelmonem, A.; Lützenkirchen, J.; Leisner, T. Probing Ice-Nucleation Processes on the Molecular Level Using Second Harmonic Generation Spectroscopy. *Atmospheric Measurement Techniques* **2015**, *8*, 3519–3526.
- (13) Abdelmonem, A.; Zhang, Y.; Braunschweig, B.; Glikman, D.; Rumpel, A.; Peukert, W.; Begović, T.; Liu, X.; Lützenkirchen, J. Adsorption of CTAB on Sapphire-c at High pH: Surface and Zeta Potential Measurements Combined with Sum-Frequency and Second-Harmonic Generation. *Langmuir* **2022**, *38*, 3380–3391.
- (14) Bulusu, A.; Kim, H.; Samet, D.; Graham, S. Improving the Stability of Atomic Layer Deposited Alumina Films in Aqueous Environments with Metal Oxide Capping Layers. *J. Phys. D: Appl. Phys.* **2013**, *46*, 084014.
- (15) Correa, G. C.; Bao, B.; Strandwitz, N. C. Chemical Stability of Titania and Alumina Thin Films Formed by Atomic Layer Deposition. *ACS Appl. Mater. Interfaces* **2015**, *7*, 14816–14821.

- (16) Abdulagatov, A. I.; Yan, Y.; Cooper, J. R.; Zhang, Y.; Gibbs, Z. M.; Cavanagh, A. S.; Yang, R. G.; Lee, Y. C.; George, S. M. Al<sub>2</sub>O<sub>3</sub> and TiO<sub>2</sub> Atomic Layer Deposition on Copper for Water Corrosion Resistance. *ACS Appl. Mater. Interfaces* **2011**, *3*, 4593–4601.
- (17) Kim, L. H.; Kim, K.; Park, S.; Jeong, Y. J.; Kim, H.; Chung, D. S.; Kim, S. H.; Park, C. E. Al<sub>2</sub>O<sub>3</sub>/TiO<sub>2</sub> Nanolaminate Thin Film Encapsulation for Organic Thin Film Transistors via Plasma-Enhanced Atomic Layer Deposition. *ACS Appl. Mater. Interfaces* **2014**, *6*, 6731–6738.
- (18) Dameron, A. A.; Davidson, S. D.; Burton, B. B.; Carcia, P. F.; McLean, R. S.; George, S. M. Gas Diffusion Barriers on Polymers Using Multilayers Fabricated by Al<sub>2</sub>O<sub>3</sub> and Rapid SiO<sub>2</sub> Atomic Layer Deposition. *J. Phys. Chem. C* **2008**, *112*, 4573–4580.
- (19) Willis, S. A.; McGuinness, E. K.; Li, Y.; Losego, M. D. Re-Examination of the Aqueous Stability of Atomic Layer Deposited (ALD) Amorphous Alumina (Al<sub>2</sub>O<sub>3</sub>) Thin Films and the Use of a Postdeposition Air Plasma Anneal to Enhance Stability. *Langmuir* **2021**, *37*, 14509–14519.
- (20) Marin, E.; Guzman, L.; Lanzutti, A.; Ensinger, W.; Fedrizzi, L. Multilayer Al<sub>2</sub>O<sub>3</sub>/TiO<sub>2</sub> Atomic Layer Deposition Coatings for the Corrosion Protection of Stainless Steel. *Thin Solid Films* **2012**, *522*, 283–288.
- (21) Lützenkirchen, J. et al. The Surface Chemistry of Sapphire-c: A Literature Review and a Study on Various Factors Influencing Its IEP. *Adv Colloid Interface Sci* **2018**, *251*, 1–25.

- (22) Musorrafiti, M. J.; Konek, C. T.; Hayes, P. L.; Geiger, F. M. Interaction of Chromium(VI) with the  $\gamma$ -Aluminum Oxide/Water Interface. *J. Phys. Chem. C* **2008**, *112*, 2032–2039.

### References for Appendix B

- (1) Grulke, C.; Patlewicz, G.; Meyer, B.; Williams, A.; Richard, A. Structure-Based Categorization of Per- & Polyfluoroalkyl Substances in the DSSTox Database and EPA's ToxCast Inventory Using Markush Representations, presentation, 2019.
- (2) Rickard, B. P.; Rizvi, I.; Fenton, S. E. Per- and Poly-Fluoroalkyl Substances (PFAS) and Female Reproductive Outcomes: PFAS Elimination, Endocrine-Mediated Effects, and Disease. *Toxicology* **2022**, *465*, 153031.
- (3) Stanifer, J. W.; Stapleton, H. M.; Souma, T.; Wittmer, A.; Zhao, X.; Boulware, L. E. Perfluorinated Chemicals as Emerging Environmental Threats to Kidney Health: A Scoping Review. *Clinical Journal of the American Society of Nephrology* **2018**, *13*, 1479.
- (4) Blake, B. E.; Fenton, S. E. Early Life Exposure to Per- and Polyfluoroalkyl Substances (PFAS) and Latent Health Outcomes: A Review Including the Placenta as a Target Tissue and Possible Driver of Peri- and Postnatal Effects. *Toxicology* **2020**, *443*, 152565.
- (5) Temkin, A. M.; Hocevar, B. A.; Andrews, D. Q.; Naidenko, O. V.; Kamendulis, L. M. Application of the Key Characteristics of Carcinogens to Per and Polyfluoroalkyl Substances. *International Journal of Environmental Research and Public Health* **2020**, *17*, 1668.
- (6) Meegoda, J. N.; Kewalramani, J. A.; Li, B.; Marsh, R. W. A Review of the Applications, Environmental Release, and Remediation Technologies of Per- and Polyfluoroalkyl Substances. *International Journal of Environmental Research and Public Health* **2020**, *17*, 8117.

- (7) Mifflin, A. L.; Gerth, K. A.; Weiss, B. M.; Geiger, F. M. Surface Studies of Chromate Binding to Fused Quartz/Water Interfaces. *J. Phys. Chem. A* **2003**, *107*, 6212–6217.
- (8) Mifflin, A. L.; Gerth, K. A.; Geiger, F. M. Kinetics of Chromate Adsorption and Desorption at Fused Quartz/Water Interfaces Studied by Second Harmonic Generation. *J. Phys. Chem. A* **2003**, *107*, 9620–9627.
- (9) Al-Abadleh, H. A.; Mifflin, A. L.; Musorrafiti, M. J.; Geiger, F. M. Kinetic Studies of Chromium (VI) Binding to Carboxylic Acid- and Methyl Ester-Functionalized Silica/Water Interfaces Important in Geochemistry. *J. Phys. Chem. B* **2005**, *109*, 16852–16859.
- (10) Al-Abadleh, H. A.; Voges, A. B.; Bertin, P. A.; Nguyen; Geiger, F. M. Chromium(VI) Binding to Functionalized Silica/Water Interfaces Studied by Nonlinear Optical Spectroscopy. *J. Am. Chem. Soc.* **2004**, *126*, 11126–11127.
- (11) Al-Abadleh, H. A.; Mifflin, A. L.; Bertin, P. A.; Nguyen, S. T.; Geiger, F. M. Control of Carboxylic Acid and Ester Groups on Chromium (VI) Binding to Functionalized Silica/Water Interfaces Studied by Second Harmonic Generation. *J. Phys. Chem. B* **2005**, *109*, 9691–9702.
- (12) Konek, C. T.; Illg, K. D.; Al-Abadleh, H. A.; Voges, A. B.; Yin, G.; Musorrafiti, M. J.; Schmidt, C. M.; Geiger, F. M. Nonlinear Optical Studies of the Agricultural Antibiotic Morantel Interacting with Silica/Water Interfaces. *J. Am. Chem. Soc.* **2005**, *127*, 15771–15777.
- (13) Mifflin, A. L.; Konek, C. T.; Geiger, F. M. Tracking Oxytetracycline Mobility Across Environmental Interfaces by Second Harmonic Generation. *J. Phys. Chem. B* **2006**, *110*, 22577–22585.

- (14) Hayes, P. L.; Gibbs-Davis, J. M.; Musorrafiti, M. J.; Mifflin, A. L.; Scheidt, K. A.; Geiger, F. M. Environmental Biogeochemistry Studied by Second-Harmonic Generation: A Look at the Agricultural Antibiotic Oxytetracycline. *J. Phys. Chem. C* **2007**, *111*, 8796–8804.
- (15) Troiano, J. M. et al. Direct Probes of 4 Nm Diameter Gold Nanoparticles Interacting with Supported Lipid Bilayers. *J. Phys. Chem. C* **2015**, *119*, 534–546.
- (16) Jacobson, K. H.; Gunsolus, I. L.; Kuech, T. R.; Troiano, J. M.; Melby, E. S.; Lohse, S. E.; Hu, D.; Chrisler, W. B.; Murphy, C. J.; Orr, G.; Geiger, F. M.; Haynes, C. L.; Pedersen, J. A. Lipopolysaccharide Density and Structure Govern the Extent and Distance of Nanoparticle Interaction with Actual and Model Bacterial Outer Membranes. *Environ. Sci. Technol.* **2015**, *49*, 10642–10650.
- (17) Troiano, J. M.; Kuech, T. R.; Vartanian, A. M.; Torelli, M. D.; Sen, A.; Jacob, L. M.; Hamers, R. J.; Murphy, C. J.; Pedersen, J. A.; Geiger, F. M. On Electronic and Charge Interference in Second Harmonic Generation Responses from Gold Metal Nanoparticles at Supported Lipid Bilayers. *J. Phys. Chem. C* **2016**, *120*, 20659–20667.
- (18) Chang, H.; Gnanasekaran, K.; Gianneschi, N. C.; Geiger, F. M. Bacterial Model Membranes Deform (Resp. Persist) upon Ni<sup>2+</sup> Binding to Inner Core (Resp. O-Antigen) of Lipopolysaccharides. *J. Phys. Chem. B* **2019**, *123*, 4258–4270.
- (19) Boamah, M. D.; Ohno, P. E.; Lozier, E.; Van Ardenne, J.; Geiger, F. M. Specifics about Specific Ion Adsorption from Heterodyne-Detected Second Harmonic Generation. *J. Phys. Chem. B* **2019**, *123*, 5848–5856.

- (20) Ma, E.; Geiger, F. M. Divalent Ion Specific Outcomes on Stern Layer Structure and Total Surface Potential at the Silica:Water Interface. *J. Phys. Chem. A* **2021**, *125*, 10079–10088.
- (21) Chang, H.; Ohno, P. E.; Liu, Y.; Lozier, E. H.; Dalchand, N.; Geiger, F. M. Direct Measurement of Charge Reversal on Lipid Bilayers Using Heterodyne-Detected Second Harmonic Generation Spectroscopy. *J. Phys. Chem. B* **2020**, *124*, 641–649.
- (22) Wang, H.; Troxler, T.; Yeh, A.-G.; Dai, H.-L. In Situ, Nonlinear Optical Probe of Surfactant Adsorption on the Surface of Microparticles in Colloids. *Langmuir* **2000**, *16*, 2475–2481.
- (23) You, Y.; Bloomfield, A.; Liu, J.; Fu, L.; Herzon, S. B.; Yan, E. C. Y. Real-Time Kinetics of Surfactant Molecule Transfer between Emulsion Particles Probed by in Situ Second Harmonic Generation Spectroscopy. *J. Am. Chem. Soc.* **2012**, *134*, 4264–4268.
- (24) Hartings, J. M.; Poon, A.; Pu, X.; Chang, R. K.; Leslie, T. M. Second Harmonic Generation and Fluorescence Images from Surfactants on Hanging Droplets. *Chemical Physics Letters* **1997**, *281*, 389–393.
- (25) Hayes, P. L.; Chen, E. H.; Achtyl, J. L.; Geiger, F. M. An Optical Voltmeter for Studying Cetyltrimethylammonium Interacting with Fused Silica/Aqueous Interfaces at High Ionic Strength. *J. Phys. Chem. A* **2009**, *113*, 4269–4280.
- (26) Panieri, E.; Baralic, K.; Djukic-Cosic, D.; Buha Djordjevic, A.; Saso, L. PFAS Molecules: A Major Concern for the Human Health and the Environment. *Toxics* **2022**, *10*, 44.

- (27) US EPA, O. W. Drinking Water Health Advisories for PFOA and PFOS <https://www.epa.gov/sdwa/drinking-water-health-advisories-pfoa-and-pfos> (accessed 06/21/2023).
- (28) Yu, Q.; Zhang, R.; Deng, S.; Huang, J.; Yu, G. Sorption of Perfluorooctane Sulfonate and Perfluorooctanoate on Activated Carbons and Resin: Kinetic and Isotherm Study. *Water Research* **2009**, *43*, 1150–1158.
- (29) Johnson, R. L.; Anschutz, A. J.; Smolen, J. M.; Simcik, M. F.; Penn, R. L. The Adsorption of Perfluorooctane Sulfonate onto Sand, Clay, and Iron Oxide Surfaces. *J. Chem. Eng. Data* **2007**, *52*, 1165–1170.
- (30) Darlington, A. M.; Gibbs-Davis, J. M. Bimodal or Trimodal? The Influence of Starting pH on Site Identity and Distribution at the Low Salt Aqueous/Silica Interface. *J. Phys. Chem. C* **2015**, *119*, 16560–16567.
- (31) Ong, S.; Zhao, X.; Eienthal, K. B. Polarization of Water Molecules at a Charged Interface: Second Harmonic Studies of the Silica/Water Interface. *Chemical Physics Letters* **1992**, *191*, 327–335.
- (32) Larsen, P.; Giovalle, E. *Perfluoroalkylated Substances: PFOA, PFOS and PFOSA*; Environmental project 1665; Denmark: The Danish Environmental Protection Agency, 2015.
- (33) Duval, Y.; Mielczarski, J. A.; Pokrovsky, O. S.; Mielczarski, E.; Ehrhardt, J. J. Evidence of the Existence of Three Types of Species at the Quartz/Aqueous Solution Interface at pH 010: XPS Surface Group Quantification and Surface Complexation Modeling. *J. Phys. Chem. B* **2002**, *106*, 2937–2945.

- (34) Zhang, Z.; Sarkar, D.; Datta, R.; Deng, Y. Adsorption of Perfluorooctanoic Acid (PFOA) and Perfluorooctanesulfonic Acid (PFOS) by Aluminum-Based Drinking Water Treatment Residuals. *Journal of Hazardous Materials Letters* **2021**, *2*, 100034.
- (35) Xing, D. Y.; Chen, Y.; Zhu, J.; Liu, T. Fabrication of Hydrolytically Stable Magnetic Core-Shell Aminosilane Nanocomposite for the Adsorption of PFOS and PFOA. *Chemosphere* **2020**, *251*, 126384.

### References for Appendix C

- (1) Walden, P. Ueber die Molekulargröße und elektrische Leitfähigkeit einiger geschmolzenen Salze. *Bulletin de l'Académie Impériale des Sciences de St.-Petersbourg. VI* **1914**, *8*, 405–422.
- (2) Greer, A. J.; Jacquemin, J.; Hardacre, C. Industrial Applications of Ionic Liquids. *Molecules* **2020**, *25*, 5207.
- (3) Marinkovic, J. M.; Riisager, A.; Franke, R.; Wasserscheid, P.; Haumann, M. Fifteen Years of Supported Ionic Liquid Phase-Catalyzed Hydroformylation: Material and Process Developments. *Ind. Eng. Chem. Res.* **2019**, *58*, 2409–2420.
- (4) Pârvulescu, V. I.; Hardacre, C. Catalysis in Ionic Liquids. *Chem. Rev.* **2007**, *107*, 2615–2665.
- (5) Geldbach, T. J.; Zhao, D.; Castillo, N. C.; Laurenczy, G.; Weyershausen, B.; Dyson, P. J. Biphasic Hydrosilylation in Ionic Liquids: A Process Set for Industrial Implementation. *J. Am. Chem. Soc.* **2006**, *128*, 9773–9780.
- (6) Timken, H. K.; Luo, H.; Chang, B.-K.; Carter, E.; Cole, M. In *Commercial Applications of Ionic Liquids*, Shiflett, M. B., Ed.; Green Chemistry and Sustainable Technology; Springer International Publishing: Cham, 2020, pp 33–47.
- (7) Haumann, M. In *Commercial Applications of Ionic Liquids*, Shiflett, M. B., Ed.; Green Chemistry and Sustainable Technology; Springer International Publishing: Cham, 2020, pp 49–67.
- (8) Niu, T.; Chao, L.; Gao, W.; Ran, C.; Song, L.; Chen, Y.; Fu, L.; Huang, W. Ionic Liquids-Enabled Efficient and Stable Perovskite Photovoltaics: Progress and Challenges. *ACS Energy Lett.* **2021**, *6*, 1453–1479.

- (9) Gu, L.; Ran, C.; Chao, L.; Bao, Y.; Hui, W.; Wang, Y.; Chen, Y.; Gao, X.; Song, L. Designing Ionic Liquids as the Solvent for Efficient and Stable Perovskite Solar Cells. *ACS Appl. Mater. Interfaces* **2022**, *14*, 22870–22878.
- (10) Shahiduzzaman, Md.; Muslih, E. Y.; Hasan, A. K. M.; Wang, L.; Fukaya, S.; Nakano, M.; Karakawa, M.; Takahashi, K.; Akhtaruzzaman, Md.; Nunzi, J.-M.; Taima, T. The Benefits of Ionic Liquids for the Fabrication of Efficient and Stable Perovskite Photovoltaics. *Chemical Engineering Journal* **2021**, *411*, 128461.
- (11) Wang, F.; Ge, C.-y.; Duan, D.; Lin, H.; Li, L.; Naumov, P.; Hu, H. Recent Progress in Ionic Liquids for Stability Engineering of Perovskite Solar Cells. *Small Structures* **2022**, *3*, 2200048.
- (12) Yin, J.; Li, X.; Yu, J.; Zhang, Z.; Zhou, J.; Guo, W. Generating Electricity by Moving a Droplet of Ionic Liquid along Graphene. *Nature Nanotech* **2014**, *9*, 378–383.
- (13) He, Y.; Lao, J.; Yang, T.; Li, X.; Zang, X.; Li, X.; Zhu, M.; Chen, Q.; Zhong, M.; Zhu, H. Galvanism of Continuous Ionic Liquid Flow over Graphene Grids. *Applied Physics Letters* **2015**, *107*, 081605.
- (14) Vu, D. L.; Vo, C. P.; Le, C. D.; Ahn, K. K. Enhancing the Output Performance of Fluid-Based Triboelectric Nanogenerator by Using Poly(Vinylidene Fluoride-Co-Hexafluoropropylene)/Ionic Liquid Nanoporous Membrane. *International Journal of Energy Research* **2021**, *45*, 8960–8970.
- (15) Anderson, J. L.; Armstrong, D. W. Immobilized Ionic Liquids as High-Selectivity/High-Temperature/High-Stability Gas Chromatography Stationary Phases. *Anal. Chem.* **2005**, *77*, 6453–6462.

- (16) Brown, L.; Earle, M. J.; Gilea, M. A.; Plechkova, N. V.; Seddon, K. R. In *Commercial Applications of Ionic Liquids*, Shiflett, M. B., Ed.; Green Chemistry and Sustainable Technology; Springer International Publishing: Cham, 2020, pp 167–189.
- (17) Talebi, M.; Patil, R. A.; Armstrong, D. W. In *Commercial Applications of Ionic Liquids*, Shiflett, M. B., Ed.; Green Chemistry and Sustainable Technology; Springer International Publishing: Cham, 2020, pp 131–165.
- (18) Faisal Elmobarak, W.; Almomani, F.; Tawalbeh, M.; Al-Othman, A.; Martis, R.; Rasool, K. Current Status of CO<sub>2</sub> Capture with Ionic Liquids: Development and Progress. *Fuel* **2023**, *344*, 128102.
- (19) Zhou, Y.; Qu, J. Ionic Liquids as Lubricant Additives: A Review. *ACS Appl. Mater. Interfaces* **2017**, *9*, 3209–3222.
- (20) Anifa Mohamed Faruck, A.; Grützmacher, P. G.; Hsu, C.-J.; Dworschak, D.; Cheng, H.-W.; Valtiner, M.; Stagel, K.; Mikšovský, P.; Sahoo, A. R.; Sainz Martinez, A.; Bica-Schröder, K.; Weigand, M.; Gachot, C. Applying Ionic Liquids as Oil Additives for Gearboxes: Going beyond the State of the Art by Bridging the Nano-Scale and Component Level. *Friction* **2023**, *11*, 1057–1078.
- (21) Wijanarko, W.; Khanmohammadi, H.; Espallargas, N. Ionic Liquid Additives in Water-Based Lubricants for Bearing Steel – Effect of Electrical Conductivity and pH on Surface Chemistry, Friction and Wear. *Frontiers in Mechanical Engineering* **2022**, *7*.
- (22) Song, J. Research Progress of Ionic Liquids as Lubricants. *ACS Omega* **2021**, *6*, 29345–29349.

- (23) Zunita, M.; Batara, B. Antibacterial-Based Ionic Liquids for Environmental Wastewater Treatment. *Case Studies in Chemical and Environmental Engineering* **2023**, *7*, 100341.
- (24) *Commercial Applications of Ionic Liquids*; Shiflett, M. B., Ed.; Green Chemistry and Sustainable Technology; Springer International Publishing: Cham, 2020.
- (25) Eisner, C.; McMillan, N. When Train Crashes Leak Harmful Chemicals, Small Town Firefighters Can Be Vulnerable. *NPR, Investigations* **2023**.
- (26) Conroy, J. O. Train Carrying Hazardous Materials Derails in North Dakota. *The Guardian, US news* **2023**.
- (27) Pati, S. G.; Arnold, W. A. Comprehensive Screening of Quaternary Ammonium Surfactants and Ionic Liquids in Wastewater Effluents and Lake Sediments. *Environ. Sci.: Processes Impacts* **2020**, *22*, 430–441.
- (28) Cho, C.-W.; Pham, T. P. T.; Zhao, Y.; Stolte, S.; Yun, Y.-S. Review of the Toxic Effects of Ionic Liquids. *Science of The Total Environment* **2021**, *786*, 147309.
- (29) Fister, S.; Mester, P.; Sommer, J.; Witte, A. K.; Kalb, R.; Wagner, M.; Rossmannith, P. Virucidal Influence of Ionic Liquids on Phages P100 and MS2. *Front Microbiol* **2017**, *8*, 1608.
- (30) Jing, B.; Lan, N.; Qiu, J.; Zhu, Y. Interaction of Ionic Liquids with a Lipid Bilayer: A Biophysical Study of Ionic Liquid Cytotoxicity. *J Phys Chem B* **2016**, *120*, 2781–2789.
- (31) Gonçalves, A. R.; Paredes, X.; Cristino, A. F.; Santos, F. J.; Queirós, C. S. Ionic Liquids—A Review of Their Toxicity to Living Organisms. *Int J Mol Sci* **2021**, *22*, 5612.

- (32) Amde, M.; Liu, J.-F.; Pang, L. Environmental Application, Fate, Effects, and Concerns of Ionic Liquids: A Review. *Environ. Sci. Technol.* **2015**, *49*, 12611–12627.
- (33) Ren, H.; Qian, H.; Hou, Q.; Li, W.; Ju, M. Removal of Ionic Liquid in Water Environment: A Review of Fundamentals and Applications. *Separation and Purification Technology* **2023**, *310*, 123112.
- (34) Sánchez-Martín, M. J.; Dorado, M. C.; del Hoyo, C.; Rodríguez-Cruz, M. S. Influence of Clay Mineral Structure and Surfactant Nature on the Adsorption Capacity of Surfactants by Clays. *Journal of Hazardous Materials* **2008**, *150*, 115–123.
- (35) Tempel, D. J.; Henderson, P. B.; Brzozowski, J. R. (Air Products and Chemicals Inc). Reactive Liquid Based Gas Storage and Delivery Systems US Patent, 7172646B2, 2007.
- (36) Deer, W. A.; Howie, R. A.; Zussman, J., *An Introduction to the Rock-Forming Minerals*; Mineralogical Society of Great Britain and Ireland: 2013.
- (37) Perkins, S. Quartz Fingers Weak Spots in Earth's Crust. *Science, News* **2011**.
- (38) Ohno, P. E.; Saslow, S. A.; Wang, H.-f.; Geiger, F. M.; Eienthal, K. B. Phase-Referenced Nonlinear Spectroscopy of the -Quartz/Water Interface. *Nat Commun* **2016**, *7*, 13587.
- (39) Ohno, P. E.; Chang, H.; Spencer, A. P.; Liu, Y.; Boamah, M. D.; Wang, H.-f.; Geiger, F. M. Beyond the Gouy–Chapman Model with Heterodyne-Detected Second Harmonic Generation. *J. Phys. Chem. Lett.* **2019**, *10*, 2328–2334.
- (40) Chang, H.; Ohno, P. E.; Liu, Y.; Lozier, E. H.; Dalchand, N.; Geiger, F. M. Direct Measurement of Charge Reversal on Lipid Bilayers Using Heterodyne-Detected Second Harmonic Generation Spectroscopy. *J. Phys. Chem. B* **2020**, *124*, 641–649.

- (41) Ma, E.; Geiger, F. M. Divalent Ion Specific Outcomes on Stern Layer Structure and Total Surface Potential at the Silica:Water Interface. *J. Phys. Chem. A* **2021**, *125*, 10079–10088.
- (42) Nesse, W. D., *Introduction to Mineralogy*; Oxford University Press: 2017; 495 pp.
- (43) Tan, K. H., *Environmental Soil Science*; CRC Press: 2009; 588 pp.
- (44) De Poel, W.; Pintea, S.; Drnec, J.; Carla, F.; Felici, R.; Mulder, P.; Elemans, J. A. A. W.; van Enkevort, W. J. P.; Rowan, A. E.; Vlieg, E. Muscovite Mica: Flatter than a Pancake. *Surface Science* **2014**, *619*, 19–24.
- (45) Lee, S. S.; Fenter, P.; Nagy, K. L.; Sturchio, N. C. Monovalent Ion Adsorption at the Muscovite (001)–Solution Interface: Relationships among Ion Coverage and Speciation, Interfacial Water Structure, and Substrate Relaxation. *Langmuir* **2012**, *28*, 8637–8650.
- (46) Franceschi, G.; Kocán, P.; Conti, A.; Brandstetter, S.; Balajka, J.; Sokolović, I.; Valtiner, M.; Mittendorfer, F.; Schmid, M.; Setvín, M.; Diebold, U. Resolving the Intrinsic Short-Range Ordering of K<sup>+</sup> Ions on Cleaved Muscovite Mica. *Nature Communications* **2023**, *14*, 208.
- (47) Lorenz, B.; Ceccato, M.; Andersson, M. P.; Dobberschütz, S.; Rodriguez-Blanco, J. D.; Dalby, K. N.; Hassenkam, T.; Stipp, S. L. S. Salinity-Dependent Adhesion Response Properties of Aluminosilicate (K-Feldspar) Surfaces. *Energy Fuels* **2017**, *31*, 4670–4680.
- (48) Flehmig, W. The Synthesis of Feldspars at Temperatures between 0 °–80 ° C, Their Ordering Behaviour and Twinning. *Contr. Mineral. and Petrol.* **1977**, *65*, 1–9.

- (49) Liu, W.-T.; Shen, Y. R. Surface Vibrational Modes of  $\alpha$ -Quartz(0001) Probed by Sum-Frequency Spectroscopy. *Phys. Rev. Lett.* **2008**, *101*, 016101.
- (50) Kao, M.-C.; Pegoraro, A. F.; Kingston, D. M.; Stolow, A.; Kuo, W.-C.; Mercier, P. H. J.; Gogoi, A.; Kao, F.-J.; Ridsdale, A. Direct Mineralogical Imaging of Economic Ore and Rock Samples with Multi-Modal Nonlinear Optical Microscopy. *Sci Rep* **2018**, *8*, 16917.
- (51) Jeon, Y.; Min, H.; Kim, D.; Oh-e, M. Determination of the Crystalline X-Axis of Quartz by Second-Harmonic Phase Measurement. *Journal of the Korean Physical Society* **2005**, *46*.
- (52) Saslow Gomez, S. A.; Jordan, D. S.; Troiano, J. M.; Geiger, F. M. Uranyl Adsorption at the Muscovite (Mica)/Water Interface Studied by Second Harmonic Generation. *Environ. Sci. Technol.* **2012**, *46*, 11154–11161.
- (53) Saslow Gomez, S. A.; Geiger, F. M. Precipitates of Al(III), Sc(III), and La(III) at the Muscovite-Water Interface. *J Phys Chem A* **2014**, *118*, 10974–10981.
- (54) Abdelmonem, A.; Lützenkirchen, J.; Leisner, T. Probing Ice-Nucleation Processes on the Molecular Level Using Second Harmonic Generation Spectroscopy. *Atmospheric Measurement Techniques* **2015**, *8*, 3519–3526.
- (55) Zilcher, J. A.; Loiacono, G. M. Non-Centrosymmetry Tests for Potassium Feldspars: An Application of the Second-Harmonic Generator Technique. *J Appl Crystallogr* **1982**, *15*, 540–541.

- (56) Xu, H.; Jin, S.; Lee, S.; Hobbs, F. W. C. Nano-Phase  $\text{KNa}(\text{Si}_6\text{Al}_2)\text{O}_{16}$  in Adularia: A New Member in the Alkali Feldspar Series with Ordered K–Na Distribution. *Minerals* **2019**, *9*, 649.
- (57) Lee, S. S.; Fenter, P.; Park, C.; Sturchio, N. C.; Nagy, K. L. Hydrated Cation Speciation at the Muscovite (001)Water Interface. *Langmuir* **2010**, *26*, 16647–16651.
- (58) Warring, S. L.; Beattie, D. A.; McQuillan, A. J. Surficial Siloxane-to-Silanol Interconversion during Room-Temperature Hydration/Dehydration of Amorphous Silica Films Observed by ATR-IR and TIR-Raman Spectroscopy. *Langmuir* **2016**, *32*, 1568–1576.
- (59) Takamura, T.; Yoshida, H.; Inazuka, K. Infrared Characteristic Bands of Highly Dispersed Silica. *Kolloid-Z.u.Z.Polymere* **1964**, *195*, 12–16.
- (60) Churchill, H.; Teng, H.; Hazen, R. M. Correlation of pH-dependent Surface Interaction Forces to Amino Acid Adsorption: Implications for the Origin of Life. *American Mineralogist* **2004**, *89*, 1048–1055.
- (61) Parks, G. A. The Isoelectric Points of Solid Oxides, Solid Hydroxides, and Aqueous Hydroxo Complex Systems. *Chem. Rev.* **1965**, *65*, 177–198.
- (62) Mroziak, W.; Kotłowska, A.; Kamysz, W.; Stepnowski, P. Sorption of Ionic Liquids onto Soils: Experimental and Chemometric Studies. *Chemosphere* **2012**, *88*, 1202–1207.
- (63) Mroziak, W.; Jungnickel, C.; Skup, M.; Urbaszek, P.; Stepnowski, P.; Mroziak, W.; Jungnickel, C.; Skup, M.; Urbaszek, P.; Stepnowski, P. Determination of the Adsorption Mechanism of Imidazolium-Type Ionic Liquids onto Kaolinite: Implications

- for Their Fate and Transport in the Soil Environment. *Environ. Chem.* **2008**, *5*, 299–306.
- (64) Kraepiel, A. M. L.; Keller, K.; Morel, F. M. M. A Model for Metal Adsorption on Montmorillonite. *Journal of Colloid and Interface Science* **1999**, *210*, 43–54.
- (65) McKinley, J. P.; Zachara, J. M.; Smith, S. C.; Turner, G. D. The Influence of Uranyl Hydrolysis and Multiple Site-Binding Reactions on Adsorption of U(VI) to Montmorillonite. *Clays Clay Miner.* **1995**, *43*, 586–598.
- (66) Turner, G. D.; Zachara, J. M.; McKinley, J. P.; Smith, S. C. Surface-Charge Properties and UO<sub>2</sub><sup>2+</sup> Adsorption of a Subsurface Smectite. *Geochimica et Cosmochimica Acta* **1996**, *60*, 3399–3414.
- (67) Wu, H.; Xu, Z.; Zhu, L.; Cheng, X.; Kang, M. Adsorption of Strontium at K-feldspar-water Interface. *Applied Radiation and Isotopes* **2022**, *181*, 110111.